1991

The dynamics of underwater explosions

John Philip Best
University of Wollongong

THE DYNAMICS OF UNDERWATER EXPLOSIONS

A thesis submitted in fulfilment of the requirements

for the award of the degree of

DOCTOR OF PHILOSOPHY

from

THE UNIVERSITY OF WOLLONGONG

by

John Philip Best B.Sc.(Hons)

DEPARTMENT OF MATHEMATICS

1991

CONTENTS

DECLARATION

This thesis is submitted to the University of Wollongong, N.S.W., Australia and I declare that the work contained herein has not been submitted for a degree to any other university or institution.

John P. Best

March 1991

ACKNOWLEDGEMENTS

Thanks are due to my supervisors, Professor John Blake and Dr. Noel Smyth, for introducing me to the respective fields of bubble dynamics and shock dynamics, and for their interest and helpful comments throughout the course of this work.

The financial support of a Defence Science and Technology Organisation Post Graduate Fellowship, awarded by the Materials Research Laboratory, is acknowledged. I would like to thank the people there, in particular Mr. Keith Gibbs, Mr. Ian Hagan and Mr. Wynford Connick, for their support and the interest they have shown in this work.

Helpful comments by Dr. T. S. Horner and Professor G. B. Whitham are acknowledged, as is the contribution of Professor J. M. Hill who acted as a supervisor during the final months of my candidacy.

A special thankyou is due to Dr. Adam Kucera who provided his boundary integral code which was modified to undertake aspects of this study, and to Helen Whiter who typed the manuscript. Apart from their technical contributions both have been wonderful friends.

Thanks also to my parents and family, George, Katrina, Lynne and Kelly for their support over the past few years.

ABSTRACT

The two principal phenomena associated with an underwater explosion are bubble motion and shock wave propagation. In this thesis both are investigated.

The study of bubble dynamics proceeds by assuming irrotational flow in an incompressible and inviscid fluid. A technique is developed for the derivation of equations of motion for a spherical bubble in flow domains of simple geometry. The concept of the Kelvin impulse is exploited in this endeavour. The spherical model is used to infer the behaviour of bubbles that deform from spherical shape.

The boundary integral method is then employed to compute the motion of underwater explosion bubbles. The pressure within the bubble is assumed to be a function of the bubble volume and it is demonstrated that under some circumstances the increasing bubble pressure upon collapse will cause the non-spherical bubble to rebound. In these cases the high speed liquid jets characteristic of bubble collapse are shown to grow during the rebound phase of the motion. Data for the behaviour of bubbles described by a wide range of the physical parameters governing the motion is presented.

The jet that forms upon collapse or rebound threads the bubble and ultimately impacts upon the far side of the bubble. To date, boundary integral methods have been unable to compute the motion beyond this time. Thus the impact is considered and a boundary integral method is developed to compute the motion of the toroidal bubble that is created by this jet penetration. The dynamics of toroidal bubbles is then investigated.

The theory of geometrical shock dynamics is considered in the context of the propagation of an underwater blast wave. The significant feature of such a wave is the non-uniform flow field behind the shock. In order to account for this flow the propagation of a shock down a tube of slowly varying cross section is reconsid-

ered. The solution of this problem is the basis for the theory of geometrical shock dynamics. It is found that the propagation is described by an infinite sequence of ordinary differential equations that can be closed by a process of truncation. Truncation at higher equations allows higher order derivatives of flow quantities evaluated at the shock to be included in the description of the shock motion. In this manner account may be taken of non-uniform flow conditions behind the shock. These equations are implemented in the numerical scheme of geometrical shock dynamics and the diffraction of an underwater blast wave is considered.

1

INTRODUCTION TO UNDERWATER EXPLOSION RESEARCH

1.1. A brief history of underwater explosion research

The detonation of a mass of explosive beneath the ocean surface causes a complex sequence of physical phenomena to occur. Supposing that the detonation occurs at the centre of the explosive, a detonation wave then propagates to the surface of the explosive where it meets the surrounding water. Left in the path of the detonation wave is an approximately spherical volume of gas at high temperature and pressure, and we will refer to this volume of gas as the explosion bubble. The interaction of the detonation wave with the surrounding water causes a rapid compression and a shock wave is transmitted into the water. Accompanying this is the reflection of a wave back into the explosion bubble. At this time we further suppose that due to the high temperature associated with the detonation the water surrounding the bubble is rapidly heated and a phase transition to the gaseous state takes place. In addition, chemical reactions may still be taking place within the bubble, amongst the remnants of the detonation.

Although this early behaviour is very complex, a short time later observations indicate that the primary behaviour can be described by a simpler picture. The principal phenomena occurring are the propagation of a spherical shock wave into the water at a speed of about $1500 ms^{-1}$ and the oscillation of the explosion bubble, with a period of about one second. The initial high pressure of the gas inside the bubble drives its expansion, with the subsequent decrease of this pressure causing the outwards motion to be brought to rest by the hydrostatic pressure in the fluid. The bubble then collapses, with the now increasing pressure ultimately arresting the collapse and causing the bubble to rebound. The motion observed is thus oscillatory.

When a plane acoustic wave is reflected normal to a rigid boundary the pressure experienced at the boundary is twice that of the incident pulse. In the case of reflection of shock waves this factor is greater than two and because of the large shock wave pressures generated by an underwater explosion, the potential for damage due to the impact of the shock upon some marine structure is clear. As an example of the bubble phenomenon, if we consider the detonation of $1000lb$ $(453.6kg)$ of the explosive TNT at a depth of $50ft$ $(15.24m)$ then the bubble formed grows to a maximum radius of about $30ft$ $(9.144m)$ and displaces 3630 *tons* (3200 *tonnes*) of water. This value is of the same order as the displacement of typical warships (a typical displacement for a destroyer is 7600 *tons* (6700 *tonnes*)). When this observation is coupled with the knowledge that this fluid at times undergoes a very high speed motion it becomes apparent that the fluid motion induced by the oscillations of the explosion bubble may be a damage causing agent of significance comparable to that of the shock wave.

Each of these phenomena may be characterised by its own time scale. For the sake of comparison we might choose a time scale for the shock wave motion to be that time it would take the shock to propagate a distance of the order of the maximum bubble radius. For the above mentioned example this yields a value of $t_s \sim 6 \times 10^{-3}s$. The bubble motion is well characterised by its period $t_b \sim 1s$, and that these values differ by two orders of magnitude gives strong support to the assumption that a very short time after the detonation has occurred the two phenomena may be considered as independent. The great majority of studies of underwater explosion effects have exploited this assumption and introduced independent models to describe the motion of the shock and bubble.

An early study of considerable significance in the field of bubble research was the investigation by Lord Rayleigh (1917) of the collapse of a spherical transient cavity in an infinite fluid. In that study it was assumed that the gas within the bubble consists of the liquid vapour, exerting a constant pressure throughout the lifetime of the bubble. The significant demonstration is the very high pressure

generated in the fluid near to the bubble surface as it collapses to a singularity. This analysis was extended in the context of underwater explosion research by Lamb (1923) who assumed that the pressure within the explosion bubble varies as

$$p = p_0(V_0/V)^\gamma, \tag{1.1.1}$$

with V the volume, γ a constant and the subscript denoting initial values. Lamb carried through the analysis for the cases $\gamma = 1$ and $\gamma = 4/3$.

Early experimental effort was due to Ramsauer (1923) who used a system of electrodes to record radius vs. time data for the expansion of the bubble produced by the firing of guncotton charges. In the apparatus used, the water between a remote electrode and a series of electrodes placed at increasing distances from the charge completes a series of electrical circuits. As the bubble expands each electrode eventually becomes isolated from the water and the circuit is broken. Recording the time at which each circuit is broken provides a radius vs. time history for the expansion phase of the bubble motion. Ramsauer found good agreement with the predictions of the simple theory of the variation of the maximum bubble radius with depth and mass of explosive.

Little work of significance was done between this time and World War II, which provided the impetus for a great experimental and theoretical effort. The work of this period consisted of modelling the explosion bubble as spherical and assuming the surrounding water to be inviscid and incompressible and the flow induced by the bubble's motion as irrotational. Advances over the previous theoretical studies were the inclusion of buoyancy forces, certainly significant given the size of an explosion bubble, and a description of the influence of boundaries, the interaction with targets and the ocean surface providing the motivation for this consideration. For motion under the influence of buoyancy alone Herring (1941) first gave the system of equations describing the evolution of the explosion bubble. This system is

$$\frac{d}{dt}\left(R^3 U\right) = 2gR^3, \tag{1.1.2}$$

$$2\pi\rho R^3\left(\frac{dR}{dt}\right)^2+\frac{\pi}{3}\rho R^3U^2+\frac{4\pi}{3}\rho R^3gz=Y-E(R), \tag{1.1.3}$$

$$U=-\frac{dz}{dt}, \tag{1.1.4}$$

where R is the bubble radius, U the velocity of the bubble centroid and z is the position of the bubble centroid measured in the direction of the gravitational acceleration, whose magnitude is given by g. The internal energy of the bubble contents is given as a function of the radius via $E(R)$, ρ is the density of the fluid, t the time and Y is the total energy of the system and hence constant. The hydrostatic pressure is ρgz. A comprehensive numerical investigation of this system was undertaken by Taylor (1942). Herring (1941) also gave the equations for motion in the neighbourhood of a free or rigid boundary and these are

$$\frac{d}{dt}\left(R^3U\right)=\mp\frac{3}{4}\frac{R^4}{z^2}\left(R\frac{d^2R}{dt^2}+3\left(\frac{dR}{dt}\right)^2\right), \tag{1.1.5}$$

and

$$2\pi\rho R^3\left(1\mp\frac{R}{2z}\right)\left(\frac{dR}{dt}\right)^2+\frac{\pi}{3}\rho R^3U^2=Y-E(R), \tag{1.1.6}$$

where buoyancy is not included, z is measured away from the boundary and U is as defined in (1.1.4). The upper sign gives the equations for motion near a free boundary and the lower sign for motion in the neighbourhood of a rigid boundary. These equations were deduced by expanding the velocity potential for the flow in terms of spherical harmonics and performing a similar expansion for the radial co-ordinate of points on the bubble surface. To the order computed by Herring the action of the perturbation due to either gravity or nearby boundaries is to merely displace the bubble as a whole, rather than deform it from spherical shape.

Accompanying these theoretical developments were experimental programs, the significant technique employed being high speed photography, which allowed accurate records of the bubble shape as a function of time and the migration behaviour of the bubble to be obtained, with data also being recorded during the collapse phase of the motion. Significant studies in this context include those of Taylor and Davies (1943) and Bryant (1944). The results of these studies indicate

good agreement with the theoretical predictions of the bubble radius and centroid position during the expansion phase and early collapse phase. It was found, however, that during the later stages of the collapse the bubble departs noticeably from spherical shape, with the bottom side of an upwards translating bubble becoming flattened as the bubble accelerates forward during its collapse. Accompanying this is a failure of the simple model to accurately predict the upwards migration of the bubble. A further study of significance is that of Swift and Decius (1947) in which up to three oscillations of the bubble produced by a deep explosion were observed. It was found that the maximum radius associated with each oscillation decreases, despite the simple model predicting an increase due to the decreasing hydrostatic pressure as the bubble rises.

This observed departure from spherical shape raises the question of the stability of the spherical form. The observation that for deep explosions a mix of gas and water, rather than a connected bubble, reaches the surface indicates a break up of the initially spherical bubble and motivated Penney and Price (1942) to consider the stability of an initially spherical bubble rising under the action of buoyancy forces. They proceeded in their analysis by expanding the radial co-ordinate of points on the bubble surface and the expression for the velocity potential at this surface in terms of spherical harmonics, and assuming small perturbations in the shape were able to compute the initial growth of these perturbations. The results of the linear analysis indicate that the growth phase is stable against perturbations, but that upon collapse any initial perturbations in the shape will grow, buoyancy being a source of such perturbation. The results of that study are, however, limited by the fact that the analysis is linear.

Although work on underwater explosion bubble dynamics has continued since this time the level of activity has not been so intense. The book *Underwater Explosions* by Cole (1948) provides an excellent and complete review of the wartime research. A more recent review is that of Holt (1977) and little progression beyond the war time modelling of Herring and Taylor is evident. A point of some

significance, however, is the postulate attributed to Snay (1960) that the bubble generated by a deep explosion rises for much of its lifetime with an attached vortex ring. This postulate is based upon the photographic records of bubbles deforming from spherical shape, with the flattening of the underside indicating the formation of a re-entrant jet that threads the bubble from the rear and ultimately penetrates it completely, generating a vortex ring. Holt presents some computations treating the bubble as a Hill's spherical vortex in order to make some assessment of this matter. The significant point is that a considerable amount of kinetic energy is bound in the vortex motion. As mentioned previously the experiments of Swift and Decius (1947) show a decreasing maximum radius as a bubble rises. Assuming a spherical form for the bubble produces estimates of a significant energy loss between pulsations. Herring (1949) presented a discussion of possible loss mechanisms including radiation of acoustic energy, turbulence and heat transfer and concluded that although the principal loss mechanism is via radiation it cannot account for the apparent losses as computed from the experimental data. The computations of Holt indicate that the quantity of kinetic energy bound in the vortex motion is of the same order as that which appears to be lost between successive pulsations, as computed assuming a spherical form. This computation thus provides some evidence in support of the postulate that the bubble develops some vortex structure upon collapse.

Although the specific problem of underwater explosion bubble dynamics has received little direct attention since WWII very significant advances have been made in the study of cavitation bubble dynamics, continuing on from the work of Lord Rayleigh. In the first instance considerable refinement and innovation has occurred in the development of experimental techniques. Landmark studies of the dynamics of cavities in the neighbourhood of solid boundaries include those of Naude and Ellis (1961) and Benjamin and Ellis (1966). These experiments respectively utilised spark discharge and the kinetic impulse method to generate cavities, but both employed high speed photography to record the bubble motion

and both demonstrated the non-spherical character of the collapse. It was found that the part of the bubble surface furthermost away from the boundary collapses at greater speed than other parts, ultimately forming a high speed liquid jet that threads the bubble and finally impacts upon the far side of the bubble, nearest the rigid boundary. It is the impact of the jet that is proposed as the mechanism for cavitation damage. Subsequent studies (see for example Gibson, 1968) have included an investigation of bubble motion near boundaries with some compliance and indicate a dependence of the character of the jet upon the nature of the boundary.

In more recent times the spark discharge technique of bubble generation has been further refined and some excellent experimental results are available in the work of Chahine (1977, 1982) and Blake and Gibson (1981). Laser technology has also been employed in the generation of bubbles and the use of modern optical techniques, including holography, coupled with filming rates of up to 10^6 frames per second have allowed a more complete description of the bubble collapse phenomenon to be obtained. These techniques have been pioneered by Lauterborn and his co-workers (Lauterborn and Bolle, 1975; Lauterborn, 1982; Lauterborn and Vogel, 1984; Lauterborn and Hentschel, 1985). In a recent study (Vogel et al., 1989) these techniques were implemented to study the motion of laser generated cavities in the neighbourhood of a rigid boundary, with significant results being the recording of multiple oscillations of the bubbles and the demonstration of the evolution into a vortex ring bubble as a result of penetration by the jet.

In the study of Tomita and Shima (1986) the question of surface damage caused by the impact of the jet was experimentally investigated by utilising photoelastic materials in the construction of a boundary and a schlieren technique in order to visualise the stress field induced in the boundary by the impact of the jet caused by adjacent cavity collapse. Furthermore, the use of a soft material, indium, as a boundary demonstrated the pitting caused by the impact of jets.

Accompanying these experimental efforts have been theoretical advances of

equal significance. In their landmark paper Benjamin and Ellis (1966) introduce the concept of the Kelvin impulse to the study of bubble dynamics. In their discussions qualitative features of the bubble collapse phenomenon, such as the deformation from spherical shape during the collapse of a translating bubble and its proposed ultimate fate as a vortex system, are plausibly explained using the properties of the Kelvin impulse. More quantitative approaches include full numerical solutions of Laplace's equation that describes the flow field, allowing the pressure and fluid velocity fields to be determined as a function of time. Plesset and Chapman (1971) employed a marker in cell technique and computed the collapse of an initially spherical vapour cavity adjacent to a rigid boundary. Their calculations demonstrate the formation of a high speed jet directed towards the boundary. The motion of the jet is followed up until the time that it impacts upon the far side of the bubble.

Since this time the boundary integral method has been shown to be a powerful technique for the computation of bubble motion. The work of Guerri et al. (1981) and Blake et al. (1986, 1987) are particularly successful applications of the technique. The computations of Kucera and Blake (1988) utilising this method compare well with the results of experiment (Vogel et al., 1989). Although the bubble produced by an underwater explosion differs from the bubbles of these studies, both in magnitude and in the nature of the bubbles contents, the fluid dynamics problem is the same and the evidence obtained during WWII indicates the formation of jets. The potential for damage due to jet impact, as demonstrated in experimental studies of small scale bubbles, gives an indication of the importance of consideration of this phenomenon in assessing the potential for damage by an underwater explosion.

The mathematical description of the propagation of shock waves underwater requires the consideration of a compressible fluid, in contrast to the incompressible fluid description employed in modelling the bubble motion. Prior to any attempt to develop a theory for the generation or propagation of the shock wave produced

by an underwater explosion it was pointed out by Hilliar (1919) that a short distance from the charge the shock is weak so that entropy changes throughout the fluid may be neglected and the pressure considered as a function of density alone. In this regime the equations of compressible flow are invariant if the time and length scales are changed by the same constant factor, with the pressure left unchanged. The Rankine-Hugoniot shock jump conditions which are satisfied at the shock front also exhibit this invariance leading to the statement by Hilliar that the peak pressure, p_i, experienced at some target point a distance r from the charge will be given as

$$p_i = f(W^{1/3}/r), \tag{1.1.7}$$

where f is an unknown function and W is the charge mass. The length scale is given by the linear dimensions of the charge, proportional to $W^{1/3}$. This concept has become known as the principle of similarity and it is discussed in some detail by Cole (1948), including a description of the criteria for it to be applicable and circumstances under which it will fail. The experimental results reported by Hilliar (1919) mark the first attempt to verify this principle. Although previous experimenters had compiled data for the peak pressure produced by a shock wave by employing crusher gauges, Hilliar developed his own variant with the significant capability of recording to some extent the pressure-time history of the wave form. His results provided not only confirmation of the principle but also a good body of data which may be applied to charges of any mass via the principle of similarity (provided of course that the constraints on its applicability are not violated). These results, although subsequently superceded by those obtained using superior apparatus, also gave an indication of what is now the generally accepted description of the pressure wave; that of an exponential decay.

It is supposed that upon passage of the shock the pressure rises to some peak value, p_i, and thereafter decays exponentially, this decay characterised by the time constant τ_i. We write

$$p = p_i e^{-t/\tau_i}. \tag{1.1.8}$$

This form has been well verified by experimental studies employing piezoelectric gauges to record pressure vs. time data, the first such investigation using this method attributed to Keys (1921). The principle of similarity asserts that the time constant must vary as

$$\tau_i = W^{1/3} g(W^{1/3}/r), \tag{1.1.9}$$

with the function g unknown. The experimental data has been successfully summarised by assuming power law functions in (1.1.7) and (1.1.9). Values for the coefficients and exponents in these power laws may be found in Cole (1948) and further data establishing an extended range of values of $W^{1/3}/r$ over which these expressions are applicable has been recorded by Arons (1954). In more recent times data for explosions near to the ocean surface has been compiled by Ross Chapman (1985) and relationships based on the principle of similarity fitted to the data.

The classical theoretical treatment of the blast wave produced by an underwater explosion is that due to Kirkwood and Bethe (1942). In their theory the character of the shock wave is related to the detonation process by considering the generation of the shock by the rapid acceleration of the bubble/water interface during the early times just after the completion of the detonation. In this way relations may be deduced that give the parameters characterising the shock wave as functions of physical quantities describing the explosive. The theory is thus valuable in assessing the usefulness of particular explosives. A most significant approximation employed in the theory is the so-called peak approximation. This approximation involves assuming an exponential decay for certain quantities characterised by a high initial peak and very large and negative initial value of the first time derivative. It is this approximation that yields from the Kirkwood-Bethe theory the result that the pressure at some target point decays exponentially, and the expressions obtained for the peak pressure and time constant as functions of range are found to be in good agreement with the experimental data.

During this time a numerical investigation of the generation and propagation of an underwater blast wave was undertaken by Penney and Dasgupta (Penney, 1941; Penney and Dasgupta, 1942) in which the equations of compressible flow were integrated along characteristics, with a shock fitted to the solution. The numerical calculation and the theory of Kirkwood and Bethe differ in their predictions close in to the charge but tend towards each other as distance increases. The difference is due to different assumptions about the conditions at the conclusion of the detonation. For further details regarding this comparison the reader is referred to Cole's book, including a discussion of the propagation theory of Kirkwood and Brinkley (1945).

The review of Holt (1977) reports refined numerical computations and the application of the point blast solution (Taylor, 1950; Sedov, 1945 a,b) to propagation in water using an appropriate equation of state. This solution assumes propagation of shocks in the strong shock limit and that the shock is generated by the instantaneous release of a finite amount of energy. As such it is only applicable to the case of a nuclear explosion and even so becomes invalid as the shock decays and the pressure ahead of the shock is no longer negligible compared to that behind. For propagation in such cases modifications must be made.

A further study since WWII that is of interest is that of Rogers (1977) in which the propagation of a weak shock in water is considered. It is assumed that at some initial range the pressure due to the passage of the shock decays exponentially. By assuming a weakly non-linear form for the solution, expressions are obtained for the variation of the peak pressure and time constant with range. Good agreement is found with the predictions of the Kirkwood-Bethe theory and available experimental data. In contrast to the Kirkwood-Bethe theory, though, this theory is merely one of propagation and does not address the relationship between the shock and the detonation. As such the initial wave form must be determined by independent methods.

Although considerable attention has been paid to the generation and prop-

agation of the blast wave produced by an underwater explosion, little work has addressed the question of its interaction with targets. The diffraction of the shock by solid boundaries gives rise to a pressure experienced at the boundary either greater or less than that in the incident wave, the exact value determined by the geometry. The phenomenon of shock diffraction thus assumes significance in assessing the potential for damage to a structure due to the impact of an underwater blast wave.

1.2. Preface to this work

As past workers have done we consider in this work the two major underwater explosion phenomena of bubble motion and shock motion as distinct. We do not concern ourselves with the very earliest times, when the detonation wave interacts with the surrounding water to initiate the shock wave, with the gaseous remains of this detonation providing the very high initial pressure that drives the bubble motion. We suppose that some short time after these occurrences we can well describe the motion of the shock wave and the bubble as independent phenomena. Indeed, the fundamental assumptions used to formulate mathematical descriptions of each are incompatible.

In part I of this work we consider the motion of a bubble as assumed to take place in an incompressible and inviscid fluid, with the flow induced by the bubble's motion irrotational. Within this model a number of investigations are pursued, the principal concern being with the jetting phenomenon so well described in studies of vapour cavities. In the first instance global studies of fluid momentum are reviewed, the concept of the Kelvin impulse being exploited. The impulse corresponds to the effective momentum of the bubble and this interpretation allows an analogy to be drawn with the momentum of particle mechanics, an analogy which has been exploited in the past to determine gross aspects of the bubble motion, in particular its migratory response towards the end of its lifetime. In that work singularities are used to represent the lowest order contributions to the

velocity potential of the fluid and image theory is exploited to consider motion in the neighbourhood of some geometries in which the flow field is three dimensional and symmetry cannot be exploited to simplify the analysis.

In this work we develop a technique for determining equations of motion for translating bubbles constrained to remain spherical throughout their lifetime. The concept of the Kelvin impulse is exploited in this endeavour and singularities are utilised to represent the velocity potential. Systems of ordinary differential equations are deduced and these may be routinely and inexpensively solved. Just as the Kelvin impulse has been exploited by Blake and his co-workers to determine aspects of the later motion of bubbles, when they deform from spherical shape, so too can the consideration of translating spherical bubbles be similarly used. It is proposed that the direction of migration at the end of the bubble life (or first oscillation), as predicted by spherical bubble dynamics, corresponds to the direction of jet formation in asymmetric collapse. The equations of spherical bubble dynamics predict that this direction is co-incident with that of the Kelvin impulse at that time. The example of cavitation bubble motion in an axisymmetric geometry is one in which there is a body of experimental and numerical data and is thus used to validate the results inferred from the spherical model. The comparison suggests the value of the approach and extension to three dimensional flows is made, the validation of such results left for later study.

Since our primary concern is with explosion bubbles, or bubbles containing non-condensible contents, the elementary model is employed to infer what behaviour we should expect upon the collapse of such bubbles. The intriguing question is whether the high pressures that arise when the bubble collapses are capable of arresting any jetting motion. The spherical model and consideration of the Kelvin impulse suggest circumstances under which this may occur. In order to validate such speculations numerical studies of explosion bubble motion are undertaken using the boundary integral method. The predictions are confirmed, with jetting being generally observed, but under the circumstances identified by

considering the spherical model, the non-spherical bubble is found to rebound. Even in these cases, however, jetting is observed with the bulk of the growth of the jet occurring as the bubble re-expands.

In all numerical simulations of bubble motion to date using the boundary integral method, it is only possible to complete the computation up until the time that the jet impinges upon the far side of the bubble. It is apparent that the bubble then evolves into a toroidal form with the flow possessing a circulation. Thus consideration is given to the moment of impact and a boundary integral method is developed to compute the motion of a toroidal bubble. To adequately deal with the circulation it is necessary to introduce a cut in the doubly connected flow domain in order to render it simply connected. Implementation of the method allows computation of the motion of the toroidal bubble and the oscillatory nature of the toroidal form is demonstrated.

The propagation of the shock wave is considered in part II, the emphasis being upon the development of a technique for the computation of the diffraction of an underwater blast wave by targets of various geometries. To model this phenomenon we must specifically include a description of the compressibility of water in order that shock wave solutions to the equations of motion exist. This contrasts with the incompressible description of the fluid used in part I.

The theory of geometrical shock dynamics, due to Whitham (1957, 1959, 1974), may be applied to propagation in water upon provision of an appropriate equation of state and is ideally suited to computing the motion of diffracting shock waves. Reformulation of the theory using the Tait equation of state for water is a routine task, however, the uniform initial flow conditions behind the shock that are assumed in this theory are not approximately satisfied in the case of an underwater blast wave, as evidenced by the exponential decay of the pressure. Thus it is necessary to reconsider the motion of a shock down a tube of slowly varying cross section, the solution of this problem being the basis for the theory of geometrical shock dynamics. A mathematical structure following from the equa-

tions of motion is noted, and this allows non-uniform flow conditions behind the shock to be included in the description of the propagation only via the value of derivatives of flow quantities evaluated at the shock. The motion of the shock can thus be computed without the necessity of obtaining a solution for the flow field behind the shock. The theory of geometrical shock dynamics is then appropriately modified and implemented in a numerical scheme in order that general problems of shock diffraction may be computed. The approach is validated by comparison with other theoretical studies of underwater shock propagation, the agreement found to be excellent. The numerical implementation for two dimensional problems allows further comparisons to be made with experimental data. With these results confirming the validity of the approach examples of the diffraction of underwater blast waves are computed.

PART I - BUBBLE DYNAMICS

2

THE DESCRIPTION OF THE FLOW FIELD

2.1. The mathematical model

We suppose that a bubble undergoes some motion in a fluid and we shall denote the domain occupied by the fluid as Ω, with $\partial\Omega$ signifying its boundary. The bubble surface, S, is a subset of $\partial\Omega$ and in the case where motion occurs in an infinite fluid $S \equiv \partial\Omega$. We shall further denote by $\mathbf{n}$ the normal to $\partial\Omega$ and choose that it be directed exterior to Ω. We allow for the presence of a uniform gravitational field and choose a cartesian set of axes, defined by the orthonormal basis $\mathbf{e}_x, \mathbf{e}_y, \mathbf{e}_z$, such that the gravitational acceleration is given by $\mathbf{g} = -g\mathbf{e}_z$. A schematic representation of this geometry is shown in figure 2.1.1.

We describe the fluid as inviscid and incompressible and the flow induced by the bubble's motion as irrotational. We may then introduce a velocity potential, ϕ, so that the fluid velocity, $\mathbf{u}$, is given by

$$\mathbf{u} = \nabla\phi, \tag{2.1.1}$$

with ϕ satisfying Laplace's equation in Ω;

$$\nabla^2\phi = 0. \tag{2.1.2}$$

On $\partial\Omega$ we must employ appropriate boundary conditions. In this study $\partial\Omega$ will only be composed of rigid and free boundaries. There is no flow normal to a rigid boundary so here we impose that the velocity potential satisfies

$$\nabla\phi \cdot \mathbf{n} = 0. \tag{2.1.3}$$

To determine the free boundary condition we appeal to the momentum equation, the integrated form of which is the Bernoulli equation, which in our co-ordinate system takes the form

$$\frac{\partial\phi}{\partial t} + \frac{1}{2}|\nabla\phi|^2 + p/\rho + gz = p_\infty/\rho. \tag{2.1.4}$$

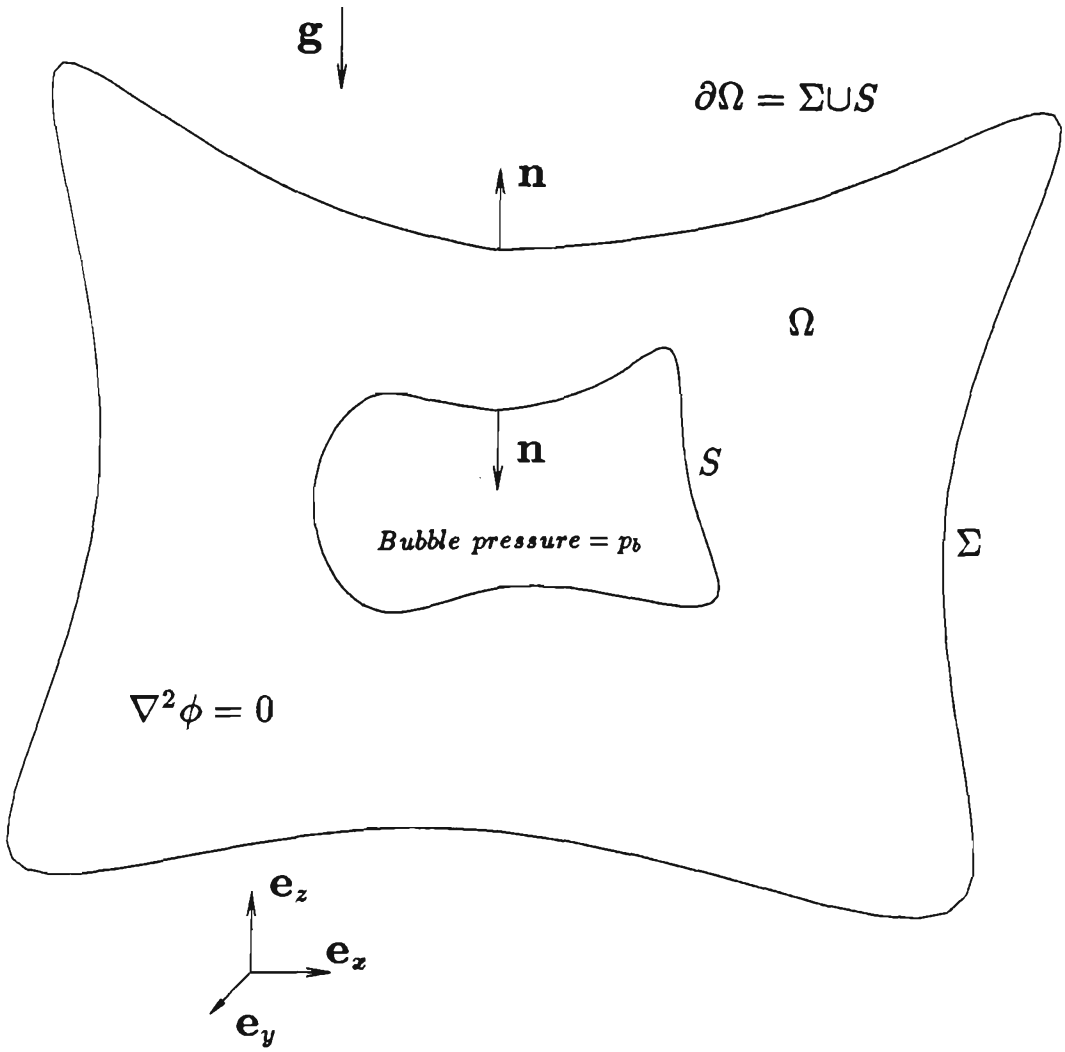

Figure 2.1.1. The geometry used to consider general bubble motion.

In this expression t, ρ, p and p_∞ respectively denote the time, density, pressure and hydrostatic pressure at $z = 0$, where ϕ and its derivatives vanish. At a free surface the pressure in the fluid is equal to the pressure external to the fluid at that point, and this is assumed to be known independently of the description of the fluid. Use of this value for the pressure at the free surface in equation (2.1.4) defines a non-linear boundary condition to be satisfied by the potential function at the free surface. We comment that the bubble surface S is a free surface, with the pressure at the surface determined by the mathematical description we choose for the bubble contents.

We will shortly have cause to employ a linearised version of (2.1.4). At an infinite free surface, defined as the plane $z = z_0$, at which the pressure remains constant (such as the ocean surface), equation (2.1.4) gives

$$\frac{\partial \phi}{\partial t} + \frac{1}{2} |\nabla \phi|^2 + g(\zeta - z_0) = 0, \tag{2.1.5}$$

when evaluated at this surface. In this expression ζ is the elevation of the free surface. If the fluid velocity there is sufficiently small, so that its modulus squared can be neglected in (2.1.5), as can the term $g(\zeta - z_0)$ due to the small displacement of the free surface, then if the initial potential there is zero we obtain the linearised free boundary condition of

$$\phi = 0. \tag{2.1.6}$$

It can be routinely shown that for the motion of a spherical bubble not too close to an infinite free surface neglect of the fluid velocity and surface displacement in (2.1.5) is valid.

We comment at this point that we have neglected surface tension effects. To account for this phenomenon would require the addition of the term

$$-\zeta \sigma / \rho \tag{2.1.7}$$

to the left hand side of (2.1.4), when applied at the surface of the bubble. In this expression σ is the surface tension and ζ is the curvature of the surface, measured

positive with respect to a centre of curvature exterior to Ω. Computations including this effect have been performed and the reader is referred to the work of Chahine and Perdue (1988) and Chahine (1990) for details.

We employ an elementary description of the bubble contents. Studies of cavitation bubble dynamics have assumed that the bubble contents consist of the liquid vapour, and that it exerts a constant pressure, p_c, throughout the lifetime of the bubble. An explosion bubble, however, contains the gaseous remnants of a detonation. We suppose that we can describe this gas as ideal, and that on the timescale of the bubble oscillation there is negligible heat exchange with the surrounding fluid, so that the expansions and compressions of this gas are adiabatic. Indeed, Herring (1949) has discussed this aspect and demonstrates that over the period of oscillation of the explosion bubble the heat lost to the surrounding fluid is negligible compared to the internal energy of the bubble contents. Hence we write the pressure, p_g, exerted by the gaseous bubble contents as a function of the volume, V, via

$$p_g = p_0(V_0/V)^\gamma, \tag{2.1.8}$$

where the subscript 0 denotes initial quantities and γ is the ratio of specific heats. For the products of various explosives γ is empirically determined. For instance TNT is characterised by $\gamma = 1.25$. We typically choose $\gamma = 1.4$ for air (diatomic gas with 5 degrees of freedom) and it is this value that we will utilise throughout this study. If we consider that the explosion bubble might also contain some liquid vapour then the pressure, p_b, inside our explosion bubble is given by

$$\begin{aligned} p_b &= p_c + p_g, \\ &= p_c + p_0(V_0/V)^\gamma. \end{aligned} \tag{2.1.9}$$

Since we are concerned with a time dependent phenomenon we complete our description of the model with the provision of initial conditions. We will have cause to perform some calculations for cavitation bubbles so we first consider the initial conditions used in this case. The equation describing the motion of a spherical

cavitation bubble in an infinite fluid is (Lord Rayleigh, 1917)

$$R\ddot{R} + \frac{3}{2}\dot{R}^2 + \Delta p/\rho = 0, \tag{2.1.10}$$

where

$$\Delta p = p_\infty - p_c, \tag{2.1.11}$$

and R is the radius of the bubble, with dots denoting time derivatives. In the study of cavitation bubble dynamics it is assumed that the infinite fluid, spherical bubble solution provides a valid description of the earliest motion of the bubble. This is not unreasonable as during this short time, when the bubble is very small, the buoyancy force is negligible and the presence of nearby boundaries is little felt. Thus we suppose that our bubble is initially spherical and has some initial radius, R_0, with the corresponding initial time determined from the solution of (2.1.10). The initial potential on the bubble surface is then uniform and given by

$$\phi_0 = -R_0\dot{R}_0. \tag{2.1.12}$$

If we denote by R_m the maximum radius to which this bubble grows, then we have (Blake et al., 1986)

$$\phi_0 = -R_0\left[\frac{2}{3}\left(\frac{\Delta p}{\rho}\right)\left\{\left(\frac{R_m}{R_0}\right)^3 - 1\right\}\right]^{1/2}, \tag{2.1.13}$$

$$t_0 = 3R_m\left(\frac{3\rho}{2\Delta p}\right)^{1/2} B_a(5/6, 3/2); \quad a = (R_0/R_m)^3, \tag{2.1.14}$$

where B_a denotes an incomplete Beta function (Abramowitz and Stegun, 1965). This provides the initial data from which we can compute the subsequent motion of the bubble. At stationary free surfaces the initial potential may be set equal to zero.

Before departing from this consideration of the Rayleigh bubble we make note of the finite lifetime of the bubble. From inception the bubble grows to a maximum radius and then collapses to a singularity. The motion is symmetrical about the time that the bubble achieves its maximum radius and we can exploit this

symmetry to compute the half life of the bubble from (2.1.10) and thus determine its lifetime. If we denote it by T_c then we have (Lord Rayleigh, 1917)

$$T_c = 6\sqrt{3/2}B(5/6, 3/2)R_m(\rho/\Delta p)^{1/2},$$
$$\approx 1.829R_m(\rho/\Delta p)^{1/2}, \tag{2.1.15}$$

where $B(x, y)$ is a Beta function (Abramowitz and Stegun, 1965).

It is useful at this point to introduce a time and length scale, and a number of the physical parameters that characterise the motion. We choose the maximum bubble radius, R_m, as a length scale and $R_m(\rho/\Delta p)^{1/2}$ as a time scale. The potential scale is thus $R_m(\Delta p/\rho)^{1/2}$. In these scaled variables we choose an initial bubble radius of 0.1 and so obtain from (2.1.13) and (2.1.14) the initial conditions for a cavitation bubble as

$$R_0 = 0.1, \ \phi_0 = -2.5806976, \ t_0 = 0.0015527, \tag{2.1.16}$$

with a consequent initial radial velocity of

$$\dot{R}_0 = 25.806976. \tag{2.1.17}$$

Using this scaling the Bernoulli equation evaluated at the surface of the cavitation bubble becomes

$$\frac{\partial \phi}{\partial t} + \frac{1}{2}|\nabla \phi|^2 + \delta^2 z - 1 = 0, \tag{2.1.18}$$

where

$$\delta = (\rho g R_m/\Delta p)^{1/2} \tag{2.1.19}$$

is the buoyancy parameter. Physically δ corresponds to the ratio of the bubble half life to the time it would take a bubble of radius R_m to rise the order of one radius from rest due to buoyancy forces. It thus provides a measure of the strength of the buoyancy force.

In the explosion bubble example, the presence of the non-condensible gas provides a much greater freedom in the choice of initial conditions. At the initial small radius, R_0, the detonation products are highly compressed and the large initial pressure, p_0, drives the motion, in addition to any initial radial velocity that

we may impose upon the system. We thus have the option of choosing a multitude of combinations of initial pressure and radial velocity, the assumption that the bubble is initially spherical being retained. This freedom of choice is, however, superfluous due to the relative unimportance of buoyancy and boundary effects during the early phases of the motion. Let us consider the equation describing the purely radial motion of a bubble whose contents are described by (2.1.9). It is

$$R\ddot{R} + \frac{3}{2}\dot{R}^2 = \epsilon(R_0/R)^{3\gamma} - 1, \tag{2.1.20}$$

where the above distance and time scales have been employed and we notice the introduction of the parameter

$$\epsilon = p_0/\Delta p \tag{2.1.21}$$

as a measure of the strength of the initial high pressure, p_0, that drives the motion. We shall call ϵ the strength parameter. Equation (2.1.20) describes oscillatory motion so that given an initial non-zero radial velocity we may integrate (2.1.20) backwards in time to obtain a new initial radius and pressure (new value of ϵ) corresponding to a zero initial radial velocity. For all except very small amplitude radial oscillations the time over which this backwards integration must take place is negligible compared to the period of the oscillation so that the motion over this time is little influenced by the presence of boundaries or the buoyancy force.

Thus we suppose that the initial radial velocity of our explosion bubble is zero, with the motion driven from rest by the very high initial pressure p_0. The initial potential on the bubble surface is thus taken to be zero. We choose our initial radius such that the maximum radius to which the bubble expands is one. Integrating (2.1.20) we have

$$\dot{R}^2 = \frac{2\epsilon R_0^{3\gamma}}{3(\gamma-1)}\left(R^{-3} - R^{-3\gamma}\right) + \frac{2}{3}\left(R^{-3} - 1\right), \tag{2.1.22}$$

where we have used $\dot{R} = 0$ at $R = 1$. $\dot{R}$ is also equal to 0 at R_0 and this condition yields from (2.1.22) an equation for R_0 which we solve using Newton's method. The value for the initial radius is dependent upon the value of the strength parameter,

ϵ, with each value of it specifying a corresponding initial radius. Typical values of ϵ and the corresponding initial radii are shown in table 2.1.1.

Finally note that we have allowed account to be taken of a constant vapour pressure, p_c, as contributing to the total pressure within the explosion bubble. In practice, we find that for those contracted phases of the motion where the non-condensible nature of the bubble contents is important, the partial pressure due to the non-condensible gas is much greater than the vapour pressure, thus we may neglect p_c in our expression for the internal bubble pressure. From a deeper viewpoint, the mathematical effect of the term p_c is simply to displace the effective hydrostatic pressure, for the dynamics is dependent upon the fundamental pressure scale $\Delta p = p_\infty - p_c$.

ϵ	R_0
10	0.3804
25	0.2706
50	0.2108
100	0.1651
200	0.1297
500	0.0947
1000	0.0748

Table 2.1.1. Values of the strength parameter and the corresponding initial radii.

2.2. The validity of the mathematical model

The model presented in section 2.1 is the simplest possible description that we could employ for the flow field induced by the motion of a bubble. We have neglected the viscosity and compressibility of the water, surface tension at the bubble wall and any flow of the gas within the bubble. If we consider viscosity first then a number of elementary observations indicate that it is not unreasonable to neglect viscous stresses.

The time scale of the motion is $R_m (\rho/\Delta p)^{1/2}$, the lifetime of the bubble being of this order. The length scale is R_m giving the Reynolds number as

$$R_e = R_m (\rho \Delta p)^{1/2} / \mu, \tag{2.2.1}$$

where μ is the dynamic viscosity of water. Now $\rho \sim 10^3 kgm^{-3}$ and $\mu \sim 10^{-1} kgms^{-1}$ and a typical value for the maximum radius of an explosion bubble is $R_m \sim 10m$. Since explosion bubble motion will typically take place in the neighbourhood of the ocean surface we have $\Delta p \sim 10^5 pa$ yielding a Reynolds number $R_e \sim 10^6$. It is also worthwhile to comment on small scale experiments of bubble dynamics. The spark discharge generated bubbles investigated in the experiments of Blake and Gibson (1981) were of maximum radius $R_m \sim 10^{-2} m$ and created at a reduced pressure of $\Delta p \sim 10^4 pa$ yielding a Reynolds number $R_e \sim 10^4$. In both cases it appears that the effect of viscosity will be small.

We can expand our consideration a little by considering the equation of motion of a spherical bubble including viscosity and surface tension. Both effects enter into the model via the consideration of the bubble/gas interface. Surface tension only acts at such a boundary and viscosity enters via the continuity of normal stress at the free surface, this effect having been first clarified by Poritsky (1952). The equation is

$$R\ddot{R} + \frac{3}{2}\dot{R}^2 + \frac{4\mu}{\rho}\frac{\dot{R}}{R} + \frac{2\sigma}{\rho R} = (p(V) + p_c - p_\infty)/\rho, \tag{2.2.2}$$

where the pressure within the bubble is given as in (2.1.9). Introducing our usual

scaling this becomes

$$R\ddot{R} + \frac{3}{2}\dot{R}^2 + \frac{4}{R_e}\frac{\dot{R}}{R} + \frac{2}{\tau}\frac{1}{R} = p(V) - 1, \tag{2.2.3}$$

where R_e is as defined in (2.2.1) and

$$\tau = \Delta p R_m/\sigma, \tag{2.2.4}$$

is a parameter indicating the magnitude of surface tension forces. In (2.2.3) $p(V)$ is the partial pressure due to the non-condensible bubble contents scaled by Δp.

That the Reynolds number defined by (2.2.1) appears naturally in the equation of motion of a spherical bubble indicates the relevance of this definition in assessing the importance of viscosity in this case. It is not, however, appropriate for the consideration of a translating bubble, in which we should seek another definition that gives some indication of the thickness of the presumed thin boundary layer surrounding the bubble. If we consider a spherical bubble of constant radius R_m rising under the action of buoyancy then the acceleration is $2g$. After translating a distance R_m the velocity of the bubble is $2(g\,R_m)^{1/2}$ which is an appropriate velocity scale and gives an expression for the Reynolds number of

$$R_e = 2\rho g^{1/2} R_m^{3/2}/\mu \sim 10^5 R_m^{3/2}, \tag{2.2.5}$$

indicating an exceedingly thin boundary layer about the translating bubble. The structure of this boundary layer and the thin wake trailing such a bubble has been considered by Moore (1963).

These considerations of both radial and translational motion of a bubble indicate that viscosity may indeed be neglected. We can take this as strong evidence that even in asymmetric collapse the role of viscous stresses is negligible on the scale of the phenomenon that is of interest to us.

Equation (2.2.3) allows us to make some estimate of the importance of surface tension via the constant τ. The surface tension between water and air at $20°C$ is $\sigma \sim 7.28\times10^{-2} Nm^{-1}$ and representative of the value between water and a gas, so that

for $\Delta p \sim 10^5 pa$ and $R_m \sim 10m$ we have $\tau \sim 10^7$. The largeness of this value indicates that unless $R \sim 10^{-7}$ then this term is negligible compared to the pressure terms on the right hand side of (2.2.3). On the scale that is of concern in the consideration of underwater explosions such small radii will never arise. Even in most small scale experiments such small values of the radius are unlikely to eventuate. In the general case of non-spherical bubble motion, surface tension is accounted for in application of the Bernoulli equation at the bubble surface and the parameter τ arises with the term quantifying surface tension being

$$2\zeta/\tau, \tag{2.2.6}$$

with ζ the local curvature of the bubble surface. Again we comment on the exceedingly large curvatures that would be required in order that this term becomes significant compared to the pressure terms in the Bernoulli equation, indicating that except for very extreme circumstances the fluid motion is inertia dominated. The circumstances under which surface tension may assume some significance arise in the case of small scale experiments with jet formation giving rise to regions of sufficiently high curvature.

Regarding our description of the water surrounding the bubble we make a few final comments on the compressibility of water. Water has a finite but small compressibility as indicated by the large value of approximately $1500ms^{-1}$ for the speed of propagation of small amplitude acoustic disturbances. There are two circumstances under which the effects of fluid compressibility may become significant. The first is if the fluid velocity becomes comparable with the speed of sound. The Rayleigh analysis yields a fluid velocity at the surface of the bubble that becomes singular as the bubble radius tends to zero. Under these circumstances compressibility must become significant and this effect has been comprehensively investigated. An excellent summary and source of further references is the book by Hammitt (1980).

In these investigations equations of motion are developed for spherical bubbles

in a fluid of small compressibility, with the results indicating a divergence from the predictions of the Rayleigh solution which becomes significant as the radius falls below about one tenth of its maximum value. However, as noted by Hammitt, in any real flow field there are asymmetries, which may be due to buoyancy or the presence of nearby boundaries, and in the presence of such perturbing influences spherical shape cannot be maintained to sufficiently small radii for such high fluid velocities to be attained, and for compressibility effects to become significant. Indeed, the experimental and numerical evidence to date confirms this. The experiments of Benjamin and Ellis (1966) and Gibson (1968) indicate peak fluid velocities in the high speed liquid jet that forms upon collapse of $50 - 75ms^{-1}$. More recent experiments by Lauterborn and Bolle (1975) and Shima et al. (1981) indicate velocities in the range $90 - 100ms^{-1}$. The numerical computations of jet formation by Blake et al. (1986) are in good agreement with these values. We note that these peak fluid velocities are small compared to the speed of sound in water and indicate that during the growth and collapse of a bubble it is not unreasonable to neglect fluid compressibility.

The fundamental difference between an explosion bubble and cavitation bubble is the nature of the bubble contents. Although as a cavitation bubble collapses some of the vapour will not condense due to the small time over which the collapse occurs, there is a much greater quantity of non-condensible gas inside an explosion bubble which generates very high pressures within the bubble and ultimately causes the bubble surface to rebound. It is at this moment of rebound that the second circumstance arises under which the compressibility of the fluid may become significant. At rebound we may consider the surface of the bubble, that changes direction over a very short period of time, as a piston driving against the inrushing fluid, generating a wave of finite amplitude and possibly a weak shock. This phenomenon of wave emission upon rebound is well documented in experimental studies of underwater explosion bubbles and is significant from the viewpoint that the periodic emission of waves may excite resonance in structures.

Computations of this phenomenon are presented by Hammitt (1980).

The incompressible model cannot provide a description of this wave emission, however, we again expect that any asymmetry in the flow field will cause non-spherical bubble collapse and that this lack of spherical symmetry will lead to reduced fluid acceleration upon rebound and somewhat mitigate the significance of this phenomenon. We further comment that the fast rebounding motion of the bubble surface that drives the emission of acoustic energy occurs only over a very short period of time. Thereafter it is again a very good approximation that the flow is incompressible. Because of the short period over which this compressible phenomenon may manifest itself we expect that the incompressible model will provide a good indication of the general behaviour. The lack of a description of compressible effects is perhaps the greatest defect of the model, but in this work we endeavour to determine significant features of the motion of explosion bubbles by describing the fluid as incompressible.

Finally, we note that the gas within the bubble is itself a fluid, however its viscosity is negligible compared to that of water. Further we note that the speed of sound in this gas is approximately $300ms^{-1}$ which is about three times greater than the peak fluid velocities observed and computed for non-spherical cavitation bubble collapse. This is not sufficient to raise the possibility of generation of pressure waves of such an amplitude that they will influence the motion of the surrounding fluid. Indeed, due to the high compressibility of gas, in order to generate a wave of significant pressure amplitude would require that the motion of the bubble boundary be at least of the same magnitude as the speed of sound in the gas. In view of these considerations it would be inconsistent with the level of approximation used in the description of the water to attempt any more detailed description of the bubble contents.

3

KELVIN IMPULSE AND SPHERICAL BUBBLES

3.1. Introduction

The phenomenon of jet formation during the collapse of transient cavities near boundaries, or underwater explosion bubbles in the neighbourhood of marine craft, is postulated as a principal mechanism for causing damage. Although asymmetry in the flow field is known to cause the formation of these jets, and buoyancy and nearby boundaries are common causes of this asymmetry, the phenomenon is not so well understood that given the physical parameters describing the motion we can completely determine the character of the jet (the time of formation, the speed, the breadth, the mass contained within it) without the necessity of computing the whole of the flow field.

If, however, we choose an aim more modest than specifying the complete character of the jet given the physical parameters governing the motion, then progress can be made. In particular, by considering the global conservation of fluid momentum via a quantity known as the Kelvin impulse it is possible to estimate the direction of migration of a bubble at the end of its lifetime, and in the case where a jet is formed identify this with the direction of the jet. This method has met with considerable success when applied to cavitation bubble motion in an axisymmetric geometry, as confirmed by the results of numerical simulations of the bubble motion. In this chapter we review the concept of the Kelvin impulse and its application to cavitation bubble dynamics, along with the extension of the ideas developed in an axisymmetric geometry to geometries where the three dimensional character of the flow field is essential.

A particular observation exploited in the analysis using the Kelvin impulse is that for much of its lifetime we can well approximate the bubble's shape as spherical. This feature is evident in a multitude of experimental (Benjamin and Ellis,

1966; Gibson, 1968; Lauterborn and Bolle, 1975; Tomita and Shima, 1986; Vogel et al., 1989) and numerical (Guerri et al., 1981; Blake et al., 1986, 1987) investigations. If we introduce this observation into the mathematical model presented in chapter 2 then we may derive a system of ordinary differential equations that determine the radius and centroid position of the bubble as functions of time. The study of the dynamics of spherical bubbles forms the remainder of this chapter. In achieving this end we exploit the Kelvin impulse to determine a momentum equation of motion and the Bernoulli equation to determine an energy equation.

The assumption of spherical shape provides a description applicable throughout much of the lifetime of a bubble. It is only in the later stages of this life, when the bubble deforms significantly from spherical shape and jets are formed, that this description is no longer applicable. Typically, the time over which this non-spherical collapse occurs is of the order of 2-3% of the bubble life. Lifetime here refers to the time from inception of the motion to the instant that the jet completely penetrates the bubble. The investigation of the Kelvin impulse indicates that we can infer aspects of the motion of deforming bubbles from the early behaviour, when the bubble is spherical. With this in mind we can compute the time dependent early behaviour of bubbles in various geometries, and from the behaviour predicted towards the end of the bubble life attempt to infer the character of the collapse of deforming bubbles. In particular, application to the problem of axisymmetric motion near a rigid boundary validates the approach.

The study of spherical bubbles also allows us to begin an investigation into the effect that a non-condensible gas inside the bubble has upon its motion. Having developed some confidence in inferring from the behaviour of spherical cavitation bubbles the later behaviour of deforming bubbles, we consider the dynamics of spherical bubbles containing a non-condensible gas and attempt to infer the behaviour we should expect from a deforming bubble. The intriguing question here is that of the possibility of bubble rebound. Of course a spherical bubble containing such a gas will oscillate, but when jets are formed it is not obvious what behaviour

we should expect. It might be supposed that the increasing pressure within the bubble as it collapses might arrest jet formation. The consideration of spherical bubbles and the Kelvin impulse suggests in what physical regimes a non-spherical bubble should rebound.

3.2. The Kelvin impulse in the context of bubble dynamics

Considerations of fluid momentum when a body moves through an infinite expanse of fluid require some care due to the possible divergence of the momentum integral. For the case of rigid body motion through a fluid the formalism that addresses this problem in an appropriate manner was investigated by Lord Kelvin who considered the impulse required to establish the rigid body/fluid motion at any instant. Lamb (1932) discusses the concept of impulse at length, noting that

> *"whatever the motion of the solid and fluid at any instant, it might have been generated instantaneously from rest by a properly adjusted impulsive 'wrench' applied to the solid."*

Equivalently, an equal and opposite impulse will bring the observed motion to rest.

Let us expand further on this concept in the context of a non-spherical bubble. In figure 3.2.1(a) we have a typical bubble shape during the later stages of the collapse when a jet has formed and is threading the bubble. Suppose that in this figure the fluid is at rest and we wish to generate the motion from rest by the application of an impulsive force over the surface S. Since the fluid is incompressible the disturbances associated with this impulse are transmitted with infinite speed throughout the fluid and establish the observed flow field. Following the discussion in Batchelor (1967) we consider the momentum equation

$$\frac{\partial \mathbf{u}}{\partial t} + \mathbf{u} \cdot \nabla \mathbf{u} = -\nabla p/\rho. \tag{3.2.1}$$

During the short interval over which the impulse is delivered the fluid velocity may change in value discontinuously. However, throughout this change the values of the velocity and its spatial derivatives remain finite and are negligible compared

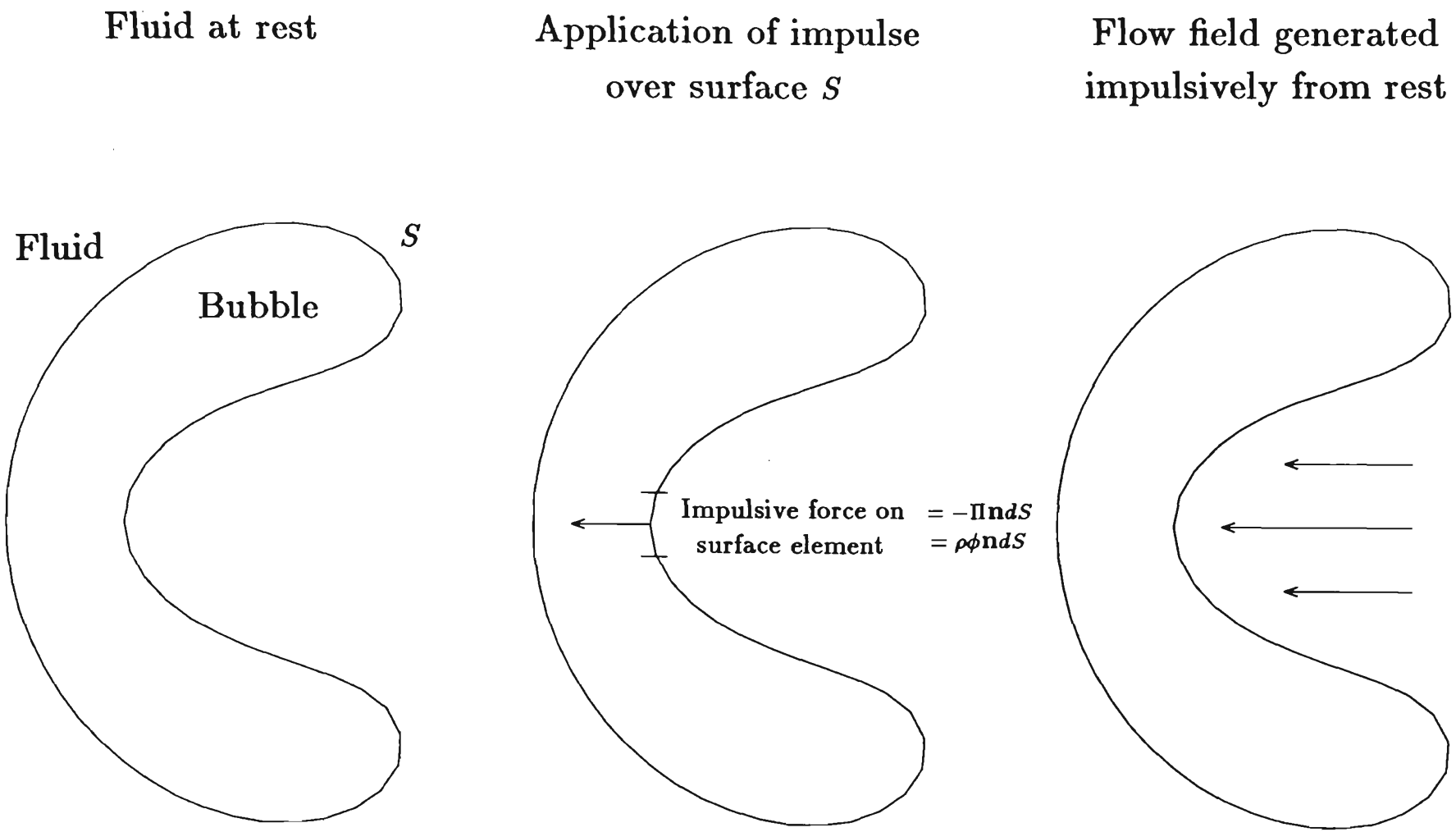

Figure 3.2.1. Establishing the flow field associated with jetting motion impulsively from rest.

to $\frac{\partial \mathbf{u}}{\partial t}$, so that over the short interval during which the impulse is delivered we can write

$$\frac{\partial \mathbf{u}}{\partial t} = -\nabla p/\rho. \tag{3.2.2}$$

Integrating over the duration of the impulse we have

$$\mathbf{u}^f - \mathbf{u}^i = -\nabla \Pi/\rho, \tag{3.2.3}$$

where

$$\Pi = \int p \, dt, \tag{3.2.4}$$

is the pressure impulse and the superscripts i and f denote values immediately prior to, and immediately after the delivery of the impulse. This argument is valid when viscosity is included, but in our case where the fluid velocity is the gradient of a velocity potential we deduce from (3.2.3) that

$$\phi^f - \phi^i = -\Pi/\rho. \tag{3.2.5}$$

In the example under consideration, where we generate the motion from rest, we take $\phi^i = 0$ and drop the superscript f. On an element of the bubble surface dS the impulse applied is

$$d\mathbf{I} = -\Pi \mathbf{n} dS = \rho \phi \mathbf{n} dS, \tag{3.2.6}$$

noting that $\mathbf{n}$ is directed into the bubble and ϕ is the potential for the observed flow field. Hence the total impulse required to establish the flow from rest is

$$\mathbf{I} = \rho \oint_S \phi \mathbf{n} dS, \tag{3.2.7}$$

and this expression has become known as the Kelvin impulse of the bubble. The procedure of generating the flow field impulsively from rest is illustrated in figure 3.2.1 and it is clear that in the case of jetting motion the Kelvin impulse and jet direction should be closely correlated.

The utility of this concept lies in the fact that the Kelvin impulse varies in response to the action of external forces just as the momentum of a finite dynamical system does. Kelvin established that for rigid body motion through an infinite fluid

$$\frac{d\mathbf{I}}{dt} = \mathbf{F}, \tag{3.2.8}$$

where **F** is the external force acting. Lamb notes that the arguments of Kelvin carry through when the body is deformable (or when we have a collection of bodies, or when we replace them by masses of fluid moving rotationally). If we consider that the bubble possesses an impulse **I**, with the impulse changing in response to the action of external forces as described by (3.2.8) then there is an obvious analogy with the dynamics of a rigid particle under the action of forces. For motion in the neighbourhood of boundaries familiarity with the phenomenon of the impact of rigid particles gives an intuitive appreciation of the potential for impact phenomena in the case of bubble motion. This view has been central to the development of the Kelvin impulse as an analytical tool in bubble dynamics, the principal work being that of Benjamin and Ellis (1966), Blake et al. (Blake and Cerone, 1982; Blake et al., 1986, 1987; Blake, 1988) and Oguz and Prosperetti (1990). This work has primarily addressed the question of what form expression (3.2.8) must take for the motion of a deformable body (bubble), when the motion takes place in some semi-infinite domain in which boundaries occur, and this expression has then been used to determine aspects of jet formation, the impact phenomenon associated with the collapse of cavities.

We shall restrict our attention to the case where conservative body forces act so that the Bernoulli equation takes the form

$$\frac{\partial \phi}{\partial t} + \frac{1}{2}|\nabla \phi|^2 + p/\rho + \Phi = p_\infty/\rho, \tag{3.2.9}$$

where Φ is the potential for the conservative force field such that the body force per unit mass, **f**, is given by

$$\mathbf{f} = -\nabla \Phi. \tag{3.2.10}$$

In the far field, where $p = p_\infty$, we assume that Φ vanishes. By considering conservation of momentum within some control volume enclosing the bubble and considering the limit where the control volume becomes the domain of the flow, we may deduce the expression for the time rate of change of the Kelvin impulse

(see Blake, 1988, for details of this calculation),

$$\frac{d\mathbf{I}}{dt} = \mathbf{F}(t) = \rho \int_{\Sigma_b} \left[\frac{1}{2} |\nabla\phi|^2 \mathbf{n} - \frac{\partial\phi}{\partial n} \nabla\phi \right] dS + \rho \int_V \nabla\Phi dV, \tag{3.2.11}$$

where V is the volume of the bubble, and Σ_b consists of any naturally occurring boundaries in the domain of the flow, excluding the bubble surface. Examples of possible geometries for Σ_b will be discussed later. In our case where $\Phi = gz$ (uniform gravitational field) the final contribution to $\mathbf{F}$ is just the buoyancy force $\rho g V \mathbf{e}_z$. The contribution to the force, $\mathbf{F}$, of the integral over the boundary Σ_b quantifies the influence upon the Kelvin impulse of the flow induced by the presence of boundaries. This force is known as the Bjerknes force.

A case of particular interest is that of the collapse of a cavitation bubble above a rigid boundary where the Bjerknes attraction of the boundary and the buoyancy force are in opposition. The bubble is characterised by a constant vapour pressure, p_c, within the cavity throughout its lifetime. The geometry is shown in figure 3.2.2. This problem has been the subject of numerical simulations using the boundary integral method (Guerri et al., 1981; Blake et al., 1986. A marker in cell technique was employed by Plesset and Chapman, 1971). During the expansion phase of the motion the bubble retains an approximately spherical shape. As the bubble collapses an initial perturbation on either the upper or lower pole develops and quickly grows into a jet which rapidly penetrates the bubble. Whether this jet forms at the upper or lower pole depends upon the distance from the boundary at which inception occurs and the magnitude of the buoyancy force (Blake et al., 1986, 1987; Vogel et al., 1989).

The Kelvin impulse has been proposed as a tool for predicting the direction of this jet. The argument proceeds as follows. Integrating (3.2.11) we have

$$\mathbf{I}(t) = \mathbf{I}(0) + \int_0^t \mathbf{F}(\tau) d\tau. \tag{3.2.12}$$

For an initially stationary spherical bubble we have $\mathbf{I}(0) = \mathbf{0}$ so that the Kelvin impulse at some later time may be determined if $\mathbf{F}$ is known. The expression of

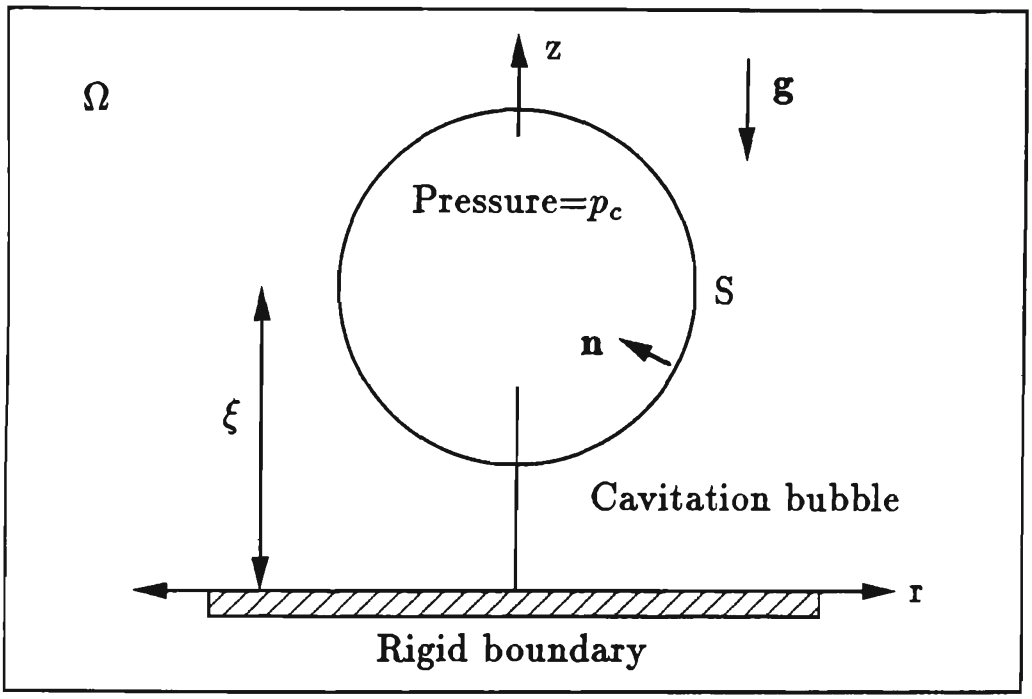

Figure 3.2.2. Geometry for the dynamics of a buoyant cavitation bubble above a rigid boundary.

(3.2.11) assumes its usefulness from the fact that we require an expression for the potential at the surface Σ_b which is remote from the bubble surface, S. Hence, in any approximate determination of $\mathbf{F}$, only the contribution to ϕ of the lowest order terms need be used. For flows in semi-infinite domains this lowest order contribution to ϕ is that due to source like terms. In this example the lowest order contribution to the potential is due to a source singularity of time dependent strength $m(t)$ located at the bubble centroid and an image source, so we may write

$$\phi \sim -\frac{m(t)}{4\pi \mid \mathbf{r} \mid} - \frac{m(t)}{4\pi \mid \mathbf{r}' \mid} + \ldots, \tag{3.2.13}$$

where $\mathbf{r}$ is the position vector of some point in the flow field relative to the bubble centroid and $\mathbf{r}'$ is the position vector of this point relative to the image of the bubble centroid reflected about the rigid boundary. The image is required so that the lowest order terms satisfy the rigid boundary condition. Making use of (3.2.13) in (3.2.11) we find that

$$F_z(t) = -\frac{\rho m^2(t)}{16\pi\xi^2(t)} + \rho g V(t), \tag{3.2.14}$$

where the only non-zero component of $\mathbf{F}$ is in the z-direction and $\xi(t)$ is the location of the bubble centroid above the rigid boundary (figure 3.2.2). In order to carry out the integration of (3.2.12) expressions for $m(t)$, $V(t)$ and $\xi(t)$ are required. The assumption made is that for much of the bubble lifetime it remains approximately spherical and so is described by the Rayleigh solution for a spherical cavitation bubble (equation (2.1.10)). Consistent with the use of the Rayleigh solution we suppose that $\xi(t)$ is constant throughout the motion and equal to its initial value ξ_0. For a spherical bubble $m(t) = 4\pi R^2 \dot{R}$ so we have

$$m(t) = \pm 4\pi R^2 \left[\frac{2}{3}\left(\frac{\Delta p}{\rho}\right)\left(\frac{R_m^3}{R^3} - 1\right)\right]^{\frac{1}{2}}, \tag{3.2.15}$$

with this quantity positive during the expansion phase of the motion and negative during the collapse phase. We make use of these results and integrate (3.2.14) over the lifetime, T_c, of the bubble to obtain the Kelvin impulse at the end of the collapse as (Blake, 1988)

$$I(T_c) = \frac{2\sqrt{6}\pi R_m^5 (\rho\Delta p)^{\frac{1}{2}}}{9\xi_0^2}\left[2\gamma^2\delta^2 B(11/6, 1/2) - B(7/6, 3/2)\right], \tag{3.2.16}$$

where $B(z,w)$ is the beta function (Abramowitz and Stegun, 1965). We have defined

$$\gamma = \xi_0 / R_m \tag{3.2.17}$$

as a dimensionless parameter specifying the point at which the motion begins. The buoyancy parameter, δ, is as discussed in chapter 2.

Having established (3.2.16) it is proposed that the direction of the Kelvin impulse at the end of the bubble lifetime determines the direction of the centroid migration and if a jet is formed, the direction of the jet. Thus, if we examine the $\gamma - \delta$ parameter space there exists a line given by

$$\gamma\delta = \left(\frac{B(7/6, 3/2)}{2B(11/6, 1/2)} \right)^{\frac{1}{2}} = 0.442 \tag{3.2.18}$$

that partitions the space into a region for which $I(T_c)$ is positive, corresponding to migration away from the boundary, and a region for which $I(T_c)$ is negative, corresponding to migration towards the boundary. Since $I(T_c) = 0$ for points on this line we shall refer to it as the null impulse line.

This simple idea appears to be a reliable predictor of bubble motion. It compares well with the results of numerical simulations (Blake et al., 1986). Success is also apparent in studies of motion in the neighbourhood of a free surface, where experimental data has been included in the comparison (Blake et al., 1987). Furthermore, extensions to the consideration of compliant boundaries are in reasonable agreement with the scarce experimental data available (Blake, 1988). The success of this technique no doubt depends upon the fact that for much of the motion the bubble is spherical, with departures from sphericity and jet formation occurring over a very short period of time, an observation that is to be important in our later considerations.

3.3. Extension to three dimensional geometries

We will now consider bubble motion occurring in a variety of simple geometries. The assumptions of section 3.2 allow us to determine the Kelvin impulse, $\mathbf{I}(T_c)$, at

the end of the collapse phase. We then propose that gross aspects of the bubble motion at the conclusion of the collapse may be inferred from knowledge of $\mathbf{I}(T_c)$.

Motion near an inclined plate

Suppose that there is an infinite rigid boundary whose normal makes some angle α with the direction of gravity, and that bubble motion takes place in its neighbourhood. The appropriate geometry is shown in figure 3.3.1. We introduce co-ordinates (ξ, η) to describe the bubble's position, where ξ measures the distance from the wall and η measures the distance travelled parallel to the wall. We choose initial conditions $\xi(0) = \xi_0$ and $\eta(0) = 0$. It is useful to note the transformation to the usual cartesian set of axes with the direction $\mathbf{e}_z$ being in opposition to the gravitational acceleration $\mathbf{g}$. We constrain our motion to occur in the x-z plane so that the relevant transformation is

$$\begin{aligned} x &= (\xi - \xi_0)\sin\alpha - \eta\cos\alpha, \\ z &= (\xi - \xi_0)\cos\alpha + \eta\sin\alpha, \end{aligned} \tag{3.3.1}$$

where α is the angle between the exterior normal to the plate and $\mathbf{g}$.

In order to evaluate $\mathbf{F}$ we require the lowest order contribution to the potential at the boundary Σ_b which consists of the rigid plate as shown in figure 3.3.1. The appropriate potential is due to a source of strength $4\pi R^2\dot{R}$ located at the bubble centroid and an image source of the same strength reflected about the rigid boundary. It is then a routine matter to evaluate (3.2.11), whence we obtain the components of $\mathbf{F}$ as

$$F_\xi = \frac{4}{3}\pi\rho\left\{-\frac{3}{4}\frac{R^4\dot{R}^2}{\xi^2} + gR^3\cos\alpha\right\}, \tag{3.3.2}$$

$$F_\eta = \frac{4}{3}\pi\rho g R^3\sin\alpha. \tag{3.3.3}$$

The behaviour that we expect to occur in general (as suggested by the experimental results of Benjamin and Ellis, 1966) is that the bubble, which is well modelled as spherical at inception, retains this shape approximately as it expands to its maximum radius, then collapses with a well defined jet formed at some characteristic angle, θ, measured with respect to the normal to the plane, exterior to the

flow domain. We propose that this angle is given by the direction of the Kelvin impulse at the end of the bubble lifetime, which is

$$\theta = \arctan\left(-I_\eta(T_c)/I_\xi(T_c)\right). \tag{3.3.4}$$

We proceed as in section 3.2 to obtain expressions for the components of the Kelvin impulse at the end of the bubble lifetime. We make use of the Rayleigh bubble solution for $R(t)$ and assume that throughout the bubble lifetime $\xi(t) = \xi_0$, its value at inception, in order that we may integrate equations (3.3.2) and (3.3.3) to obtain expressions for the components of the Kelvin impulse required for evaluation of θ. We routinely obtain (Blake and Prosperetti, 1989)

$$\theta = \arctan\left[\frac{2\gamma^2\delta^2 B(11/6,1/2)\sin\alpha}{B(7/6,3/2) - 2\gamma^2\delta^2 B(11/6,1/2)\cos\alpha}\right], \tag{3.3.5}$$

where the dimensionless parameters γ and δ are as previously defined. Example computations of θ will follow shortly.

Motion near a horizontal free surface and vertical rigid wall

In the previous example the motion of the bubble was influenced by the presence of the rigid boundary and the effects of buoyancy. The rigid boundary attracts the bubble whereas buoyancy causes the bubble to rise in the direction opposite to the gravitational field. It is possible to proceed to further examples in which a third influence on the bubble is present and it is expected that interesting behaviours will result. A case of particular interest is that of motion occurring both in the neighbourhood of a vertical rigid wall and the free ocean surface, an example in which we have the further effect of repulsion from the free surface. From a practical viewpoint this may represent a simplified model of some marine structure which is subject to attack by an underwater explosion. The geometry is shown in figure 3.3.2.

We introduce a co-ordinate ξ to measure the displacement from the vertical wall and a co-ordinate η to measure the depth of the bubble below the ocean surface. The appropriate image set that gives the lowest order contribution to

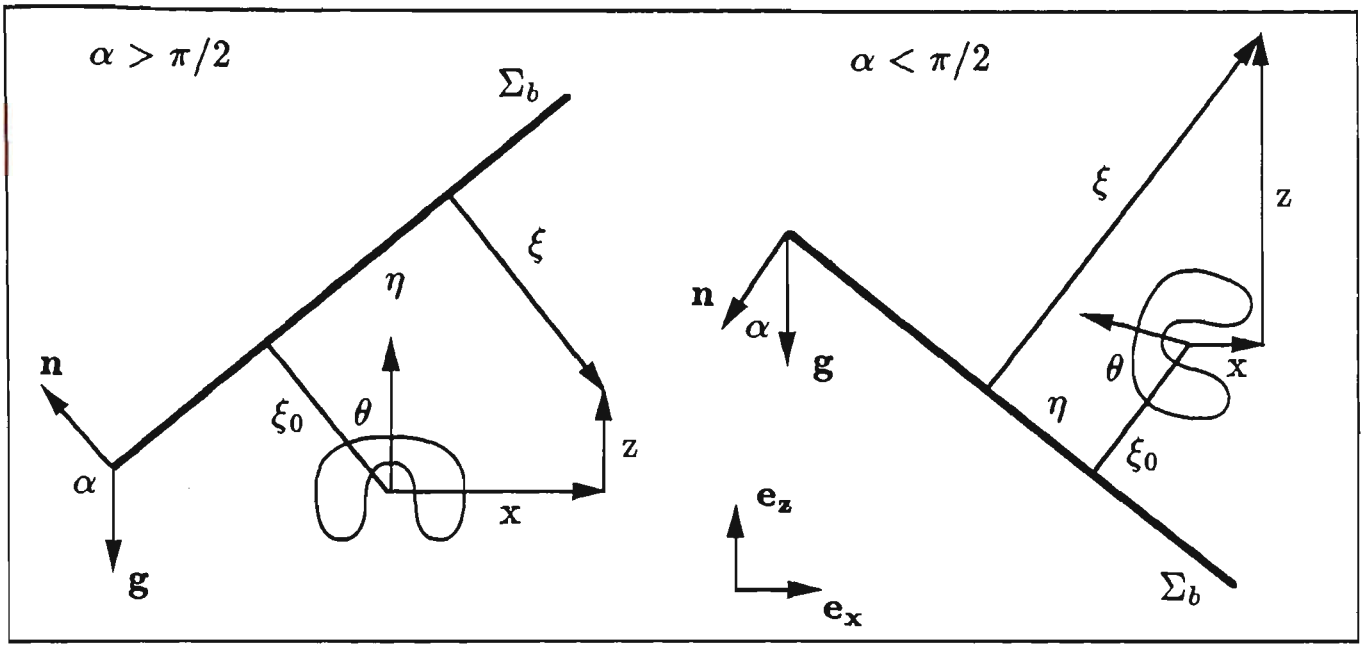

Figure 3.3.1. Geometry for the dynamics of a buoyant bubble in the neighbourhood of an inclined plane. We show the cases $\alpha > \pi/2$ and $\alpha < \pi/2$.

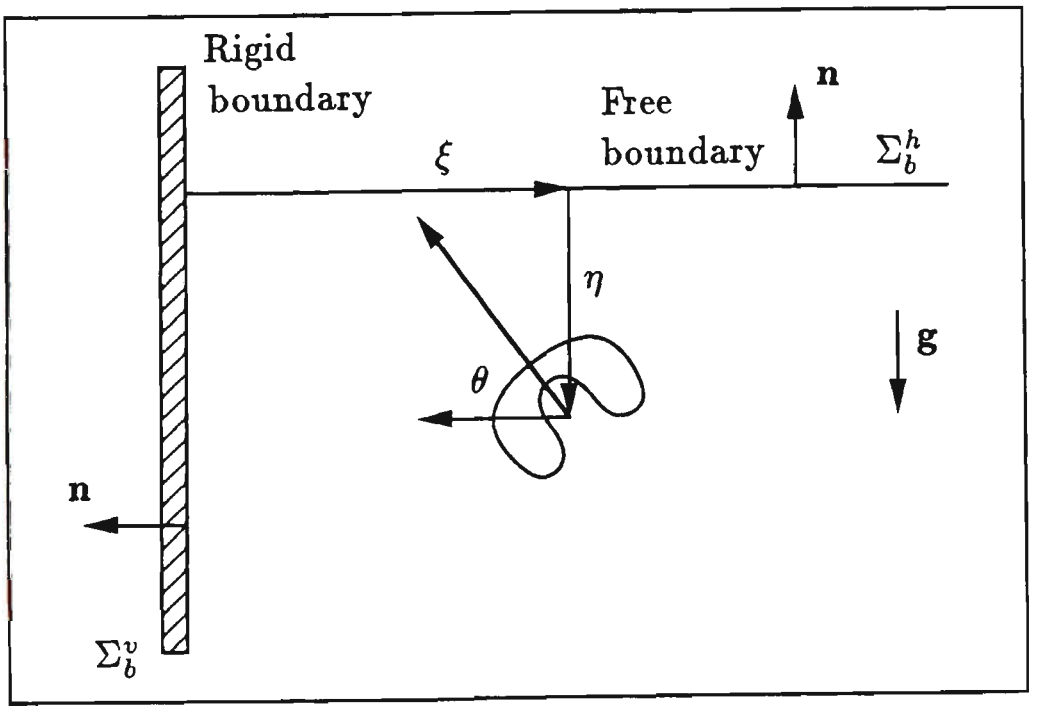

Figure 3.3.2. Geometry for the dynamics of a buoyant bubble in the neighbourhood of a rigid vertical wall and horizontal free surface.

the potential at the boundaries consists of sources of strength $4\pi R^2\dot{R}$ at $(\pm\xi,\eta)$ and sinks of strength $4\pi R^2\dot{R}$ at $(\pm\xi,-\eta)$. This image set satisfies the zero normal velocity condition at the rigid boundary, and the linearized boundary condition that the potential vanishes at the free surface. In this example the surface Σ_b is given by

$$\Sigma_b = \Sigma_b^v \cup \Sigma_b^h,$$

with

$$\Sigma_b^v = \{(\xi,\eta) \ : \xi = 0, \ \eta \geq 0\}, \tag{3.3.6}$$

$$\Sigma_b^h = \{(\xi,\eta) \ : \eta = 0, \ \xi \geq 0\},$$

and integration over this surface allows evaluation of the components of $\mathbf{F}$, which are given as

$$F_\xi = -\pi\rho R^4\dot{R}^2\left[\frac{1}{\xi^2} - \frac{\xi}{(\eta^2+\xi^2)^{3/2}}\right], \tag{3.3.7}$$

$$F_\eta = \pi\rho R^4\dot{R}^2\left[\frac{1}{\eta^2} + \frac{\eta}{(\eta^2+\xi^2)^{3/2}}\right] - \frac{4\pi}{3}\rho g R^3. \tag{3.3.8}$$

Introducing the dimensionless parameter

$$\beta = \eta_0/R_m, \tag{3.3.9}$$

and with γ and δ as defined previously, we may proceed making use of our usual set of assumptions to expressions for the components of the Kelvin impulse at the conclusion of the bubble lifetime. We furthermore propose that the angle θ, measured with respect to the normal to the rigid boundary, exterior to the domain of the flow, that defines the orientation of the jet formed on collapse, is given by the direction of the Kelvin impulse at the time T_c, so we have

$$\theta = \arctan\left(I_\eta(T_c)/I_\xi(T_c)\right). \tag{3.3.10}$$

Carrying out the appropriate time integration yields (Blake and Prosperetti, 1989)

$$\theta = \arctan\left[\frac{2\delta^2 B(11/6,1/2) - \left[\frac{1}{\beta^2} + \frac{\beta}{(\beta^2+\gamma^2)^{3/2}}\right]B(7/6,3/2)}{\left[\frac{1}{\gamma^2} - \frac{\gamma}{(\beta^2+\gamma^2)^{3/2}}\right]B(7/6,3/2)}\right]. \tag{3.3.11}$$

Motion in shallow waters

The problem of the underwater explosion provides motivation for this further example of bubble motion in shallow waters. We will suppose that the motion

occurs in water of depth ξ_m with the free surface being at atmospheric pressure. Furthermore, the motion will commence at a depth ξ_0. The geometry is shown in figure 3.3.3, where we retain the option of measuring distances downwards (ξ) or upwards (z). In order to satisfy the boundary conditions at the parallel free and rigid surfaces we require an infinite set of images to represent the lowest order contribution to the potential there. The image set consists of sources of strength $(-1)^n 4\pi R^2\dot{R}$ at $z = 2n\xi_m + \xi, -(2n\xi_m - \xi)$ and of strength $(-1)^{n+1}4\pi R^2\dot{R}$ at $z = 2n\xi_m - \xi, -(2n\xi_m + \xi)$, with $n \in (1, 2, ...)$. This choice of n excludes the image source of strength $-4\pi R^2\dot{R}$ at $z = \xi$, and the source of strength $4\pi R^2\dot{R}$ at the bubble centroid (figure 3.3.4). The potential, ϕ_S, due to this distribution of sources may be written in the useful form

$$\phi_S(r,z) = \begin{cases} 2\pi R^2\dot{R}\int_0^\infty J_0(r\tau)\frac{\cosh\tau(\xi_m-\xi)\sinh\tau z}{\cosh\tau\xi_m}d\tau, & z > -\xi \\ -2\pi R^2\dot{R}\int_0^\infty J_0(r\tau)\frac{\sinh(\tau\xi)\cosh\tau(z+\xi_m)}{\cosh\tau\xi_m}d\tau, & z < -\xi \end{cases}, \tag{3.3.12}$$

which is obtained by solving the equation $\nabla^2\phi = 4\pi R^2\dot{R}\delta(x)\delta(y)\delta(z+\xi)$ using the Hankel transform. In this notation (r, z) are cylindrical polar co-ordinates, (x, y, z) are cartesian co-ordinates and J_0 is a Bessel function of zeroth order. This expression for the potential expediates the determination of the force driving the Kelvin impulse.

In order to determine $F_\xi = dI_\xi/dt$ we notice that the surface Σ_b consists of the upper and lower surfaces of the flow domain, as shown in figure 3.3.3. If we introduce

$$u = \frac{\partial\phi}{\partial r}, \quad v = \frac{\partial\phi}{\partial z}, \tag{3.3.13}$$

then we may write

$$F_\xi = \pi\rho\left[\int_0^\infty v^2(r,0)rdr + \int_0^\infty u^2(r,-\xi_m)rdr\right] - \frac{4}{3}\pi\rho g R^3, \tag{3.3.14}$$

where the axial symmetry of the problem allows the surface integral to be written only in terms of the cylindrical co-ordinate r and we can routinely show that $u(r,0) = 0$. If we denote by $\bar{v}_0(\tau,0)$ the zeroth order Hankel transform of $v(r,0)$ and let $\bar{u}_1(\tau,-\xi_m)$ denote the first order Hankel transform of $u(r,-\xi_m)$ then application

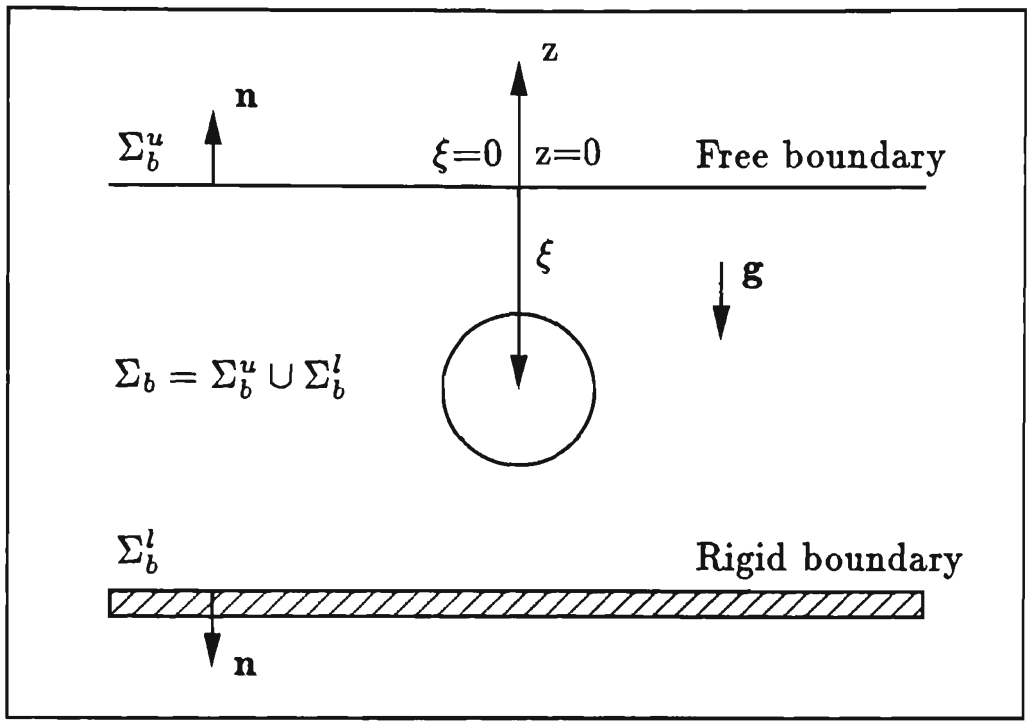

Figure 3.3.3. Geometry for the dynamics of a buoyant bubble in shallow waters.

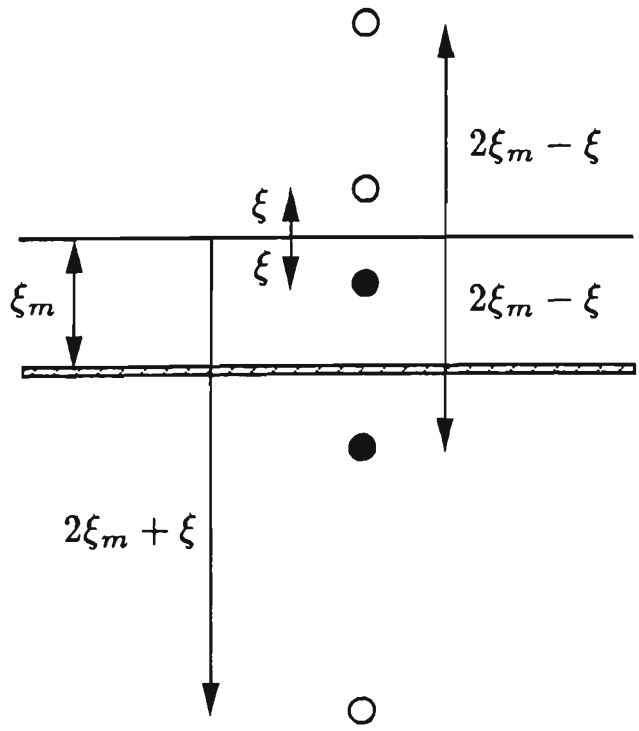

Figure 3.3.4. Principal image set used to represent the potential at the boundaries for buoyant bubble motion in shallow waters.

of Parseval's theorem to (3.3.14) yields

$$F_\xi = \pi\rho\left[\int_0^\infty \bar{v}_0^2(\tau,0)\tau d\tau + \int_0^\infty \bar{u}_1^2(\tau,-\xi_m)\tau d\tau\right] - \frac{4}{3}\pi\rho g R^3. \tag{3.3.15}$$

We deduce the appropriate Hankel transforms from (3.3.12), whence we obtain

$$F_\xi = 4\pi\rho R^4\dot{R}^2\int_0^\infty \left[\frac{\cosh^2\tau(\xi_m-\xi)+\sinh^2\tau\xi}{\cosh^2\tau\xi}\right]\tau d\tau - \frac{4}{3}\pi\rho g R^3, \tag{3.3.16}$$

which may equivalently be written as the infinite series

$$F_\xi = \pi\rho R^4\dot{R}^2\sum_{n=0}^{\infty}(-1)^n\left[\frac{1}{(n\xi_m+\xi)^2}+\frac{1}{((n+1)\xi_m-\xi)^2}\right] - \frac{4}{3}\pi\rho g R^3. \tag{3.3.17}$$

We may evaluate the Kelvin impulse as the bubble collapses to a singularity with the help of our usual set of assumptions and we obtain

$$I_\xi(T_c) = \frac{2\sqrt{6}\pi R_m^3(\rho\Delta p)^{\frac{1}{2}}}{9\bar{\gamma}^2}\left[B(7/6,3/2) - 2\bar{\gamma}^2\delta^2 B(11/6,1/2)\right], \tag{3.3.18}$$

with $\bar{\gamma}$ defined as

$$\bar{\gamma} = \left[R_m^2\sum_{n=0}^{\infty}(-1)^n\left[\frac{1}{(n\xi_m+\xi_0)^2}+\frac{1}{((n+1)\xi_m-\xi_0)^2}\right]\right]^{-1/2}. \tag{3.3.19}$$

We note that just as in the case of motion near a rigid boundary (as discussed by Blake, 1988) we have a null impulse line given by

$$\bar{\gamma}\delta = 0.442, \tag{3.3.20}$$

and we propose that for $\bar{\gamma}\delta < 0.442$ the Kelvin impulse at the conclusion of the collapse is directed downwards and thus the jet formed is directed downwards, and for $\bar{\gamma}\delta > 0.442$ the jet formed is directed upwards. The concept of a null impulse state in this geometry is alluded to in the war time work of Shiffman and Friedman (1944).

3.4. Spherical bubble dynamics

A bulk of work on the dynamics of spherical bubbles was carried out in WWII in the context of underwater explosion research. A summary of this work may be found in the book by Cole (1948). The significant point is that if we further

restrict the model presented in chapter 2 by introducing the assumption that the bubble remains spherical throughout its lifetime then we may derive a system of ordinary differential equations that describes the motion. We exploit the Kelvin impulse and Bernoulli equation to determine respectively momentum and energy equations. The theory of images is used to obtain expressions for the velocity potential of the flow.

Application of the Kelvin impulse

Let us suppose that a bubble of radius $R(t)$ exists in a fluid and that there is a uniform gravitational field $-g\mathbf{e}_z$ acting. The expression for the force, $\mathbf{F}$, driving the Kelvin impulse becomes

$$\mathbf{F}(t) = \rho \int_{\Sigma_b} \left\{ \frac{1}{2} |\nabla\phi|^2 \mathbf{n} - \frac{\partial\phi}{\partial n} \nabla\phi \right\} dS + \rho g V(t) \mathbf{e}_z. \tag{3.4.1}$$

We make use of the Kelvin impulse as follows. The impulse, $\mathbf{I}$, may be evaluated using the definition (3.2.7) in conjunction with an appropriate expression for the potential at the surface of the bubble. The force, $\mathbf{F}(t)$, may be evaluated by integrating over the bounding surface Σ_b. We then substitute into the equation

$$\frac{d\mathbf{I}}{dt} = \mathbf{F}, \tag{3.4.2}$$

to establish an equation of motion for our dynamical system. The utility of this method follows from the observation that in many geometries only those components of the potential that vary as $1/r$ (r is the distance from the bubble centroid) need be considered in the evaluation of $\mathbf{F}$, as exemplified by the results of section 3.3.

Energy conservation

For the geometry chosen, with a uniform gravitational field acting, the Bernoulli equation is given by (2.1.4). We suppose that the pressure within the bubble is uniform and may be written as a function of V (and consequently R as $V = \frac{4}{3}\pi R^3$). This constraint includes the important cases of transient cavities and explosion

bubbles. At the surface of the bubble continuity of pressure allows us to write the Bernoulli equation there as

$$\frac{\partial \phi}{\partial t} + \frac{1}{2}|\nabla \phi|^2 + (p(R) - p_\infty)/\rho + gz = 0, \tag{3.4.3}$$

which, upon substitution of an appropriate expression for the potential and integration over the surface of the bubble, yields an equation of motion complementing that derived via the Kelvin impulse:

$$\oint_S \left[\frac{\partial \phi}{\partial t} + \frac{1}{2}|\nabla \phi|^2 + \left\{\frac{p(R) - p_\infty}{\rho}\right\} + gz\right] dS = 0. \tag{3.4.4}$$

We now proceed to establish that, in the case of the spherical bubble, (3.4.4) yields an equation equivalent to that of energy conservation for the dynamical system. In this case the area element is $R^2 \sin\theta d\theta d\phi$ and letting the bubble centre be located at $z = -\zeta$ the integral of (3.4.4) yields

$$\oint_S \left[\frac{\partial \phi}{\partial t} + \frac{1}{2}|\nabla \phi|^2\right] dS + 4\pi R^2 p(R)/\rho - 4\pi R^2 \left[p_\infty/\rho + g\zeta\right] = 0. \tag{3.4.5}$$

Let us now integrate with respect to R, from R to R_0, with R_0 being some arbitrary initial condition. We obtain

$$\int_R^{R_0} \left\{\oint_S \left[\frac{\partial \phi}{\partial t} + \frac{1}{2}|\nabla \phi|^2\right] dS\right\} dR' + (4\pi/\rho)\int_R^{R_0} R'^2 p(R') dR' - \frac{4}{3}\pi\left(R_0^3 - R^3\right)\left[p_\infty/\rho + g\zeta\right] = 0. \tag{3.4.6}$$

Interpretation of the terms appearing here leads us to deduce this equation as being that of energy conservation. The term $4\pi \int_R^{R_0} R'^2 p(R') dR'$ is the work done on the gaseous bubble contents in expanding from R_0 to R and if we assume that the thermodynamic processes are adiabatic is equal to the change in internal energy of the gas. The expression $-(4\pi/3)\left(R_0^3 - R^3\right)\left[p_\infty + \rho g h\right]$ is the work done against the hydrostatic pressure at infinity and thus represents the change in potential energy of the system. We are thus led to interpret $\rho \int_R^{R_0} \left\{\oint_S \left[\frac{\partial \phi}{\partial t} + \frac{1}{2}|\nabla \phi|^2\right] dS\right\} dR'$ as the change in the kinetic energy of the flow and the expression of (3.4.6) as describing energy conservation in our dissipationless system.

Proceeding as with the Kelvin impulse we will make use of appropriate expressions for the potential at the surface of the bubble in substituting into (3.4.5)

to obtain the equation of motion complementary to that derived via the Kelvin impulse. The dynamics of the bubble motion is completely embodied in equations (3.4.2) and (3.4.4). Supplementary kinematical conditions will be required to solve the appropriate equations. To proceed we require an expression for the potential for the flow induced by the bubble motion. Since we have chosen simple geometries the theory of images is most useful, and it is pertinent to discuss the relevant features which will allow us to proceed directly to equations of motion for the bubble dynamics. Since we require expressions for the potential at the bubble surface we must expand upon the image systems utilised in the previous computations of the Kelvin impulse.

Image theory for spherical bubbles

The potential for the flow induced by the motion of a spherical bubble in an infinite fluid is given as

$$\phi = -\frac{m(t)}{4\pi\,|\mathbf{r}|} - \frac{\mathbf{d}(t)\cdot\mathbf{r}}{4\pi\,|\mathbf{r}|^3}, \tag{3.4.7}$$

where $\mathbf{r}$ is the position vector of some point in the flow field relative to the bubble centroid. The time dependent source and dipole strengths, $m(t)$ and $\mathbf{d}(t)$, are given as

$$m(t) = 4\pi R^2 \dot{R}, \tag{3.4.8}$$

$$\mathbf{d}(t) = 2\pi R^3 \mathbf{U}, \tag{3.4.9}$$

where R is the radius of the bubble and $\mathbf{U}$ is the velocity of the centroid. We note that the source term describes changes of the bubble's volume and the dipole term describes translation of the bubble centroid. For motion in the neighbourhood of boundaries we introduce images in order to satisfy the appropriate boundary conditions.

Since plane boundaries are of interest the following geometry assumes significance. Suppose that we have a plane boundary with a bubble of radius $R(t)$ located a distance $\xi(t)$ from it. We define a set of orthonormal axes such that the unit vector

$\mathbf{e}_z$ is perpendicular to the boundary with the origin located at the bubble centre. The plane boundary is thus defined as $z = \xi$. In the first instance, we introduce an image of strength $\pm m(t)$ at $(0, 0, 2\xi)$ in order to satisfy the boundary condition at the plane. We choose $+m(t)$ for a rigid boundary and $-m(t)$ for a free boundary noting that we are utilising the linearised free boundary condition. This image subsequently induces a net flow across the surface of the bubble which we correct by placing a source of strength $\pm m(t)R(t)/(2\xi(t))$ at $(0, 0, R(t)^2/(2\xi(t)))$ and a uniform linear distribution of sinks of density $\pm m(t)/R(t)$ from $(0, 0, 0)$ to $(0, 0, R(t)^2/(2\xi(t)))$ (Milne-Thomson, 1960), noting that a sink of negative strength is a source. This image set further disturbs the boundary condition at the plane which can be corrected by the addition of further images which contribute to higher order in (R/ξ) than the previous set. For the problem at hand only the lowest order corrections to the infinite fluid case are of interest so only the above mentioned images are of concern.

Recall that we also have a dipole contribution to the potential. We will restrict our attention to motion constrained to 2-dimensions so we write $\mathbf{d}(t) = (d_x(t), 0, d_z(t))$. We may introduce images reflected about the plane $z = \xi$, however the contribution to the potential is of higher order in (R/ξ) than the contribution of the source images and is therefore not of interest in the current formulation. We display this image system in figure 3.4.1. The expressions for the potentials $\phi_i\,(i = 1, \ldots, 6)$ due to these singularities (as shown in figure 3.4.1) are

$$\phi_1 = -\frac{1}{4\pi}\frac{m(t)}{|\mathbf{r}|}, \quad \phi_2 = -\frac{1}{4\pi}\frac{d_z(t)\mathbf{r}\cdot\mathbf{e}_z}{|\mathbf{r}|^3}, \quad \phi_3 = -\frac{1}{4\pi}\frac{d_x(t)\mathbf{r}\cdot\mathbf{e}_x}{|\mathbf{r}|^3}, \quad \phi_4 = -\frac{1}{4\pi}\frac{m(t)}{|\mathbf{r} - (0, 0, 2\xi)|},$$

$$\phi_5 = -\frac{1}{8\pi}\frac{R(t)m(t)}{\xi(t)\,|\mathbf{r} - (0, 0, R^2/(2\xi))|} \quad \phi_6 = \frac{m(t)}{4\pi R(t)}\int_0^{R^2/(2\xi)} \frac{d\delta}{|\mathbf{r} - (0, 0, \delta)|}. \tag{3.4.10}$$

Without loss of generality we have chosen the specific case where the boundary is rigid. To proceed to equations of motion for spherical bubbles we write the

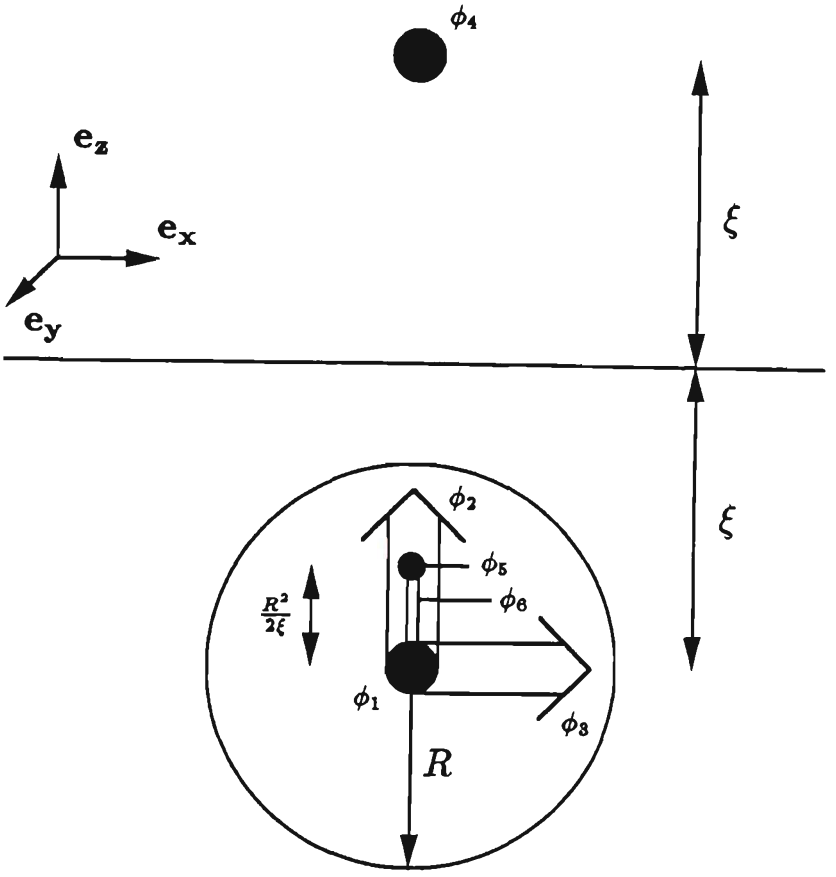

Figure 3.4.1. Image system for spherical bubble dynamics in the neighbourhood of a boundary. The potentials ϕ_1, ϕ_4 and ϕ_5 are due to sources. The potentials ϕ_2 and ϕ_3 are due to dipoles, graphically displayed as arrows. ϕ_6 represents a linear distribution of sinks.

potential as

$$\phi = \sum_i \phi_i, \tag{3.4.11}$$

where the ϕ_i are the contributions to the potential of the singularities (sources and dipoles) used to represent the flow field. In this study the ϕ_i will have the form of those potentials listed in (3.4.10).

The integral quantities required are

$$\oint_S \phi \mathbf{n} dS = \sum_i \oint_S \phi_i \mathbf{n} dS, \tag{3.4.12}$$

$$\oint_S \frac{\partial \phi}{\partial t} dS = \sum_i \oint_S \frac{\partial \phi_i}{\partial t} dS, \tag{3.4.13}$$

$$\oint_S |\nabla \phi|^2 \, dS = \sum_{i,j} \oint_S \nabla \phi_i \cdot \nabla \phi_j dS. \tag{3.4.14}$$

We thus evaluate the above integrals for the potentials ϕ_i $(i = 1, \ldots, 6)$. Evaluating the integral of (3.4.12) we find that the only non-zero contributions are

$$\begin{aligned} &\oint_S \phi_2 \mathbf{n} dS = \frac{1}{3} d_x(t) \mathbf{e}_x, \quad \oint_S \phi_3 \mathbf{n} dS = \frac{1}{3} d_x(t) \mathbf{e}_x, \quad \oint_S \phi_4 \mathbf{n} dS = \frac{m(t) R^3(t)}{12 \xi^2(t)} \mathbf{e}_x, \\ &\oint_S \phi_5 \mathbf{n} dS = \frac{m(t) R^3(t)}{12 \xi^2(t)} \mathbf{e}_x, \quad \oint_S \phi_6 \mathbf{n} dS = \frac{-m(t) R^3(t)}{24 \xi^2(t)} \mathbf{e}_x. \end{aligned} \tag{3.4.15}$$

The integral of (3.4.14) yields

$$\begin{aligned} &\oint_S \nabla \phi_1 \cdot \nabla \phi_1 dS = \frac{m^2(t)}{4\pi R(t)^2}, \quad \oint_S \nabla \phi_1 \cdot \nabla \phi_5 dS = \frac{m^2(t)}{8\pi R(t) \xi(t)}, \\ &\oint_S \nabla \phi_1 \cdot \nabla \phi_6 dS = \frac{-m^2(t)}{8\pi R(t) \xi(t)}, \quad \oint_S \nabla \phi_2 \cdot \nabla \phi_2 dS = \frac{d_x^2(t)}{2\pi R^4(t)}, \\ &\oint_S \nabla \phi_2 \cdot \nabla \phi_5 dS = \frac{d_x(t) m(t)}{8\pi R(t) \xi^2(t)}, \quad \oint_S \nabla \phi_2 \cdot \nabla \phi_6 dS = \frac{-d_x(t) m(t)}{16\pi R(t) \xi^2(t)}, \\ &\oint_S \nabla \phi_3 \cdot \nabla \phi_3 dS = \frac{d_y^2(t)}{2\pi R^4(t)}. \end{aligned} \tag{3.4.16}$$

All other integrals of this kind are either zero or of higher order in (R/ξ). In order to determine $\oint_S \frac{\partial \phi_i}{\partial t} dS$ we introduce explicit expressions for the ϕ_i using equations (3.4.8) and (3.4.9). We then find, that to appropriate order in (R/ξ), the integral

of (3.4.13) yields

$$\begin{aligned}
\oint_S \frac{\partial \phi_1}{\partial t} dS &= -4\pi R^2(2\dot{R}^2 + R\ddot{R}), \\
\oint_S \frac{\partial \phi_4}{\partial t} dS &= -2\pi R^3(2\dot{R}^2 + R\ddot{R})/\xi, \\
\oint_S \frac{\partial \phi_5}{\partial t} dS &= -2\pi R^3(3\dot{R}^2 + R\ddot{R})/\xi, \\
\oint_S \frac{\partial \phi_6}{\partial t} dS &= 2\pi R^3(3\dot{R}^2 + R\ddot{R})/\xi,
\end{aligned} \tag{3.4.17}$$

with ϕ_2 and ϕ_3 contributing integrals of value zero. In cases where more than one boundary is present (for example, the geometries discussed in section 3.3) each boundary requires the introduction of a principal source (of appropriate strength) reflected about the boundary. Each such source necessitates the introduction of a corresponding source and uniform linear distribution of sinks within the bubble, as discussed in this section. We can then write the potential in the form of (3.4.11) and use the integral quantities of (3.4.15), (3.4.16) and (3.4.17) to proceed immediately to equations for spherical bubble dynamics in the neighbourhood of boundaries with simple geometry.

3.5. Spherical bubble dynamics in particular geometries

Using the results of the previous section we may, upon introduction of appropriate image sets, proceed directly to equations of motion for spherical bubble dynamics in the geometries discussed in section 3.3.

Motion near an inclined plate

Consider the motion near an inclined plate as presented in section 3.3. We let the velocity components of the bubble centroid parallel and perpendicular to the wall be U_η and U_ξ respectively, so that we have

$$U_\eta = \dot{\eta}, \quad U_\xi = \dot{\xi}. \tag{3.5.1}$$

The image set for this motion is exactly that discussed in section 3.4. We have a source of strength $4\pi R^2\dot{R}$ at (ξ, η), a source of strength $4\pi R^2\dot{R}$ at $(-\xi, \eta)$, a dipole of strength $(2\pi R^3 U_\xi, 2\pi R^3 U_\eta)$ at (ξ, η), a source of strength $2\pi R^3\dot{R}/\xi$ at $(\xi - R^2/(2\xi), \eta)$

and a uniform linear distribution of sinks of density $4\pi R\dot{R}$ per unit length from $(\xi - R^2/(2\xi), \eta)$ to (ξ, η). Using the integrals of (3.4.15) we find that the components of the Kelvin impulse are

$$I_\xi = \frac{2}{3}\pi\rho\left\{R^3 U_\xi - \frac{3}{4}\frac{R^5\dot{R}}{\xi^2}\right\}, \tag{3.5.2}$$

$$I_\eta = \frac{2}{3}\pi\rho R^3 U_\eta, \tag{3.5.3}$$

where only the lowest order correction in (R/ξ) to the infinite fluid case has been retained. Notice the form of this correction. During the expansion phase, when $\dot{R}$ is positive, the impulse has an extra component directed towards the wall. This reflects the fact that the fluid near to the wall is less mobile compared with the infinite fluid case and an extra impulse is required to generate the given bubble motion from rest. During the collapse $\dot{R}$ is negative so that the correction is directed away from the boundary again reflecting the extra impulse required to draw the fluid in from the side of the boundary. The components of the force, $\mathbf{F}$, driving the Kelvin impulse are given by (3.3.2) and (3.3.3) and on substituting the expressions for I_ξ and I_η into the equation $d\mathbf{I}/dt = \mathbf{F}$ we obtain

$$\frac{d}{dt}(R^3 U_\xi) = \frac{3}{4}\frac{R^4}{\xi^2}\left[3\dot{R}^2 + R\ddot{R}\right] + 2R^3 g\cos\alpha, \tag{3.5.4}$$

$$\frac{d}{dt}(R^3 U_\eta) = 2R^3 g\sin\alpha, \tag{3.5.5}$$

where a term of $O(R/\xi)^3$ that arises in differentiating (3.5.2) has been neglected. These equations differ from the infinite fluid case in the appearance of the term $\frac{3}{4}\frac{R^4}{\xi^2}\left[3\dot{R}^2 + R\ddot{R}\right]$ which describes the effect upon the bubble motion of the flow field induced by the presence of the boundary. For much of the motion it is negative, since $\ddot{R}$ is negative for most of the motion, and thus describes the Bjerknes attraction of the wall. If gravity is neglected then these equations reduce to that given by Herring for motion in the neighbourhood of a single boundary (see chapter 1).

We now proceed, as described in section 3.4, to an equation equivalent to energy conservation. Integrating the Bernoulli equation over the surface of the

bubble we obtain, with the help of (3.4.16) and (3.4.17),

$$R\ddot{R}\left[1+R/\left(2\xi\right)\right]+\frac{3}{2}\dot{R}^2\left[1+2R/\left(3\xi\right)\right]-\frac{1}{4}\left[U_\xi^2+U_\eta^2\right]=\frac{p_\infty}{\rho}\left[\frac{p(R)}{p_\infty}+\frac{\rho g z}{p_\infty}-1\right], \tag{3.5.6}$$

where p_∞ is the hydrostatic pressure at the initial depth of the bubble. If, for instance, the bubble was initially at a depth of H below a surface at atmospheric pressure then

$$p_\infty = p_a + \rho g H. \tag{3.5.7}$$

The co-ordinate of the bubble centroid, z, may be transformed using (3.3.1), whence we obtain

$$\begin{aligned} &R\ddot{R}\left[1+R/\left(2\xi\right)\right]+\frac{3}{2}\dot{R}^2\left[1+2R/\left(3\xi\right)\right]-\frac{1}{4}\left[U_\xi^2+U_\eta^2\right] \\ &=\frac{p_\infty}{\rho}\left[\frac{p(R)}{p_\infty}+\frac{\rho g}{p_\infty}\left[\left(\xi-\xi_0\right)\cos\alpha+\eta\sin\alpha\right]-1\right]. \end{aligned} \tag{3.5.8}$$

The bubble motion is thus described by (3.5.1), (3.5.4), (3.5.5) and (3.5.8).

Motion near a horizontal free surface and vertical rigid wall

Recall also the example of motion in the neighbourhood of a horizontal free surface and vertical rigid wall as discussed in section 3.3 and which geometry we will refer to as a quarter plane. The components of the centroid velocity are

$$U_\xi = \dot{\xi}, \quad U_\eta = \dot{\eta}. \tag{3.5.9}$$

Upon introducing the appropriate image set we may routinely proceed to the equations of motion for the bubble dynamics. The set of singularities representing the flow consists of a source of strength $4\pi R^2\dot{R}$ and a dipole of strength $(2\pi R^3 U_\xi, 2\pi R^3 U_\eta)$ located at (ξ,η). The image set required consists of the following: a source of strength $4\pi R^2\dot{R}$ at $(-\xi,\eta)$, sources of strength $-4\pi R^2\dot{R}$ (sinks) at $(-\xi,-\eta)$ and $(\xi,-\eta)$, sources of strength $2\pi R^3\dot{R}/\xi, -2\pi R^3\dot{R}/\eta, -2\pi R^3\dot{R}/(\eta^2+\xi^2)^{\frac{1}{2}}$ at $(\xi-R^2/\left(2\xi\right),\eta), (\xi,\eta-R^2/\left(2\eta\right))$ and $(\xi-R^2\xi/\left(2(\xi^2+\eta^2)\right),\eta-R^2\eta/\left(2(\xi^2+\eta^2)\right))$ respectively, with corresponding uniform linear distributions of sinks of density $4\pi R\dot{R}, -4\pi R\dot{R}$ and $-4\pi R\dot{R}$ from these points to (ξ,η). This distribution of singularities is shown in figure 3.5.1.

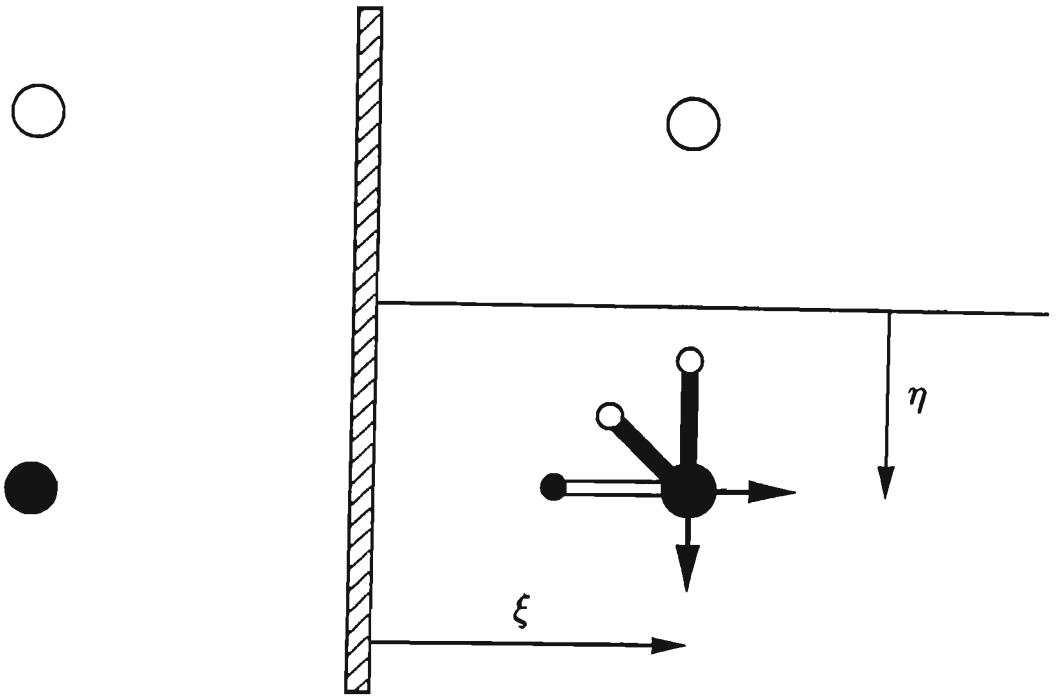

Figure 3.5.1. Image system for the motion of a spherical bubble in the neighbourhood of a horizontal free surface and vertical rigid wall. Circles denote sources/sinks, rectangles denote linear distributions of sources/sinks and arrows denote dipoles.

The components of the Kelvin impulse are

$$I_\xi = \frac{2}{3}\pi\rho\left\{R^3U_\xi - \frac{3}{4}R^5\dot{R}\left[\frac{1}{\xi^2} - \frac{\xi}{(\eta^2+\xi^2)^{3/2}}\right]\right\}, \tag{3.5.10}$$

$$I_\eta = \frac{2}{3}\pi\rho\left\{R^3U_\eta + \frac{3}{4}R^5\dot{R}\left[\frac{1}{\eta^2} + \frac{\eta}{(\eta^2+\xi^2)^{3/2}}\right]\right\}, \tag{3.5.11}$$

so with the help of (3.3.7) and (3.3.8) we obtain the equations of motion

$$\frac{d}{dt}\left(R^3U_\xi\right) = \frac{3}{4}R^4\left[3\dot{R}^2 + R\ddot{R}\right]\left[\frac{1}{\xi^2} - \frac{\xi}{(\eta^2+\xi^2)^{3/2}}\right], \tag{3.5.12}$$

$$\frac{d}{dt}\left(R^3U_\eta\right) = -\frac{3}{4}R^4\left[3\dot{R}^2 + R\ddot{R}\right]\left[\frac{1}{\eta^2} + \frac{\eta}{(\eta^2+\xi^2)^{3/2}}\right] - 2gR^3. \tag{3.5.13}$$

Integrating the Bernoulli equation over the surface of the bubble completes the description of the dynamics. We obtain

$$\frac{3}{2}\dot{R}^2\left\{1 + \frac{2}{3}R\left[\frac{1}{\xi} - \frac{1}{\eta} - \frac{1}{(\xi^2+\eta^2)^{1/2}}\right]\right\} + R\ddot{R}\left\{1 + \frac{1}{2}R\left[\frac{1}{\xi} - \frac{1}{\eta} - \frac{1}{(\xi^2+\eta^2)^{1/2}}\right]\right\} - \frac{1}{4}\left[U_\xi^2 + U_\eta^2\right]$$
$$= \frac{p(R)}{\rho} - \left(\frac{p_\infty}{\rho} + g(\eta - \eta_0)\right), \tag{3.5.14}$$

where η_0 is the initial depth of the bubble below the free ocean surface and p_∞ is the hydrostatic pressure at this depth.

Motion in shallow waters

Finally we consider again the problem of bubble motion in shallow waters. Measuring the centroid velocity downwards we have

$$U_\xi = \dot{\xi}. \tag{3.5.15}$$

The image set consists of those sources as described in section 3.3 along with their associated sources and uniform linear distributions of sinks within the bubble. Furthermore, we have a dipole singularity at the bubble centroid. We find that the Kelvin impulse (in the direction of increasing ξ) is

$$I_\xi = \frac{2}{3}\pi\rho\left[R^3U_\xi - \frac{3}{4}R^5\dot{R}\left\{\sum_{n=0}^{\infty}(-1)^{n+1}\left[\frac{1}{\{[n+1]\xi_m - \xi\}^2} + \frac{1}{\{n\xi_m + \xi\}^2}\right]\right\}\right]. \tag{3.5.16}$$

Making use of (3.3.17) we obtain the equation of motion

$$\frac{d}{dt}(R^3U_\xi) = \frac{3}{4}R^4\left[3\dot{R}^2 + R\ddot{R}\right]\sum_{n=0}^{\infty}(-1)^{n+1}\left[\frac{1}{\{(n+1)\xi_m - \xi\}^2} + \frac{1}{\{n\xi_m + \xi\}^2}\right] - 2gR^3. \tag{3.5.17}$$

Integrating the Bernoulli equation over the surface of the bubble we establish the complementary equation of motion

$$R\ddot{R}\left[1-R\left\{\frac{1}{2\xi}+\sum_{n=1}^{\infty}\frac{(-1)^n\xi^2}{n\xi_m(n^2\xi_m^2-\xi^2)}\right\}\right]+\frac{3}{2}\dot{R}^2\left[1-\frac{4R}{3}\left\{\frac{1}{2\xi}+\sum_{n=1}^{\infty}\frac{(-1)^n\xi^2}{n\xi_m(n^2\xi_m^2-\xi^2)}\right\}\right]-\frac{1}{4}U_\xi^2$$
$$=\frac{p(R)}{\rho}-\left(\frac{p_\infty}{\rho}+g(\xi-\xi_0)\right), \tag{3.5.18}$$

with p_∞ the hydrostatic pressure at ξ_0 and all other notation is as previously defined. These equations were derived by Shiffman and Friedman (1944) using a different approach.

3.6. Axisymmetric computations - Predictions of jet direction

We have developed the ideas of the previous sections under the premise that certain gross aspects of the bubble motion during the non-spherical collapse phase can be inferred from the early motion, a time during which the bubble is spherical to a very good level of approximation, and a time which occupies much of the bubble life. The bulk of experimental and numerical results clearly establish these facts. For instance, the numerical studies of Blake et al. (1986) demonstrate the approximate spherical growth and collapse of axisymmetric cavitation bubbles, with asymmetry in the flow field induced either by the ambient pressure gradient or the presence of boundaries causing a jet to form and penetrate the bubble in only a small fraction of the bubble lifetime. These numerical results compare well with experimental results (Gibson, 1968; Blake and Gibson, 1987) with such studies alluding to the speed of the non-spherical collapse phase. As an example of this we note the results reported by Benjamin and Ellis (1966) which demonstrate rebounding bubbles with the bubble at minimum volume not being photographically captured due to the collapse and rebound occurring faster than the filming rate.

It is this speed of collapse that we wish to exploit. Over some interval, Δt, the

change in the Kelvin impulse is

$$\Delta \mathbf{I} = \int_t^{t+\Delta t} \mathbf{F}(t')dt', \tag{3.6.1}$$

so that

$$|\Delta \mathbf{I}| \leq \Delta t \sup_{(t,t+\Delta t)} |\mathbf{F}(t)|, \tag{3.6.2}$$

where sup denotes the supremum value. We can reasonably presume that $\mathbf{F}$ is bounded throughout the motion (in the case of a buoyancy force alone this is obvious as $|\mathbf{F}| = \rho g V$ and the bubble volume is bounded) so that over a sufficiently small time interval the magnitude of the impulse change is small. If we consider a collapsing spherical bubble then, up until the time that the bubble enters the rapid collapse phase and becomes highly non-spherical, we can estimate the Kelvin impulse using the results of sections 3.2 and 3.3, or obtain a more accurate result using the equations of spherical bubble dynamics (at the expense of having to solve a system of coupled non-linear ordinary differential equations, but this is a routine matter). If we can then identify the time at which the collapse is initiated, then because of the generally short time, Δt, over which the collapse occurs the estimate obtained from our simple theory should provide an excellent predictor of the impulse of the non-spherical collapsed bubble, the change in the impulse brought about by the deformation from spherical shape being small.

We then propose to relate the direction of the impulse to the direction of migration of the collapsing bubble, and if a jet is formed to the direction of the jet. Recalling that we can interpret the Kelvin impulse as the impulse that we would have to apply over the surface of the bubble to generate the observed motion from rest, it is clear that in order to generate this jetting motion from rest the Kelvin impulse at collapse must be closely correlated with the direction of the jet. This is the physical basis for the calculations of sections 3.2 and 3.3 where by making various assumptions we may estimate the Kelvin impulse at the end of the bubble life.

The case that we particularly address is that of motion above a rigid boundary

in which we have postulated the existence of a null impulse line that partitions the $\gamma - \delta$ parameter space. Although the existence of such a partition has been established by Blake et al. (1986) we can demonstrate its existence using the equations of spherical bubble dynamics derived in section 3.5. To obtain the appropriate equations of motion we set $\alpha = 0$ in (3.5.4) and (3.5.5) and for a cavitation bubble set $p(R) = p_c$, the constant vapour pressure within the bubble throughout its lifetime. Introducing the length and time scales discussed in chapter 2 and applying the initial conditions chosen for a cavitation bubble we may proceed to solve the coupled equations of spherical bubble dynamics by standard techniques. We have used the 4'th order Runge-Kutta method. Examples of such calculations are shown in figure 3.6.1. For the example of figure 3.6.1(a) we have plotted the centroid velocity as a function of time for the buoyancy parameter $\delta = 0.15$, with the motion beginning at $\gamma = 2.0$. As the bubble expands it moves little but upon collapse it undergoes a period of rapid acceleration towards the rigid boundary. In this example the influence of the boundary is the dominant factor. If, however, we increase the buoyancy parameter to $\delta = 0.25$ we note the motion depicted in figure 3.6.1(b). As the bubble collapses it accelerates away from the rigid boundary, again with characteristic high acceleration. Buoyancy is dominant in this case.

Thus the equations of spherical bubble dynamics demonstrate the existence of a partition of the $\gamma - \delta$ parameter space. Furthermore, the phase of the motion during which time the bubble undergoes a rapid acceleration is identified with that phase during which collapse and jet formation will occur. If we consider our expression for the Kelvin impulse in this case,

$$I_\xi = \frac{2}{3}\pi\rho\left\{R^3 U_\xi - \frac{3}{4}\left(\frac{R}{\xi}\right)^2 R^3\dot{R}\right\}, \tag{3.6.3}$$

we note that as the terms R^3U_ξ and $R^3\dot{R}$ are of the same order we find that upon collapse ($R \to 0$) the term $(R/\xi)^2$ vanishes, resulting in the Kelvin impulse and centroid velocity being similarly directed at the conclusion of the collapse. This result is conceptually appealing as we expect the jet direction to be related to the Kelvin impulse, but furthermore, the rapid acceleration of the bubble centroid and

the asymmetric pressure field associated with it is the cause of bubble collapse and we expect the jet direction to be closely correlated with the direction of centroid acceleration just prior to collapse. Since the rapid centroid migration upon collapse almost begins from rest, and the direction of the acceleration varies little as the collapse proceeds, the directions of acceleration and centroid migration are almost identical. The coincidence of the direction of migration and Kelvin impulse at the end of the collapse, in the simplified theory of spherical bubble dynamics, is comforting in that both approaches to predicting the direction of jet formation appear to be consistent with each other.

We may use the equations of spherical bubble dynamics to calculate the null impulse line by running the full dynamics and using a bracketting type procedure. The results are illustrated in figure 3.6.2 along with the null impulse line computed in section 3.2. The data points shown as triangles are from the original analysis of this question, as found in Blake et al. (1986). The direction of the triangle apex denotes the direction of centroid migration (and jet formation, if a jet was observed) at the end of the bubble lifetime as calculated by the boundary integral method described in that same paper. It is clear that the two null impulse lines diverge as we approach the rigid boundary. In order to clarify which null impulse line provides a more exact partition of the parameter space we have run a number of simulations using the improved boundary integral method of Kucera (1991). This numerical algorithm will be discussed in some detail in the next chapter and the data points are shown as arrows and listed in table 3.6.1. It is clear from inspection of this figure that spherical bubble dynamics allows us to predict with some certainty aspects of the motion during the collapse phase, in particular the direction of centroid migration and jet formation. We find, however, that at $\gamma = 1.0$ we have results that violate the predictions of our simple model. This is not unexpected as in our theory we have only corrected the equations of motion to lowest order in (R/ξ) and in any case the results of boundary integral simulations (see for instance Blake et al., 1986, 1987) demonstrate that the close proximity of

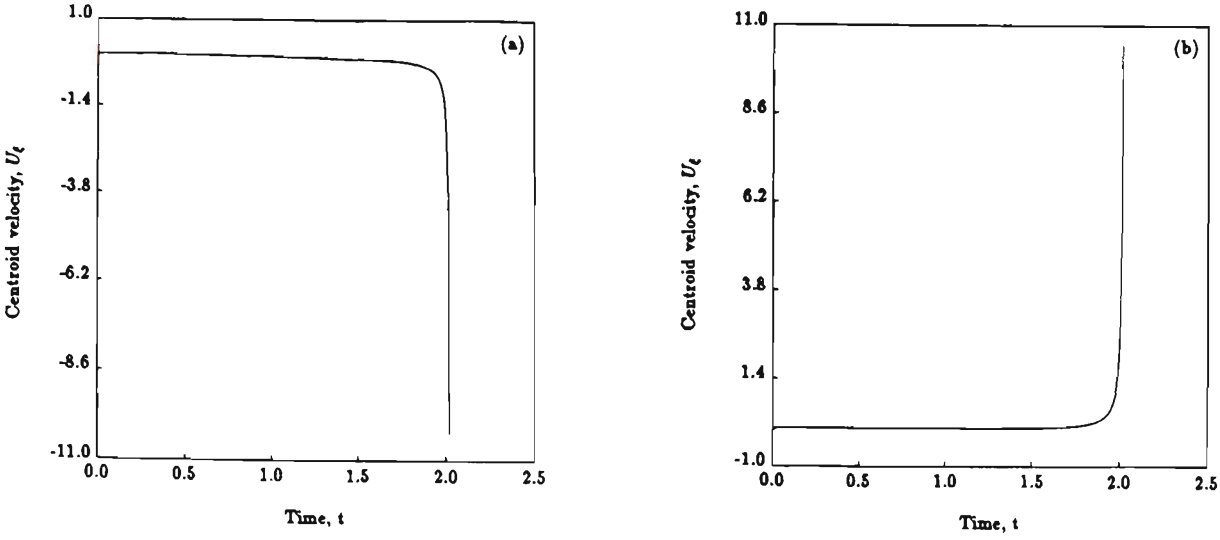

Figure 3.6.1. Centroid velocity as a function of time for the motion of a buoyant, spherical cavitation bubble above a rigid boundary. In both cases the point of inception is $\gamma = 2.0$. The buoyancy parameter is (a) $\delta = 0.15$, (b) $\delta = 0.25$.

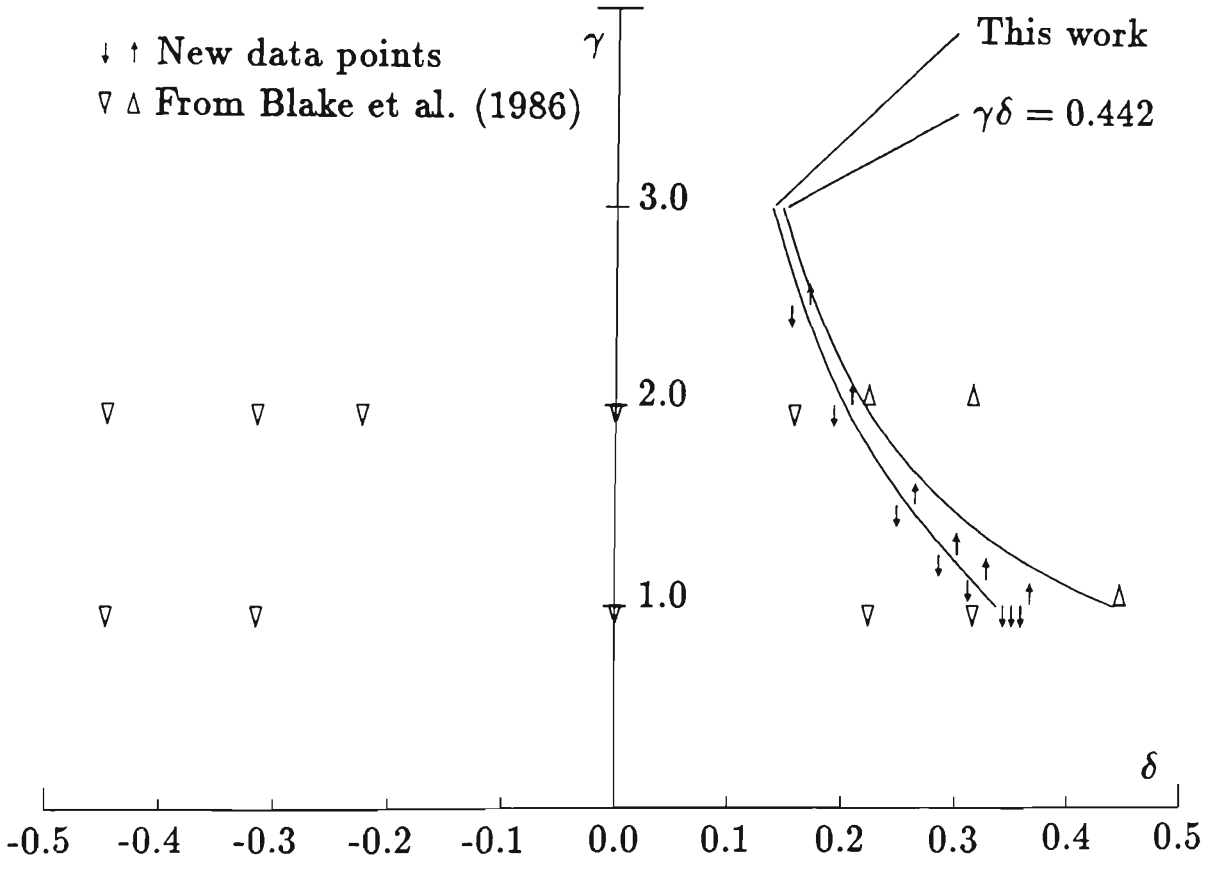

Figure 3.6.2. The null impulse line in the $\gamma - \delta$ parameter space as determined by the method of section 3.2 and also by spherical bubble dynamics. The direction of the triangle or arrow denotes the direction of centroid migration (jet formation) at the conclusion of the bubble lifetime as determined via the boundary integral method. The equations of spherical bubble dynamics predict well this partition to $\gamma = 1.125$.

γ	δ	Jet direction
2.5	0.155	−
2.5	0.171	+
2.0	0.193	−
2.0	0.209	+
1.5	0.249	−
1.5	0.265	+
1.25	0.286	−
1.25	0.302	+
1.125	0.312	−
1.125	0.328	+
1.0	0.343	−
1.0	0.351	−
1.0	0.359	−
1.0	0.367	+

Table 3.6.1. Cavitation bubble migration data computed using the boundary integral method. The notation $+, -$ signifies respectively upwards and downwards jet formation. For $\gamma = 1$ a jet was not formed so the direction given denotes that of the centroid migration at the end of the bubble lifetime.

the boundary causes the bubble to be non-spherical for much of its lifetime, not only that time when it collapses. In fact, the observation that the null impulse line is well predicted to $\gamma = 1.125$ is remarkable.

These calculations have established the value of studying the dynamics of spherical bubbles. We will now proceed to consider features of the motion in the geometries considered in sections 3.3 and 3.5 that can be inferred from the dynamics of spherical bubbles. The value of this consideration lies in the fact that for these essentially 3-dimensional motions the computational requirements are no greater than in the axisymmetric case. To do simulations of the 3-dimensional problem using boundary integral techniques is computationally very demanding and still in the early stages of development (Chahine and Perdue, 1988).

3.7. Motion in some three dimensional geometries

We have derived in section 3.5 equations for the dynamics of spherical bubbles in geometries in which the three-dimensionality of the problem is essential. In the first instance, we have considered the case of cavitation motion near a plate inclined at some angle to the uniform gravity vector, with the equations of motion given in section 3.5. Let us solve these equations for a cavitation bubble, imposing the usual initial conditions. We choose the plate inclination $\alpha = 135°$, the buoyancy parameter $\delta = 0.1$ and the point of inception is at $\gamma = 2.0$. Pertinent features of the motion are displayed in figure 3.7.1.

During the early stages of the expansion the bubble drifts away from the rigid boundary, with buoyancy causing an upwards component of drift parallel to the boundary. As the bubble expands, however, this drift away from the boundary slows, and then reverses so that the bubble migrates towards the rigid boundary. The time scale of the motion depicted by the trajectory of figure 3.7.1(a) is displayed by the points shown denoting equal time intervals. We note that for much of the motion the bubble moves little, however, during the collapse phase we observe the large displacement of the bubble centroid, the speed of this motion

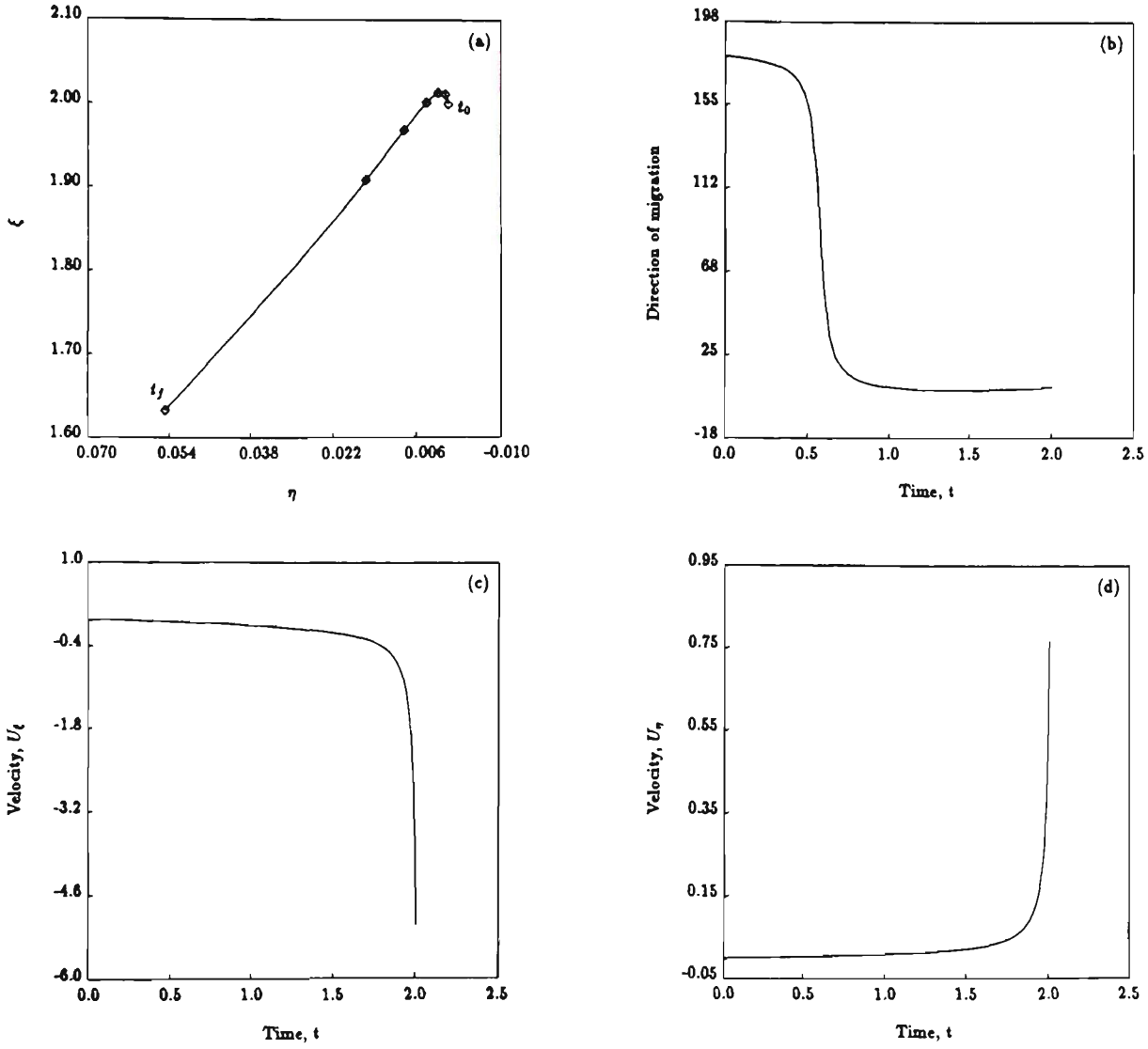

Figure 3.7.1. Buoyant cavitation bubble motion in the neighbourhood of an inclined plate. The plate inclination is $\alpha = 135^o$. The buoyancy parameter is $\delta = 0.1$. The point of inception is $\gamma = 2.0$. The frames display (a) the trajectory, (b) the direction of migration vs. time, (c) the component of the velocity perpendicular to the plate, (d) the component of the velocity parallel to the plate. The points marked on the trajectory are at equally spaced times with the initial and final times respectively denoted by t_0 and t_f.

displayed by the plots of the velocity components vs. time (figures 3.7.1(c), (d)). A particularly interesting feature of the trajectory is the well defined direction of migration as the bubble collapses, this aspect being exemplified by the graph of the direction of migration vs. time (figure 3.7.1(b)). We again propose that this direction provides us with information regarding the direction of migration of deforming bubbles and that in cases where we observe jet formation, gives the orientation of the jet. As in the case considered in section 3.6, at the conclusion of the collapse phase the Kelvin impulse and centroid velocity are similarly directed.

Since the direction of migration at the conclusion of the collapse phase is at some well defined orientation to the rigid boundary we may consider how it varies with varying plate orientation. In this way we may obtain a plot of jet-angle vs. plate angle. We have introduced the term jet-angle to refer to the direction of migration at the conclusion of the collapse phase. We may then compare this with the analytic expression of (3.3.5). We display the results for $\delta = 0.15$ in figure 3.7.2. Shown as a solid line is the result deduced from spherical bubble dynamics and the dashed line indicates the analytic expression of (3.3.5). The predominant feature is that the curve is skewed to the left. We expect this behaviour on physical grounds. Recall that the effect of the boundary alone is to cause migration towards it. We can then think of buoyancy as a perturbing influence, causing a deviation from motion normal to the boundary. For a given pair of plate inclinations, $\pi/2 - \alpha$ and $\pi/2 + \alpha$ $(0 < \alpha < \pi/2)$, the angle between $-\mathbf{g}$ (the direction of the buoyancy force) and the normal exterior to the plate (the direction of the Bjerknes force) is greater for $\pi/2 - \alpha$ so that the perturbing effect of buoyancy is greater in this case. Thus we expect a greater deviation of the direction of migration from the normal in this case. Thus the displayed curves are skewed to the left.

We also observe the effect of varying the distance from the plate at which inception occurs (γ). As we increase γ the influence of the boundary is felt less by the bubble. With buoyancy then becoming a greater relative perturbing influence we note the greater deviations from normal motion. This is further exemplified

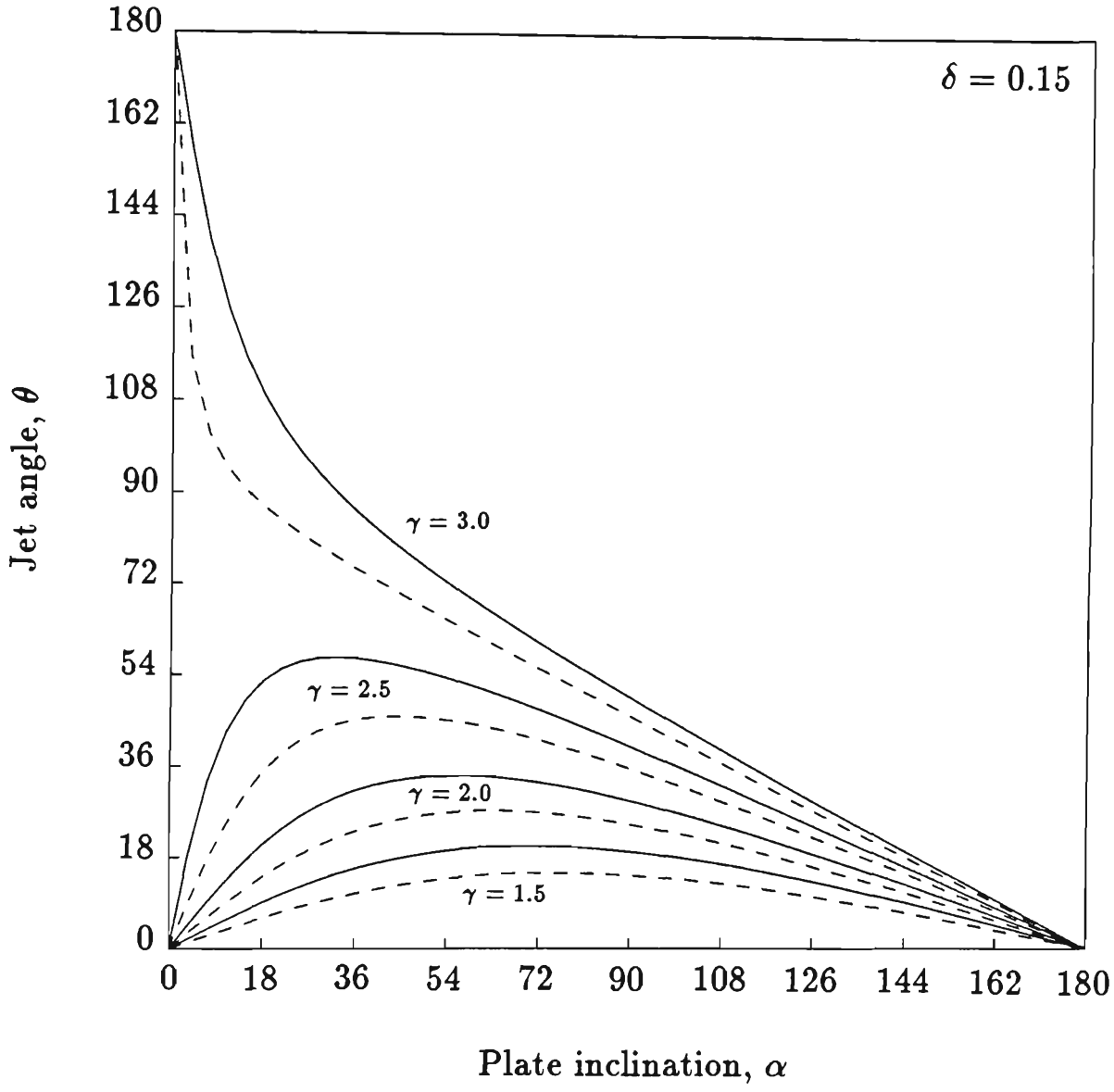

Figure 3.7.2. Jet angle vs. plate angle for cavitation bubble motion in the neighbourhood of an inclined plate. The buoyancy parameter is $\delta = 0.15$. The solid line represents the results of spherical bubble dynamics. The dashed line is the analytic expression obtained in section 3.3. The term jet angle is used for the direction of migration of the spherical bubble as it collapses to a singularity. Note that the curve is skewed to the left.

by the result for $\gamma = 3.0$. In this case we note that for small plate inclinations, the perturbing influence of buoyancy is so great that the migration is away from the rigid boundary. For smaller values of γ an increase in the buoyancy parameter gives rise to a similar effect. Finally, we note the difference in the results predicted by spherical bubble dynamics and the expression of (3.3.5). On all occasions the expression of (3.3.5) understates the deviation of the jet from the normal, the neglect of bubble migration and the sharing of kinetic energy between translational and radial motion (as expressed in equation (3.5.8)) being major factors in this regard. In any case, the simple ideas of sections 3.2 and 3.3 and consequent analytical expression for the jet angle display well the general features of the motion and are thus valuable from this viewpoint.

Similarly we may consider the motion of a cavitation bubble near a vertical rigid wall and horizontal free surface, the equations of motion having been derived in section 3.5. We propose that the direction of migration at the conclusion of the bubble life well predicts the direction of migration and jet formation for deforming bubbles, noting the coincidence of this direction with that of the Kelvin impulse, in this model. In figure 3.7.3 we have plotted the variation of the jet angle as a function of the distance of inception from the rigid boundary (γ), for given values of β (distance of inception from the free surface), for a buoyancy parameter of 0.15. The jet angle, θ, is measured with respect to the normal exterior to the rigid boundary. We have an analytic expression for this jet angle, obtained in section 3.3, and this is shown as a dashed line. We see that for a given value of γ, as we increase β the jet angle increases, reflecting the fact that the deeper the bubble the less felt is the Bjerknes repulsion of the free surface. Also note the interesting result that for a chosen value of β, as we increase γ the jet angle, in general, either increases or decreases, depending upon the value of β. We can explain this feature generally by considering the rigid boundary as a perturbing influence upon the two similarly directed effects of the free surface and buoyancy. For small values of γ we have a large perturbation of the upwards effects, and this perturbation

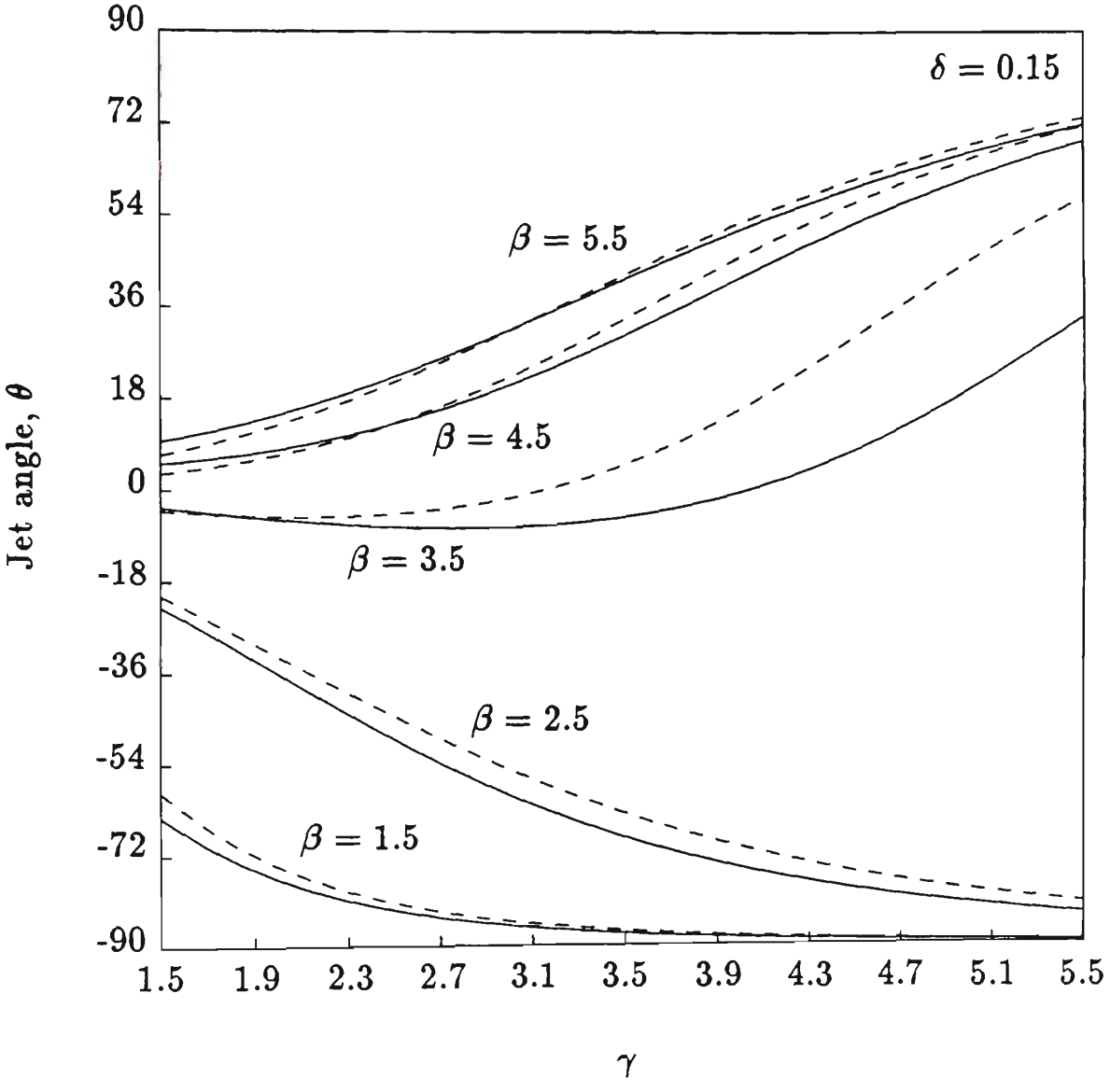

Figure 3.7.3. Jet angle vs. distance of inception from the rigid wall (γ) for motion in a quarter plane. Respective curves are for different distances of inception below the free surface (β). The buoyancy parameter is $\delta = 0.15$. The solid line was obtained using spherical bubble dynamics. The dashed line represents the analytic expression derived in section 3.3.

decreases as the point of inception moves further from the rigid boundary. In essence what we are considering is a vector sum of the forces acting on the bubble, namely the horizontal and vertical Bjerknes forces and buoyancy. Consequently, as this horizontal force decreases, whether the jet angle increases or decreases then depends upon which of the vertical effects is predominant. For large β buoyancy becomes the predominant factor and so the jet angle increases with γ, however for small β the influence of the free surface dominates, causing the jet angle to decrease as the influence of the rigid boundary becomes less important.

Along this line of reasoning, we could perhaps be led to expect that the jet angle should be a monotonic function of γ, for a given β. If we note the result of figure 3.7.3 for $\beta = 3.5$ we notice that $\theta(\gamma)$ has a stationary point. Furthermore, we may perhaps suppose that the jet angle should remain either positive or negative, depending upon the relative strengths of the buoyancy and vertical Bjerknes forces. Inspection of the results shows this to be true in general but there are exceptions. Thus we see that we can deduce qualitative features of the motion by considering Bjerknes and buoyancy effects as combining as forces in the manner in which the forces of mechanics do. We expect this from the analogy between the impulse of a bubble and the momentum of a rigid particle, and the expression of (3.2.8). We must note, however, that under some circumstances the coupling of these effects via the energy equation (equation (3.5.14)) renders these interpretations incorrect. It is clear that such violations occur for jet angles about zero and are thus associated with the bubble being in the neighbourhood of the vertical null impulse state. Since we are in this neighbourhood we expect that any small perturbations to this null impulse state due to bubble migration could cause migration in directions both greater than or less than zero. Finally, we again note the value of the simple considerations of section 3.3. The analytic expression for the jet angle appears to provide an excellent indicator of the general behaviour.

3.8. Discussion - The effect of non-condensible bubble contents

A principal aim is to begin an investigation of the effect that non-condensible bubble contents have upon the motion of the bubble, the dynamics of the bubble caused by an underwater explosion being a practical example in this regard. We may proceed to study the bubble motion using the techniques of spherical bubble dynamics. Experimental results and elementary theoretical considerations point to the behaviour that we expect. On collapse the contents compress until a stage is reached where the inwards motion of the fluid is arrested and the bubble then rebounds, so that an oscillatory motion is observed. The work of Herring (1941), Taylor (1942) and others during WWII displayed these features. Similarly, the experimental work of the period was in qualitative agreement with such predictions.

Our concern is to consider these bubbles in the context of the previous section, for much experimental work, in which the importance of the non-condensible nature of the bubble contents is clear, displays the characteristic jetting phenomena that we have much knowledge of in the context of cavitation bubble dynamics (Taylor and Davies, 1943; Bryant, 1944; Benjamin and Ellis, 1966; Lauterborn, 1980; Tomita and Shima, 1986; Vogel et al., 1989). Thus we shall make use of spherical bubble dynamics to determine the early motion of these bubbles and attempt to infer from the early behaviour aspects of the later motion when the bubbles deform from spherical shape. We choose this course of investigation as the results for the case of axisymmetric cavitation motion confirm that by careful interpretation of the analysis of spherical bubbles we can predict with some confidence aspects of the motion of deforming bubbles. Of special concern is the effect of a non-condensible gas when jets are formed. We might suppose that as the bubble contracts the high pressure developed within the bubble might be sufficient to arrest this jetting motion and cause the non-spherical bubble to rebound.

The first geometry in which we have chosen to investigate the motion of explosion bubbles is that axisymmetric geometry in which motion occurs above a rigid

boundary, as considered in section 3.6. We consider the motion for various values of the strength parameter, ϵ, the details of the motion being displayed in figure 3.8.1. Also shown on the graph, for comparison, is the behaviour of a cavitation bubble characterised by the same physical parameters (buoyancy parameter, δ), as determined by spherical bubble dynamics. The graphs of quantities for the cavitation example stop as derivatives become singular and the simple numerical scheme fails. We notice the phenomenon of rebound as indicated in the plot of bubble radius vs. time (figure 3.8.1(a)). We observe that the rebound is characterised by very high radial acceleration (figure 3.8.1(b)). As with the motion of cavitation bubbles the reducing added mass upon collapse gives rise to a period of rapid acceleration. As the bubble rebounds the increasing added mass causes the bubble to decelerate rapidly to a very small velocity. These features are well displayed in the plots of centriod position vs. time and centroid velocity vs. time (figures 3.8.1(c), (d)).

Of interest is the behaviour as we increase the strength parameter, ϵ, through the values 50, 200, 800 and 3200. As the increase occurs the gross behaviour tends to that of the cavitation bubble, the essential difference being that the compression of the bubble contents must eventually arrest the collapse of the explosion bubble. In any case, for large ϵ, we notice that for all except those brief contracted phases of the motion about rebound the non-condensible nature of the bubble contents has negligible influence upon the dynamics of the bubble. In view of this we may speculate as to the behaviour of real explosion bubbles in which the bubble is not constrained to remain spherical. Our experience of cavitation bubble phenomena indicates that for large regions of the physical parameter space governing the motion, the initial deformation from spherical shape that ultimately results in the formation of a jet is caused at volumes greater than the initial value. From our current observations we deduce that at such volumes the explosion bubble is virtually indistinguishable from a cavitation bubble characterised by the same buoyancy parameter. Thus we conclude that the modes of non-spherical collapse will gen-

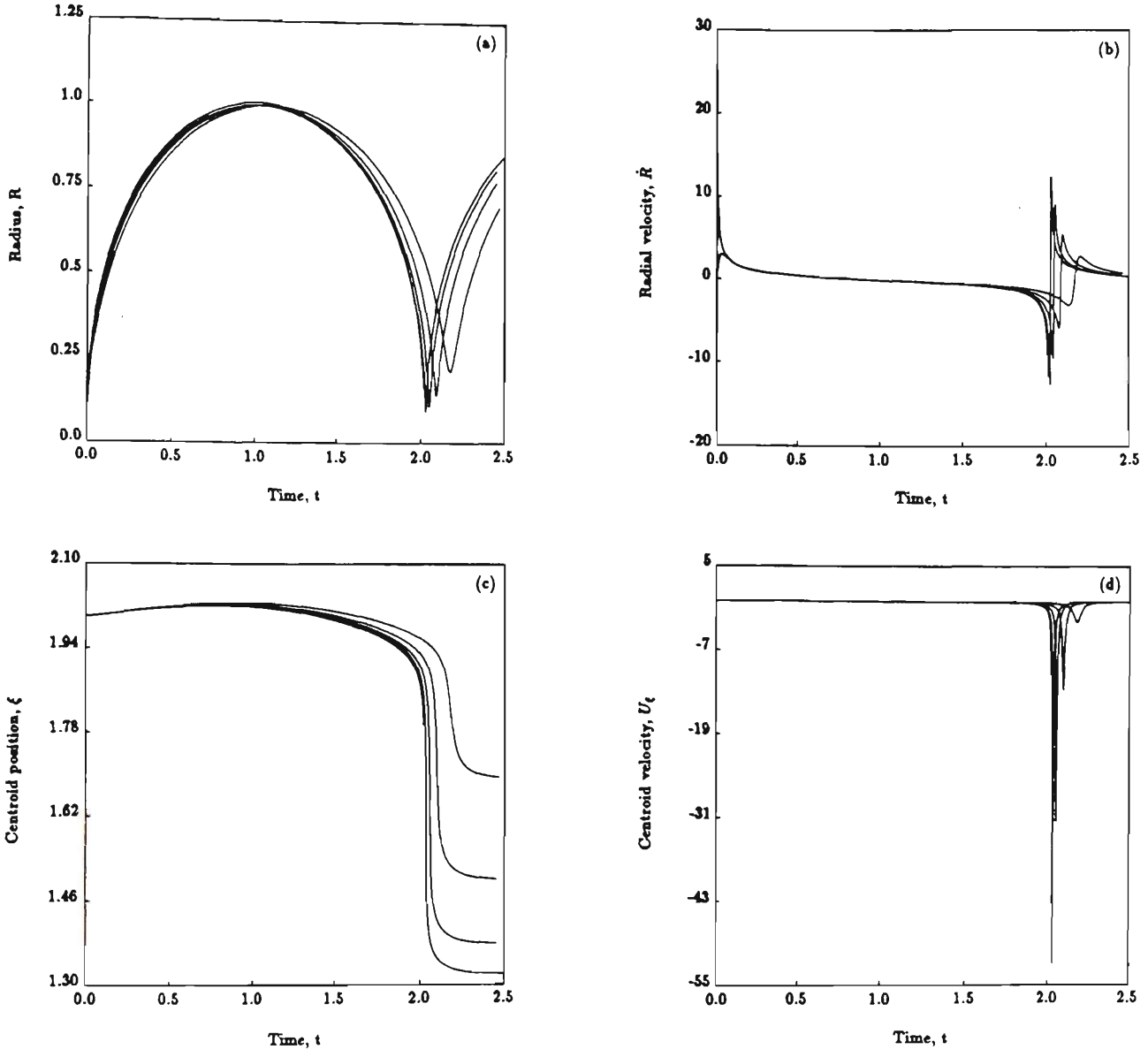

Figure 3.8.1. Buoyant explosion bubble motion for various values of the strength parameter, ϵ, compared with cavitation bubble motion. The buoyancy parameter is $\delta = 0.15$. Inception has occurred at $\gamma = 2.0$ above a horizontal rigid boundary. The strength parameter takes on the values $\epsilon = 50, 200$, 800 and 3200. The frames display (a) the radius vs. time, (b) the radial velocity vs. time, (c) the centroid position vs. time, (d) the centroid velocity vs. time. The incomplete curve describes the cavitation bubble. The curve corresponding to the greatest period denotes $\epsilon = 50$. As ϵ increases there is a systematic trend towards the cavitation example.

erally be very similar in character, with jets forming and completely penetrating the bubble.

The possibility of rebound should not be dismissed and we speculate as to the circumstances under which it may occur. We comment that in the theory of spherical bubble dynamics the behaviour of explosion and cavitation bubbles diverges as the strength parameter decreases (figure 3.8.1). We therefore speculate that a corresponding divergence in the behaviour of real, deforming bubbles will be evident in this regime. In particular, the decrease of the peak radial velocity with decreasing ϵ, as predicted by the spherical model, is suggestive that in the case of a real explosion bubble the increasing gas pressure upon collapse may sufficiently arrest the inwards motion of the fluid so that jetting is suppressed, with the bubble retaining much of its spherical character as it approaches a minimum of volume. Under such circumstances we propose that the non-spherical bubble will indeed rebound prior to the complete penetration by any jet. We further speculate that the rebound phenomenon may be observed in the neighbourhood of a null impulse state. In support of this contention we note the results of Blake et al. (1986) in which characteristic jets were not observed, or very weak jetting was observed, upon the collapse of cavitation bubbles in the neighbourhood of the null impulse state. In this region of the physical parameter space jetting is suppressed and the bubble may retain a spherical character to very small volumes, thus suggesting the possibility of rebound.

It is pertinent to note that since the behaviour of the explosion bubble tends to that of the cavitation bubble with increasing ϵ, the ideas pertaining to the Kelvin impulse as applied to cavitation bubbles should provide a valuable tool for understanding gross aspects of the motion. This behaviour is to be expected as a result of the internal bubble pressure varying as $V^{-\gamma}$. It is only during the highly contracted phases of the motion that this pressure becomes a significant factor in the dynamics, as exemplified by the case of purely radial motion described by equation (2.1.20). The term $\epsilon\,(R_0/R)^{3\gamma}$ only assumes significance for $(R-R_0)/R_m \ll 1$,

that is when the bubble volume is in the neighbourhood of its initial value.

We can proceed to examine explosion bubble motion in some essentially 3-dimensional geometries, as discussed in section 3.7. The character of the motion is much as that predicted for a cavitation bubble, however, as indicated by figure 3.8.1 the bubble has an oscillatory behaviour. As in the cavitation example the first collapse phase is characterised by a very high acceleration of the centroid and it is this motion that precipitates the non-spherical collapse and formation of a jet. If we consider the expressions for the components of the Kelvin impulse,

$$I_\xi = \frac{2}{3}\pi\rho\left\{R^3 U_\xi - \frac{3}{4}\frac{R^5\dot{R}}{\xi^2}\right\}, \tag{3.8.1}$$

$$I_\eta = \frac{2}{3}\pi\rho R^3 U_\eta, \tag{3.8.2}$$

then at rebound $\dot{R} = 0$ so that the centroid velocity and Kelvin impulse are similarly directed. We should note that in the cavitation example the impulse and centroid velocity become similarly directed as the bubble collapses and $\dot{R} \to -\infty$ due to $R^5/(\xi^2)$ vanishing at a greater rate, however in this case the similarity of these orientations is exact at rebound because $\dot{R} \to 0$. This apparent difference in the causes of coincidence should not be seen to cast doubt upon our assertion that both the Kelvin impulse and direction of migration should be closely correlated with the jet angle. Since the motion of the explosion bubble is so closely described by the cavitation solution (especially for large ϵ) the radial velocity upon collapse is very high, except in the small interval about rebound. Thus for those times during the collapse not in this interval it is the smallness of the ratio $(R/\xi)^2$ that causes the Kelvin impulse and centroid velocity to be nearly similarly directed, just as in the cavitation case. From our previous considerations we expect that jets will form upon collapse prior to the time of rebound, when the spherical model predicts high radial velocities, and so the cause of the close relation between the direction of the impulse and the centroid velocity is exactly as in the cavitation example. As a consequence, for motion in the neighbourhood of an inclined rigid plate we may

prepare a graph of jet angle vs. plate inclination and this is shown in figure 3.8.2 for a buoyancy parameter of 0.1. The value chosen as the jet angle is the direction of migration at the end of the first oscillation. We have shown as the dashed line the analytic expression of section 3.3 as well as the results for $\epsilon = 50, 200, 800$ and a cavitation bubble, as predicted by spherical bubble dynamics. For each value of γ the uppermost curve in the corresponding set of curves is described by $\epsilon = 50$. As ϵ increases there is a systematic trend towards the curve corresponding to the cavitation bubble. From previous considerations we expect this behaviour.

3.9. Concluding remarks to chapter 3

In this chapter we have considered the motion of bubbles constrained to remain spherical throughout their lifetime. By varying the description of the bubble contents we may describe the motion of cavitation or explosion bubbles. Such a model is valid during much of the bubble lifetime as experimental observations show that to a good level of approximation the bubble does indeed remain spherical. By considering the fluid momentum via the concept of the Kelvin impulse we have attempted to infer aspects of the bubble's later motion, when experimental and numerical studies indicate that the spherical model must fail. In particular, by relating the direction of the Kelvin impulse of spherical bubbles (and co-incident direction of migration) at the end of the bubble lifetime to the direction of jet formation in non-spherical collapse, we have been able to successfully determine the partition in the $\gamma - \delta$ parameter space for axisymmetric motion above a rigid boundary. The success achieved in the axisymmetric geometry motivates us to develop these techniques for geometries in which the fluid motion is essentially three-dimensional, and full numerical solutions are computationally demanding. It remains for future experimental and numerical work to establish how closely our ideas model the physical and mathematical reality. In any case, we have confidence that the salient features of the motion may be well inferred from our simple study, the elementary considerations providing considerable insight into the

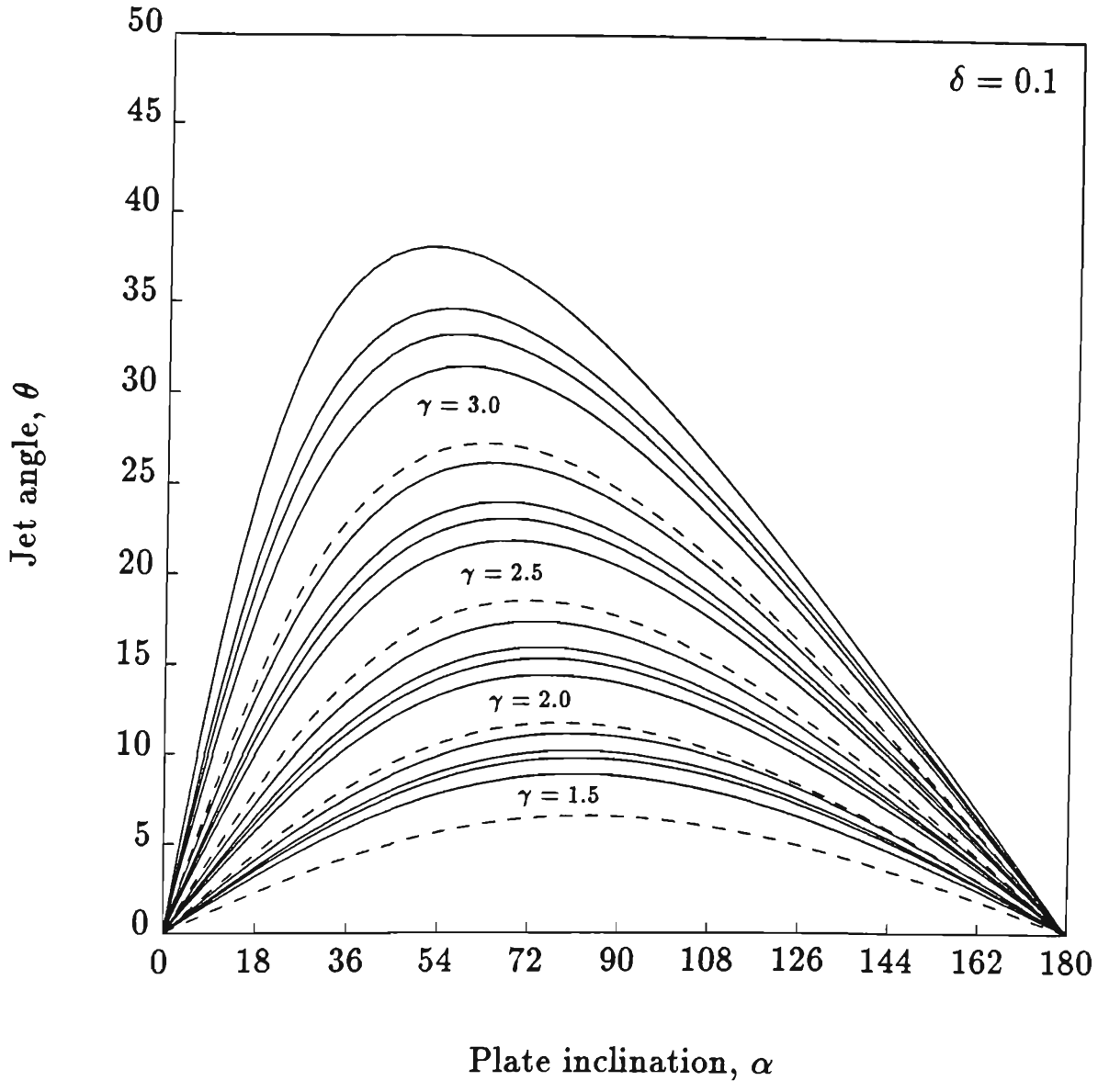

Figure 3.8.2. Jet angle vs. plate angle for explosion bubble motion in the neighbourhood of an inclined plate. Also shown for comparison are the results for a cavitation bubble and the analytic expression derived in section 3.2 (the dashed line). The values of the strength parameter are $\epsilon = 50, 200, 800$. For each set of solid curves for a given value of γ, the uppermost curve corresponds to $\epsilon = 50$. As ϵ increases there is a systematic trend towards the cavitation example which is the lowest curve.

physics of the bubble collapse phenomenon.

Finally, we have made comparisons of explosion bubble motion with the cavitation bubble motion of which we have much knowledge. The essential difference in the explosion example is the presence of a non-condensible gas within the bubble. The close correspondence between the motion of an explosion bubble and cavitation bubble for large values of the strength parameter leads us to expect similar non-spherical collapse modes for the explosion bubble case. We do, however, propose that as the strength parameter decreases, and in the neighbourhood of null impulse states, a range of interesting behaviours will be observed as under such circumstances the possibility exists that the non-spherical bubble will rebound. We devote the next two chapters to this question.

4

THE BOUNDARY INTEGRAL METHOD

The boundary integral method has become one of the standard techniques for computing the motion of cavities in an incompressible, inviscid and irrotational flow. Guerri et al. (1981) applied the technique to compute the flow field induced by the collapse of a vapour cavity adjacent to a rigid boundary. Blake et al. (1986, 1987) demonstrated that the growth phase of the bubble motion may significantly influence the character of the collapse. This work also set a benchmark against which many subsequent numerical investigations have been compared (see for example Chahine and Perdue, 1988).

It is the boundary integral method which will here be used to investigate the motion of explosion bubbles, whose internal pressure is a function of the bubble volume. It is pertinent, then, to outline the theoretical origin of this method and discuss in some detail the algorithm of Kucera (1991) which has formed the basis for these studies. The algorithm of Kucera was developed to describe the motion of cavitation bubbles. Subtle modification is required to adequately describe explosion bubble motion and detailed discussion of the algorithm at this point will facilitate a rapid description of these modifications at a later time.

Application of Green's theorem allows us to write the solution of Laplace's equation in the domain Ω as

$$c(\mathbf{p})\phi(\mathbf{p}) = \int_{\partial\Omega} \left(\frac{\partial \phi}{\partial n} G - \phi \frac{\partial G}{\partial n} \right) dS, \tag{4.1}$$

with

$$c(\mathbf{p}) = \begin{cases} 2\pi & \mathbf{p} \in \partial\Omega, \\ 4\pi & \mathbf{p} \in \Omega/\partial\Omega. \end{cases} \tag{4.2}$$

The surface $\partial\Omega$ bounds Ω and is supposed to be everywhere smooth. The point $\mathbf{p}$ is somewhere in the flow domain and $\partial/\partial n \equiv \mathbf{n} \cdot \nabla$ is the normal derivative at the boundary. The Green's function is given by G and the notation $\Omega/\partial\Omega$ denotes the complement of $\partial\Omega$ in Ω. We comment that if $\partial\Omega$ were not smooth (such as in cases

where there are corners) then the expression of (4.1) remains valid but the value of the function c at the points where the surface is not smooth would differ from 2π. It is a routine matter to determine the value of this function given the surface geometry. The reader may consult Seybert et al. (1985) for details.

In developing the boundary integral method for the solution of problems in bubble dynamics we note that the surface, $\partial\Omega$, that bounds the flow domain includes the bubble surface S. If we consider motion in an infinite fluid then $\partial\Omega$ is indeed the surface of the bubble and the Green's function is

$$G_{inf} = \frac{1}{|\mathbf{p}-\mathbf{q}|}, \tag{4.3}$$

where $\mathbf{q}$ is the position vector of some point on S. We notice that when $\mathbf{p} \in S$ the integrand of (4.1) exhibits a singularity at $\mathbf{p}$. In this case the integral over S is in a principal value sense.

In cases where the geometry of the flow domain is particularly simple we may circumvent the need to include boundaries, other than the bubble surface, in our description by appropriate choice of the Green's function. The geometry of particular relevance here is that of motion in the neighbourhood of a rigid boundary. If we choose our Green's function as

$$G_{rig} = \frac{1}{|\mathbf{p}-\mathbf{q}|} + \frac{1}{|\mathbf{p}-\mathbf{q}'|}\ , \tag{4.4}$$

where $\mathbf{q}'$ is the image of $\mathbf{q}$ reflected about the rigid boundary then we need only take $\partial\Omega$ in (4.1) as the surface of the bubble. From a computational point of view this alleviates the necessity of having a description of the rigid boundary and evaluating integrals over this surface.

The spirit of the method is as follows. We suppose that at some time, t, the bubble geometry, S, and the potential on S are known. Equation (4.1) is then a Fredholm integral equation of the first kind for the normal fluid velocity, $\partial\phi/\partial n$, at the bubble surface. Solution for this quantity allows the fluid velocity at the bubble surface to be determined. We obtain the tangential component of the

velocity from our assumed knowledge of ϕ on S. Knowledge of this velocity allows the bubble surface at some short time, δt, later to be determined. The potential on the surface at $t + \delta t$ may similarly be determined and we may solve (4.1) for $\partial\phi/\partial n$ at $t + \delta t$. In this manner we iterate the solution for the flow field in time.

In particular, if $\mathbf{X}$ denotes the position vector of some point on the bubble surface and $\mathbf{u}$ denotes the fluid velocity there, then solution of (4.1) allows determination of $\mathbf{u}$ and hence integration of the equation

$$\frac{d\mathbf{X}}{dt} = \mathbf{u}, \tag{4.5}$$

describing the motion of points on the bubble surface in the Lagrangian sense. The rate of change of the velocity potential following some fluid element is

$$\begin{aligned} \frac{d\phi}{dt} &= \frac{\partial\phi}{\partial t} + |\nabla\phi|^2 \\ &= \frac{1}{2}|\nabla\phi|^2 + (p_\infty - p)/\rho - g(z - z_0), \end{aligned} \tag{4.6}$$

where we have eliminated $\partial\phi/\partial t$ using the Bernoulli equation and p_∞ is the hydrostatic pressure at $z = z_0$. If the fluid element is at the bubble surface then the pressure in (4.6) is known as a function of the bubble volume and our prior knowledge of $|\nabla\phi|^2$ $(= |\mathbf{u}|^2)$ allows (4.6) to be integrated simultaneously with (4.5), thus giving the potential on the bubble surface as a function of time.

To solve (4.1) Kucera (following Blake et al. (1986)) employs a collocation method in an axisymmetric geometry. A set of $n + 1$ nodes are chosen on the surface of the bubble, with the assumption of axisymmetric motion necessitating only the description of a curve in two dimensions. We denote the cylindrical coordinates of the i'th node as (r_i, z_i) with $i \in \{0, 1, \ldots, n\}$. The surface of the bubble is then represented by a cubic spline, constrained to pass through the node points. The spline parameter is the arclength along the curve that is the bubble surface. We denote this arclength by ξ. We shall further denote the arclength from node 0 to node i by ξ_i and shall write

$$\delta\xi_i = \xi_i - \xi_{i-1}, \quad i = 1, \ldots, n, \tag{4.7}$$

as the arclength between adjacent nodes. Note that $\xi_0 = 0$. We write the spline functions $\tilde{r}$ and $\tilde{z}$ as

$$\tilde{r}(\xi) = r_{1i} + (\xi - \xi_i)\left(r_{2i} + (\xi - \xi_i)(r_{3i} + (\xi - \xi_i)r_{4i})\right), \tag{4.8}$$

$$\tilde{z}(\xi) = z_{1i} + (\xi - \xi_i)\left(z_{2i} + (\xi - \xi_i)(z_{3i} + (\xi - \xi_i)z_{4i})\right), \tag{4.9}$$

for

$$\xi_i < \xi < \xi_{i+1}, \quad i = 0, \ldots, n-1. \tag{4.10}$$

In (4.8) and (4.9) r_{ji} and z_{ji} ($j = 1, \ldots, 4,\ i = 0, \ldots, n-1$) are the spline parameters and $r_{1i} = r_i$ and $z_{1i} = z_i$. The spline functions $\tilde{r}$ and $\tilde{z}$ are clamped at the end nodes 0 and n in order that the bubble shape remains axisymmetric throughout the computation. The geometry is shown in figure 4.1.

The arclength along the spline is not known, a priori, but Kucera obtains it in an iterative manner. If we denote by a superscript the order of the approximation to the arclength and corresponding spline functions then we may write

$$\delta\xi_i^{(0)} = \left|\mathbf{X}_i - \mathbf{X}_{i-1}\right|, \qquad i = 1, \ldots, n, \tag{4.11a}$$

$$\delta\xi_i^{(j+1)} = \int_{\xi_{i-1}^{(j)}}^{\xi_i^{(j)}} \left[\left(\frac{\partial\tilde{r}^{(j)}}{\partial\xi}\right)^2 + \left(\frac{\partial\tilde{z}^{(j)}}{\partial\xi}\right)^2\right]^{\frac{1}{2}} d\xi, \quad j = 0, 1, \ldots, \tag{4.11b}$$

with $\mathbf{X}_i$ denoting the position vector of the i'th node. In order to implement this method an initial approximation to the arclength is chosen to be the linear distance between nodes. This is then used to determine an initial approximation to the spline functions, $\tilde{r}^{(0)}(\xi)$ and $\tilde{z}^{(0)}(\xi)$. Using these functions we obtain a further approximation by evaluating (4.11b) and using the resultant arclength to generate new spline functions. Integration of (4.11b) is performed numerically and Kucera found that a highly accurate representation of the arclength is obtained after 2 or 3 iterations of (4.11).

The potential is considered known at the nodes and we represent its value over the surface S using a cubic spline, parameterised with respect to the above numerically found arclength. We write this as

$$\tilde{\phi}(\xi) = \phi_{1i} + (\xi - \xi_i)(\phi_{2i} + (\xi - \xi_i)(\phi_{3i} + (\xi - \xi_i)\phi_{4i})), \tag{4.12}$$

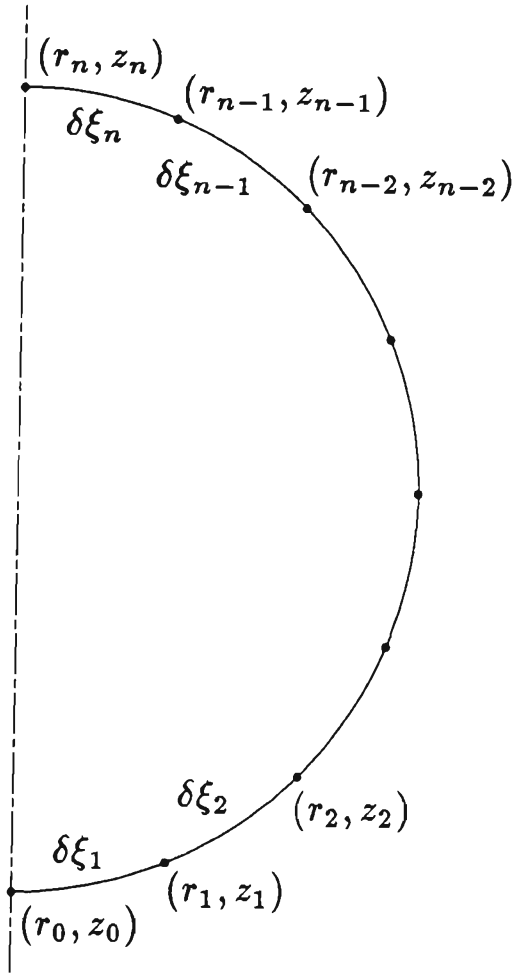

Figure 4.1. The discretisation of the bubble surface as employed in the boundary integral algorithm.

with the notation as previously defined. We shall denote the value of $\partial\phi/\partial n$ at node i by ψ_i. It is these quantities that are unknown and for which we seek a solution. We choose to represent $\partial\phi/\partial n$ on S linearly with respect to the arclength, so we write

$$\tilde{\psi}(\xi) = \psi_{i-1}(\xi_i - \xi)/\delta\xi_i + \psi_i(\xi - \xi_{i-1})/\delta\xi_i, \quad i = 1, \ldots, n. \tag{4.13}$$

Collocation of (4.1) at the node points, using the expressions of (4.8), (4.9), (4.12) and (4.13) yields the set of linear equations

$$2\pi\phi_i + \sum_{j=1}^{n} A_{ij} = \sum_{j=1}^{n} (B_{ij}\psi_{j-1} + C_{ij}\psi_j), \quad i = 0, \ldots, n, \tag{4.14}$$

with

$$\begin{aligned} A_{ij} &= \int_{\xi_{j-1}}^{\xi_j} \tilde{\phi}(\xi) \left\{ \int_0^{2\pi} \tilde{r}(\xi,\theta) \frac{\partial G_i}{\partial n}(\xi,\theta) d\theta \right\} d\xi, \\ B_{ij} &= \int_{\xi_{j-1}}^{\xi_j} \left(\frac{\xi_j - \xi}{\delta\xi_j} \right) \left\{ \int_0^{2\pi} \tilde{r}(\xi,\theta) G_i(\xi,\theta) d\theta \right\} d\xi, \\ C_{ij} &= \int_{\xi_{j-1}}^{\xi_j} \left(\frac{\xi - \xi_{j-1}}{\delta\xi_j} \right) \left\{ \int_0^{2\pi} \tilde{r}(\xi,\theta) G_i(\xi,\theta) d\theta \right\} d\xi. \end{aligned} \tag{4.15}$$

In (4.15) we have denoted by G_i the value of the Green's function evaluated at the i'th node. In the case of motion in an infinite fluid we may write it as

$$G_i(\xi,\theta) = 1/\left|\mathbf{X}_i - \mathbf{x}(\xi,\theta)\right|, \tag{4.16}$$

where $\mathbf{x}(\xi,\theta)$ is the position vector of some point on the bubble surface and $r(\xi,\theta)$ is the radial co-ordinate of this point, parametrised with respect to arclength, ξ, and azimuthal angle, θ. Integration over θ and ξ yields the surface integral of (4.1). The integration over θ is performed analytically, yielding expressions involving elliptic integrals of the first and second kind. The integration over ξ is performed numerically using Gauss-Legendre quadrature formulae. When the integrand is singular, the logarithmic singularity is subtracted and an appropriate quadrature scheme is utilised to complete the integration. For details concerning these aspects the reader is referred to the work of Taib (1985).

The system of (4.14) is solved using standard techniques and yields $\psi_i, i = 0, \ldots, n$. The radial and vertical components (denoted respectively by u and v) of

the fluid velocity may be evaluated at the bubble surface via

$$u(\xi) = \frac{\partial \tilde{\phi}}{\partial \xi}\frac{\partial \tilde{r}}{\partial \xi} - \tilde{\psi}\frac{\partial \tilde{z}}{\partial \xi},$$
$$v(\xi) = \frac{\partial \tilde{\phi}}{\partial \xi}\frac{\partial \tilde{z}}{\partial \xi} + \tilde{\psi}\frac{\partial \tilde{r}}{\partial \xi}. \tag{4.17}$$

We note that the normal interior to the bubble is given by $(-\partial\tilde{z}/\partial\xi,\ \partial\tilde{r}/\partial\xi)$. In particular, we may evaluate (4.17) at the nodes and use an Euler integration scheme to determine the position of the nodes after some small time interval δt. We have

$$r_i(t+\delta t) = r_i(t) + u_i(t)\delta t + O(\delta t^2),$$
$$z_i(t+\delta t) = z_i(t) + v_i(t)\delta t + O(\delta t^2), \tag{4.18}$$

and may also determine the potential at this time using

$$\phi_i(t+\delta t) = \phi_i(t) + \left[\frac{d\phi}{dt}(t)\right]_i \delta t + O(\delta t^2), \tag{4.19}$$

with $d\phi/dt$ given by (4.6). Having determined the geometry of the bubble surface, and potential distribution on it, at $t+\delta t$ we may again solve (4.1) for $\partial\phi/\partial n$ and in this way the motion of the bubble surface is computed as a function of time.

In the algorithm of Kucera (and that of some previous studies, such as that of Blake et al., 1986, 1987) the motion of the initial node points used to represent the bubble surface is followed in time. In this manner the trajectories executed by these points are readily computed and are a valuable aid in visualising the flow and interpreting the behaviour of the bubble. As an example of such computations see the work of Blake et al. (1986, 1987) and that of Kucera and Blake (1988). To initiate the computation the initial conditions for a cavitation bubble, as discussed in chapter 2, are utilised.

A final point that we should note is the employment of a variable time step δt. The Euler time stepping is robust and produces excellent results with the computational effort somewhat optimised by the choice of δt according to the expression

$$\delta t = \frac{\Delta\phi}{\max_i \left[1 + \frac{1}{2}|\mathbf{u}|^2 - \delta^2(z - z_0)\right]}, \tag{4.20}$$

where $\Delta\phi$ is some constant, the scaling of chapter 2 has been introduced and $\max_i$ denotes the maximum value over all node points. In the example of cavitation bubble motion use of this expression imposes that the change in potential at all nodes is bounded above by $\Delta\phi$ for each step of the Euler integration scheme.

5

REBOUNDING BUBBLES

5.1. Modification of the boundary integral algorithm for the computation of explosion bubble motion

The models utilised in this study for cavitation and explosion bubble phenomena differ only in the description of the bubble contents and the conditions used to initiate the computation. The significant new feature we expect to be characteristic of the explosion phenomenon is that of bubble rebound due to the non-condensible nature of the gaseous explosion products. Experimental evidence suggests that even in cavitation bubble motion the later stages of the collapse proceed so quickly that the liquid vapour inside the bubble cannot completely condense and the cavitation bubble rebounds. This feature has not been evident in numerical computations to date as the bubble pressure has been assumed to remain constant. Thus the investigation undertaken here may equally be considered as one of cavitation bubble motion in which not all of the liquid vapour condenses upon collapse. In order that the boundary integral method provides an accurate description of this behaviour, modification of the basic algorithm discussed in chapter 4 is required. At a given time, the bubble surface and potential at this surface are known and the collocation method described in chapter 4 for the determination of $\partial\phi/\partial n$ is applied unchanged. It is only the time iteration process that is in need of modification.

The Bernoulli equation evaluated at the surface of the bubble is

$$\frac{\partial\phi}{\partial t} + \frac{1}{2}|\nabla\phi|^2 + \epsilon(V_0/V)^\gamma + \delta^2(z - z_0) = 1, \tag{5.1.1}$$

where we have chosen a reference depth of z_0 and defined ϵ and δ in terms of the hydrostatic pressure at this depth. It is this expression which we now use in (4.6) to eliminate $\partial\phi/\partial t$ from the expression for $d\phi/dt$, which is then integrated to give the potential at the surface of the bubble as a function of time. The computation

is initiated by supposing that the bubble surface is a sphere of radius R_0 and at rest, so that the potential everywhere is zero. A high initial pressure inside the bubble drives the motion from rest and this is characterised by the parameter ϵ. As discussed in chapter 2 the initial radius R_0 is chosen, given the value of ϵ, such that radial oscillations in an infinite fluid would give rise to a bubble of maximum radius 1.

It was noted in chapter 3 that spherical bubble dynamics, when applied to the explosion bubble phenomenon, predicts very high radial velocities about the moment of rebound. At rebound, however, the radial velocity is zero although the acceleration remains high, due to the change in sign of the velocity occurring over a very short time interval. In order to capture this fast motion numerically considerable care must be exercised in the choice of the time step. The formula of (4.20), extensively utilised in cavitation research, has the particularly advantageous feature that during those phases of the motion characterised by high fluid velocities, such as during the later stages of the collapse, very small time steps are given in order to accurately capture this fast motion. In the case of spherical oscillations of an explosion bubble in an infinite fluid, at least, the radial velocity of the bubble surface is zero at rebound and (4.20) consequently gives a large time step. Provided second and higher order time derivatives were small at the time of rebound the Euler time stepping scheme utilising this choice of time step would provide a good estimate of the change in position of the bubble surface and potential on it for such large time steps. However, as we have just remarked the radial acceleration of the bubble surface is very high at this time and causes large errors in the integration of the bubble surface and potential. In particular, we have that the Euler time stepping formula yields

$$R(t+\delta t) = R(t) + \dot{R}(t)\delta t + O(\delta t^2), \tag{5.1.2}$$

with the error term of order δt^2 given by

$$\tilde{R}(t')\delta t^2/2, \quad t' \in (t, t+\delta t), \tag{5.1.3}$$

which is large. In practice the magnitude of this error causes the bubble to undershoot or overshoot its minimum volume and the subsequent computation of the motion fails. This problem is quite dramatic in the integration of the equations of spherical bubble dynamics and even more so in the case of non-spherical bubbles computed by the boundary integral method.

In order to capture numerically the moment of rebound, then, it is necessary to reconsider the choice of time step. At the bubble surface we have

$$\frac{d\phi}{dt} = \frac{1}{2}|\nabla\phi|^2 - \epsilon(V_0/V)^\gamma - \delta^2(z - z_0) + 1. \tag{5.1.4}$$

Following the philosophy utilised in selection of the time step via (4.20) we might maximise this expression over the bubble surface and choose δt such that, in an Euler integration scheme, the change in ϕ at all nodes is bounded above by $\Delta\phi$. This, however, is not an appropriate choice because $d\phi/dt$ may be close to zero shortly after inception and about the time of rebound, yielding a very large time step. For the motion of spherical explosion bubbles in an infinite fluid it may be routinely verified that $d\phi/dt = 0$ at times about the minimum volume. This is in contrast to the cavitation behaviour, modelled by a constant bubble pressure, where $d\phi/dt$ is always greater than zero.

Taking the sum of the absolute values of the terms in (5.1.4) we note that $d\phi/dt$ is bounded above by

$$\max_S \left(\frac{1}{2}|\nabla\phi|^2 + \epsilon(V_0/V)^\gamma + \delta^2|z - z_0| + 1 \right), \tag{5.1.5}$$

and this expression is always greater than one. If we choose

$$\delta t = \frac{\Delta\phi}{\max_S \left(\frac{1}{2}|\nabla\phi|^2 + \epsilon(V_0/V)^\gamma + \delta^2|z - z_0| + 1 \right)}, \tag{5.1.6}$$

then the change in ϕ at each node is bounded above by $\Delta\phi$ over the time interval δt in an Euler integration scheme. This formula, with the maximum evaluated over all the nodes defining the bubble surface, possesses the necessary features to enable an Euler time stepping formula to capture bubble rebound with the

computational effort somewhat optimised. When the fluid motion is fast the time step is reduced. Furthermore, when the bubble is contracted and $V_0/V \sim 1$, then irrespective of the value of $|\nabla\phi|$ the expression of (5.1.6) yields very small time steps due to the largeness of ϵ and this allows the rebound of the bubble to be numerically captured using an Euler time stepping scheme. For the computations presented here, $\Delta\phi$ was chosen to be in the range 0.05-0.08.

The largeness of the second derivative about rebound is the apparent cause of the difficulty in capturing rebound using an Euler time stepping scheme and this identification of the cause is suggestive that implementation of higher order time stepping schemes may be advantageous. In the work of Guerri et al. (1981) a second order accurate multistep time integration scheme was employed, but found to be unstable during the expansion phase of the bubble motion. In view of this, second and fourth order Runge-Kutta integration schemes were implemented, the particular feature of the Runge-Kutta scheme that we wish to exploit is the fact that it is a single step method. In order to implement the second order method we proceed as follows. At time t the bubble surface is defined by the nodes $(r_i(t), z_i(t))$ with the potential at node i given by $\phi_i(t)$. Equation (4.1) is then solved, using this data, for $\partial\phi/\partial n$ at the nodes and the fluid velocity there may be computed. We define

$$dr_{i1} = u_{i1}\delta t, \tag{5.1.7}$$

$$dz_{i1} = v_{i1}\delta t, \tag{5.1.8}$$

$$d\phi_{i1} = \left[\frac{d\phi}{dt}\right]_{i1}\delta t, \tag{5.1.9}$$

with (u_{i1}, v_{i1}) the fluid velocity at node i and $\left[\frac{d\phi}{dt}\right]_{i1}$ is determined in the usual manner. We further define

$$r_{i1} = r_i(t) + dr_{i1}, \tag{5.1.10}$$

$$z_{i1} = z_i(t) + dz_{i1}, \tag{5.1.11}$$

$$\phi_{i1} = \phi_i(t) + d\phi_{i1}, \tag{5.1.12}$$

as the intermediate bubble geometry and surface distribution of potential. We solve (4.1) in this intermediate geometry to obtain the fluid velocity at the surface of the intermediate bubble, and if (u_{i2}, v_{i2}) denotes this velocity then we write

$$dr_{i2} = u_{i2}\delta t, \tag{5.1.13}$$

$$dz_{i2} = v_{i2}\delta t, \tag{5.1.14}$$

$$d\phi_{i2} = \left[\frac{d\phi}{dt}\right]_{i2} \delta t, \tag{5.1.15}$$

so that the bubble surface and potential on it at time $t + \delta t$ are given by

$$r_i(t + \delta t) = r_i(t) + (dr_{i1} + dr_{i2})/2, \tag{5.1.16}$$

$$z_i(t + \delta t) = z_i(t) + (dz_{i1} + dz_{i2})/2, \tag{5.1.17}$$

$$\phi_i(t + \delta t) = \phi_i(t) + (d\phi_{i1} + d\phi_{i2})/2, \tag{5.1.18}$$

with the error of order δt^3. The fourth order method is implemented similarly.

Both second order and fourth order schemes were implemented with the computational effort per time step respectively two and four times greater than for the Euler scheme. Despite this the higher accuracy of the integration allows larger time steps to be taken and the overall effect is a saving in computational effort whilst achieving a solution of superior accuracy. The example of the oscillation of a spherical explosion bubble in an infinite fluid was used to validate these high order time stepping routines and in this specialised geometry the fourth order method gives considerable improvement over the second order scheme. It was found, however, that for the computation of the motion of deforming bubbles the fourth order method offers no noticeable increase in the accuracy of the solution over the second order scheme, but merely increases the effort. It is believed that this is due to the errors associated with the solution of (4.1) being comparable with the errors of the Runge-Kutta scheme of order greater than 2. For this reason all subsequent calculations were performed using the second order scheme.

During the early attempts to compute the rebound of non-spherical bubbles it was found that a saw tooth type instability developed in the bubble shape in that

region where the jet was about to form. In the first instance the mesh representing the bubble surface was redefined such that the nodes were evenly spaced, with respect to arclength along the bubble surface, and although allowing the computation to proceed to a slightly greater time did not prevent the development of, and rapid growth of this instability. Thus a smoothing scheme is employed and that chosen is the 5-point formula first used by Longuet-Higgins and Cokelet (1976) in their study of steep surface waves on water. If a function f is defined on an evenly spaced mesh $\xi_i\,(i = 0, 1, ..., n)$ and exhibits an oscillatory behaviour of period 2 in i about some mean curve then we can approximate the value f_i of f at ξ_i by

$$f_i = (a_0 + a_1\xi_i + a_2\xi_i^2 + \cdots + a_n\xi_i^n) + (-1)^i(b_0 + b_1\xi_i \cdots + b_{n-1}\xi_i^{n-1}), \tag{5.1.19}$$

where the first term represents some mean behaviour and the second represents the oscillatory behaviour of period 2. We choose a smoothed value $\bar{f}_i$ of the function f at ξ_i as

$$\bar{f}_i = a_0 + a_1\xi_i + a_2\xi_i^2 + \cdots + a_n\xi_i^n, \tag{5.1.20}$$

and the coefficients $a_0, \cdots, a_n, b_0, \cdots, b_{n-1}$ in (5.1.19) may be chosen uniquely such that this expression holds at the $2n+1$ points $\xi_j\,(j = n-i, \ldots, n+i)$. Choice of $n = 2$ gives the 5-point smoothing formula

$$\bar{f}_i = \frac{1}{16}\,(-f_{i-2} + 4f_{i-1} + 10f_i + 4f_{i+1} - f_{i+2})\,. \tag{5.1.21}$$

Application of this formula requires that the mesh upon which the function f is defined is evenly spaced. Thus before applying this scheme the nodes representing the bubble surface must be redistributed so that they are evenly spaced with respect to arclength. The functions representing r, z and ϕ are then smoothed by application of (5.1.21). It was further found that a slight improvement in the accuracy of the method could be obtained by redefining the mesh after every time step so that all nodes are evenly spaced. When this strategy is adopted it becomes essential that the integration in time is performed by a single step method. The smoothing formula is applied every 5-20 iterations, with this application only being essential when attempting to numerically capture rebound. The application of smoothing

raises many questions regarding the stability of the bubble phenomenon. It is pertinent to postpone comments regarding this matter until after the numerical results have been presented.

5.2. Non-spherical explosion bubble collapse

We consider first a typical example of explosion bubble motion. The motion commences at a distance $\gamma = -2.0$ from a rigid boundary, the negative value indicating that the motion occurs below the boundary at $z = 0$. The buoyancy parameter is $\delta = 0.0$ so that the only asymmetry in the flow field is due to the presence of the rigid boundary. The strength parameter is $\epsilon = 100$ with the corresponding initial radius equal to 0.1651. The bubble surface is initially stationary.

The bubble shapes at various times throughout the growth and collapse are shown in figure 5.2.1. We make a few pertinent observations. Firstly we note that to a very good level of approximation the bubble remains spherical in shape as it expands and also during the early stages of the collapse. As the collapse proceeds the rear side of the bubble becomes noticeably flattened and this perturbation from spherical shape grows rapidly to form the high speed liquid jet that threads the bubble. The computation cannot proceed beyond the time that the jet impacts upon the far side of the bubble. If we consider that the flattening of the rear of the bubble denotes the beginning of jet formation then inspection of the times corresponding to the profiles shown in figure 5.2.1 indicates that the jet forms and completely penetrates the bubble in about 2.5% of the bubble lifetime.

In chapter 3 much was made of this speed of collapse. In particular, our assumption that the change in the Kelvin impulse during jet formation is small compared with the impulse itself allows us to make an estimate of the impulse of the deformed, jet pierced bubble using the spherical model, and is based upon the swiftness of the collapse. In this context it is of interest to compute the Kelvin impulse as a function of time for this example and the result of this computation is shown in figure 5.2.2, along with the value computed via the spherical model

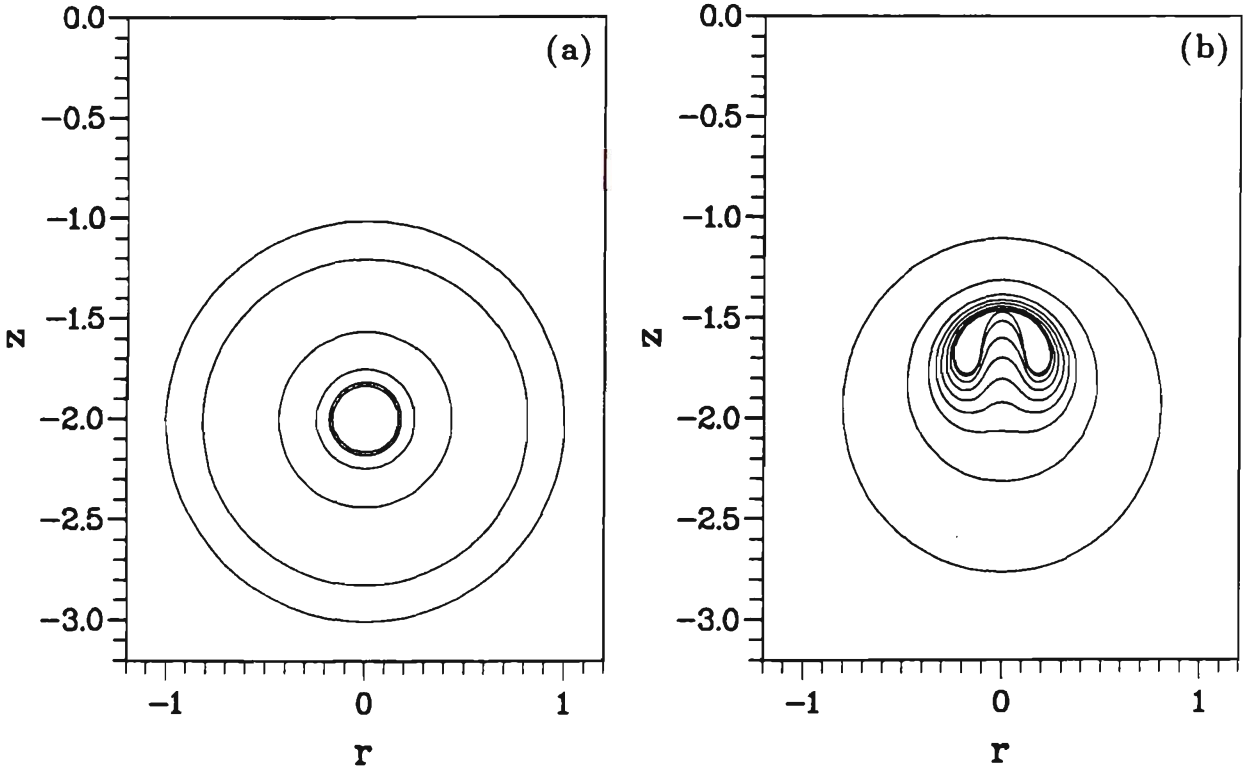

Figure 5.2.1. Successive bubble shapes for the growth and collapse of an explosion bubble characterised by $\gamma = -2.0$, $\delta = 0.0$, $\epsilon = 100$. The times corresponding to successive profiles are: (a) Growth phase: 0.0000 (innermost), 0.0082, 0.0237, 0.0860, 0.4108, 1.0692 (outermost). (b) Collapse phase: 1.7213 (outermost), 2.0197, 2.0719, 2.0878, 2.0984, 2.1076, 2.1158, 2.1231, 2.1269 (innermost).

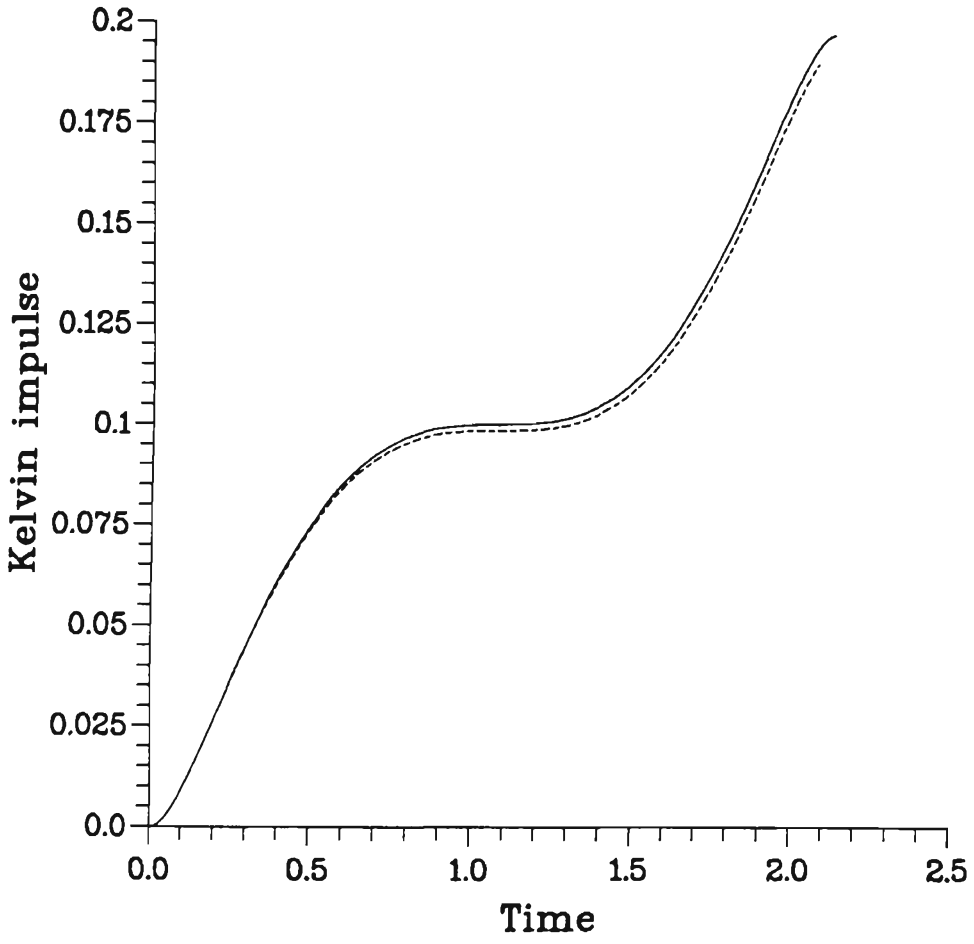

Figure 5.2.2. The Kelvin impulse as a function of time for the bubble motion illustrated in figure 5.2.1. The solid line shows the impulse of the deforming bubble. The dashed line denotes the approximation to the impulse computed using the equations of spherical bubble dynamics developed in chapter 3.

developed in chapter 3. If we consider that the jet forms at about $t = 2.072$, the time of the third collapse profile in figure 5.2.1 in which the rear of the bubble has become noticeably flattened, then inspection of figure 5.2.2 reveals a very small change in the Kelvin impulse over the small time that the jet is formed. We further note that the value of the impulse predicted by the spherical model is in good agreement with this final value. Since the change in the impulse over the time that the jet is formed is small this is no surprise. The main source of error in this approximation appears to be in the estimation of the bubble lifetime. Up until the time that jet formation occurs, in this example at least, the bubble may be well considered to be spherical and the model of chapter 3 is a good approximation. We shall present more data regarding this aspect of the study later in this chapter.

We can consider the mechanism by which the jet is formed in a number of ways. In this case of motion in the neighbourhood of a rigid boundary, upon collapse fluid may be drawn preferentially from the side of the bubble furthermost from the rigid boundary. The increased mobility of the flow from this region causes that part of the bubble surface to collapse more quickly than other parts and it is this initial perturbation in the bubble shape that is the first element of the jet.

We consider the mechanism in an alternative manner after computing the pressure field in the fluid by making use of the Bernoulli equation, as has been done previously by Blake et al. (1986, 1987). The pressure field in the fluid about the bubble at the times $t = 2.0197$ and $t = 2.1230$ is shown in figure 5.2.3. At $t = 2.0197$ (figure 5.2.3(a)) the bubble is approximately spherical, the pressure inside the bubble is 1.08 and the computed pressure field is typical of an accelerating sphere. There is a peak of pressure located behind the bubble, with respect to the direction of centroid acceleration. As the bubble accelerates this peak value increases and drives the jet into the bubble. This is indicated in figure 5.2.3(b) where at $t = 2.1230$ the jet has pierced the bubble with the peak of pressure continuing to drive the fluid in the jet. The pressure within the bubble at this time is 47.63. Thus we can say that for motion in the neighbourhood of a rigid boundary the Bjerknes

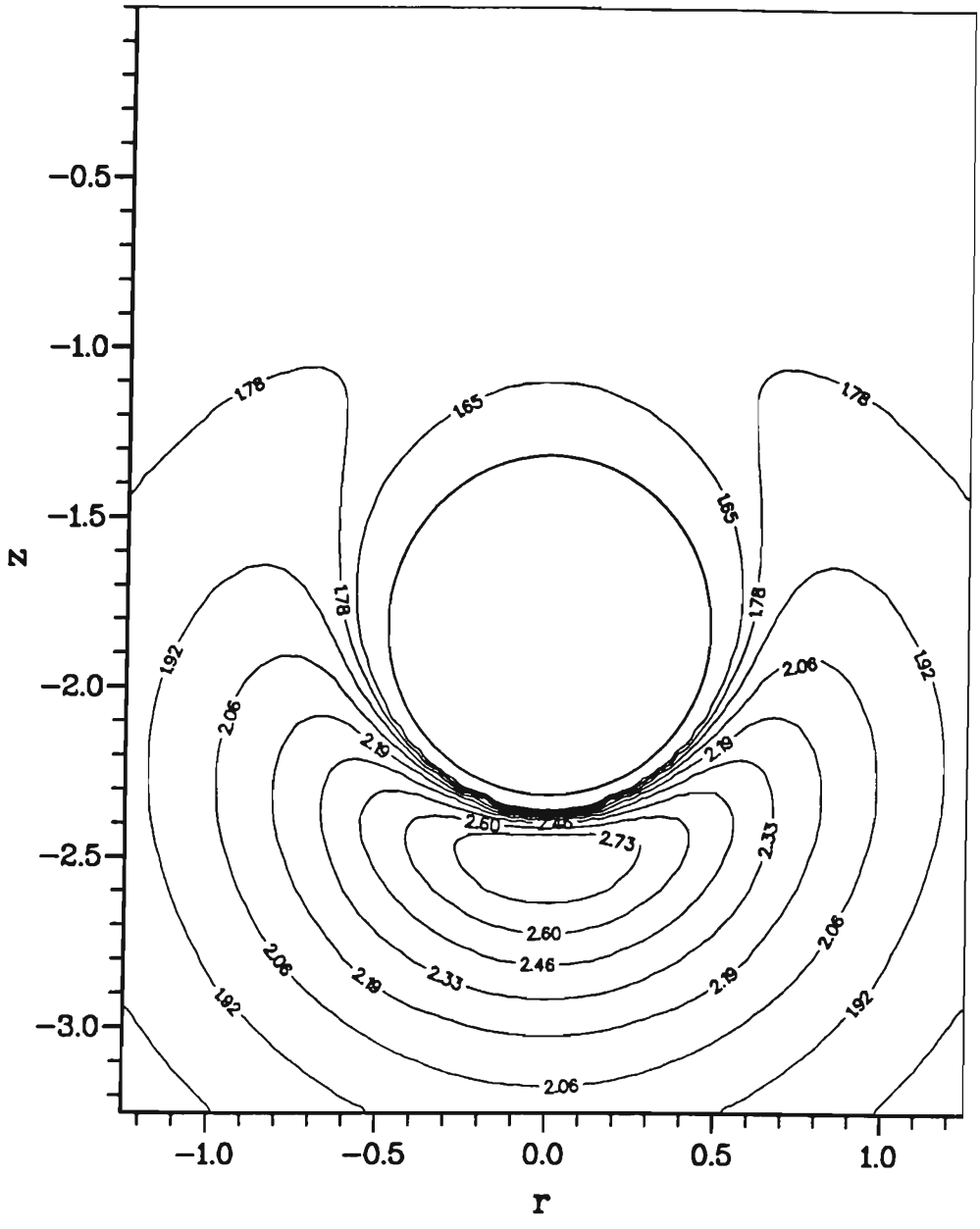

Figure 5.2.3(a). The pressure field in the fluid computed for the motion illustrated in figure 5.2.1 at time $t = 2.0197$.

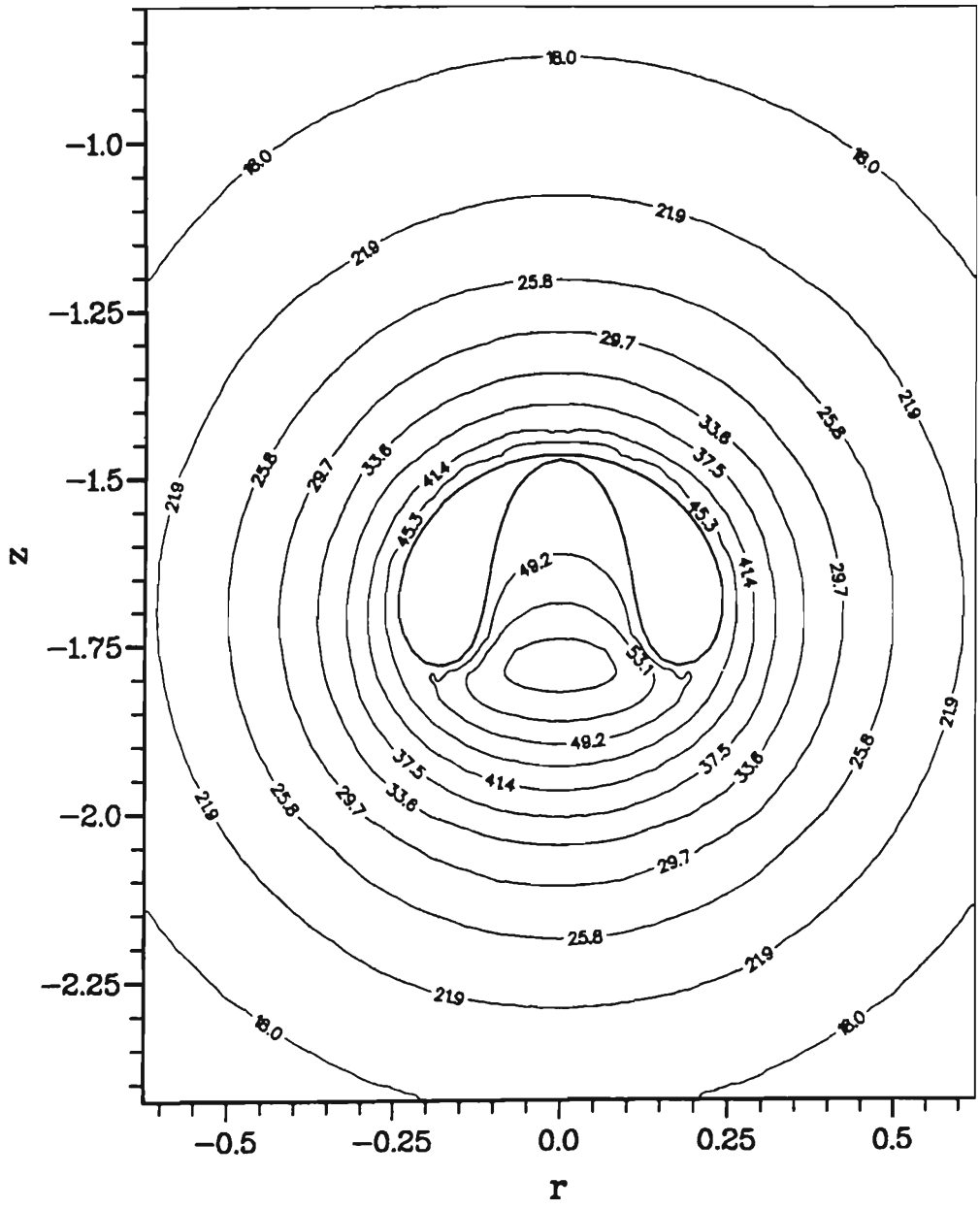

Figure 5.2.3(b). The pressure field in the fluid computed for the motion illustrated in figure 5.2.1 at time $t = 2.1230$.

attraction of the boundary causes the bubble to accelerate towards it upon collapse, with the resultant peak of pressure that develops behind the bubble being the agent that drives the jet into the bubble. This latter view of the cause of jet formation is particularly useful when considering bubble collapse due to buoyancy forces alone. Upon collapse the reducing added mass of the bubble causes it to accelerate upwards causing the formation of, and rapid intensification of the pressure maximum which is sufficient to drive a jet into the bubble from the rear.

In this example the qualitative behaviour of the bubble is as documented for the collapse of cavitation bubbles. There is no qualitative evidence to suggest that the high pressure developed within the bubble as the volume decreases acts to arrest the formation of the jet. It was postulated in chapter 3, however, that for small values of the strength parameter and in the neighbourhood of the null impulse state we should expect that the bubble may retain its spherical integrity upon collapse sufficiently that it may rebound before jet penetration is complete. We thus proceed to investigate this matter by considering various regions of the physical parameter space.

5.3. Variation of the buoyancy parameter

Let us investigate that subset of the physical parameter space characterised by a constant value of $|\gamma|$ and ϵ. We consider motion above and below a rigid boundary and choose $\gamma = \pm 1.5$ with $\epsilon = 100$. Our aim is twofold. In the first instance, for $\gamma = 1.5$ the values of the buoyancy parameter chosen lie between 0.0 and 0.35 and this region of the parameter space includes the state that we have referred to in chapter 3 as the null impulse state, in which neighbourhood we expect non-spherical bubble rebound to occur. Secondly, we know that buoyancy induces jet formation in a direction opposite to the gravitational field and that the Bjerknes attraction of a rigid boundary induces jet formation directed towards it so that for motion below and above such a boundary these effects will respectively act together and in opposition. It is of interest to investigate the features of

the collapse that vary as the buoyancy and Bjerknes forces vary and determine qualitative principles describing this variation.

The primary result is shown in figure 5.3.1 where the computed bubble shape is shown at the time when the jet completely penetrates the bubble, or when the bubble achieves a minimum of volume. The time corresponding to the shown profile is given below each bubble shape. The outstanding result on a first inspection of this figure is for $\gamma = 1.5$ and $\delta = 0.25$ where the bubble has achieved a minimum of volume, indicating that the non-spherical bubble rebounds before a jet penetrates it completely. We observe, however, that the beginnings of a jet is evident and we consider this further when we present the results of the computation of the whole motion. Of secondary interest is the bubble shape for $\gamma = 1.5$ and $\delta = 0.30$. The jet penetration is not quite complete at minimum volume and the upper part of the jet has spread radially outwards, so that the radius of the jet there is greater than that at the base. We also consider this aspect shortly.

Consider the upper sequence, characterised by $\gamma = -1.5$, as δ decreases from 0.35 to 0.00. In this case the buoyancy and Bjerknes forces are similarly directed. As δ decreases the time at which jet penetration is complete generally tends to decrease but this variation is negligible compared to the lifetime of the bubble. It thus appears that the lifetime of the bubble depends little upon the buoyancy parameter. As δ decreases the breadth of the jet decreases, as does the volume of the bubble at the end of the life. To provide some quantitative data with which to assist in the interpretation of this behaviour we have computed the velocity of that point on the bubble surface that eventually evolves into the jet tip, as a function of time, and we call this the jet velocity. This variation for the bubbles currently under consideration is shown in figure 5.3.2(a). We have also computed the Kelvin impulse of the bubbles at the times shown in figure 5.3.1 and this data may be found in table 5.3.1. Also recorded in this table are the estimates of the final Kelvin impulse computed using the equations of spherical bubble dynamics derived in chapter 3.

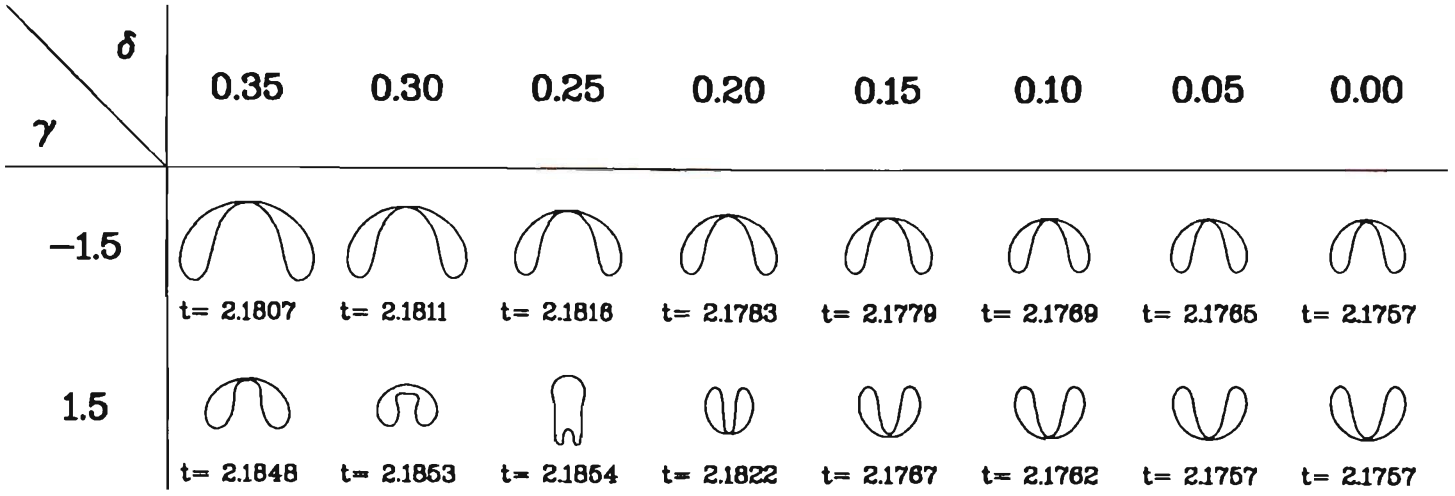

Figure 5.3.1. Bubble shapes at the time of jet penetration, or minimum volume, for a range of buoyancy parameters. The motion begins at a distance of 1.5 above ($\gamma = 1.5$) and below ($\gamma = -1.5$) a rigid boundary. The strength parameter is $\epsilon = 100$.

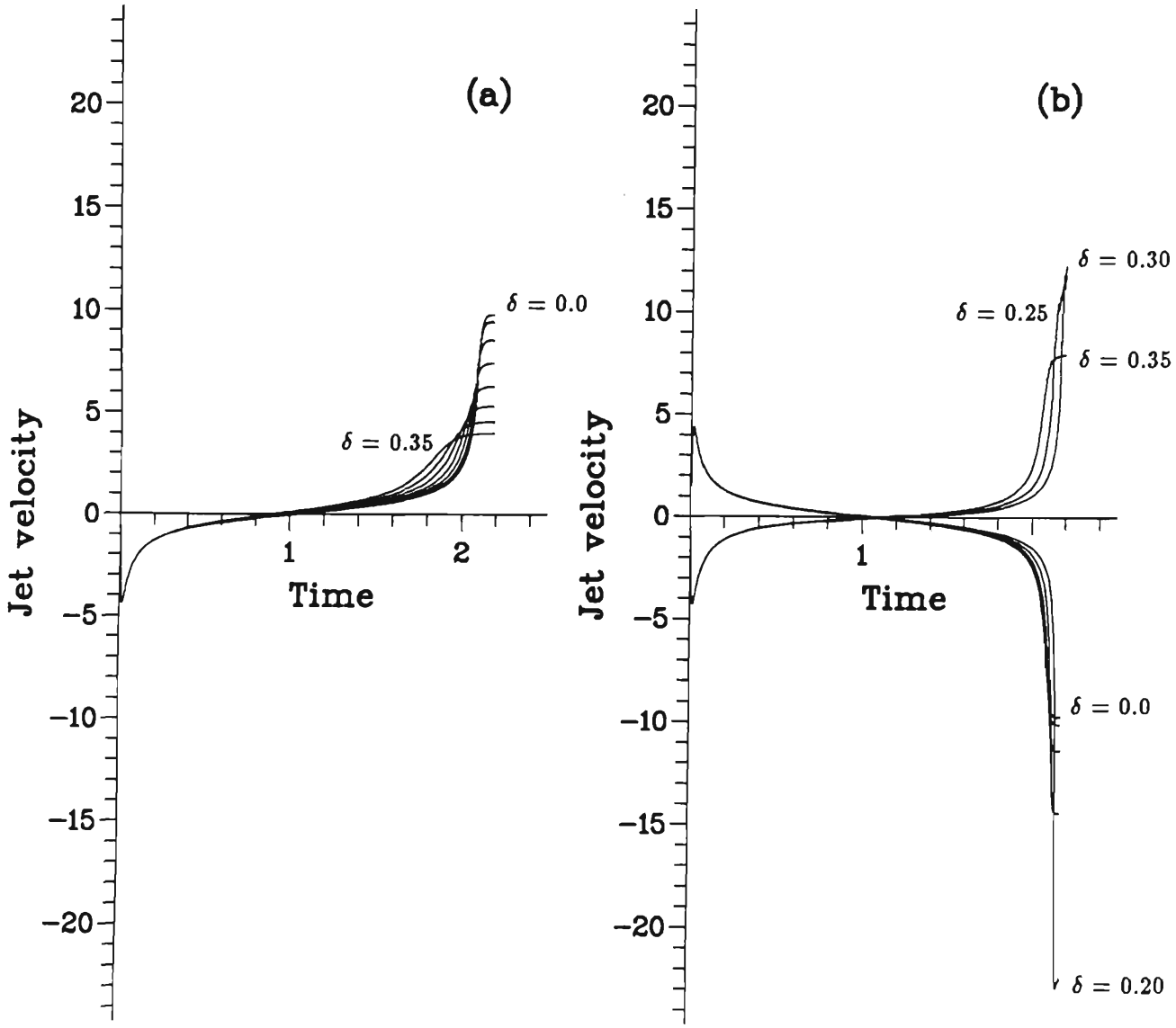

Figure 5.3.2. Jet tip velocity as a function of time for each of the motions considered in figure 5.3.1. The frames display this velocity for the cases (a) $\gamma = -1.5$ and (b) $\gamma = 1.5$. In cases where each curve is not individually labelled there is a systematic trend in the corresponding value of δ, between the extremes noted.

γ	δ	Final Kelvin impulse	
		Deformed bubble	Spherical bubble
-1.5	0.35	1.0103	–
-1.5	0.30	0.8293	–
-1.5	0.25	0.6763	–
-1.5	0.20	0.5523	0.4709
-1.5	0.15	0.4554	0.4100
-1.5	0.10	0.3863	0.3547
-1.5	0.05	0.3447	0.3188
-1.5	0.00	0.3309	0.3065
1.5	0.35	0.3774	0.3873
1.5	0.30	0.1798	0.1921
1.5	0.25	0.0223	0.0320
1.5	0.20	-0.1080	-0.0950
1.5	0.15	-0.2057	-0.1903
1.5	0.10	-0.2752	-0.2560
1.5	0.05	-0.3169	-0.2941
1.5	0.00	-0.3309	-0.3065

Table 5.3.1. Final Kelvin impulse data for the bubble motions depicted in figure 5.3.1. Also tabulated is the estimate of the impulse obtained from the spherical model of chapter 3. No value of this estimate is shown in cases where the spherical computation failed, for reasons discussed in the text. The strength parameter is $\epsilon = 100$.

The jet velocity data reveals a number of interesting features. In all cases the departure from spherical shape is signified by a rise in the velocity of that part of the surface, where the jet will form, above that value expected for a spherical bubble. The larger the value of δ the sooner this occurs. This is due to the large value of the buoyancy force coupling with the Bjerknes force to accelerate the bubble more rapidly as it collapses, causing a premature departure from spherical shape. If we consider the buoyancy and Bjerknes forces as agents perturbing the spherical shape then the magnitude of the perturbation increases with δ leading to premature collapse and a larger jet. Accompanying this behaviour, though, is a final jet velocity that increases with decreasing δ and a final Kelvin impulse that increases with δ.

There appears to be some inverse relationship between the jet velocity and the breadth of the jet, although these quantities are not well defined. This qualitative inverse relationship bears a remarkable similarity to the inverse relationship between mass and velocity for a particle of given momentum in rigid particle mechanics. This is not unexpected in view of the previously noted analogy between particle momentum and the Kelvin impulse. It must be noted, though, that the final values of the impulse are different for each of these examples and this must impose some limit upon the extent of the analogy. We could perhaps proceed in quantifying this analogy by introducing mathematically precise quantities associated with the jet width and jet velocity and investigating their relationship with the Kelvin impulse. These quantities may be appropriate averages over the volume of the jet but it is not obvious how we should proceed in such an endeavour. We leave such an investigation for later attention.

A further significant feature of the jet velocity vs. time data is what we shall refer to as the terminal velocity characteristic. The jet accelerates rapidly shortly after formation, but this acceleration subsequently slows and the jet tip velocity levels to some constant terminal value. That this should occur may be explained in a number of ways. Recall the local maximum of pressure that develops in the

fluid behind the bubble, as it accelerates forward upon collapse. This causes the flow into the high speed jet, but as the flow continues this maximum of pressure is relieved and the pressure gradient between this point and the bubble surface, that accelerates the fluid here, falls and the jet tip decelerates and achieves a terminal velocity. Alternatively, as the bubble collapses much of the fluid momentum manifests itself in the jet. Since only a finite amount of momentum may be transferred to the jet it cannot continue to accelerate after this transfer of finite momentum has occurred.

Consider now the collection of bubble shapes for motion at $\gamma = 1.5$ above a rigid boundary as δ ranges between 0.00 and 0.35. In this case the buoyancy and Bjerknes forces act in opposition and we note the transition in behaviour as δ varies. In the case of small δ the Bjerknes attraction of the rigid boundary dominates and the jet is directed towards the boundary. As δ increases buoyancy assumes dominance and for large δ the jet is directed upwards. The very interesting behaviour occurs at $\delta = 0.25$ where the buoyancy force and Bjerknes force are nearly equal in their effect. This set of physical parameters is in the neighbourhood of the null impulse state as confirmed from inspection of the final value of the Kelvin impulse shown in table 5.3.1. In this case the bubble shape at minimum volume is shown indicating that the non-spherical bubble rebounds. We consider this case in more detail.

The collapse and rebound of an explosion bubble characterised by $\gamma = 1.5$, $\delta = 0.25$, $\epsilon = 100$ is shown in figure 5.3.3. The bubble remains approximately spherical during the growth phase. Due to the approximately equal and opposite buoyancy and Bjerknes forces there is little translational motion of the bubble upon collapse, the result being that fluid is preferentially drawn in from the sides leading to an elongation of the bubble along the axis of symmetry. Buoyancy is slightly dominant in this case and the slight upwards acceleration upon collapse leads to the elements of a jet being evident at minimum volume. In this neighbourhood of the null impulse state jetting has been suppressed sufficiently that the bubble rebounds, this phase of the motion shown in figure 5.3.3(b). As the bubble re-expands the

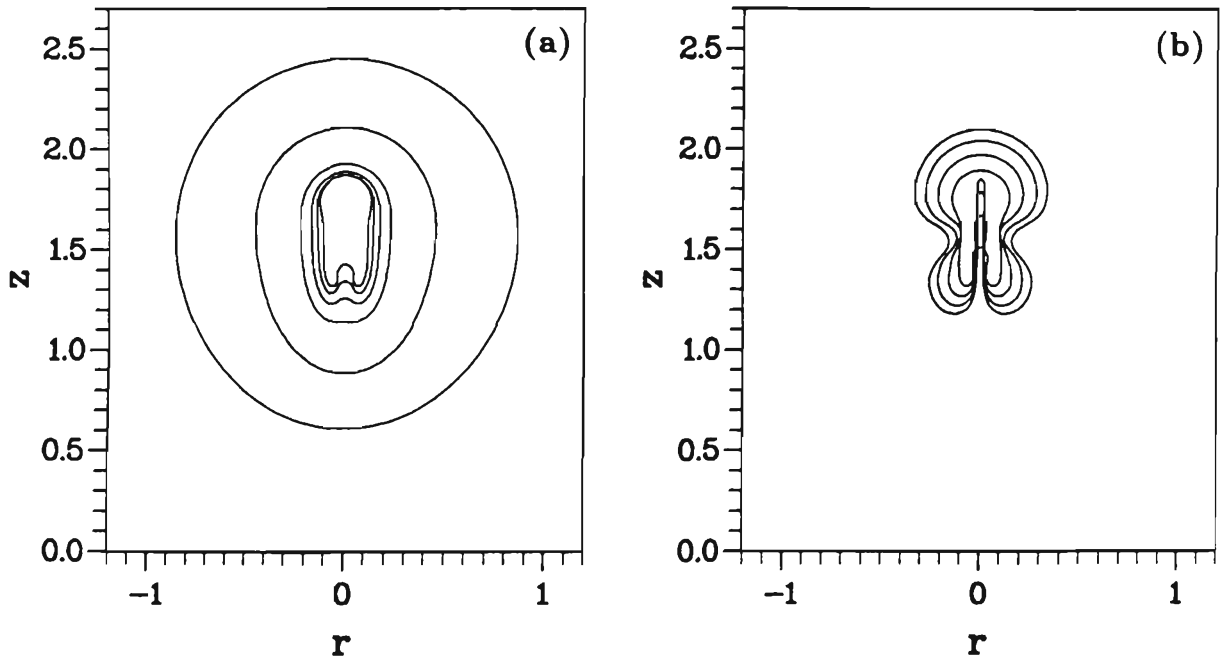

Figure 5.3.3. Successive bubble shapes for the collapse and rebound of an explosion bubble characterised by $\gamma = 1.5$, $\delta = 0.25$, $\epsilon = 100$. The times corresponding to successive profiles are: (a) Collapse phase: 1.6458 (outermost), 2.0656, 2.1537, 2.1677, 2.1754, 2.1829 (innermost). (b) Rebound phase: 2.1904 (innermost), 2.2055, 2.2214, 2.2380 (outermost).

jet continues to be driven into the bubble. The inwards radial motion of the fluid, about the centre of the bubble, is arrested at rebound but causes what we shall call upper and lower lobes of the bubble to develop. As a result of this inwards flow the high pressure within the bubble at minimum volume preferentially causes the rapid re-expansion of the upper and lower parts of the bubble leading to the observed lobe structure.

It is interesting to consider the jet tip velocity as a function of time for this example and this is shown in figure 5.3.4. As previously discussed the opposite coupling of buoyancy and Bjerknes forces gives rise to a very small initial perturbation in the bubble shape resulting in delayed jet formation and a thin jet. Accompanying this small amount of mass in the jet, however, is a very high peak jet velocity achieved at around minimum volume. As the bubble re-expands the jet velocity falls, although the jet continues to travel through the bubble. The rebound causes the bulk of the fluid surrounding the bubble to flow outwards, this outflow reducing the rate of flow into the jet, causing it to decelerate.

We consider the computed pressure field in the fluid. The pressure field at $t = 2.1829$ is shown in figure 5.3.5(a). This is the time at which the bubble has achieved minimum volume and the pressure within the bubble is 88.97. We note the point of high pressure located behind the jet and its close proximity to the bubble surface. This closeness gives rise to the very high pressure gradient that drives the thin jet into the bubble at high speed. The pressure field is shown at $t = 2.2295$ in figure 5.3.5(b). At this time the bubble has rebounded to a significant volume and the pressure within the bubble is 5.72. We notice that the peak of pressure behind the jet evident at earlier times is no longer a characteristic of the pressure field, so that the mechanism driving the jet is absent, an observation that is in accord with that of decreasing jet velocity during rebound. We also note the horseshoe shape contours around the top of the bubble, this region being where the maximum of pressure occurs. This region of high pressure begins to arrest the expansion of the upper part of the bubble and that this region extends around the

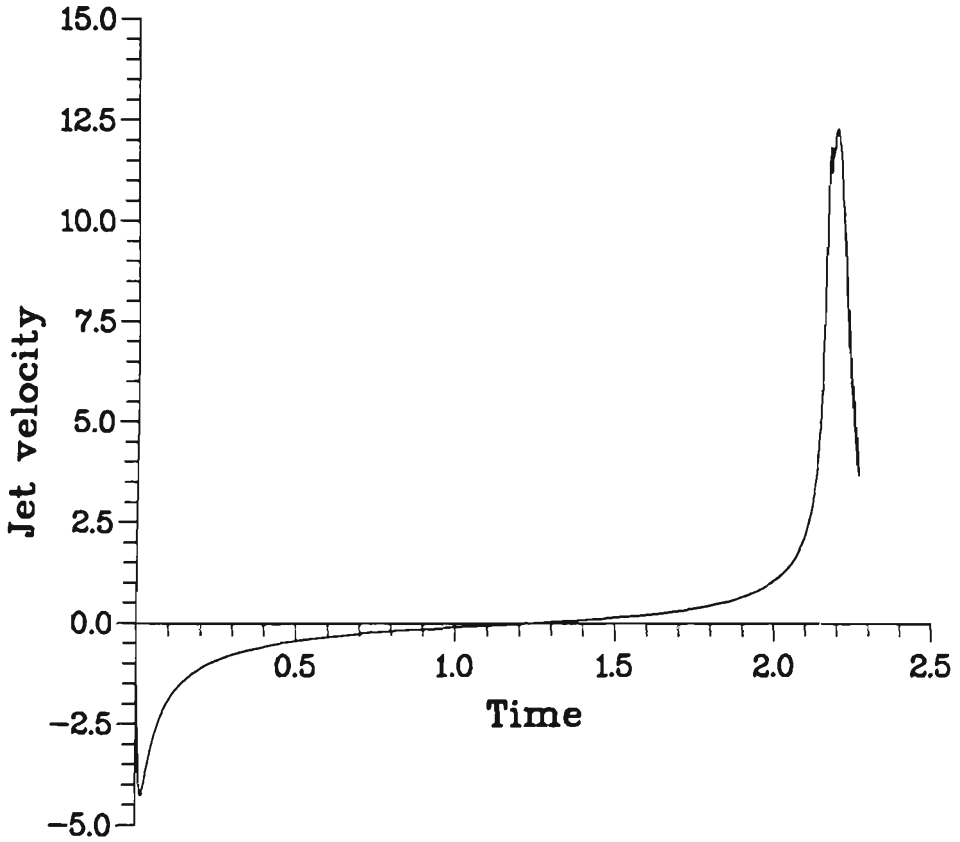

Figure 5.3.4. Jet tip velocity as a function of time for the motion depicted in figure 5.3.3.

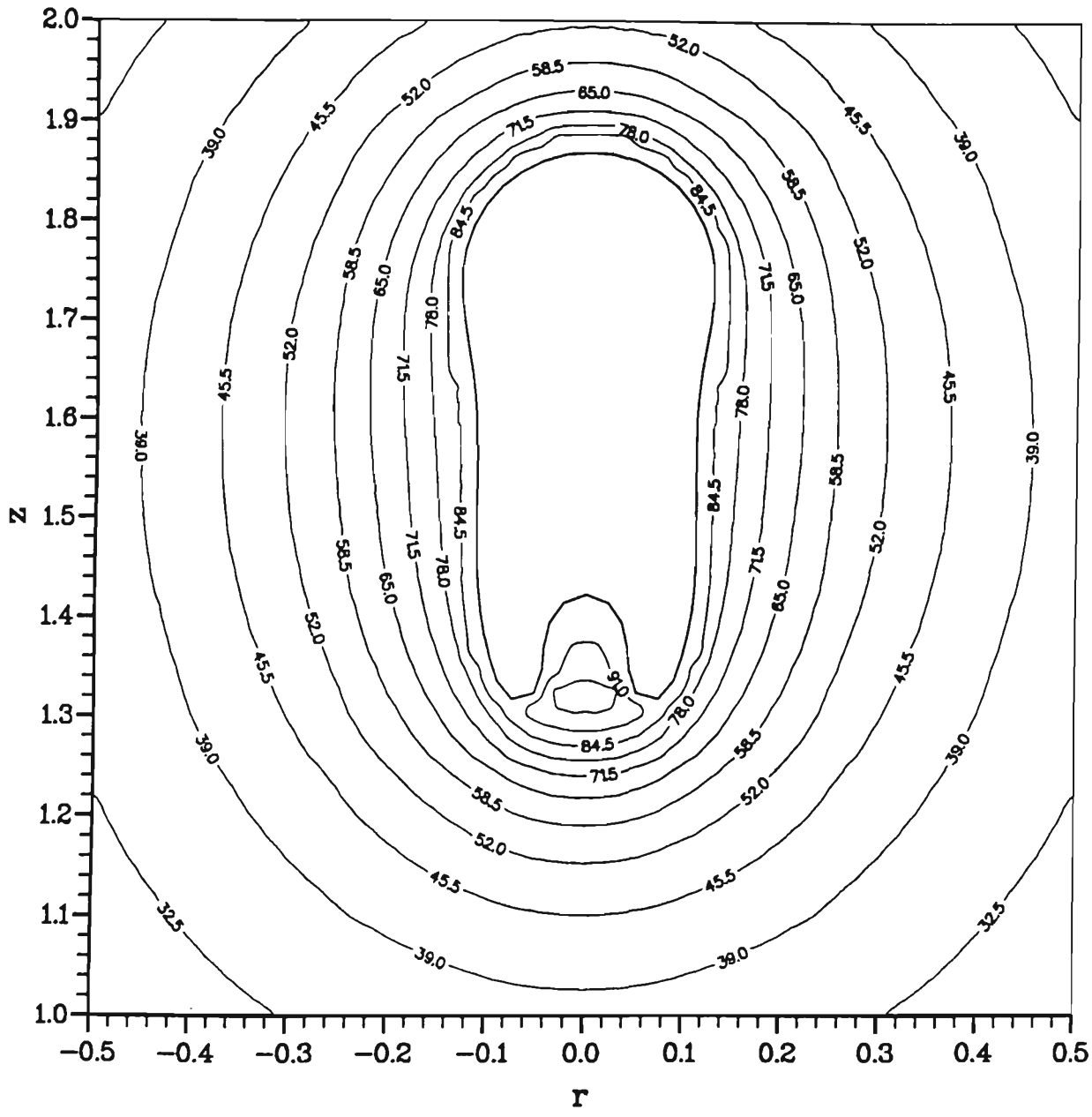

Figure 5.3.5(a). The pressure in the fluid computed for the motion illustrated in figure 5.3.3 at time $t = 2.1829$.

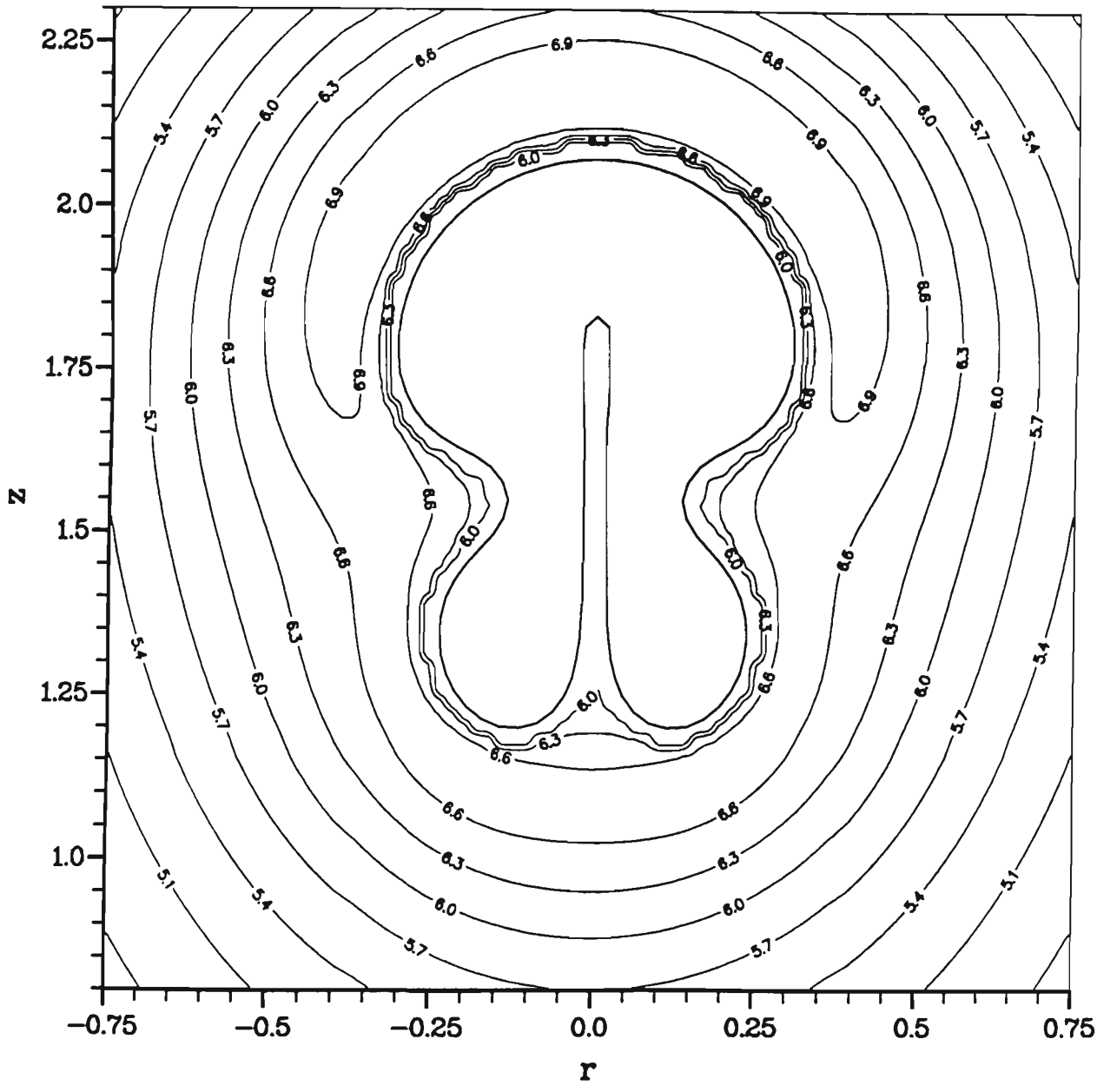

Figure 5.3.5(b). The pressure in the fluid computed for the motion illustrated in figure 5.3.3 at time $t = 2.2295$.

sides of the bubble prevents the outwards motion of the central part of the bubble, leading to the formation of upper and lower lobes.

It is also of interest to consider the behaviour for values of the buoyancy parameter about the value of 0.25 just considered. The collapse and rebound of an explosion bubble characterised by $\gamma = 1.5$, $\delta = 0.23$, $\epsilon = 100$ is shown in figure 5.3.6. In this example the Bjerknes force slightly dominates the buoyancy force and the jet is thus directed towards the boundary. As the bubble collapses we note the elongation along the axis of symmetry. Since the buoyancy and Bjerknes forces act in opposition jet formation is delayed and the jet that forms contains a small amount of mass. Accompanying this is a very high jet velocity as evident from inspection of figure 5.3.4. We observe that the bubble achieves a minimum of volume just prior to the time that the jet completely penetrates the bubble.

The collapse and rebound of an explosion bubble characterised by $\gamma = 1.5$, $\delta = 0.27$, $\epsilon = 100$ is shown in figure 5.3.7. This example exhibits many of the features discussed above although in this case the buoyancy force is slightly dominant with the jet that forms directed upwards. The interesting feature here is the pluming of the jet. As the jet is driven into the bubble the top broadens so that its radius there is greater than at its base. This appears to be a feature of explosion bubble collapse in the neighbourhood of the null impulse state, in the case where buoyancy is slightly dominant. This behaviour has been observed experimentally for the motion of two dimensional bubbles of constant volume rising slowly under the action of buoyancy forces alone (Walters and Davidson, 1962) and computations of this motion are in good agreement (Baker and Moore, 1989; Lundgren and Mansour, 1991).

We remark that trends in the bubble behaviour upon collapse follow the general principles discussed for the case where buoyancy and the Bjerknes attraction act together. For a larger resultant perturbing effect jet formation is initiated early and a larger amount of mass is contained in the jet. This is accompanied by a smaller final jet velocity. About the null impulse state the initial perturbation

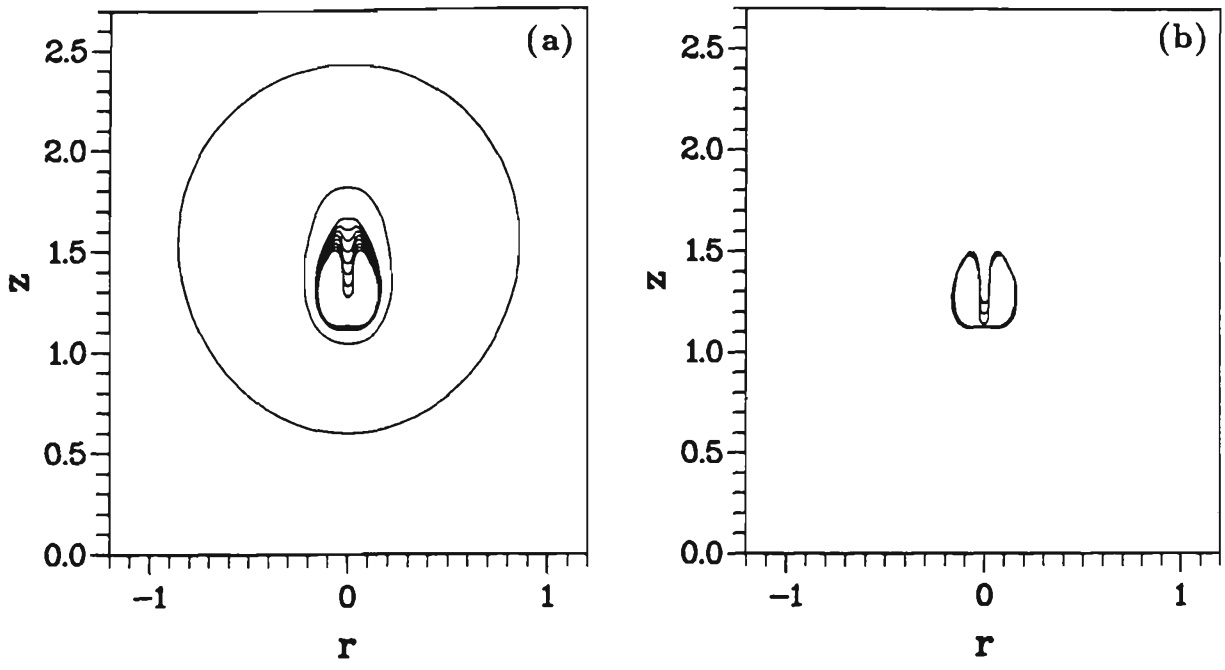

Figure 5.3.6. Successive bubble shapes for the collapse and rebound of an explosion bubble characterised by $\gamma = 1.5$, $\delta = 0.23$, $\epsilon = 100$. The times corresponding to successive profiles are: (a) Collapse phase: 1.6578 (outermost), 2.1566, 2.1742, 2.1758, 2.1771, 2.1787, 2.1803, 2.1820, 2.1838, 2.1857 (innermost). (b) Rebound phase: 2.1866 (innermost), 2.1886, 2.19068 (outermost).

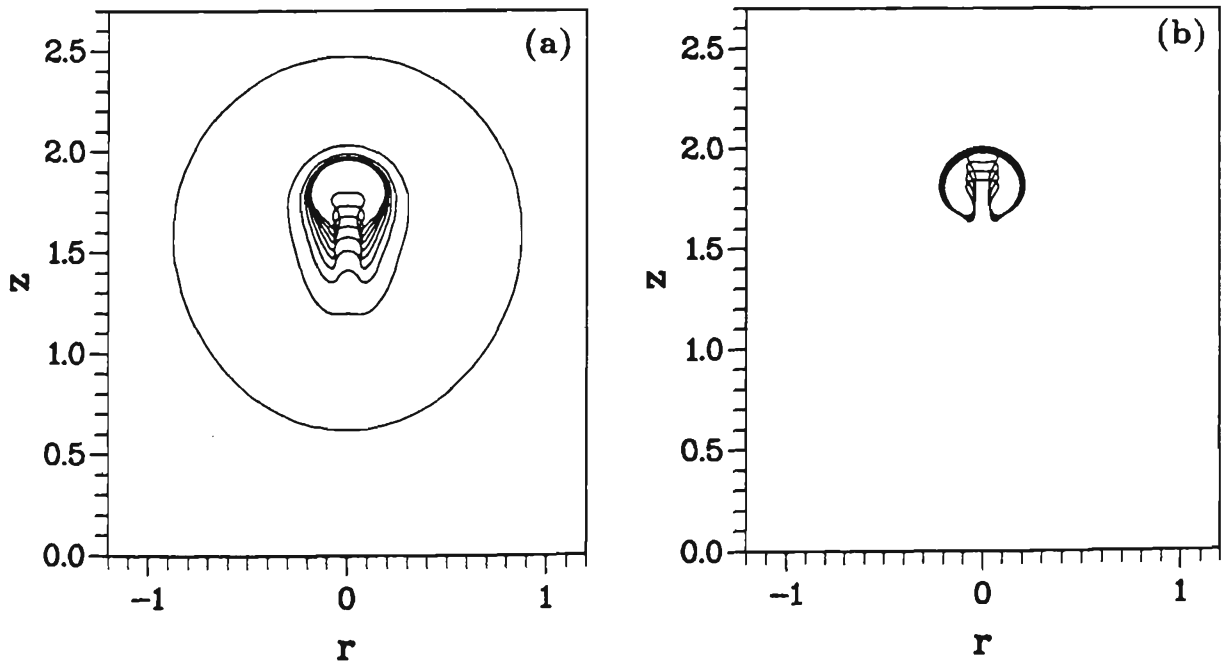

Figure 5.3.7. Successive bubble shapes for the collapse and rebound of an explosion bubble characterised by $\gamma = 1.5$, $\delta = 0.27$, $\epsilon = 100$. The times corresponding to successive profiles are: (a) Collapse phase: 1.6304 (innermost), 2.1499, 2.1612, 2.1688, 2.1739, 2.1776, 2.1810, 2.1845, 2.1888 (innermost). (b) Rebound phase: 2.1912 (innermost), 2.1939, 2.1966, 2.1993 (outermost).

in the bubble shape is small with narrow jets being formed and characterised by the highest speeds. As postulated in chapter 3, in the neighbourhood of the null impulse state the non-spherical bubble has been shown to rebound. If we compare cases characterised by the same buoyancy parameter then we note a greater absolute value for the final Kelvin impulse in the case where the two forces act together. In this case we again note a broader jet and smaller jet velocity, in accord with our general principles. In the case where the forces are in opposition we have a smaller initial perturbing effect, giving rise to narrower jets of higher velocity.

These examples for $\gamma = 1.5$ also demonstrate the little influence that the buoyancy parameter has upon the lifetime of the bubble, the variation over the range of δ considered here being insignificant compared with the lifetime of the bubble. Although it is tempting to infer trends in this variation of lifetime with δ, the variation is of the order of the computational error (especially in deciding the exact time that jet penetration has occurred) and is probably not significant.

Finally, we compare the value of the Kelvin impulse computed for the deformed bubble with the value computed using the spherical model of chapter 3. The results are shown in table 5.3.1. For motion above the rigid boundary the agreement is quite good. For motion below the boundary the agreement is acceptable for small δ and becomes worse with increasing δ. We can explain this by recalling that in the spherical model we modified the infinite fluid equations of motion to lowest order in R/ξ, where R is the bubble radius and ξ the distance from the rigid boundary. For motion below such a boundary the coupling of the buoyancy and Bjerknes forces causes a very high acceleration upon collapse, this acceleration increasing with δ. Thus as the bubble collapses in these cases it migrates rapidly towards the boundary and the ratio R/ξ is of order one. The failure of the spherical model to compute an adequate estimate of the Kelvin impulse in this case is no surprise. For motion above the boundary the opposite coupling of the forces results in reduced migration upon collapse and the bubble does not come so close to the

boundary that the spherical model fails completely. This data thus provides some confirmation that as long as the bubble is not too close to the rigid boundary the equations of spherical bubble dynamics provide a good estimate of the Kelvin impulse of a deformed bubble and from this we can infer aspects of the jetting motion.

5.4. Variation of the distance of inception from a rigid boundary

Let us now consider the varying behaviour of a deforming explosion bubble as we vary the distance of inception from a rigid boundary. The bubble shapes at the time of complete jet penetration, or minimum volume, are shown in figure 5.4.1 over a range of values of γ between 1 and ∞, for a strength parameter $\epsilon = 100$. Motion is considered both above and below a rigid boundary and we have indicated this in the figure by assigning $\delta > 0$ for motion above the boundary and $\delta < 0$ for motion below. Again we consider both the positive and negative coupling of the buoyancy and Bjerknes forces. For each of the bubbles depicted in this figure the jet tip velocity is shown as a function of time in figure 5.4.2.

As for the results presented for varying δ we note similar trends in the changing character of the collapse with varying γ, although there are subtle differences. Whereas in section 5.3 the force perturbing the spherical bubble was varied by changing the buoyancy parameter it is here varied by changing the distance of inception from the rigid boundary. The larger the resultant perturbation the broader the jet and smaller the final jet tip velocity. For motions characterised by the same absolute value of the physical parameters, in the case of motion above the boundary the perturbing force is smaller due to the opposite coupling of the buoyancy and Bjerknes forces, giving rise to a smaller jet with higher velocity.

For motion above the boundary we note the transition from jet formation directed upwards to jet formation directed downwards as the relative strengths of the buoyancy and Bjerknes forces change. It is interesting to consider the collapse and rebound of a bubble about the null impulse state. This is shown in figure 5.4.3

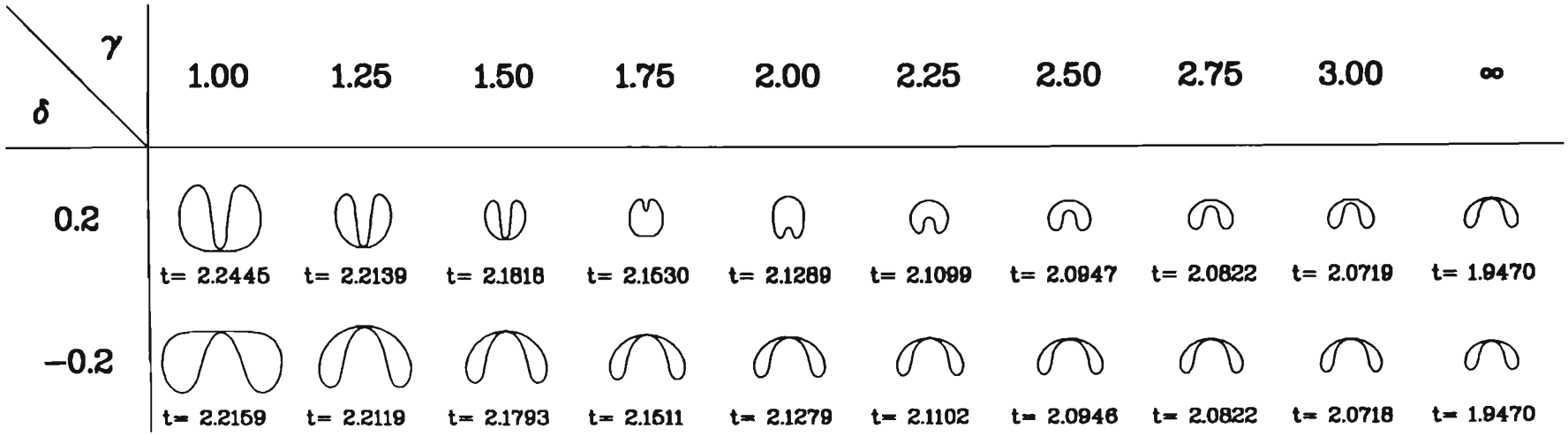

Figure 5.4.1. Bubble shapes at the time of jet penetration, or minimum volume, for a range of distances of inception from a rigid boundary. The buoyancy parameter is $\delta = 0.2$ with the sign of this quantity indicating motion above (+) or below (−) the boundary. The strength parameter is $\epsilon = 100$.

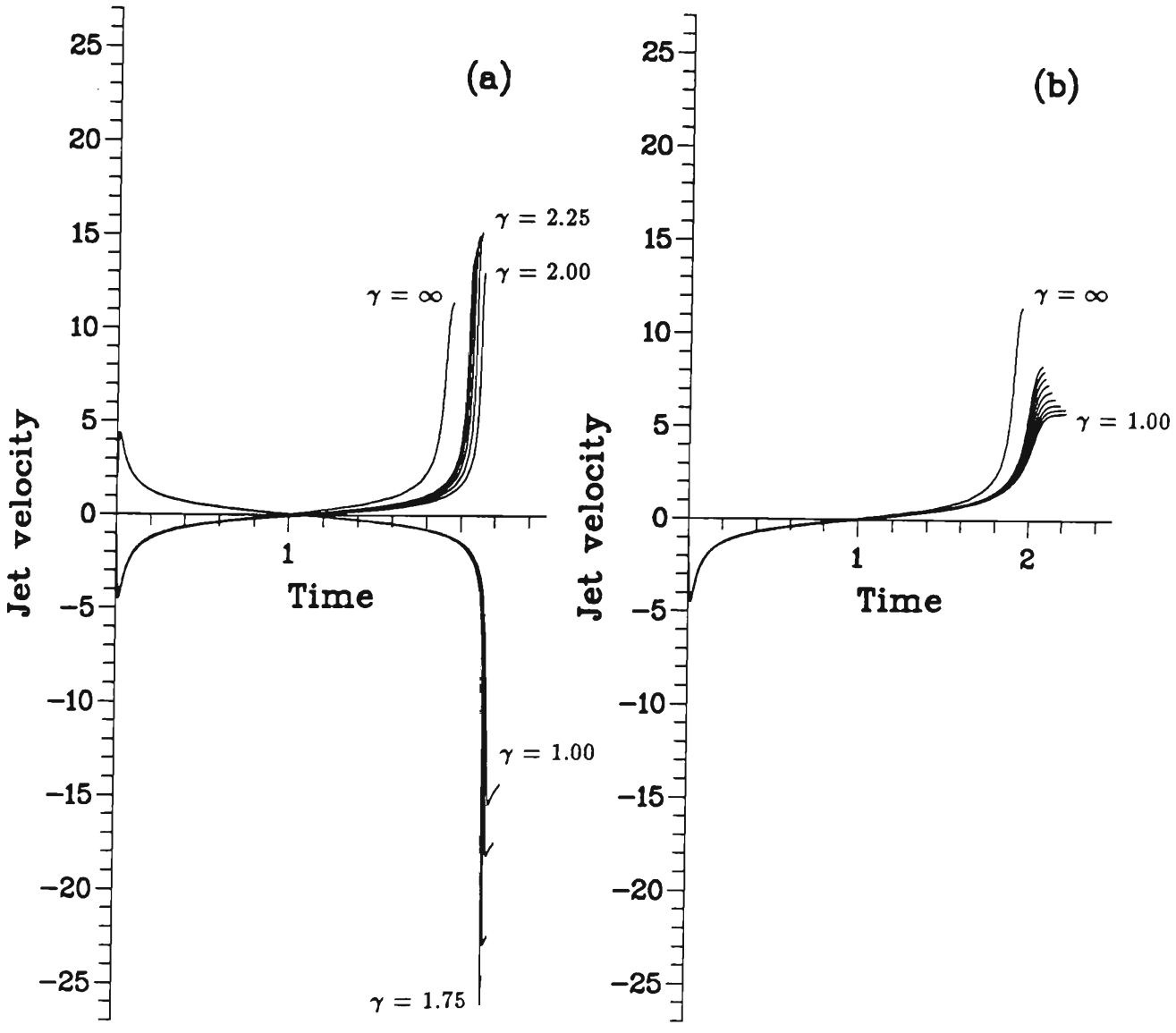

Figure 5.4.2. Jet tip velocity as a function of time for each of the motions considered in figure 5.4.1. The frames display this velocity for motion above (a) and below (b) a rigid boundary. In cases where each curve is not individually labelled there is a systematic trend in the corresponding value of γ, between the extremes noted.

γ	δ	Final Kelvin impulse	
		Deformed bubble	Spherical bubble
1.0	0.2	−0.3902	–
1.25	0.2	−0.2262	−0.1899
1.5	0.2	−0.1080	−0.0950
1.75	0.2	−0.0291	−0.0239
2.0	0.2	0.0237	0.0262
2.25	0.2	0.0606	0.0620
2.5	0.2	0.0874	0.0883
2.75	0.2	0.1075	0.1079
3.0	0.2	0.1229	0.1230
∞	0.2	0.1991	0.1988
−1.0	0.2	0.8274	–
−1.25	0.2	0.6675	–
−1.5	0.2	0.5524	0.4709
−1.75	0.2	0.4718	0.4494
−2.0	0.2	0.4154	0.4060
−2.25	0.2	0.3747	0.3700
−2.5	0.2	0.3447	0.3420
−2.75	0.2	0.3220	0.3201
−3.0	0.2	0.3042	0.3029
$-\infty$	0.2	0.1991	0.1988

Table 5.4.1. Final Kelvin impulse data for the bubble motions depicted in figure 5.4.1. Also tabulated is the estimate of the impulse obtained from the spherical model of chapter 3. No value of this estimate is shown in cases where the spherical computation failed, for reasons discussed in the text. The strength parameter is $\epsilon = 100$.

for an explosion bubble charactertised by $\gamma = 1.85$, $\delta = 0.20$, $\epsilon = 100$. The significant features are much as for the rebounding bubble shown in the previous section. Upon collapse fluid is preferentially drawn in radially, leading to an elongation of the bubble along the axis of symmetry. The elements of a jet are evident at minimum volume. Upon rebound the thin jet continues to travel into the bubble and we note the formation of upper and lower lobes. Although the inwards radial motion of the fluid is arrested the rapid re-expansion of the lobes leads to a ring of very high surface curvature about the centre of the bubble. The thin jet also exhibits very high curvature during the later stages of the bubble's life. Beyond this time the computational scheme cannot proceed. In reality surface tension and pressure fluctuations within the bubble contents will break up this high curvature surface. Especially significant in the case of explosion bubble motion is the temperature of the bubble contents which may lead to a phase transition at the bubble surface and provide a further mechanism for the break up of these high curvature regions of the bubble surface.

The behaviour of the explosion bubble as γ varies exhibits a number of subtle differences from that noted in section 5.3. In this case there is a systematic trend in the lifetime of the bubble over the range of γ. In view of previous considerations we might expect that for motion below the boundary the increased perturbing force as γ decreases would give rise to premature collapse. The opposite is the case as evident from inspection of the jet tip velocity data in figure 5.4.2(b). Despite this the final jet velocity exhibits the terminal velocity feature and a qualitative inverse relationship with the breadth of the jet. We also note that for motion above the boundary the lifetime of the bubble (or time to first minimum of volume) is virtually indistinguishable from that for motion below the boundary (except for $\gamma = 1.00$). This behaviour is as found in section 5.3.

It is apparent that the lifetime of the deforming bubble is fundamentally dependent upon γ, and little upon δ. We can explain this behaviour as follows. It is the peak of pressure that develops in the fluid behind the bubble upon collapse that

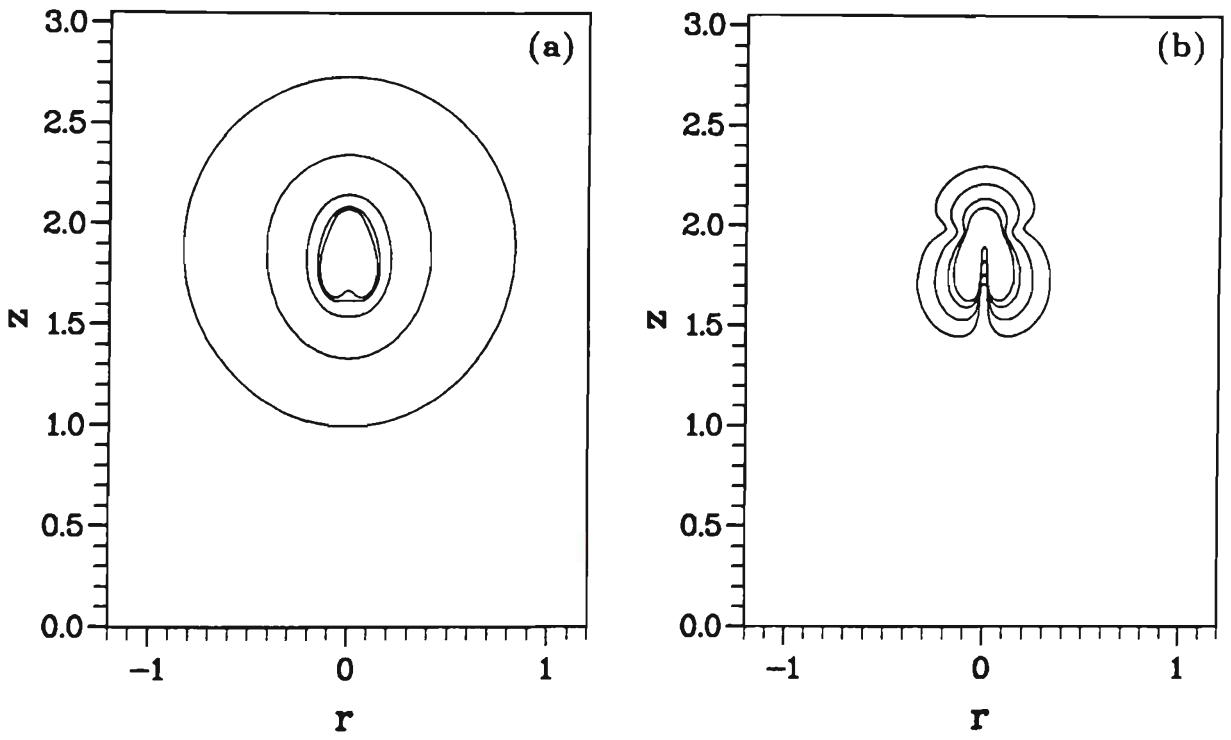

Figure 5.4.3. Successive bubble shapes for the collapse and rebound of an explosion bubble characterised by $\gamma = 1.85$, $\delta = 0.20$, $\epsilon = 100$. The times corresponding to successive profiles are: (a) Collapse phase: 1.6823 (outermost), 2.0528, 2.1201, 2.1341, 2.1410 (innermost). (b) Rebound phase: 2.1470 (innermost), 2.1553, 2.1963, 2.2747 (outermost).

drives the jet into the bubble. It is the early acceleration of the almost spherical collapsing bubble that causes this to occur. For motion close in to the boundary the increased difficulty in displacing the fluid between the boundary and the bubble inhibits this initial acceleration of the bubble, delaying the development of a sufficient peak of pressure behind the bubble and thus delaying the formation of the jet. Further away from the rigid boundary this difficulty in displacing fluid ahead of the bubble is reduced and jet formation occurs sooner. The ease with which the fluid between the bubble and the boundary may be displaced is dependent upon the geometry of the flow field and quite generally γ alone. Thus the bubble lifetime is found to be quite independent of δ although the early migration due to buoyancy forces may have some minor influence.

We close this discussion by considering the Kelvin impulse of the bubbles depicted in figure 5.4.1. This data is compiled in table 5.4.1 along with the approximation computed using the spherical model. For motion in the closest proximity to the rigid boundary the spherical model fails to give an adequate estimate of the final Kelvin impulse. As the point of inception moves away from the boundary the agreement improves substantially. For a given value of γ the estimate of the final Kelvin impulse is better for motion above the boundary due to the smaller translation of the bubble upon collapse. This behaviour is as discussed in section 5.3.

5.5. Variation of the strength parameter

It was proposed in chapter 3 that non-spherical bubbles should rebound in connected form not only in the neighbourhood of the null impulse state but also for small strength parameters. We thus consider some examples of bubble motion over a range of strength parameters and the bubble shapes at the time of jet penetration, or minimum volume, are shown in figure 5.5.1, along with a cavitation bubble for comparison. The upper sequence shows motion under the influence of the buoyancy force alone and the lower sequence motion in the neighbourhood of

a rigid boundary alone. The jet tip velocity for each of these examples is shown in figure 5.5.2.

The behaviour observed is as expected. As the strength parameter decreases the fluid velocities upon collapse decrease so that jet formation is incomplete at the time of minimum volume and the bubble rebounds in connected form. As the strength parameter increases the behaviour becomes similar to that of a vapour cavity, for the reasons discussed in chapter 3. This trend is also evident in the jet velocity data. The terminal velocity feature of the jet tip is generally evident, except for the examples of cavitation bubbles and motion under the influence of buoyancy alone, for larger values of the strength parameter. In these cases the pressure gradient that develops in the fluid behind the bubble is sufficiently large that a terminal velocity is not reached, although the jet tip is beginning to decelerate as the jet nears the far side of the bubble.

For interest we consider the collapse and rebound of a bubble characterised by $\gamma = \infty$, $\delta = 0.15$, $\epsilon = 10$. The bubble shapes are shown in figure 5.5.3 and the vertical scale is arbitrary. Due to the smallness of the strength parameter the amplitude of the radial oscillations is small. Since it is the reducing added mass of the bubble upon collapse that gives rise to the rapid acceleration phase that precipitates jet formation, the relative smallness of the change in added mass over the oscillation period of the bubble in this example gives rise to a smaller upwards acceleration upon collapse, so that only the elements of a jet are evident at rebound. As the bubble rebounds, however, the jet continues to travel into the bubble, the reducing pressure within the bubble assisting in this endeavour. Despite the formation of a jet, the bubble retains much of its spherical character.

Finally we present data in table 5.5.1 for the final Kelvin impulse of the bubbles illustrated in figure 5.5.1. Also tabulated for comparison is the approximation to this value obtained using spherical bubble dynamics. For motion under the influence of buoyancy alone the agreement is excellent. For motion in the neighbourhood of a rigid boundary the agreement is not as good, but still excellent.

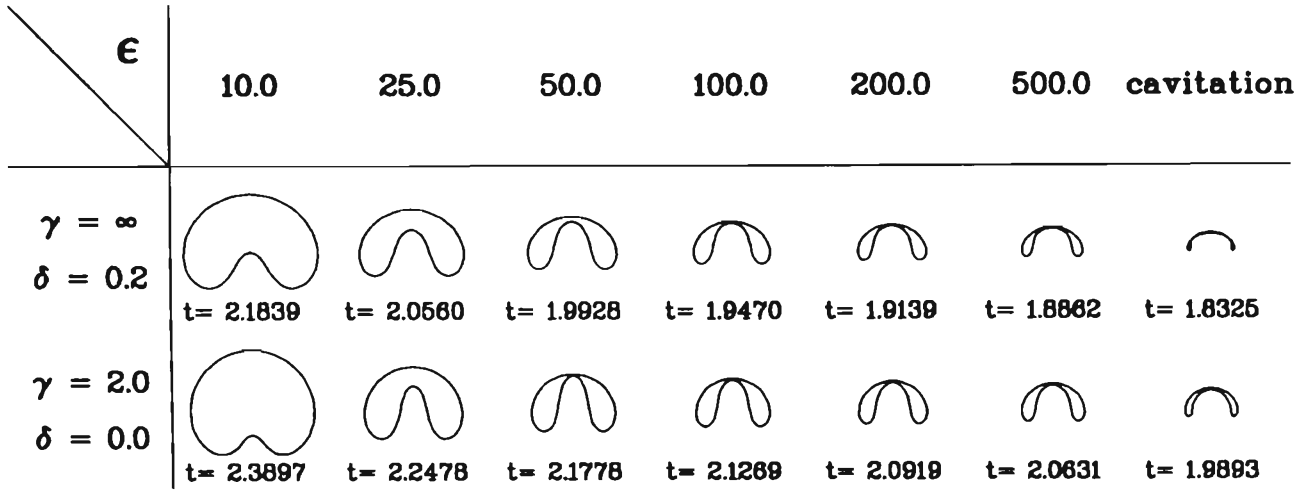

Figure 5.5.1. Bubble shapes at the time of jet penetration, or minimum volume, for a range of values of the strength parameter. In the upper sequence the motion is under the influence of buoyancy alone, characterised by $\delta = 0.2$. The lower sequence depicts motion in the neighbourhood of a rigid boundary alone, the motion beginning at a distance of 2.0 below the boundary.

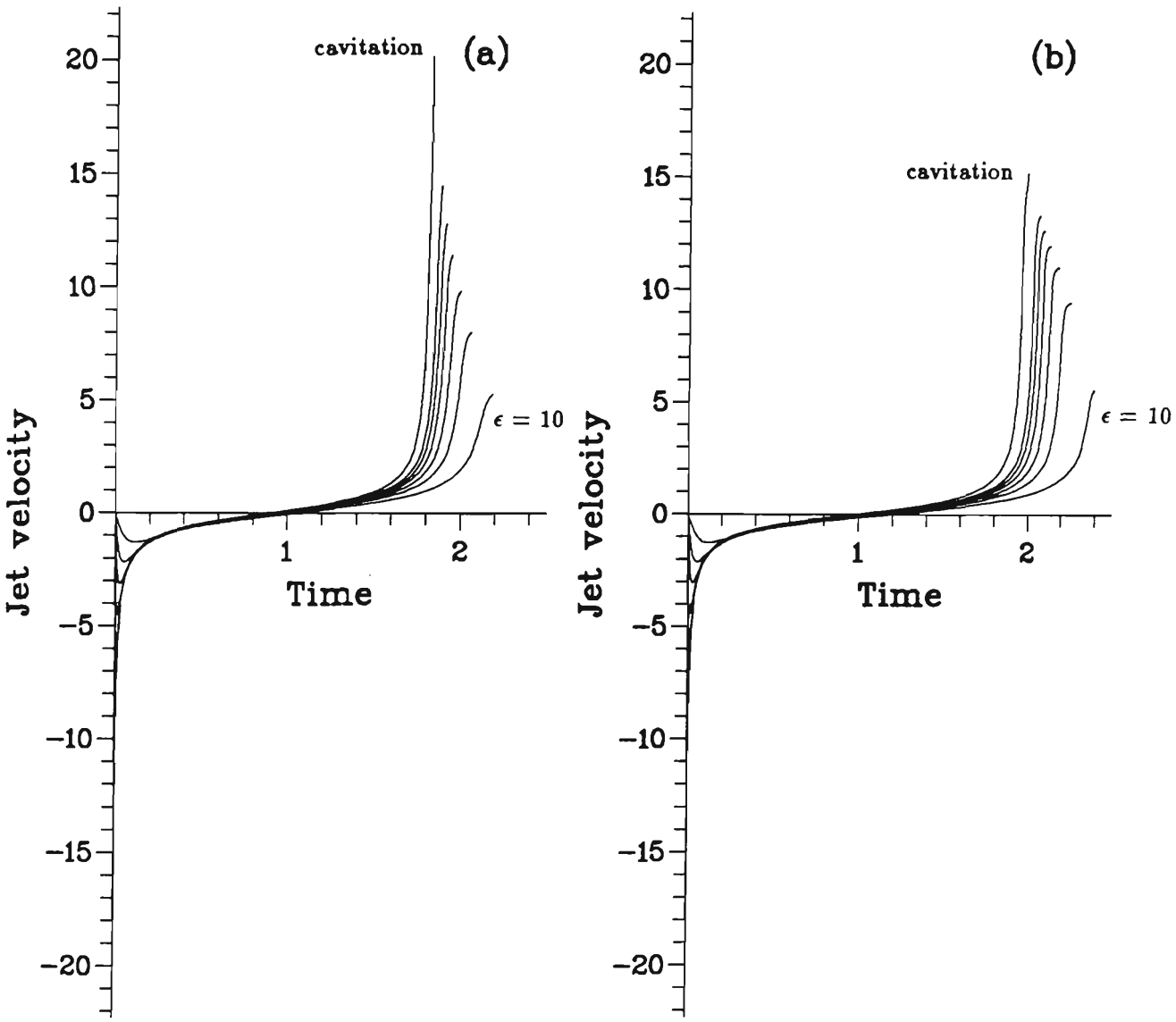

Figure 5.5.2. Jet tip velocity as a function of time for each of the motions considered in figure 5.5.1. The frames display this velocity for motion under the action of buoyancy forces alone, (a), and in the neighbourhood of a rigid boundary alone, (b). In each case there is a systematic trend in the value of ϵ corresponding to each curve from $\epsilon = 10$ to the cavitation example.

γ	δ	α	Final Kelvin impulse	
			Deformed bubble	Spherical bubble
∞	0.2	10	0.2194	0.2193
∞	0.2	25	0.2070	0.2067
∞	0.2	50	0.2019	0.2018
∞	0.2	100	0.1991	0.1988
∞	0.2	200	0.1969	0.1968
∞	0.2	500	0.1954	0.1951
∞	0.2	cavitation	0.1915	0.1918
-2.0	0.0	10	0.1549	0.1518
-2.0	0.0	25	0.1791	0.1754
-2.0	0.0	50	0.1896	0.1857
-2.0	0.0	100	0.1968	0.1925
-2.0	0.0	200	0.2011	0.1970
-2.0	0.0	500	0.2052	0.2009
-2.0	0.0	cavitation	0.2088	0.2163

Table 5.5.1. Final Kelvin impulse data for the bubble motions depicted in figure 5.5.1. Also tabulated is the estimate of the impulse obtained from the spherical model of chapter 3.

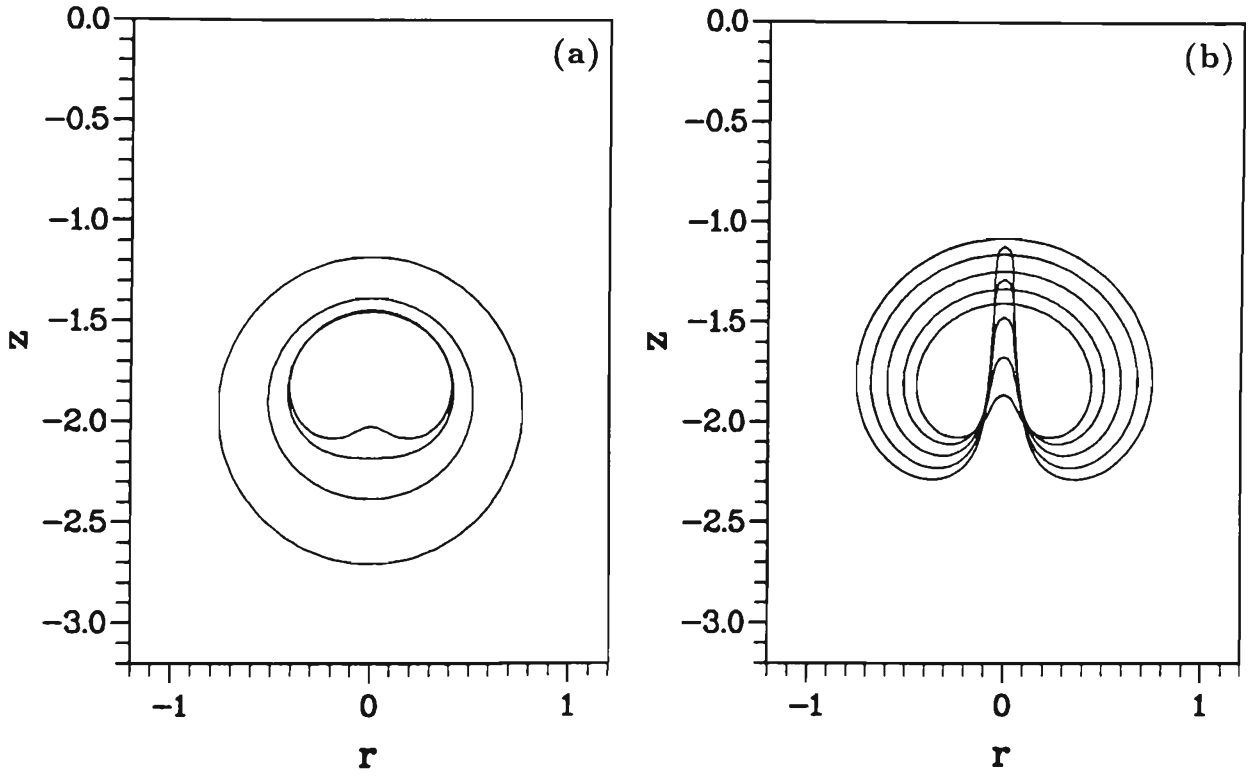

Figure 5.5.3. Successive bubble shapes for the collapse and rebound of an explosion bubble characterised by $\gamma = \infty$, $\delta = 0.15$, $\epsilon = 10$. The times corresponding to successive profiles are: (a) Collapse phase: 1.7991 (outermost), 2.0490, 2.1398, 2.1905 (innermost). (b) Rebound phase: 2.2336 (innermost), 2.2857, 2.3493, 2.4207, 2.4978 (outermost).

Note that these results are for $\gamma = 2$. As indicated in previous sections the success of the spherical model improves with increasing γ.

5.6. Concluding remarks to chapter 5

We conclude this chapter by considering a number of other examples of bubble motion that are of interest and remark upon some of the implications of the results presented. It was postulated in chapter 3 that in the neighbourhood of the null impulse state, and for small strength parameters, non-spherical bubbles should rebound. The results presented in this chapter have demonstrated this. The specific examples shown have only considered a strength parameter of 100. The behaviour that occurs in the neighbourhood of the null impulse state for increased strength parameters is of interest. Thus we consider two further examples for a strength parameter of 1000. The example shown in figure 5.6.1 is of the growth and collapse of a bubble characterised by $\gamma = 2.0$, $\delta = 0.1948$, with this value of δ determined so that according to the spherical model the bubble is at the null impulse state. The significant feature is that both upper and lower jets have formed in this case. Note that the lower jet is broader than the upper jet. In this case the fluid speed upon collapse is so high that both jets penetrate the bubble sufficiently that the bubble does not rebound in connected form.

We consider the further example characterised by $\gamma = 1.0, \delta = 0.33$, as shown in figure 5.6.2 with the value of δ again determined from the spherical model such that the bubble is at the null impulse state. The behaviour in this case is very different. Due to the close proximity of the rigid boundary fluid cannot be easily drawn in from near to the rigid boundary and jet formation at the base of the bubble is thus resisted. As a consequence fluid is preferentially drawn in radially leading to the formation of upper and lower bubble lobes. Although the fluid is more mobile away from the rigid boundary, the formation of a jet here would lead to a significant value of the impulse but this cannot occur in this neighbourhood of the null impulse state. The formation of such a lobe structure

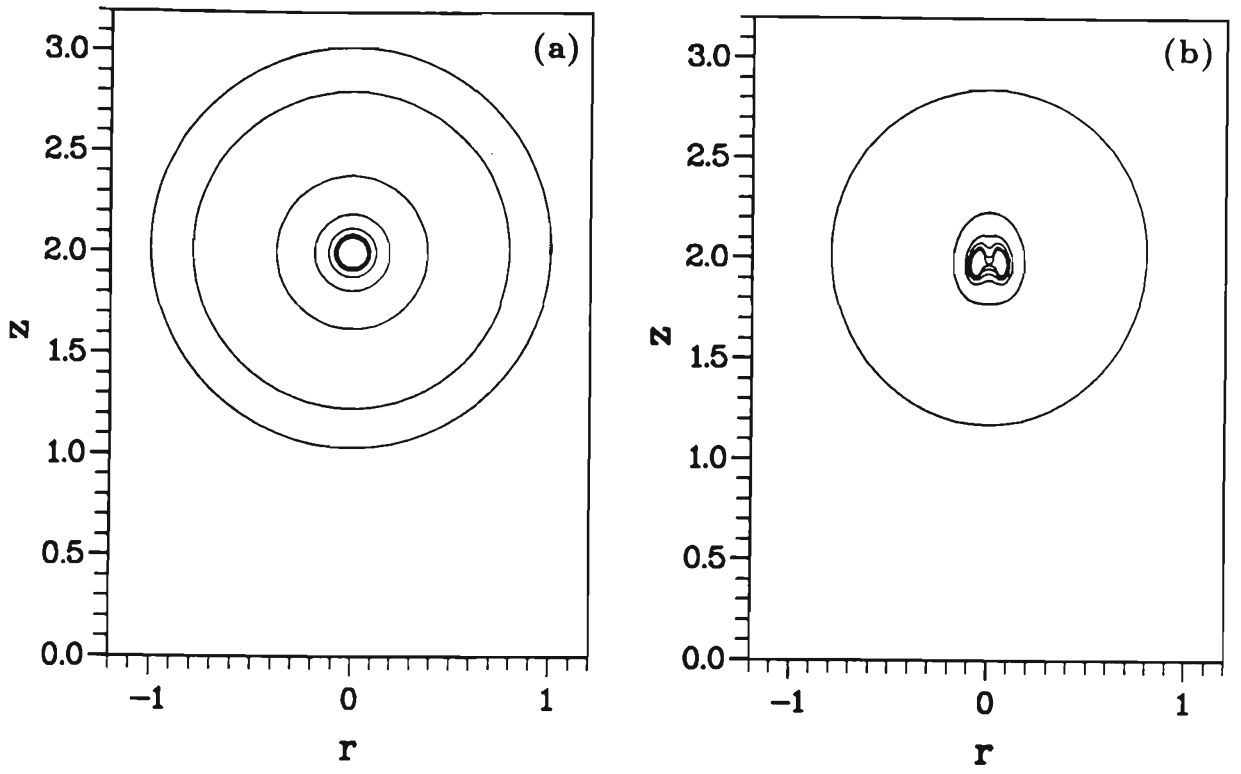

Figure 5.6.1. Successive bubble shapes for the growth and collapse of an explosion bubble characterised by $\gamma = 2.0$, $\delta = 0.1948$, $\epsilon = 1000$. The times corresponding to successive profiles are: (a) Growth phase: 0.0000 (innermost), 0.0008, 0.0019, 0.0040, 0.0109, 0.0526, 0.3520, 1.0032 (outermost). (b) Collapse phase: 1.6728 (outermost), 2.0371, 2.0446, 2.0461, 2.0472, 2.0479 (innermost).

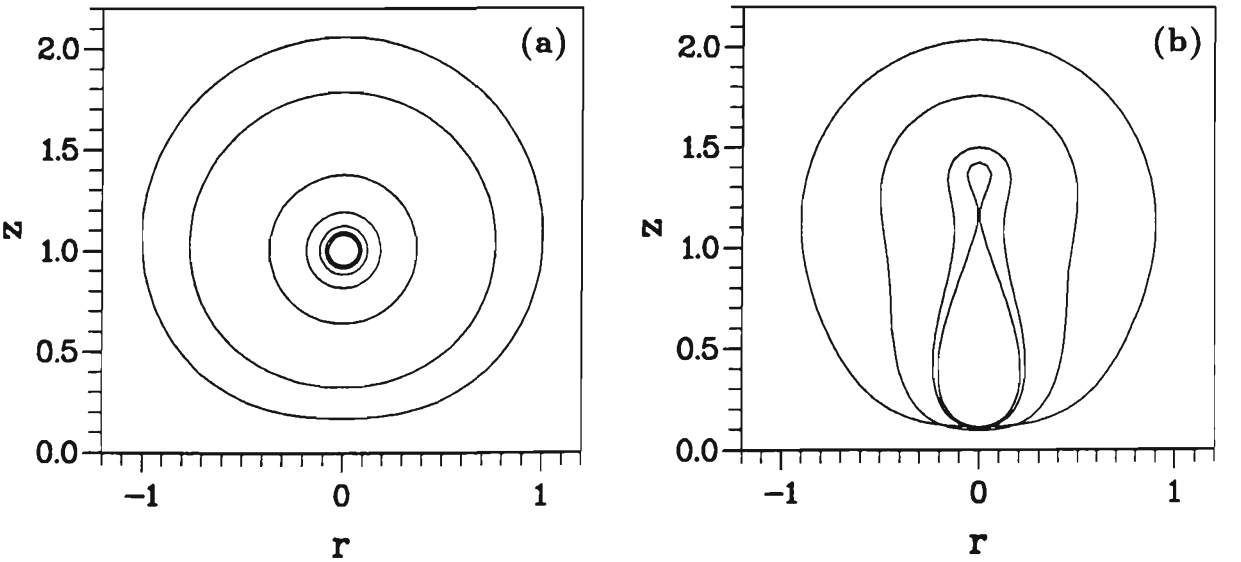

Figure 5.6.2. Successive bubble shapes for the growth and collapse of an explosion bubble characterised by $\gamma = 1.0$, $\delta = 0.33$, $\epsilon = 1000$. The times corresponding to successive profiles are: (a) Growth phase: 0.0000 (innermost), 0.0008, 0.0019, 0.0040, 0.0107, 0.0501, 0.3218, 0.9107 (outermost). (b) Collapse phase: 1.5548 (outermost), 2.0347, 2.1758, 2.1892 (innermost).

has been experimentally observed for motion near a compliant surface (Gibson and Blake, 1982) and between parallel rigid boundaries (Chahine, 1982) in the case where the bubble is in the neighbourhood of the null impulse state.

The results for rebounding bubbles, although computed using an incompressible model, have implications for the emission of pressure pulses upon rebound. We might propose that such emission will be enhanced in the case where the bubble can preserve much of its spherical character about the time of rebound. In the bulk of cases jet penetration occurs before the bubble rebounds, with kinetic energy then becoming bound in the proposed vortex ring structure which must then surely evolve. In the case of motion in the neighbourhood of the null impulse state, however, for not too large values of the strength parameter, it is evident that the bubble rebounds before the jet has completely penetrated it. We might suppose that in this case the emission of acoustic energy at rebound will be enhanced, but such a speculation must be investigated either experimentally or computationally by a solution of the equations of compressible flow. Such an investigation has practical implications for underwater explosions occurring in the neighbourhood of the ocean floor.

In the case of larger strength parameters we have examples where jet penetration has occurred despite being in the close neighbourhood of the null impulse state. This observation and the general behaviour away from this state, where the jet completely penetrates the bubble upon collapse, indicate that in order to make further progress in understanding the full range of bubble phenomena we must develop techniques for computing the motion beyond the time that jet impact occurs.

We finally remark on questions of stability. It was found to be generally necessary to implement smoothing in order to capture rebound. Analyses of the stability of spherical bubbles include those of Penney and Price (1942) and Plesset and Mitchell (1956), both of which showed the stability of the growth phase and instability of the collapse phase, this instability ultimately manifesting itself in the

formation of the jet. Both analyses are linear and the one of particular relevance to this work is that of Penney and Price, as Plesset and Mitchell assumed a constant pressure exerted by the bubble contents. This study demontrated that the rate of growth of initial shape perturbations increases as the bubble collapses, with significant departures occurring near rebound. In this regime, however, the linear analysis is no longer valid due to the significant departure from spherical shape.

Thus we appeal to experimental results which give some indication of the general stability of the rebound phase. The recent investigation of Vogel et al. (1989) has included the compilation of high speed photographic records of the multiple oscillations of laser generated bubbles in the neighbourhood of a rigid boundary. Several oscillations of bubbles are observed, the later oscillations evidently of a vortex ring bubble. Although the internal structure of the jet travelling through the bubble cannot be observed in these photos, the rebound is not characterised by any instability of the nature of the saw-tooth behaviour that was removed by application of smoothing techniques. We are led to believe that this instability is numerical in its origin.

6

THE TOROIDAL BUBBLE

While the boundary integral method has proved to be particularly successful in the computation of the motion of bubbles, to date these calculations may only proceed up until the time that the jet impinges upon the far side of the bubble. We remark in this context, however, that the computation of the motion of constant volume vortex ring bubbles using this method has recently been undertaken (Lundgren and Mansour, 1991). The fluid dynamics of the impact is complex, with compressibility, viscosity and surface tension expected to play a role. The magnitude of their contributions is expected to vary in different physical regimes, and we discuss this matter later in this chapter in view of both our numerical results and recent experimental observations. The aim of this study is to neglect such complicating factors and seek a solution of Laplace's equation in the doubly connected geometry that evolves from the solution in the singly connected domain that describes the flow field just before impact. Thus we are seeking to determine the motion in the regime where the fluid inertia is the dominant feature. In this context the moment of impact poses several difficulties. In the first instance there is a jump in the potential across the impact site. Secondly, there is a jump in the normal derivative of the potential, $\frac{\partial \phi}{\partial n}$, across the impact site, but this discontinuity cannot persist after the impact. Thus we give some consideration to the moment of impact.

6.1. Evolution into a toroidal geometry

Consider the schematic representation of jet impact in figure 6.1.1. The geometry depicted is axisymmetric, but we need not constrain ourselves to the consideration of such a simplified geometry. We suppose that the flow domain Ω collapses from a singly connected to a doubly connected topology via an impact over a surface T, with the remainder of the bubble surface denoted by S. We shall

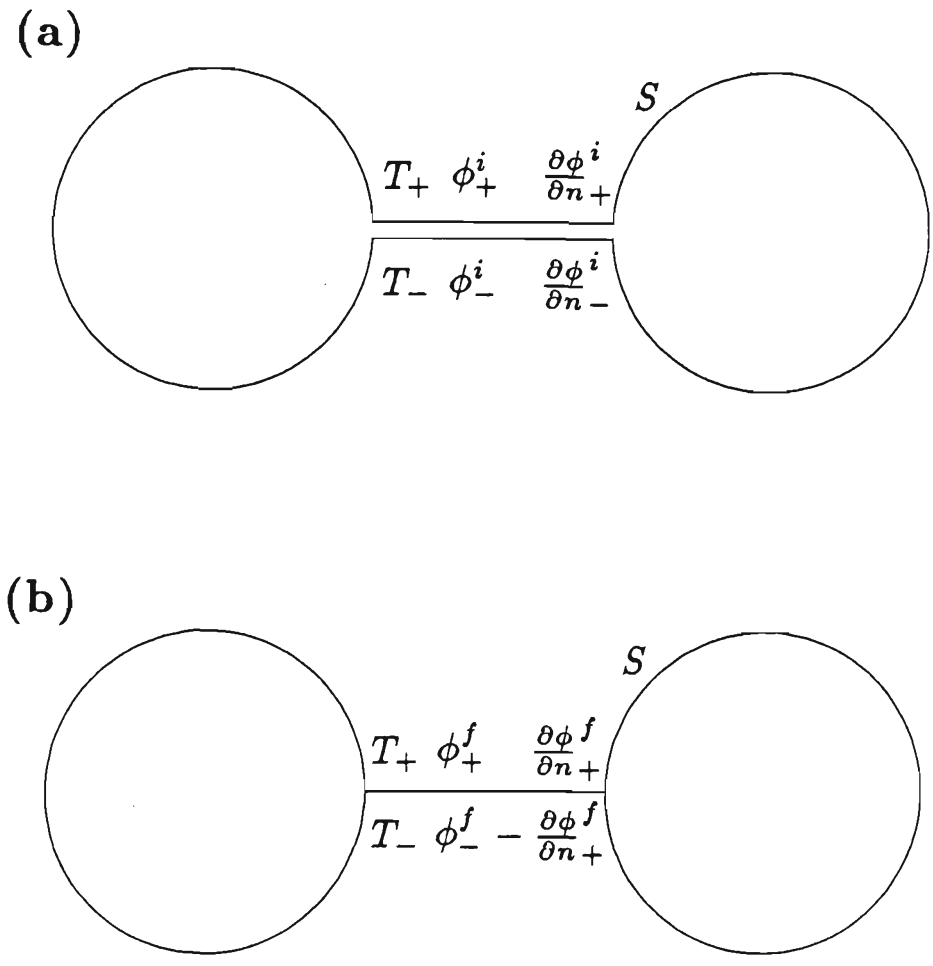

Figure 6.1.1. Schematic representation of the transition to the toroidal bubble geometry. The conditions at the surface T are shown (a) before impact and (b) after impact.

denote the upper part of this surface by T_+ and the lower part by T_-. In what follows the subscript $\pm$ shall denote quantities evaluated on $T_\pm$. In particular, the unit normals to $T_\pm$, exterior to the flow domain, will be denoted by $\mathbf{n}_\pm$ and we note that these vectors are oppositely directed. We denote by superscripts i and f values immediately prior to and immediately after the impact. If we let $\mathbf{t}$ be the position vector of an arbitrary point on $T (\equiv T_+ \cup T_-)$ then just prior to the impact ϕ and $\frac{\partial \phi}{\partial n}$ are, in general, discontinuous across T. We shall write

$$\phi^i_+(\mathbf{t}) - \phi^i_-(\mathbf{t}) = \Delta\phi(\mathbf{t}), \tag{6.1.1}$$

which is generally a non zero function.

In considering the evolution into a toroidal geometry we must address the physical significance of these discontinuities and determine whether they can persist after impact. Let us first address the discontinuity in ϕ. As postulated by Benjamin and Ellis (1966), and others, the collapse of the flow domain into a doubly connected geometry will give rise to a flow with circulation, the existence of which is necessary to conserve the Kelvin impulse. If the flow in the doubly connected domain possesses a circulation we obtain the value of the circulation, Γ, by integrating the velocity around some closed curve that threads the torus;

$$\Gamma = \int_C \mathbf{u} \cdot d\mathbf{s} = \phi_1 - \phi_0, \tag{6.1.2}$$

where ϕ_1 and ϕ_0 are respectively the final and initial values of the potential on the curve C, provided Laplace's equation is satisfied at all points on C. Let us suppose, for convenience, that the initial point of C is somewhere on T and that the curve C proceeds from T_- to T_+. In order to perform this computation we require some information regarding the value of the potential on $T_\pm$ immediately after the impact has occurred.

The action of the impact is to deliver an impulse to the fluid as discussed in chapter 3. Applying (3.2.5) at T_+ and T_- we have

$$\begin{aligned} \phi^f_+(\mathbf{t}) - \phi^i_+(\mathbf{t}) &= -\Pi_+/\rho, \\ \phi^f_-(\mathbf{t}) - \phi^i_-(\mathbf{t}) &= -\Pi_-/\rho, \end{aligned} \tag{6.1.3}$$

where Π is the pressure impulse. Since both surfaces experience a common pressure for the duration of the impact we have that $\Pi_+ = \Pi_-$, so

$$\Delta\phi^f(\mathbf{t}) = \phi^f_+(\mathbf{t}) - \phi^f_-(\mathbf{t}) = \phi^i_+(\mathbf{t}) - \phi^i_-(\mathbf{t}) = \Delta\phi(\mathbf{t}). \tag{6.1.4}$$

Hence we see that the value of Γ will, in general, depend upon the point on T that we choose to begin and end our curve, C, of integration. If $\Delta\phi(\mathbf{t})$ is not uniform then the flow field that exists after the impact will be rotational. It is only in the case where $\Delta\phi$ is uniform that the flow field after impact is irrotational and possesses a circulation of $\Delta\phi$.

The consideration of the pressure impulse allows us to make further pertinent comments. On that part of the bubble surface denoted by S the pressure for the duration of the impact is equal to p_b, the pressure inside the bubble that remains constant for the duration of the impact. This is so because S is a free surface. Hence at some point on S the pressure impulse is

$$\Pi_S = \int p dt = p_b \delta t, \tag{6.1.5}$$

where δt is the duration of the impact. In modelling the impact as an impulse we take the limit $\delta t \to 0$ so that Π_S is equal to zero. Thus we deduce from (3.2.5) that for points on S the potential does not change due to the occurrence of the impact, a property that is exploited shortly.

The fluid velocity at T immediately after the impact is of interest noting that the values of the normal velocity at T_+ and T_- must then be equal in magnitude. It is not possible to obtain a simple expression for this velocity, but we may derive an equation the solution of which allows the computation of this speed. We consider first the tangential component of the fluid velocity at T. Since the upper and lower surfaces of T experience a common pressure impulse at each point we have

$$\nabla\Pi_+(\mathbf{t}) \cdot \tau(\mathbf{t}) = \nabla\Pi_-(\mathbf{t}) \cdot \tau(\mathbf{t}), \tag{6.1.6}$$

where $\tau(\mathbf{t})$ is the tangent vector to T at $\mathbf{t}$. Hence we have from (3.2.3) that

$$\left(\mathbf{u}^f_+(\mathbf{t}) - \mathbf{u}^i_+(\mathbf{t})\right) \cdot \tau(\mathbf{t}) = \left(\mathbf{u}^f_-(\mathbf{t}) - \mathbf{u}^i_-(\mathbf{t})\right) \cdot \tau(\mathbf{t}). \tag{6.1.7}$$

Thus at any point on T the tangential components of the fluid velocity at T_+ and T_- change by the same amount due to the impact. If they are unequal before impact then this inequality will persist after impact and a vortex sheet will be created. This fact relates to the previous considerations regarding the line integral of the fluid velocity around some curve enclosing the torus. In the case where $\Delta\phi(\mathbf{t})$ is not uniform across T we deduced that the flow would be rotational. Such an example gives rise to a vortex sheet by the mechanism discussed above, this sheet being the source of the rotation in the flow field.

We have been able to show that the potential on S does not change as a result of the impact. We may exploit this knowledge to determine an equation which gives the normal derivative of the potential on S just after the impact. Making use of (4.1) we may write the potential at $\mathbf{p} \in S$ immediately *prior* to impact as

$$2\pi\phi^i(\mathbf{p}) = \int_S \left(\frac{\partial\phi^i}{\partial n}G - \phi^i\frac{\partial G}{\partial n}\right)dS + \int_T \left(\frac{\partial\phi^i}{\partial n_+}G - \phi^i_+\frac{\partial G}{\partial n_+}\right)dS + \int_T \left(\frac{\partial\phi^i}{\partial n_-}G - \phi^i_-\frac{\partial G}{\partial n_-}\right)dS. \tag{6.1.8}$$

Now $\dfrac{\partial G}{\partial n_+} = -\dfrac{\partial G}{\partial n_-}$ so we have (see figure 6.1.1(a))

$$2\pi\phi^i(\mathbf{p}) = \int_S \left(\frac{\partial\phi^i}{\partial n}G - \phi^i\frac{\partial G}{\partial n}\right)dS + \int_T \left(\frac{\partial\phi^i}{\partial n_+} + \frac{\partial\phi^i}{\partial n_-}\right)G\,dS - \int_T \Delta\phi\frac{\partial G}{\partial n_+}\,dS. \tag{6.1.9}$$

Immediately *after* the impact we may write the potential at $\mathbf{p}$ as

$$2\pi\phi^f(\mathbf{p}) = \int_S \left(\frac{\partial\phi^f}{\partial n}G - \phi^f\frac{\partial G}{\partial n}\right)dS - \int_T \Delta\phi^f\frac{\partial G}{\partial n_+}dS. \tag{6.1.10}$$

We have shown that $\Delta\phi = \Delta\phi^f$ and exploiting the fact that $\phi^i(\mathbf{p}) = \phi^f(\mathbf{p})$ for $\mathbf{p} \in S$ we obtain from (6.1.9) and (6.1.10) the relation

$$\int_S \frac{\partial\phi^f}{\partial n}G\,dS = \int_S \frac{\partial\phi^i}{\partial n}G\,dS + \int_T \left(\frac{\partial\phi^i}{\partial n_+} + \frac{\partial\phi^i}{\partial n_-}\right)G\,dS, \tag{6.1.11}$$

which is satisfied at all points $\mathbf{p} \in S$. This is an integral equation from which $\dfrac{\partial\phi^f}{\partial n}$ may be determined. In the toroidal geometry the expression for the potential is

$$c(\mathbf{p})\phi(\mathbf{p}) = \int_S \left(\frac{\partial\phi}{\partial n}G - \phi\frac{\partial G}{\partial n}\right)dS - \int_T \Delta\phi\frac{\partial G}{\partial n_+}dS, \tag{6.1.12}$$

with $c(\mathbf{p})$ given as in (4.2) provided $\mathbf{p} \notin T$. For $\mathbf{t} \in T$ ($\notin T \cap S$) we have

$$4\pi\phi(\mathbf{t}) = \int_S \left(\frac{\partial\phi}{\partial n}G - \phi\frac{\partial G}{\partial n}\right)dS - \int_T \Delta\phi\frac{\partial G}{\partial n_+}dS + 2\pi\Delta\phi(\mathbf{t}). \tag{6.1.13}$$

Having obtained from (6.1.11) the value of $\frac{\partial \phi}{\partial n}$ on S after the impact we may use (6.1.13) to evaluate the potential at points on T and (6.1.12) to evaluate the potential in the neighbourhood of T and hence determine the component of the fluid velocity normal to T.

We now turn our attention to the impact of the jet in the collapse of bubbles. In the idealised model impact occurs at one point. Across this point the potential is discontinuous by an amount $\Delta\phi$, which corresponds to the circulation in the flow. Since the surface over which the impact occurs is a point and $\Delta\phi$ is uniform over this surface there is no vortex sheet created by the impact. In order to describe such a flow using a boundary integral method we introduce a cut, T, in the domain Ω which allows us to once again consider it as singly connected. The initial cut consists of the point of impact, but as the flow develops the geometry of the cut changes. At any point on the cut, however, the jump in potential across it is $\Delta\phi$ with the geometry as in figure 6.1.1(b) and the velocity potential is given by (6.1.12) and (6.1.13). In the limit of contact at a point the integral over T appearing in (6.1.11) vanishes so that over the surface S we have that $\frac{\partial \phi^f}{\partial n} = \frac{\partial \phi^i}{\partial n}$, except perhaps at points in $T \cap S$ where the normal is undefined. From our integral formulation the initial velocity of the impact point is indeterminate, as the surface T has been reduced to a set of measure zero. For the development of a numerical algorithm, however, this value is not necessary. Thus we have the theoretical basis for the transition to a doubly connected flow geometry in the collapse of a bubble. We develop in the next section a boundary integral technique for the solution of (6.1.12) for $\frac{\partial \phi}{\partial n}$ at the bubble surface. The algorithm must be modified to include the term in this equation that involves integration over the cut T. This evaluation requires that the geometry of T is known. Thus we follow the cut as a material surface in the fluid. The details are discussed in the next section.

Before closing this discussion we make some remarks regarding the Kelvin impulse and kinetic energy of the fluid. The Kelvin impulse of the bubble is

defined as

$$\mathbf{I} = \rho \oint_{S \cup T} \phi \mathbf{n} \, dS. \tag{6.1.14}$$

We may write the impulse before impact as

$$\mathbf{I}^i = \rho \int_S \phi^i \mathbf{n} \, dS + \rho \int_T \Delta\phi \mathbf{n}_+ \, dS, \tag{6.1.15}$$

having exploited $\mathbf{n}_+ = -\mathbf{n}_-$ in evaluating the integral over T. The impulse immediately after impact is

$$\mathbf{I}^f = \rho \int_S \phi^f \mathbf{n} \, dS + \rho \int_T \Delta\phi^f \mathbf{n}_+ \, dS. \tag{6.1.16}$$

Since $\phi^i = \phi^f$ on S and $\Delta\phi = \Delta\phi^f$ on T we see that

$$\mathbf{I}^i = \mathbf{I}^f, \tag{6.1.17}$$

and the impulse is conserved on impact. Note that this result is independent of whether the impact occurs at a point or over some surface, and is also independent of whether or not a vortex sheet is created by the impact. The kinetic energy of the flow is

$$E = \frac{1}{2} \rho \oint_{S \cup T \cup \Sigma} \phi \nabla\phi \cdot \mathbf{n} \, dS, \tag{6.1.18}$$

where Σ represents the boundaries of the flow domain. In general, since $\nabla\phi \cdot \mathbf{n} = \dfrac{\partial \phi}{\partial n}$ changes over $S \cup T \cup \Sigma$ due to the impact, as does ϕ change over the impact site and boundary Σ, we would expect a loss in the kinetic energy of the flow due to the impact. In the case of impact at a point, though, all quantities in the integrand of (6.1.18) are unchanged, except perhaps at the point of impact, which is a set of measure zero. In that case energy is conserved on impact. For impact over some surface, the energy loss may manifest itself in the form of heat or acoustic energy.

6.2. The algorithm for computing the motion of a toroidal bubble

The motion of the bubble up until the time of impact may be computed using the boundary integral method described in chapters 4 and 5. This computation yields the geometry of the bubble surface, the potential on it and the normal fluid

velocity at this surface just prior to impact. The geometry just prior to impact is shown in figure 6.2.1(a). The number of nodes representing the bubble surface is $n+1$, with the initial node labelled as 0. The impact occurs at the nodes 0 and n, so that the circulation of the flow that evolves is

$$\Delta\phi = \phi_n - \phi_0, \tag{6.2.1}$$

with the subscript denoting evaluation at the node.

Over S the potential is unchanged by the impact and due to its occurrence at a point the normal derivative of the potential is unchanged over S. Thus we may evaluate the fluid velocity at the node points $i = 1, 2, ..., n-1$ in the usual manner and determine their positions a short time, δt_i, later via the Euler time stepping scheme of chapter 4.

Similarly, the potential may be evaluated at these nodes at time $t + \delta t_i$ using the Euler scheme, where t here denotes the time of impact. The node 0 ($\equiv n$) is the initial cut, T, and the initial speed of this point of unknown. Regardless of what this initial speed is, it is finite, and in determining the position of this point at some later time by an Euler time stepping scheme we can make its displacement arbitrarily small by letting our initial time step, δt_i, tend to zero. As $\delta t_i \to 0$ the displacement of the bubble surface and change in potential on it also tend to zero.

The value of δt for later iterations is given following the criterion discussed in chapter 5. After this initial time step, however, we have no knowledge of where the cut, T, meets the bubble surface. Although no analytic solution has been found for the early motion of the free surface about the impact point we might suppose that the very high surface curvature here gives rise to very high fluid velocities, the action of which is to immediately smooth the free surface. We perform this smoothing numerically by deleting the nodes $0, 1, n-1$ and n and fitting a smooth closed surface to the remaining nodes. Thus our bubble at time $t+\delta t_i$ is represented by $n-2$ nodes, including as a node the point where the cut meets the bubble. This point where the cut meets the bubble surface is taken to be half-way (with respect

to arc-length) between nodes 2 and $n-2$. This is the second node representing the cut, the first being that point at which impact occurs. If we denote the two nodes representing the cut as (r_{c0}, z_{c0}) and (r_{c1}, z_{c1}) then at (r_{c1}, z_{c1}) the cut meets the bubble surface at right angles. This geometry is shown in figure 6.2.1(b).

We are now in a position to implement the boundary integral method to solve (6.1.12) for $\frac{\partial \phi}{\partial n}$ on S. The technique is unchanged from that discussed in chapters 4 and 5 apart from the appearance of the term $\Delta\phi \int_T \frac{\partial G}{\partial n_+} dS$. The cut is represented by a cubic spline parametrised with respect to the arclength, ξ_c, along the cut and knowledge of its geometry in this form allows evaluation of this term.

At this point we shall define $N = n-2$ and the number of nodes representing the bubble surface is then $N+1$, noting that by this choice of N nodes 0 and N are co-incident. Since the potential is discontinuous at node $0/N$ we have that

$$\phi_N = \phi_0 + \Delta\phi \tag{6.2.2}$$

for the duration of the motion. In the boundary integral expression for the potential (equation (6.1.12)) the normal that appears is that normal to the surface $S \cup T$. Despite the existence of a normal to S at node $0/N$, the normal to $S \cup T$ is undefined there, and so then is $\partial\phi/\partial n$. Hence we choose to collocate at nodes $i = 1, 2, ..., N-1$. Despite choosing not to collocate at node $0/N$ knowledge of the whereabouts of this node is essential to the computation as it defines that point on the bubble surface at which ϕ is discontinuous.

Although $\partial\phi/\partial n$ is undefined at node $0/N$ we may assign it a value here, and the appropriate value is the limit of $\partial\phi/\partial n$ as we approach the node along S. This value is then the component of the fluid velocity normal to S, noting that despite the discontinuity in ϕ here, the fluid velocity is everywhere continuous so that the limit we choose is independent of the direction of approach along S. As noted above, knowledge of the fluid velocity here is crucial as the motion of node $0/N$ must be followed in order that the bubble motion can be computed. We evaluate the appropriate limiting value by utilising the linear representation that we have

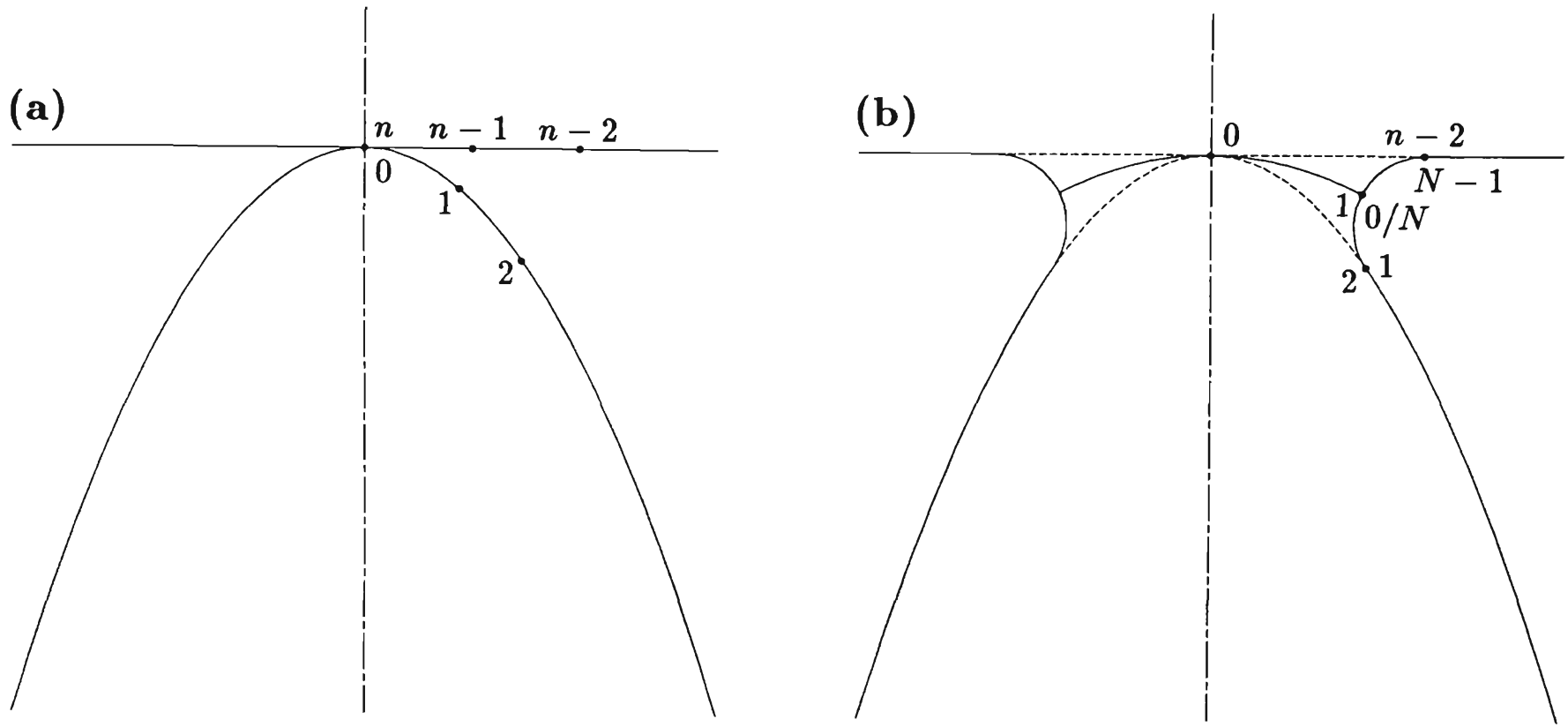

Figure 6.2.1. The numerical transition to the toroidal bubble geometry. The geometry is shown (a) immediately before and (b) immediately after impact.

chosen for $\partial\phi/\partial n$ as discussed in chapter 4. If we consider the interval between node $N-1$ and node 1 as a single segment upon which we define a linear expression for $\partial\phi/\partial n$ then evaluation of this function at node $0/N$ yields

$$\psi_{0/N} = \frac{\delta\xi_N\psi_1 + \delta\xi_1\psi_{N-1}}{\delta\xi_1 + \delta\xi_N}, \tag{6.2.3}$$

the notation as defined in chapter 4. Collocation at nodes $i = 1, 2, ..., N-1$ then yields the $N-1$ linear equations

$$2\pi\phi_i + \Delta\phi D_i + \sum_{j=1}^{N} A_{ij} = \sum_{j=2}^{N-1} \left(\tilde{B}_{ij}\psi_{j-1} + \tilde{C}_{ij}\psi_j \right), \tag{6.2.4}$$

where

$$\begin{aligned} D_i &= \int_T \frac{\partial G}{\partial n_+} dS, \\ &= \sum_{k=1}^{N_c} \int_{\xi_{c_{k-1}}}^{\xi_{c_k}} \left\{ \int_0^{2\pi} r_c(\xi_c, \theta) \frac{\partial G_i}{\partial n}(\xi_c, \theta)\, d\theta \right\} d\xi_c, \end{aligned} \tag{6.2.5}$$

is the contribution to the potential that arises from integration over the cut T. In this expression the notation is exactly analogous to that used for the bubble surface. The number of nodes representing the cut is $N_c + 1$. The arclength along the cut to the k'th node is ξ_{c_k}, r_c is the radial co-ordinate of points on the cut and the Green's function is as defined in chapter 4 and parametrised with respect to azimuthal angle, θ, and arclength, ξ_c, along the spline. The coefficients $\tilde{B}_{ij}$ and $\tilde{C}_{ij}$ are defined as

$$\begin{aligned} \tilde{B}_{ij} &= B_{ij}, && j = 3, 4, ..., N-1, \\ &= B_{ij} + C_{i1} + \delta\xi_N(B_{i1} + C_{iN})/(\delta\xi_1 + \delta\xi_N), && j = 2, \end{aligned} \tag{6.2.6}$$

$$\begin{aligned} \tilde{C}_{ij} &= C_{ij}, && j = 2, 3, ..., N-2, \\ &= C_{ij} + B_{iN} + \delta\xi_1(B_{i1} + C_{iN})/(\delta\xi_1 + \delta\xi_N), && j = N-1, \end{aligned} \tag{6.2.7}$$

with A_{ij}, B_{ij} and C_{ij} as defined in chapter 4. We obtain the expressions of (6.2.4), (6.2.6) and (6.2.7) from (4.14) and (4.15) by adding the contribution $\Delta\phi D_i$ that arises from integration over the cut and substituting for $\psi_{0/N}$ using (6.2.3). Equation (6.2.4) may then be solved for the unknown ψ_1, $\psi_2, ..., \psi_{N-1}$. The positions of, and potential at each node are then updated using the Euler time stepping formulae of chapter 4.

In order that we may evaluate the coefficients D_i via (6.2.5) we must know the whereabouts of the cut, T, so we follow its motion throughout the computation and this necessitates a knowledge of the fluid velocity normal to this surface. We obtain this velocity as follows. Let $\mathbf{n}$ denote the normal to T at some point $\mathbf{t}$, with $\mathbf{n}$ directed interior to the fluid on T_+. If we further let $\delta\tau$ be some small distance then we can obtain a second order finite difference approximation to the normal fluid velocity at T via

$$\nabla\phi \cdot \mathbf{n} \approx \frac{1}{2}\left[\frac{\phi(\mathbf{t}+\mathbf{n}\delta\tau) - \phi_+(\mathbf{t})}{\delta\tau} + \frac{\phi_-(\mathbf{t}) - \phi(\mathbf{t}-\mathbf{n}\delta\tau)}{\delta\tau}\right], \tag{6.2.8}$$

but noting that

$$\phi_+(\mathbf{t}) = \phi_-(\mathbf{t}) + \Delta\phi, \tag{6.2.9}$$

this becomes

$$\nabla\phi \cdot \mathbf{n} \approx \frac{\phi(\mathbf{t}+\mathbf{n}\delta\tau) - \phi(\mathbf{t}-\mathbf{n}\delta\tau) - \Delta\phi}{2\delta\tau}. \tag{6.2.10}$$

Note that we have avoided the need to calculate the potential on the surface T itself. With this expression for the normal velocity we may propagate nodes on T along their normals, using the Euler scheme, to determine the position of this surface a small interval of time, δt, later. We have chosen to use an Euler time integration scheme as the accuracy of the method is now limited by the second order accurate estimate of the fluid velocity at the cut. To use a higher order method as discussed in chapter 5 would be inappropriate. Note that we are not following the motion of fluid particles at T. To do so would require knowledge of the tangential component of the fluid velocity, which could be obtained, but at the expense of significant computation. Since only the geometry of this surface is required the extra computational effort needed to follow points on T in a Lagrangian fashion is seen to be superflous. In any case, we are following the motion of T as a material surface in the fluid and as we shall see shortly this provides considerable assistance in visualisation of the flow.

Every 5-15 iterations it is necessary to smooth the bubble surface, the cut surface and the potential on S according to the 5-point formula discussed in chapter

5. The surface S and the potential on it are smoothed first. In order to apply the smoothing formula to the potential at nodes $N-1, 0/N$ and 1, where application of the 5 point formula includes points on the other side of the discontinuity in ϕ, those points on the other side are artificially redefined by the addition (or subtraction) of $\Delta\phi$ for use in the formula. When smoothing the cut, node N_c is considered as fixed, having already experienced smoothing as part of S. In order to apply the formula at node $N_c - 1$ an artificial node $N_c + 1$ is defined as the reflection of node $N_c - 1$ about the plane tangent to the bubble surface at node N_c. This choice is made to preserve the orthogonality of the cut and bubble surface at this point, noting that these surfaces are initially orthogonal and this orthogonality is preserved throughout the motion by virtue of the fact that S is a free surface and T a material surface in the fluid. In a similar manner, artificial cut nodes -2 and -1, consisting of cut nodes 2 and 1 respectively reflected about the axis of symmetry, are used to facilitate smoothing of cut nodes 0 and 1. In the case where less than three nodes represent the cut no smoothing is performed. As discussed in chapter 5, the results of the computation were found to be slightly improved by a redefinition of the mesh after every time step so that the nodes representing the bubble surface and those representing the cut are evenly spaced, noting that the spacing on the cut is not necessarily the same as the spacing on the bubble. As the computation proceeds in time the length of the cut increases. Thus nodes are added in order that this surface remains adequately resolved. An appropriate strategy in the addition of nodes is to endeavour to keep the spacing on the bubble and the cut approximately equal.

The spline representing the bubble surface is made continuous at node $0/N$ by specifying a common value of the derivatives $\partial r/\partial\xi$ and $\partial z/\partial\xi$ at the respective end-points. In order to gain an appropriate estimate of these derivatives an auxillary cubic spline is fitted to the nodes $N-n_s, N-n_s+1, ..., N, 1, 2, ..., n_s$, with the not-a-knot condition (de Boor, 1978) applied at the free ends. The value n_s must be chosen as greater than or equal to 1 but is typically chosen to be 8. Having fitted a spline to

these points the derivatives at node N are evaluated and used to clamp the ends of the spline representing the bubble surface. A similar procedure is used to fit a spline to the potential on S. In determining the derivative $\partial\phi/\partial\xi$ at node $0/N$ a method similar to the above is used, but values $\phi_1 + \Delta\phi, \phi_2 + \Delta\phi, ..., \phi_{n_s} + \Delta\phi$ are used in fitting the auxiliary spline, in order to account for the discontinuity in ϕ at node $0/N$.

6.3. Example computations of the motion of toroidal bubbles

The first example of toroidal bubble motion that we shall consider is for a bubble characterised by $\gamma = -2.0$, $\delta = 0.0$, $\epsilon = 100$. This example was considered in section 5.2 and the motion up until the time of impact is shown in figure 5.2.1. The time of impact is taken as 2.1265 and the circulation is $\Delta\phi = 4.155$. The computed motion is shown in figure 6.3.1. The jet tip velocity is shown in figure 6.3.2, with the velocity of the uppermost point of the cut shown as this velocity for times after the impact. The centroid position as a function of time is illustrated in figure 6.3.3, the small discontinuity in this curve at the time of impact purely a feature of the numerical transition to a toroidal geometry.

After the impact has occurred the fluid flows through the torus at a reduced speed. The initial speed of the cut is approximately equal to the average of the fluid velocities at the upper and lower impact surfaces just prior to impact. The bubble continues to collapse after impact and the speed of the tip of the cut increases as fluid is drawn in by this collapse. The rebound of the bubble then slows this motion. We further note that the collapse is characterised by the fast migration of the bubble centroid towards the rigid boundary. After impact migration continues towards the boundary but slows as the bubble re-expands. The circulation in the velocity field manifests itself in a flow of fluid around the torus that is the bubble. This initial flow around impinges upon the bubble surface forming a depression that travels around the side of the bubble. As the bubble re-expands, however, this depression vanishes.

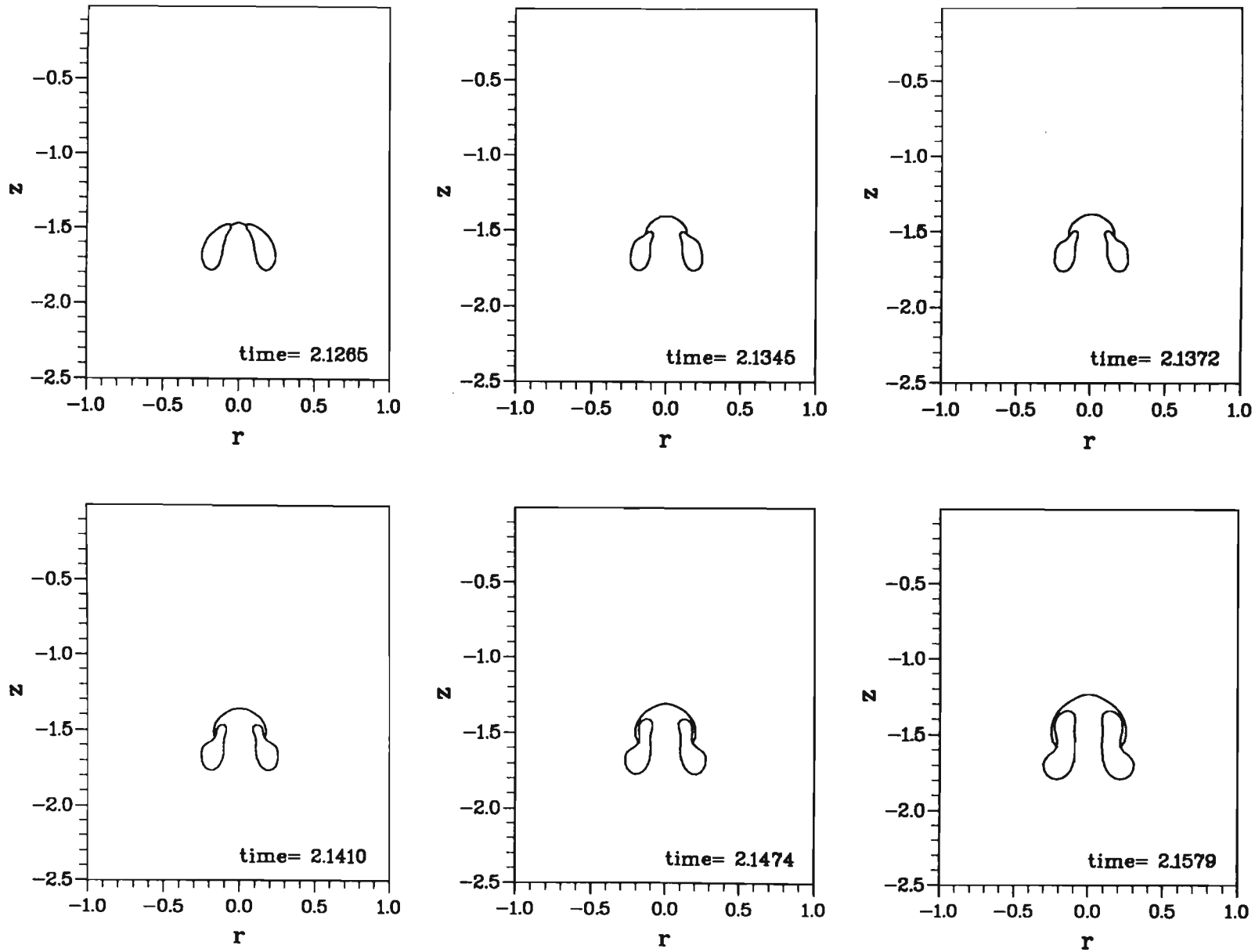

Figure 6.3.1. The motion of the toroidal bubble that evolves from the collapse of an explosion bubble characterised by $\gamma = -2.0$, $\delta = 0.0$, $\epsilon = 100$. The circulation is $\Delta\phi = 4.155$.

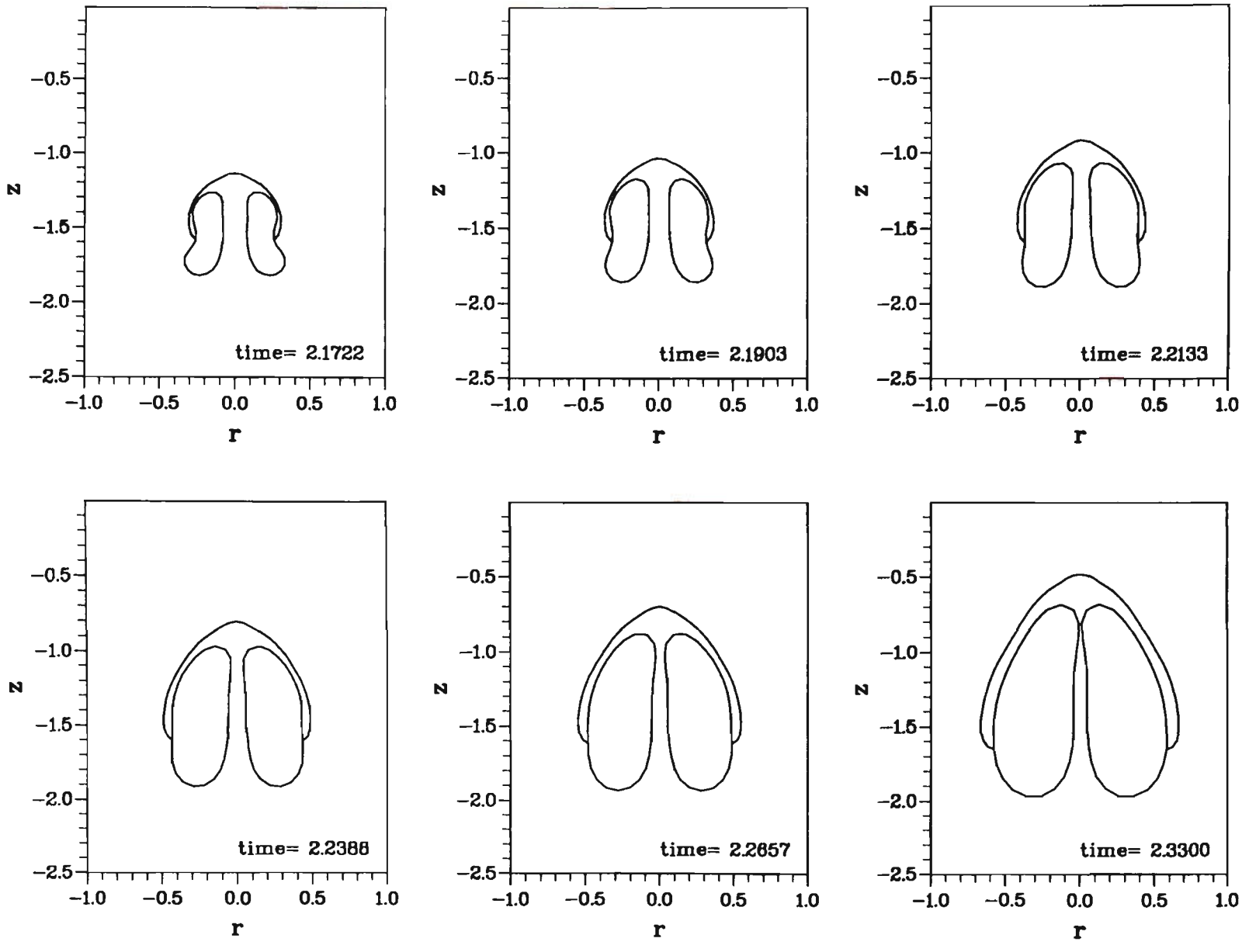

Figure 6.3.1. Continued.

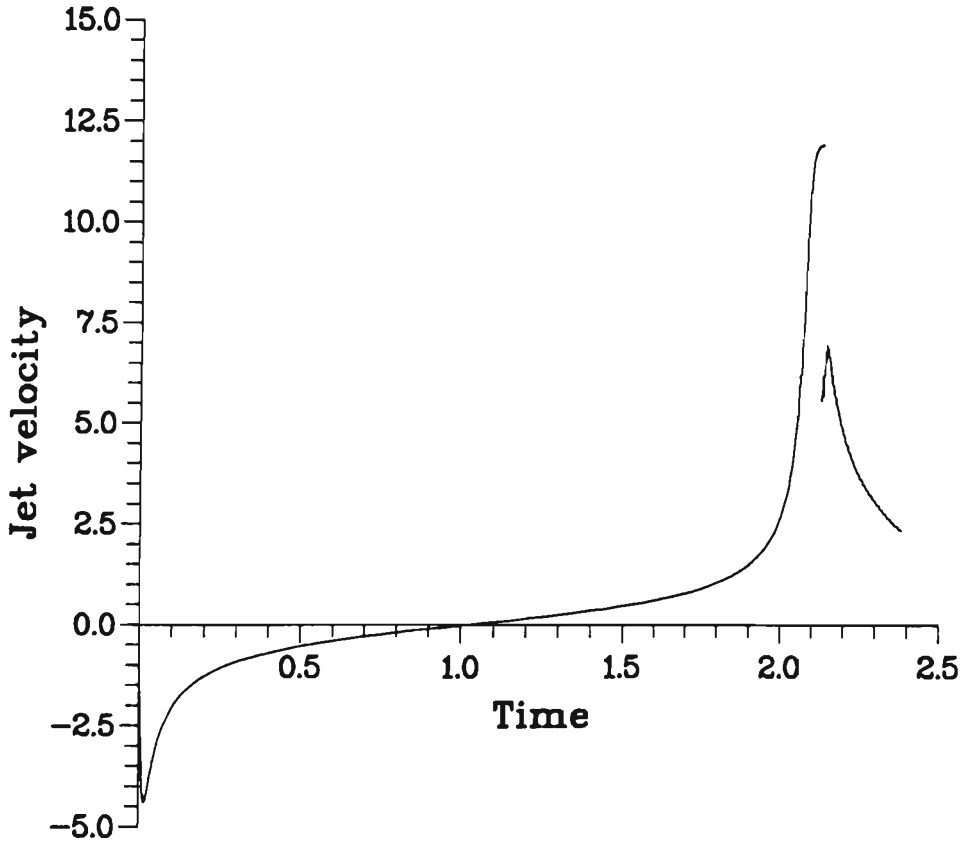

Figure 6.3.2. The jet tip velocity as a function of time for bubble motion characterised by $\gamma = -2.0$, $\delta = 0.0$, $\epsilon = 100$. The curve is discontinuous at the time that the transition to the toroidal geometry occurs. After this time the velocity plotted is that of the point on the cut on the axis of symmetry.

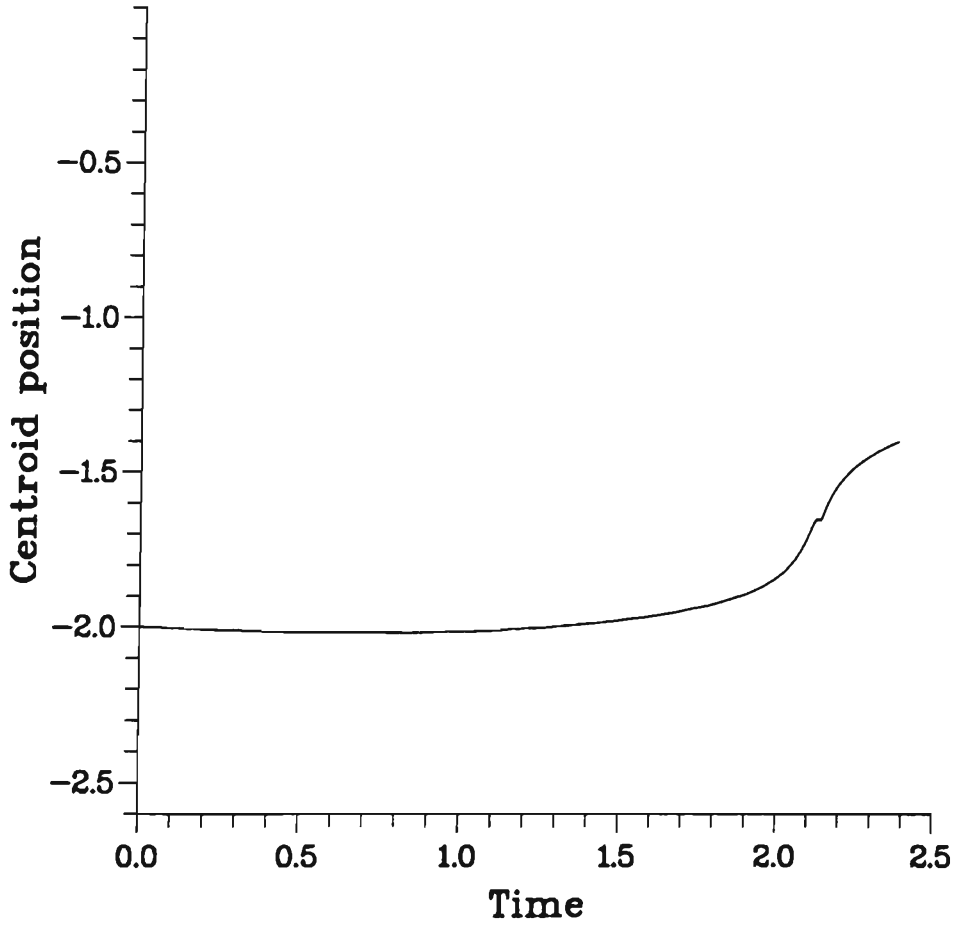

Figure 6.3.3. The centroid position as a function of time for bubble motion characterised by $\gamma = -2.0$, $\delta = 0.0$, $\epsilon = 100$. The curve is discontinuous at the time that the transition to the toroidal geometry occurs.

The pressure field in the fluid at $t = 2.1345$ is shown in figure 6.3.4. This figure reveals a transition in the point of peak pressure from behind the bubble to ahead, noting that the pressure field just prior to impact is shown in figure 5.2.3. The action of this peak is to decelerate the rush of the fluid through the torus towards the wall and drive the motion of the fluid around the bubble. This finding is significant in assessing possible mechanisms for the damage to boundaries due to cavitation or underwater explosion bubble collapse. It is apparent that even if the collapse is not so close to the boundary that we have water hammer impact pressures, the transition to the toroidal geometry creates a region of very high pressure in the fluid between the bubble and the boundary leading to a loading of the boundary. For this example we have further computed the pressure at the rigid boundary just prior to, and just after impact, and this is shown in figure 6.3.5. Even though the bubble collapse is somewhat remote from the rigid boundary the pressure experienced at the boundary is increased by about 50% due to the impact and the pressure distribution shows larger radial gradients.

We compare this result with the motion of a toroidal bubble characterised by $\gamma = -1.5$, $\delta = 0.0$, $\epsilon = 100$, as shown in figure 6.3.6. Due to the closer proximity of the boundary in this case the jet formed is broader but moving with lower speed at impact. The circulation in this example is $\Delta\phi = 4.617$. The motion shares many features with the previous example and we are able to here follow the motion up until the time that the fluid initially in the jet has flowed completely around the bubble. A difference of some significance is that in the first example the central region through the torus thins and we propose that the fluid here disconnects and the flow domain resumes a simply connected topology, whereas in this case the initial breadth of the jet creates a broader central region through the torus and no mechanism for reconnection in this case is apparent. In the first example neglected physical effects such as surface tension and pressure fluctuations within the bubble will accelerate the disconnection of fluid flowing through the torus.

In both of these examples the bubble continues to collapse after jet penetration,

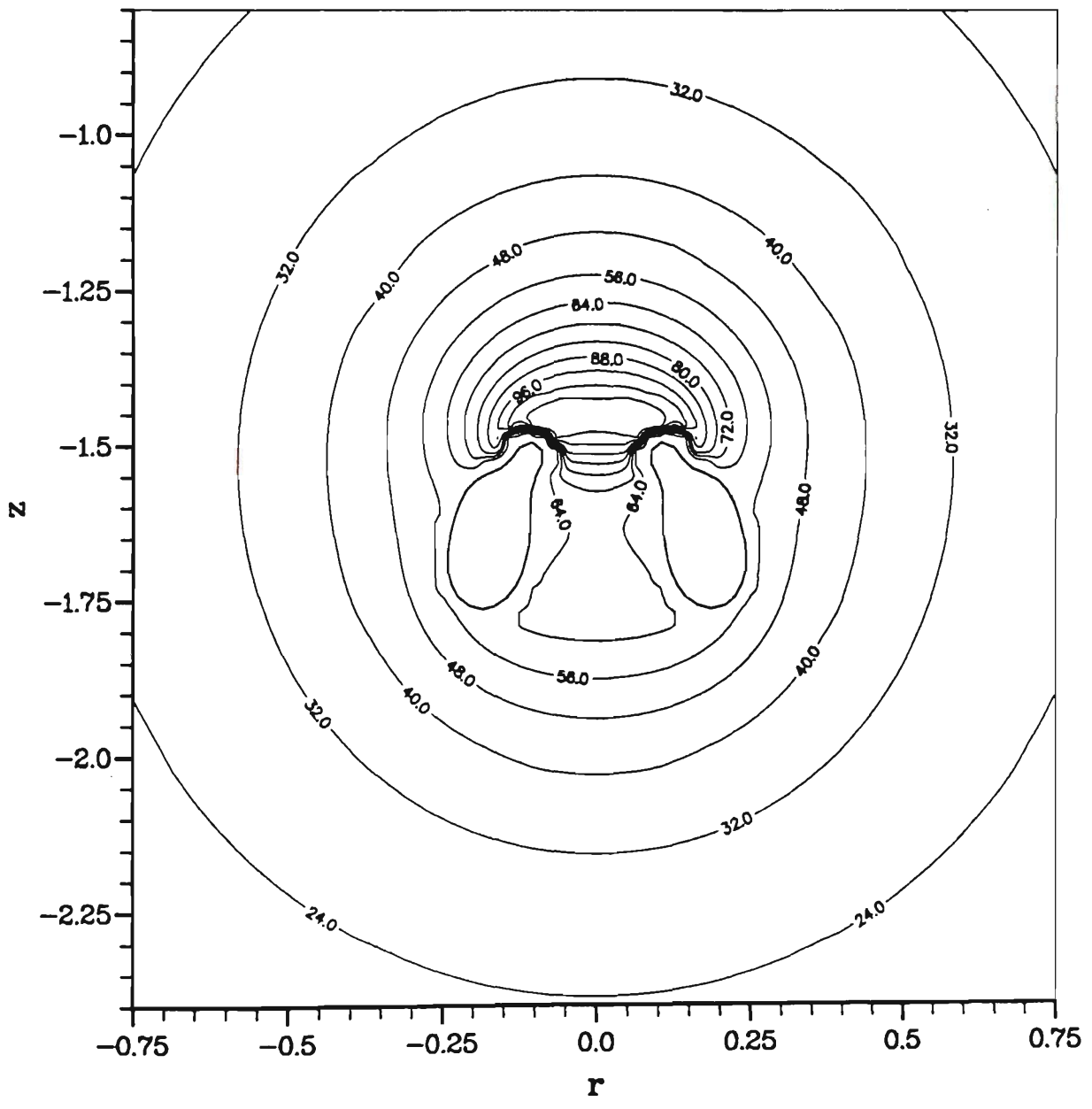

Figure 6.3.4. The pressure field in the fluid computed for the motion depicted in figure 6.3.1 at time $t = 2.1345$.

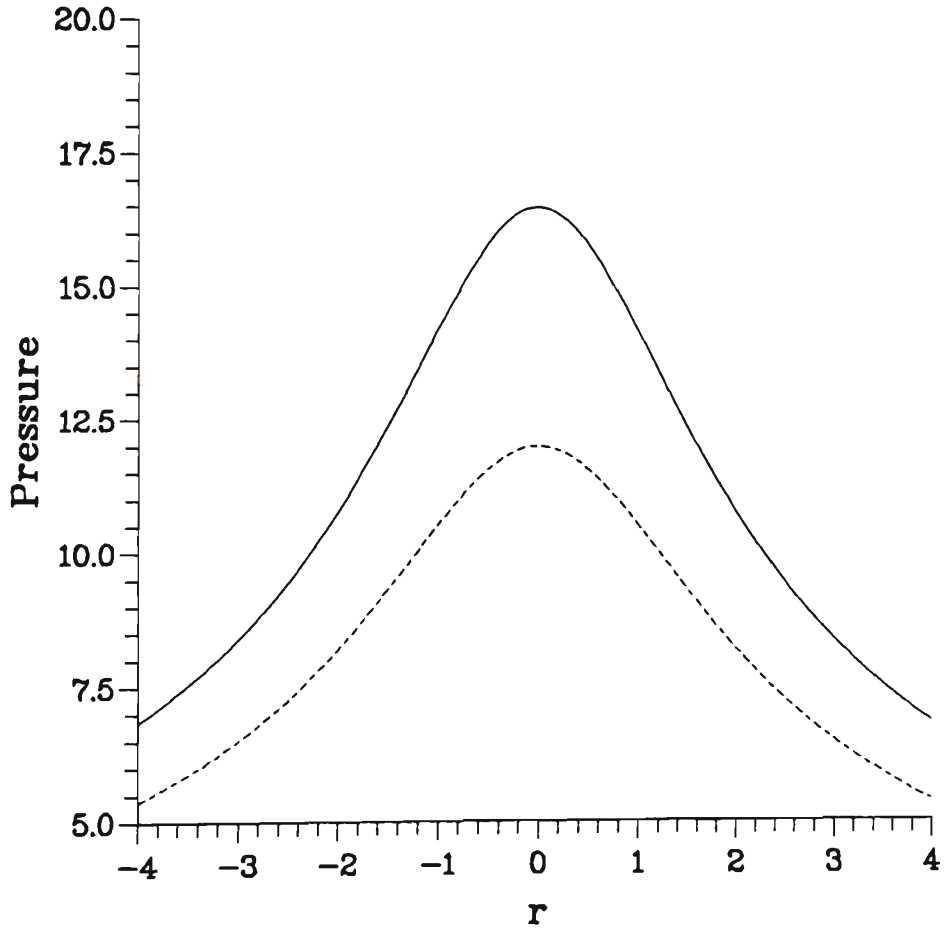

Figure 6.3.5. The pressure at the rigid boundary just prior to (dashed curve, $t = 2.1230$) and just after (solid curve, $t = 2.1300$) the transition to the toroidal geometry that occurs during motion characterised by $\gamma = -2.0$, $\delta = 0.0$, $\epsilon = 100$.

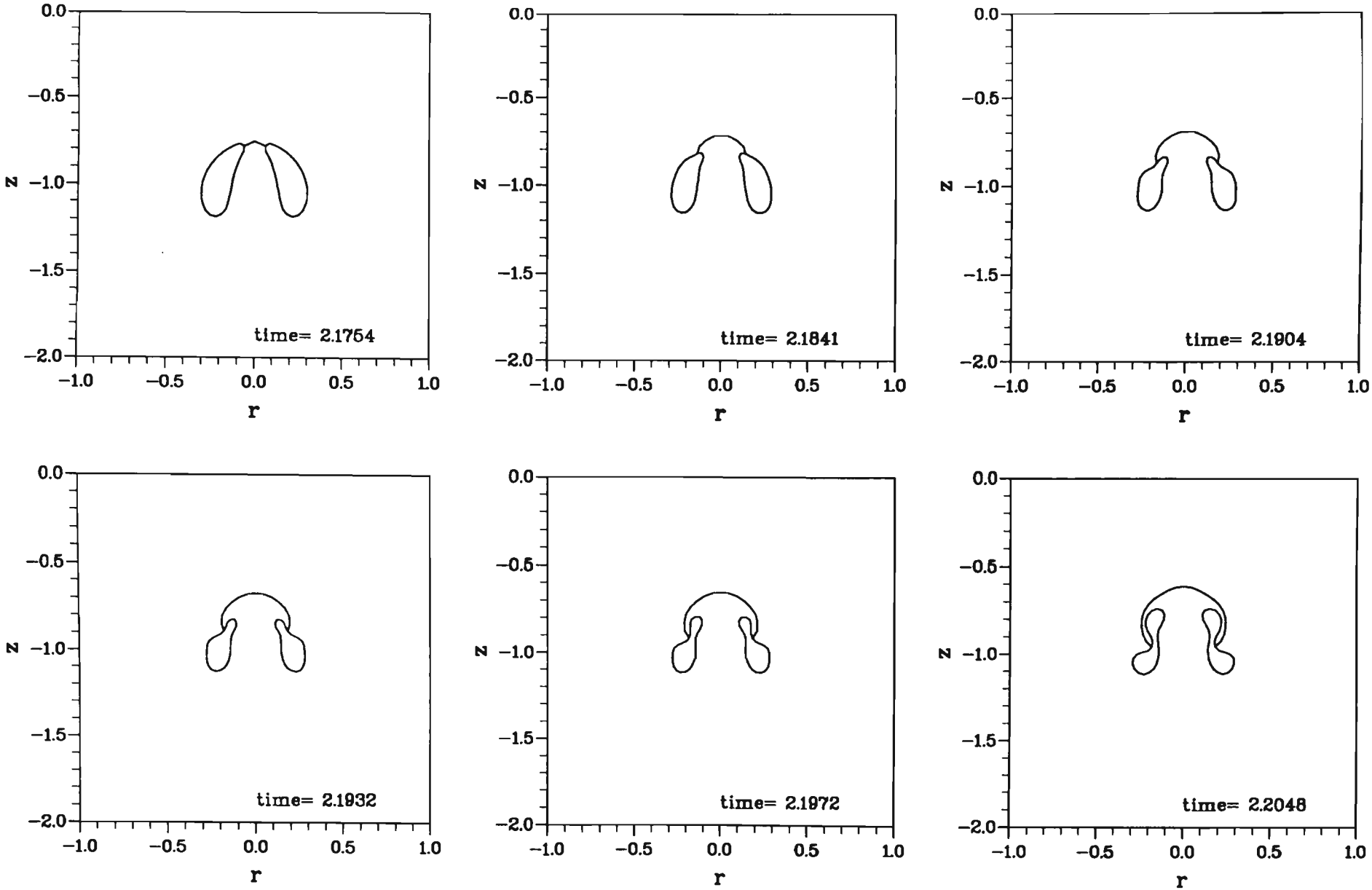

Figure 6.3.6. The motion of the toroidal bubble that evolves from the collapse of an explosion bubble characterised by $\gamma = -1.5$, $\delta = 0.0$, $\epsilon = 100$. The circulation is $\Delta\phi = 4.617$.

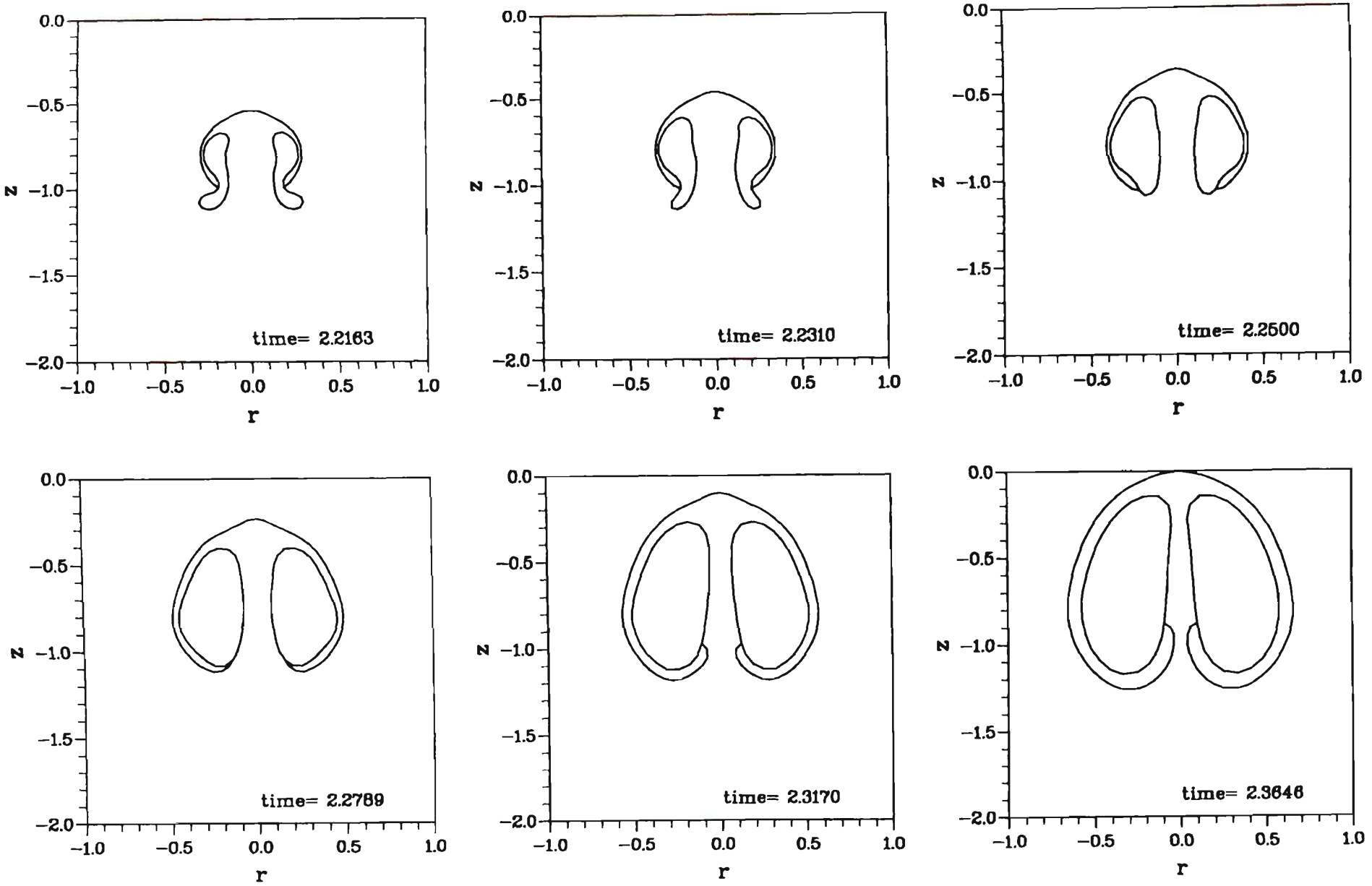

Figure 6.3.6. Continued.

until the pressure inside is sufficiently high that further collapse is arrested and rebound occurs. In view of this it is interesting to consider an example in which jet impact occurs after rebound. The example we consider is characterised by $\gamma = -2.0$, $\delta = 0.0$, $\epsilon = 10$ and the collapse and rebound of the connected bubble is shown in figure 6.3.7. The jet at impact is slowing and the circulation in this case is given by $\Delta\phi = 2.710$. The motion of the toroidal bubble is shown in figure 6.3.8 and since the circulation is low in this case the fluid flowing through the torus tends to continue flowing forward in preference to flowing around the bubble. Thus the cut develops quite a sharp structure. It again appears that the fluid flowing through the bubble will disconnect.

We consider this example in the context of the recent experimental results of Vogel et al. (1989). In that work bubbles were generated by a laser in a fluid possessing a temperature gradient so that the fluid in the jet is at a different temperature to the fluid into which the jet impacts. The fluid at different temperature has a different refractive index and is thus visible by a schlieren technique. Some of these results indicate profiles similar to those computed here, noting that such a visualisation technique would give rise to an image of a bubble with a cap corresponding to the cut computed here. Other results show what appear to be very sharp jets penetrating a large distance beyond the bubble. In such examples this structure does not usually become evident until after the bubble has rebounded. The computational results just presented indicate a sharpness in the geometry of the cut in such cases but this is not as pronounced as that evident in the experimental results. It is of interest the behaviour that will occur if the fluid flowing through the torus disconnects. We give brief consideration to this in the next section.

6.4. Reconnection of the toroidal bubble

From the computational results presented in the previous section it is apparent that the possibility exists that the fluid flowing through the torus thins sufficiently

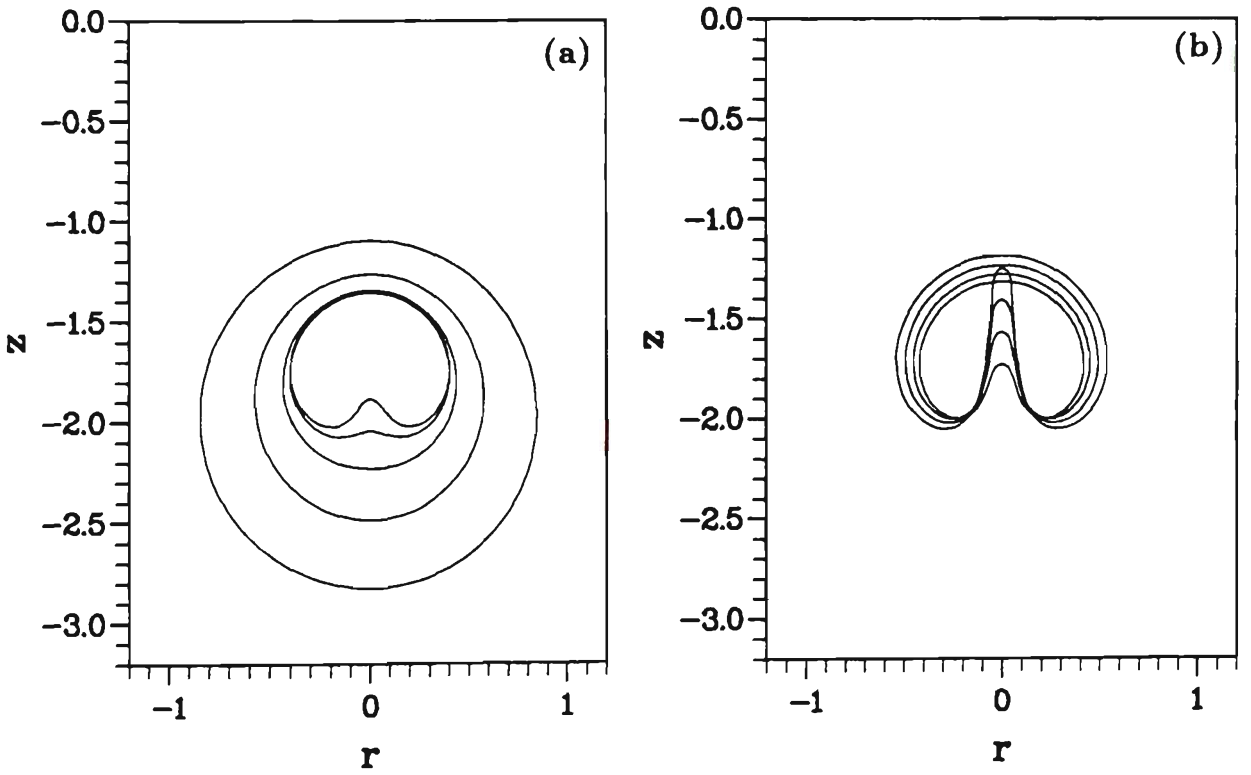

Figure 6.3.7. The collapse and rebound of an explosion bubble characterised by $\gamma = -2.0$, $\delta = 0.0$, $\epsilon = 10$. The times corresponding to successive profiles are: (a) Collapse phase: 1.8314 (outermost), 2.1814, 2.3084, 2.3605, 2.3917 (innermost). (b) Rebound phase: 2.4212 (innermost), 2.4533, 2.4886, 2.5264 (outermost).

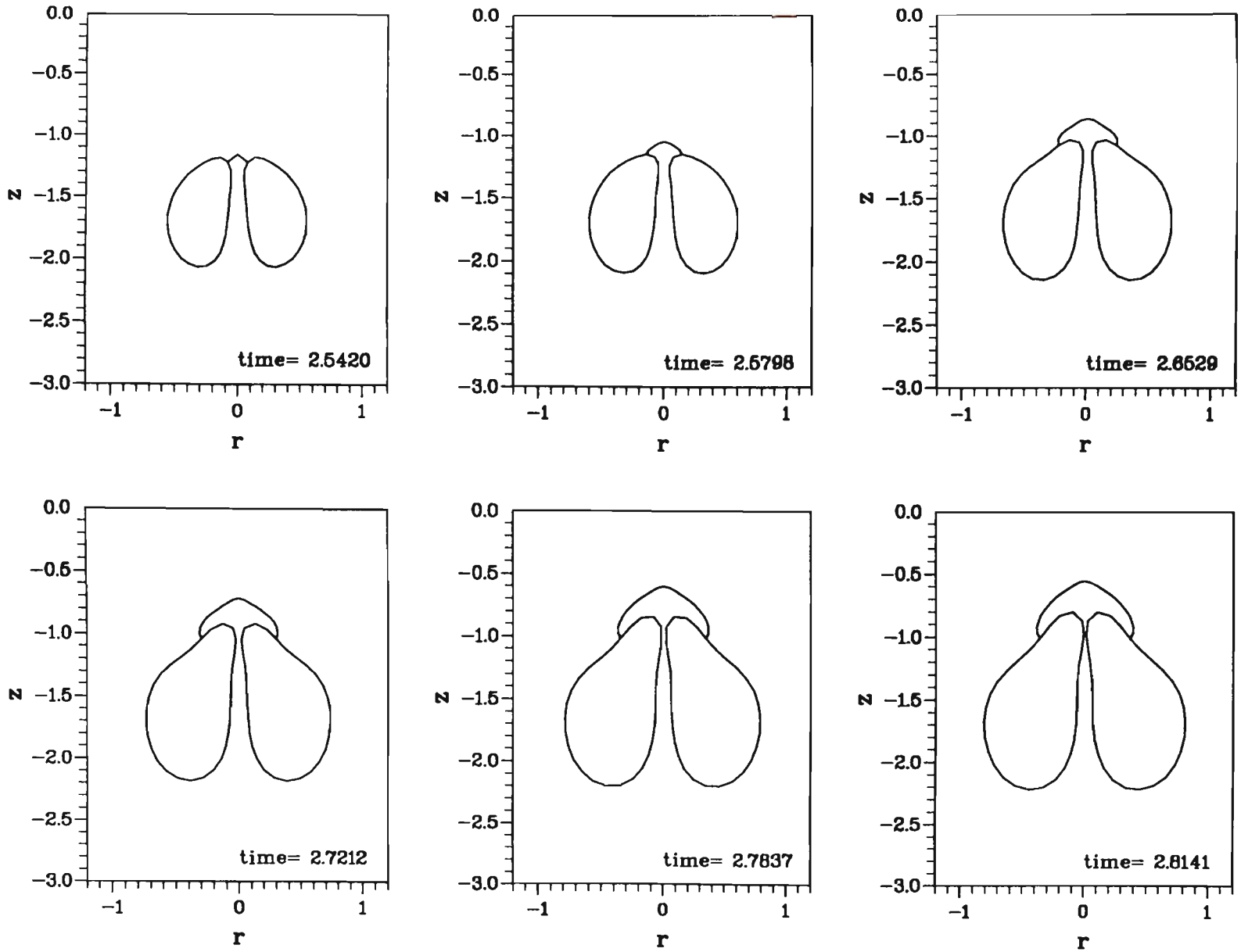

Figure 6.3.8. The motion of the toroidal bubble that evolves from the bubble collapse and rebound shown in figure 6.3.7. The circulation is $\Delta\phi = 2.710$.

as the bubble re-expands that the fluid here disconnects and the flow domain is once again simply connected. In such cases the algorithm of chapters 4 and 5 may be used to compute the motion of the bubble. We will perform this calculation for the bubble illustrated in figure 6.3.8. At the point of disconnection we have an initial curvature of the bubble surface that is infinite, but as we have done in considering the transition to a toroidal geometry we will suppose that this high curvature generates a high local acceleration of the fluid whose action is to smooth the surface here. We take the geometry at the time of disconnection to be that computed using the algorithm presented here. At the point of reconnection we introduce two nodes representing the upper and lower points of the now singly connected bubble, each of these being respectively vertically displaced by $\pm\delta$ from the point of reconnection in order to numerically smooth the surface here. This is illustrated in figure 6.4.1 where the reconnection point is denoted by c and $c_\pm$ denotes this point displaced by $\pm\delta$, where δ is small. The smooth surface of the now singly connected bubble is indicated by the solid line with the initially doubly connected bubble shown as a dashed line. Since the flow domain is now singly connected the cut, T, is superfluous from a computational viewpoint, however, since it is this surface that is visible in the recent experimental results we continue to follow its motion with the fluid.

In order to employ the algorithm of chapters 4 and 5 it is necessary that the potential is continuous on S. Hence we redefine the potential and we shall denote by ϕ' the new potential function which is defined as

$$\phi'(\mathbf{p}) = \phi_{c_-} + \int_{c_-}^{\mathbf{p}} \mathbf{u} \cdot d\mathbf{s}, \tag{6.4.1}$$

where ϕ_{c_-} is the original potential at the point c_- and the line integral is over any curve in the fluid connecting c_- with $\mathbf{p}$. If $\mathbf{p}$ is a point on S that lies between c_- and t, the point where the cut T meets the surface S, then the potential at $\mathbf{p}$ is

$$\phi'(\mathbf{p}) = \phi_{c_-} + (\phi(\mathbf{p}) - \phi_{c_-}) = \phi(\mathbf{p}), \tag{6.4.2}$$

which we see is unchanged from its original value. If $\mathbf{p}$ lies on S between t and c_+

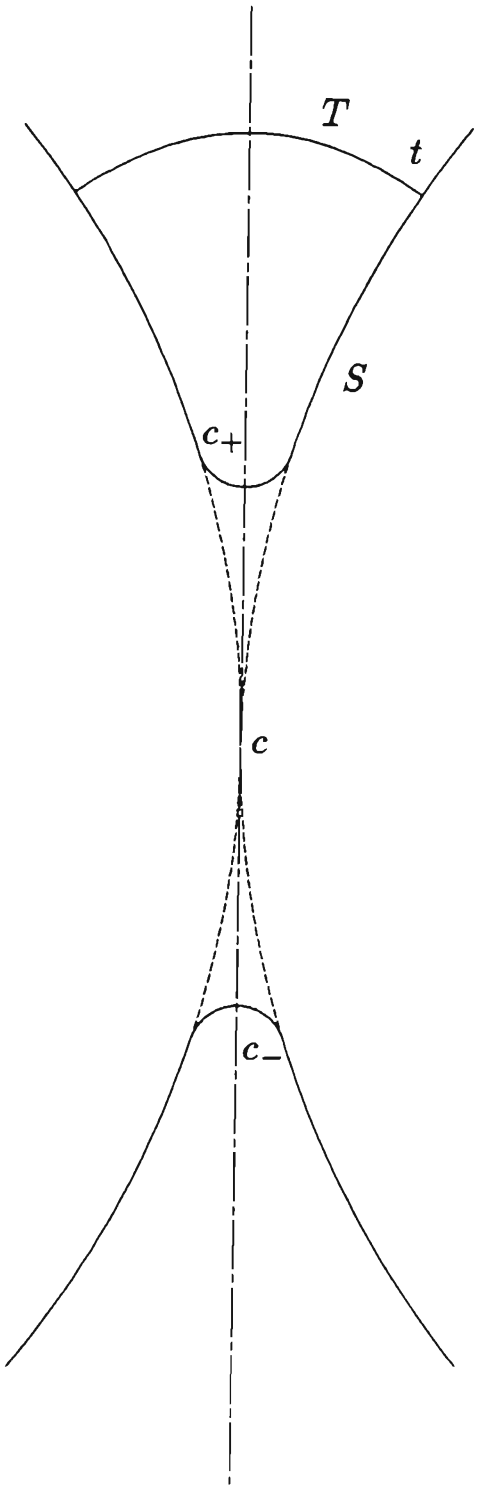

Figure 6.4.1. Schematic representation of the reconnection of the toroidal bubble.

we have

$$\phi'(\mathbf{p}) = \phi_{c_-} + (\phi(\mathbf{p}) - \phi_{c_-} + \Delta\phi) = \phi(\mathbf{p}) + \Delta\phi, \tag{6.4.3}$$

since the path of integration in (6.4.1) crosses the cut T. At these points on S the potential is redefined by the addition of $\Delta\phi$. With this definition, the potential ϕ' is continuous on S.

The motion computed is shown in figure 6.4.2. The fluid element that penetrates the bubble from the top is rapidly ejected as the bubble re-expands, however, this effect is insufficient to cause a sharp spike to be evident in the geometry of the cut.

6.5. Concluding remarks to chapter 6

In this chapter we have considered an algorithm for the computation of the motion of toroidal bubbles. The results have demonstrated the oscillatory nature of these bubbles with rebound observed. The results have further demonstrated that in some cases the fluid flowing through the torus thins upon re-expansion and presumably then disconnects resulting in a flow domain that is singly connected. This result is of interest in view of recently reported experimental results (Vogel et al., 1989) in which it appears that in some cases a vortex ring bubble is formed on the second collapse, despite jet penetration occurring on the first collapse. The results presented here have indicated a mechanism by which this may occur.

This process by which the toroidal bubble resumes a connected topology may provide a mechanism for the formation of what appear to be very sharp jets penetrating a large distance beyond the main part of the bubble surface (Vogel et al., 1989). We have numerically reconnected the surface of the bubble and continued the computation of the bubble motion. This has not revealed these characteristic sharp jets. We may postulate that the ejection of the element of fluid that remains penetrating the bubble after reconnection is the source of this sharp jet but that the current model does not predict this suggests that other physical phenomena must be considered in order to provide an adequate description of this behaviour.

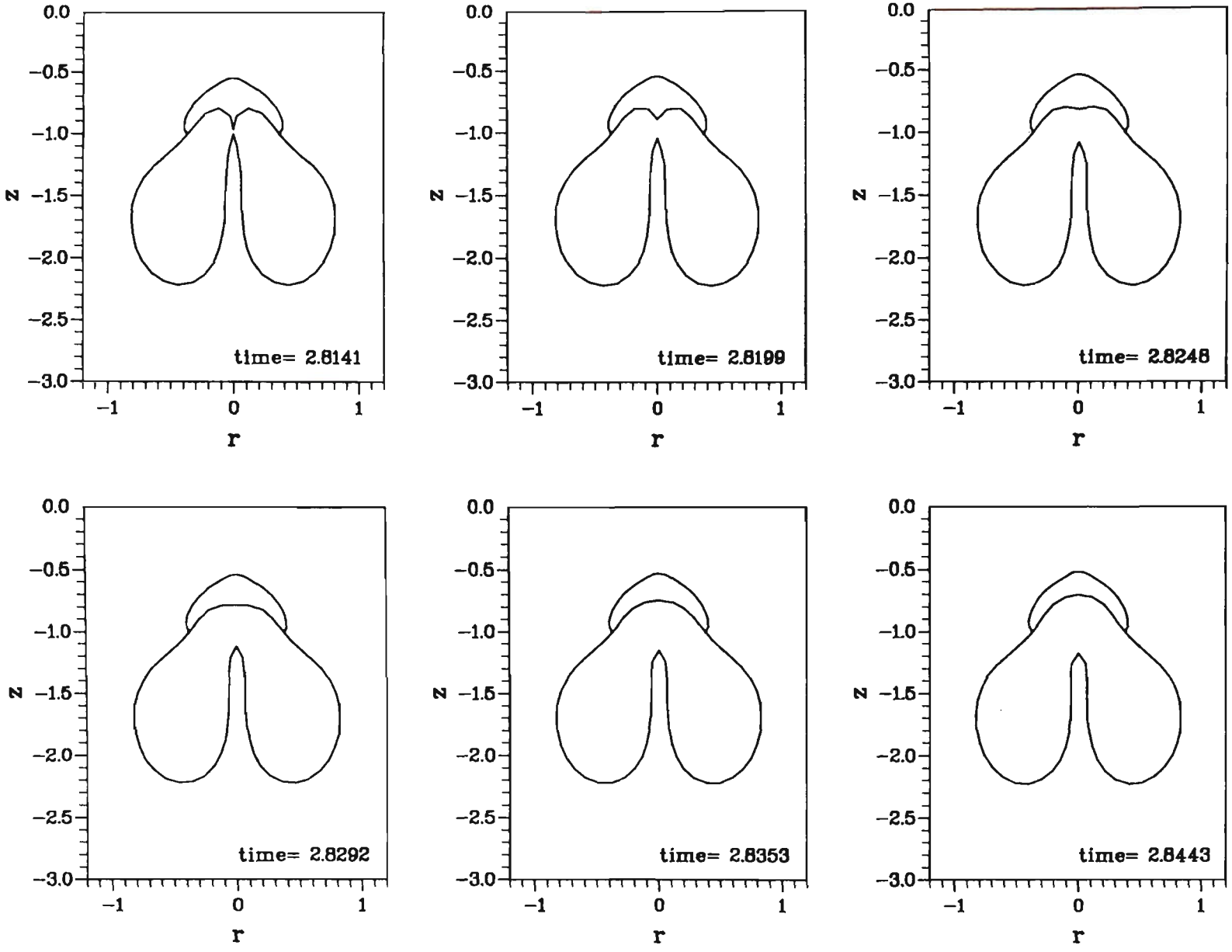

Figure 6.4.2. The motion of the bubble shown in figure 6.3.8 after reconnection has occurred and the flow domain is again simply connected.

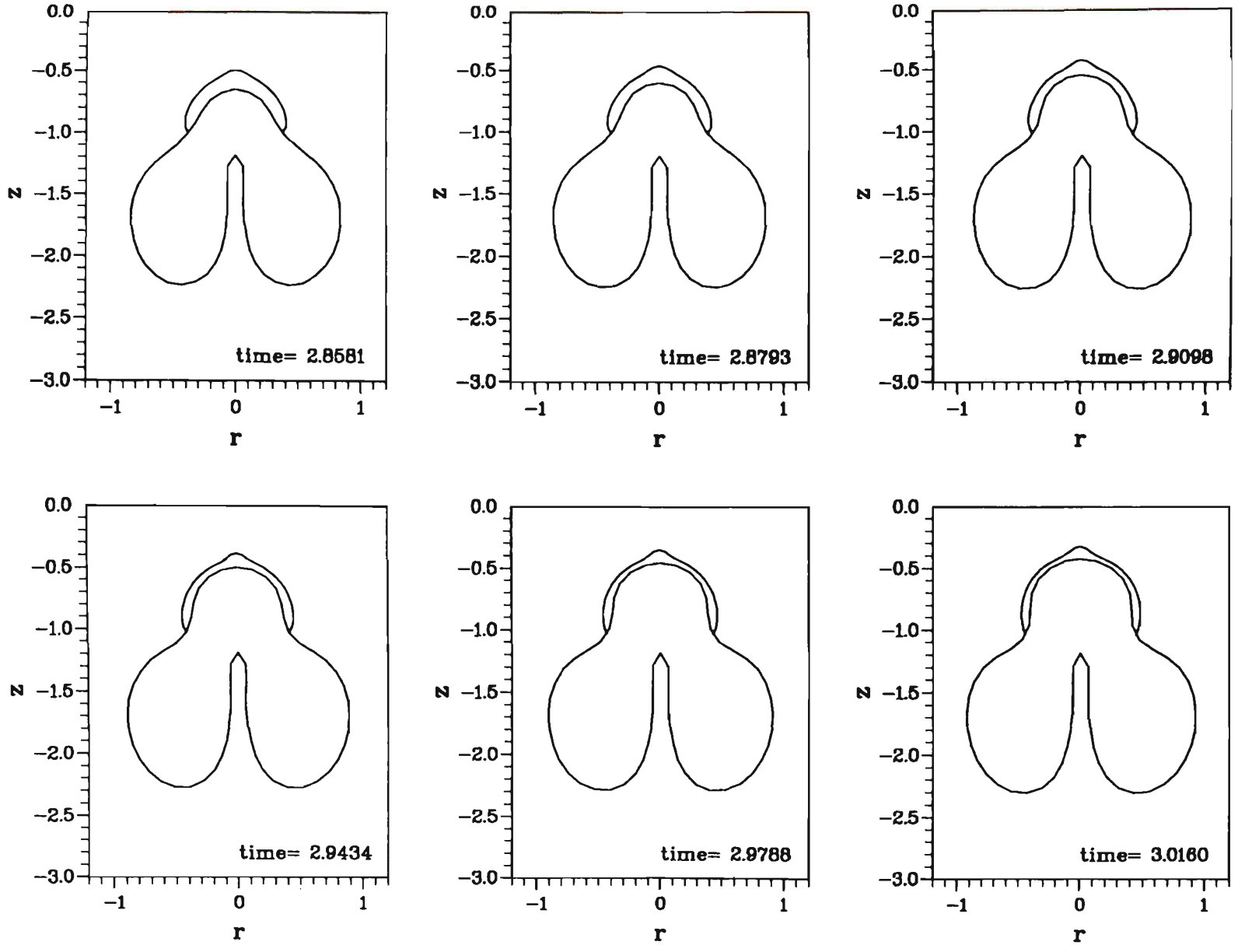

Figure 6.4.2. Continued.

We remark in this context that the surface about the reconnection point is characterised by very high curvatures. Hence we might suppose that the surface tension forces acting on the elements of the fluid about this point are significant and the action of this force will be to eject these elements of fluid from the bubble. This is perhaps a mechanism for the creation of what appear to be sharp jets. We further note that this behaviour is evident in experiments involving bubbles whose maximum radii are of the order of $10^{-3}m$, so that the radii of curvature associated with jet formation may be several orders of magnitude less than these maximum values.

An initial investigation of this question may be pursued by including surface tension in the model, this being a fairly routine task as indicated in chapter 2. However, to do so would necessitate an understanding of the role that surface tension plays in the initial impact of the jet upon the far side of the bubble, noting that the jet tip is characterised by a very high curvature. This aspect is an open question and a very difficult one as the mechanism by which the two contacting surfaces break down and become one is not well understood. Oguz and Prosperetti (1989) have recently considered this question, but perform calculations of the motion of two surfaces after such a contact by assuming that they are initially connected by an element of fluid. It has been put forward by Vogel et al. (1989) that in some cases the surfaces at contact do not break down and form one but remain separated by a thin layer of gas, with the impact of the jet pushing the surface of the bubble ahead, the behaviour much as if a jet impacted upon a membrane. Surface tension must play a significant role in preventing the breakdown of the surfaces if this is a feasible behaviour.

On the scale of the explosion bubble phenomenon, however, surface tension is not expected to play a major role at any stage of the motion, although in the context of reconnection, if the fluid flowing through the torus becomes sufficiently thin the high temperature of the detonation products or fluctuations in the pressure field may be sufficient to cause this fluid to break up, yielding a singly connected

flow domain. We further remark that the evidence of experiment is that the pulsating toroidal bubble is a stable phenomenon, the results of Vogel et al. (1989) showing multiple oscillations of such bubbles. It is only after several oscillations that a wave-like disturbance, travelling around the torus, appears and ultimately leads to the break up of the bubble.

We close by making a comment of a mathematical nature. In order to perform the reconnection of the bubble after it has evolved into toroidal form it is necessary to redefine the potential throughout the fluid. If we follow such a redefinition procedure for the toroidal geometry we may deform the cut, T, into any geometry that we choose. In order to interpret our results in view of recent experimental results we have followed T as a material surface but we could equivalently proceed by redefining the potential throughout the fluid in order that the geometry of T is particularly simple.

PART II - SHOCK DYNAMICS

7

THE PROPAGATION OF UNDERWATER BLAST

7.1. The character of underwater blast

A particularly well documented characteristic of the blast wave generated by a conventional underwater explosion is the time history of the pressure pulse experienced at some target point. The initial decay upon passage of the shock is approximately exponential, so that we may write

$$p(t) = p_m e^{-t/\tau}, \tag{7.1.1}$$

where $t = 0$ is the time of arrival of the shock, p_m is the peak pressure and τ the time constant of the decay. The variation of p_m and τ with distance, r, from the detonation has been the subject of extensive experimental investigation and it has been found (Arons, 1954) that for the explosive TNT the variation is well described by the relations

$$p_m = \kappa_p \left(W^{1/3}/r\right)^{1.13}, \tag{7.1.2}$$

$$\tau = \kappa_\tau W^{1/3} \left(W^{1/3}/r\right)^{-0.22}, \tag{7.1.3}$$

where κ_p and κ_τ are constants and W is the charge mass. If W is measured in kilograms and r in metres then the values of κ_p and κ_τ are

$$\kappa_p = 5.19 \times 10^4, \qquad \kappa_\tau = 9.25 \times 10^1. \tag{7.1.4}$$

The functional dependence of p_m and τ upon $W^{1/3}$ and r may be deduced from similarity arguments and for a fuller discussion the reader is referred to Cole (1948).

The classic theoretical treatment of underwater blast is that of Kirkwood and Bethe (1942). The Kirkwood-Bethe theory is significant from a number of viewpoints. In the first instance it was the first general theory of the propagation of shock waves underwater and secondly it remains the only theoretical treatment that attempts to relate the character of the blast wave to the detonation process and early motion of the bubble surface.

At this point we shall introduce U as the speed of propagation of the shock and define the Mach number, M, of the shock as

$$M = U/a_0, \tag{7.1.5}$$

where a_0 is the speed of propagation of small amplitude acoustic disturbances in the undisturbed fluid ahead of the shock. The Mach number is always greater than or equal to one, noting that the speed of finite amplitude disturbances, of which the shock is a manifestation, is greater than a_0. The theory of Kirkwood and Bethe assumes that the shock is weak so that the Mach number is close to one and entropy changes may be neglected. Although the shock is weak in the sense that the Mach number is small, very high pressures may be associated with the shock due to the small compressibility of water. The specific enthalpy (enthalpy per unit mass of fluid) is

$$h = e + p/\rho, \tag{7.1.6}$$

with e the specific internal energy, p the pressure and ρ the density, and Kirkwood and Bethe define

$$\omega = h - h_0 \tag{7.1.7}$$

as the enthalpy increment anywhere in the fluid, where h_0 is the specific enthalpy of the undisturbed fluid. Thermodynamic considerations establish that

$$d\omega = TdS + dp/\rho \tag{7.1.8}$$

for small increments, where T is the temperature and S the entropy. Since entropy changes are neglected this becomes

$$d\omega = dp/\rho, \tag{7.1.9}$$

an expression that assumes particular significance shortly. The Tait equation of state is employed in the description of the thermodynamic properties of water and this takes the form

$$T = \frac{p + \gamma\pi}{C_v(\gamma - 1)\rho}, \tag{7.1.10}$$

$$e = C_v T, \tag{7.1.11}$$

where C_v is the specific heat and γ and π are constants empirically determined so that this relation adequately fits experimental data for pressures up to about 10,000 atmospheres. In this expression γ is analagous to the ratio of specific heats of an ideal gas and a value of 7.15 is chosen (as used by Cole, 1948, although in their original paper Kirkwood and Bethe utilise $\gamma = 7$). The constant π is taken as 3.047×10^3 atmospheres. The local sound speed, a, is defined as

$$a^2 = \left(\frac{\partial p}{\partial \rho}\right)_S, \tag{7.1.12}$$

where the subscript S denotes that the pressure is considered as a function of the density and entropy alone. It may be deduced from (7.1.10) and (7.1.11) that

$$a^2 = \gamma(p + \pi)/\rho, \tag{7.1.13}$$

and neglecting entropy changes at the shock allows us to write

$$(p + \pi)\rho^{-\gamma} = \text{constant} \tag{7.1.14}$$

everywhere, so that we may consider a to be a function of density alone. Kirkwood and Bethe then define

$$\sigma = \int_{\rho_0}^{\rho} (a/\rho) d\rho, \tag{7.1.15}$$

with ρ_0 the density of the undisturbed fluid and further introduce Riemann functions $\hat{r}$ and s as

$$\hat{r} = (\sigma + u)/2, \tag{7.1.16}$$

$$s = (\sigma - u)/2, \tag{7.1.17}$$

with u the fluid velocity. For propagation of weak shocks it is a good approximation that either $\hat{r}$ or s is zero, depending upon the of direction of propagation. In the case of propagation of simple waves this approximation is exact. These facts are exploited both in the theory of the propagation and in determining conditions at the bubble/water interface at the time that the detonation is completed and the shock is propagated into the water. The introduction of these variables allows the

equations of motion to be cast into characteristic form in a particularly convenient manner, a form which will later be exploited in the current investigation. A further quantity known as the kinetic enthalpy is introduced and it is defined as

$$\Omega = \omega + u^2/2. \tag{7.1.18}$$

A solution is obtained for this quantity and an expression for the pressure as a function of time at some target point is subsequently deduced.

The behaviour of Ω at any point in the flow field is mathematically related to its value on the surface of the bubble at some retarded time so that the problem is then reduced to that of determining Ω on the surface of the bubble during the early phases of the bubble motion. It is in this determination that the so called peak approximation is employed. It may be readily deduced from the equations describing the early motion of the bubble that dp/dt evaluated at the bubble surface is negative and initially very large in absolute value. From the relation of (7.1.9) this behaviour is also exhibited by the enthalpy increment, ω. Thus Kirkwood and Bethe suppose that the early behaviour of ω at the bubble surface can be approximated by

$$\omega(t) = \omega_1 e^{-t/\theta_1}, \tag{7.1.19}$$

where ω_1 is the initial value and θ_1 is given by

$$\theta_1 = -\frac{1}{\omega_1} \lim_{t \to 0} \frac{d\omega}{dt}. \tag{7.1.20}$$

This is the peak approximation and we note from (7.1.9) that it may be equivalently applied to the pressure. The value of θ_1 may be determined from the equations describing the early motion of the bubble surface and is dependent upon the material properties of water and the detonation products within the bubble. It is in this way that the motion of the shock is related to the character of the detonation. Use of (7.1.19) allows computation of the early motion of the bubble surface and a solution is obtained for Ω throughout the fluid. The motion of the shock is determined by application of the Rankine-Hugoniot shock jump conditions which

give the discontinuities in the flow quantities at the shock. These expressions are

$$[\rho v] = 0, \tag{7.1.21}$$

$$[p + \rho v^2] = 0, \tag{7.1.22}$$

$$\left[\rho v \left(h + \frac{1}{2}v^2\right)\right] = 0, \tag{7.1.23}$$

where [ ] denotes the difference in the value of the quantity across the shock and v is the fluid velocity relative to the shock. Since the conditions ahead of the shock are known, as are the conditions behind known from the solution for Ω, (7.1.21) - (7.1.23) give the speed of the shock in terms of these quantities and the motion of the shock may thus be determined.

The time behaviour deduced for the pressure at some distance r from the charge is

$$p(r, t') = \frac{x R_0 P_0}{r} e^{-t'/\theta}, \tag{7.1.24}$$

$$P_0 = \rho_0 \Omega_1, \ \theta = \gamma_1 \theta_1. \tag{7.1.25}$$

In these expressions R_0 is the radius of the charge, Ω_1 is the initial value of the kinetic enthalpy of the water at the bubble surface, t' is the time measured from the instant of arrival of the shock and the exponential form of the decay is a direct consequence of the peak approximation. The variables x and and γ_1 are functions of r and are respectively known as the dissipation and time spread parameters and they must, in general, be evaluated numerically.

This theory stands as a landmark as the character of the blast may be determined given the physical properties of the explosive. However, the formulation in terms of the variables of kinetic enthalpy and Riemann function necessitates a somewhat extensive series of substitutions in order to obtain from a given solution readily interpretable physical quantities such as the pressure and particle velocity. For this reason the majority of studies requiring information regarding the pressure-time history of the blast wave produced by an underwater explosion appeal to empirical relations such as those of (7.1.2) and (7.1.3).

Before departing our discussion of the Kirkwood-Bethe theory we should perhaps comment that the early motion of the bubble surface determined in this theory bears little relationship to that determined by the theory of part I. The model of part I is applied at those times after the shock wave has propagated sufficiently far that the motion of the bubble has little influence upon its propagation. The time taken for this to occur is of the order of the timescale of the shock wave phenomenon discussed in the introduction, which is about two orders smaller than the timescale of the bubble motion, and is thus insignificant in the context of determining the inertia dominated features of the bubble motion, that being the aim of the modelling undertaken in part I. The motion of the bubble surface determined in the Kirkwood-Bethe theory is valid only during the earliest stages of the motion, shortly after the impact of the detonation wave upon the explosive/water interface, when the peak is approximation is valid and the initial bubble surface acts as a piston, driving the motion of the shock. The incompressible model of part I and peak approximation applied here impose that the physical regimes described by each are disjoint.

The not inconsiderable effort required to obtain expressions for physical quantities of interest from the Kirkwood-Bethe theory motivated the more recent study of Rogers (1977). In this work the concern is with the propagation of an initially exponential waveform. No attempt is made to relate the character of the shock wave to the detonation. The pressure experienced at some reference distance R_i is assumed to be exponential and thus characterised by the peak pressure, p_i, and time constant, τ_i, there. As Kirkwood and Bethe have done, Rogers exploits the fact that a short distance away from the charge the shock is weak, and in this regime the local speed of sound is well approximated by

$$a = a_0 + \beta u, \tag{7.1.26}$$

where β is constant. The speed of propagation of the shock front is given by

$$U = a_0 + \frac{1}{2}\beta u. \tag{7.1.27}$$

Note that the speed of propagation of the disturbance behind the shock is greater than the speed of the shock, so that disturbances behind catch up with the shock and modify its motion. It is precisely this interaction that causes the peak pressure to decay faster than the $1/r$ characteristic of small amplitude spherical waves. Rogers further assumes that the pressure disturbance in the wave is everywhere related linearly to the fluid velocity via

$$p = \rho_0 a_0 u. \tag{7.1.28}$$

In the spirit of the technique first proposed by Landau (1945) the solution for the fluid velocity in that part of the wave where the flow is continuous is assumed to be of the form

$$u = \frac{1}{r} f\left(t - (1 - \beta u \ell n(r/R_i)/a_0) r/a_0\right), \tag{7.1.29}$$

with the motion of the shock determined by (7.1.27) and the function f determined from the assumption of an exponential time decay of u at the reference distance R_i. Rogers is able to carry through the solution to obtain analytical expressions for the pressure, p_m, at the shock and time constant, τ, of the decay as functions of the range, r, where the time constant is defined as

$$\tau = \frac{-u}{\partial u/\partial t}, \tag{7.1.30}$$

evaluated at the shock. These expressions are

$$p_m(r) = \frac{p_i \left\{ [1 + 2(R_i/\ell_i)\ell n(r/R_i)]^{1/2} - 1 \right\}}{(r/\ell_i)\ell n(r/R_i)}, \tag{7.1.31}$$

and

$$\tau(r) = \tau_0 \left\{ 1 + 2(R_i/\ell_i)\ell n(r/R_i) \right\}^{1/2}, \tag{7.1.32}$$

with

$$\ell_i = \frac{\rho_0 a_0^3 \tau_i}{\beta p_i}. \tag{7.1.33}$$

Since this theory assumes a linear relationship between the pressure and the fluid velocity the expression for τ given by (7.1.32) is equivalent to the more usual expression in terms of the pressure;

$$\tau = \frac{-p}{\partial p/\partial t} \tag{7.1.34}$$

evaluated at the shock.

Rogers compares his solution with both the results of the Kirkwood-Bethe theory and the experimental data of Arons and that presented in Cole's book. The expression for the peak pressure is in excellent agreement with the Kirkwood-Bethe theory and the experimentally determined relation of (7.1.2). The expression for the time constant compares well with that predicted by the Kirkwood-Bethe theory, but the agreement with (7.1.3) is not so good. As noted by Rogers, however, the available data for the time constant exhibits a considerable amount of scatter and the agreement between various experiments is not good. In particular, data from experiments for small charge weights, and consequently very weak shocks, is not even in approximate agreement with the empirical relation (Osborne and Taylor, 1946; Poché, 1972). This is no doubt partly due to the considerable experimental difficulty in obtaining accurate measurements of the time constant.

Both of the theoretical treatments discussed are valuable contributions to the study of underwater blast. A particular restriction that is a feature of both is the limitation to propagation of spherical waves. Neither offers a description of the interaction of an underwater blast wave with any structure, and it is this question we wish to address here. A method particularly suited to the study of problems of shock interaction with structures of quite general geometry is the theory of geometrical shock dynamics developed by Whitham (1957). Thus in the next section we review the elements of this theory, as formulated for the propagation of shocks in gases, and give consideration to its applicability to propagation of the shock produced by an underwater explosion. The theories discussed above must form the basis for the validation of any theory of propagation that we might develop.

7.2. Geometrical shock dynamics

Geometrical shock dynamics is the name given to the theory, due to Whitham (1957, 1959), for determining the motion of a shock wave, independently of deter-

mining the flow field behind the shock. Development of the theory proceeds by considering the motion of a shock wave down a tube of slowly varying cross section $A(x)$. Linearisation of the equations of motion about the assumed uniform initial state behind the shock allows their immediate integration. By substituting for the flow quantities in the equation for the forward propagating (C_+) characteristic in terms of their values at the shock (written as functions of the Mach number via the shock jump conditions), an expression is obtained relating the Mach number, M, to the local cross sectional area, A, of the tube. This is the so called A-M relation.

It is this A-M relation that is the basis for the theory of geometrical shock dynamics. If a shock is propagating into a uniform gas at rest then we may introduce rays normal to the shock front and suppose that each small element of the shock is propagated down a tube whose boundaries are defined by the rays. Application of the A-M relation to this elementary tube allows determination of the changes in M as the shock propagates. The details of the development of this theory may be found in the above references or in Whitham (1974). Geometrical shock dynamics has proved to give excellent results in a wide variety of examples. Comparisons with known solutions show remarkable accuracy and when implemented numerically (Henshaw et al., 1986) is a very versatile tool indeed. That the theory should achieve such success is not clear, for the A-M relation is not deduced as a formal approximation to the equations of motion. This aspect is worthy of further discussion but it is helpful to first review the derivation of the A-M relation, following Whitham (1957, 1974).

Suppose that a shock propagates down a tube of slowly varying cross section, with the cross sectional area, $A(x)$, being given as a function of x, the distance propagated down the tube. For $x < 0$ the tube is supposed to be uniform and we write

$$A(x) = A_0 \quad \text{for} \quad x < 0, \tag{7.2.1}$$

with A_0 constant. That the tube is slowly varying in the neighbourhood of $x = 0$

is expressed by the relation

$$|A(x) - A_0| / A_0 << 1. \tag{7.2.2}$$

Averaging the equations of inviscid compressible flow across the tube we obtain a set of equations dependent only upon the one spatial variable x,

$$\partial_t \rho + u\partial_x \rho + \rho \partial_x u + \rho u A'(x)/A(x) = 0, \tag{7.2.3}$$

$$\partial_t u + u\partial_x u + \partial_x p/\rho = 0, \tag{7.2.4}$$

$$\partial_t p + u\partial_x p - a^2 (\partial_t \rho + u\partial_x \rho) = 0. \tag{7.2.5}$$

The time variable is denoted by t and ∂_t and ∂_x denote respectively partial time and space derivatives. We shall suppose that the shock propagates into a uniform medium at rest, characterised by a density and sound speed of ρ_0 and a_0 respectively. We shall furthermore suppose that the fluid is polytropic and thus the sound speed is given everywhere as

$$a^2 = \gamma p/\rho, \tag{7.2.6}$$

where for an ideal gas γ is the ratio of specific heats.

With the Mach number defined by (7.1.5) the Rankine-Hugoniot relations for the jumps in the flow quantities at the shock (equations (7.1.21) - (7.1.23)) may be written as

$$u = \frac{2a_0}{\gamma + 1} \left(M - \frac{1}{M} \right), \tag{7.2.7}$$

$$p = \frac{\rho_0 a_0^2}{\gamma(\gamma + 1)} \left(2\gamma M^2 - (\gamma - 1) \right), \tag{7.2.8}$$

$$\rho = \frac{\rho_0 (\gamma + 1) M^2}{(\gamma - 1) M^2 + 2}, \tag{7.2.9}$$

and although a is given by (7.2.6) it is convenient to introduce

$$\mu^2 = \frac{(\gamma - 1) M^2 + 2}{2\gamma M^2 - (\gamma - 1)}, \tag{7.2.10}$$

in which case we write

$$a = \frac{a_0 \mu \left(2\gamma M^2 - (\gamma - 1) \right)}{(\gamma + 1) M}. \tag{7.2.11}$$

In the above, values of u, p, ρ and a are those immediately behind the shock.

In the problem at hand, it is assumed that the physical conditions a large distance behind $x = 0$ are such as to maintain an initially uniform flow in the region $x < 0$, characterised by a sound speed, density and particle velocity of a_1, ρ_1 and u_1 respectively. In order to obtain a solution of (7.2.3) - (7.2.5) for $x > 0$ we linearise the equations of motion about the initially uniform state in $x < 0$, as the tube is slowly varying. The linearised equations are

$$\partial_t \rho + u_1 \partial_x \rho + \rho_1 \partial_x u + \rho_1 u_1 A'(x)/A_0 = 0, \tag{7.2.12}$$

$$\partial_t u + u_1 \partial_x u + \partial_x p/\rho_1 = 0, \tag{7.2.13}$$

$$\partial_t p + u_1 \partial_x p - a_1^2 (\partial_t \rho + u_1 \partial_x \rho) = 0. \tag{7.2.14}$$

In the above ρ, p, u and $A'(x)$ respectively represent $\rho - \rho_1$, $p - p_1$, $u - u_1$, and $(A(x) - A_0)'$. These equations may be routinely cast into characteristic form, whence they become

$$C_+ : \{\partial_t + (u_1 + a_1)\partial_x\}(p + \rho_1 a_1 u) + \rho_1 a_1^2 u_1 A'(x)/A_0 = 0, \tag{7.2.15}$$

$$C_- : \{\partial_t + (u_1 - a_1)\partial_x\}(p - \rho_1 a_1 u) + \rho_1 a_1^2 u_1 A'(x)/A_0 = 0, \tag{7.2.16}$$

$$P : \{\partial_t + u_1 \partial_x\}(p - a_1^2 \rho) = 0, \tag{7.2.17}$$

with C_+, C_- and P denoting the characteristic trajectories. Immediate integration yields

$$(p - p_1) + \rho_1 a_1 (u - u_1) = \frac{-\rho_1 a_1^2 u_1}{u_1 + a_1} \frac{A(x) - A_0}{A_0} + F(x - (u_1 + a_1)t), \tag{7.2.18}$$

$$(p - p_1) - \rho_1 a_1 (u - u_1) = \frac{-\rho_1 a_1^2 u_1}{u_1 - a_1} \frac{A(x) - A_0}{A_0} + G(x - (u_1 - a_1)t), \tag{7.2.19}$$

$$(p - p_1) - a_1^2 (\rho - \rho_1) = H(x - u_1 t), \tag{7.2.20}$$

with F, G and H arbitrary functions that must be determined from the initial conditions of the problem and the boundary conditions at the shock. A crucial point in the derivation is that F must be identically zero. That this is so we deduce from the fact that the C_+ characteristics, approximated by the straight lines $x - (u_1 + a_1)t =$ constant < 0, originate in the uniform region.

We proceed from (7.2.18) to the A-M relation. If we denote by M_0 the Mach number of the shock upon entering the non-uniform part of the tube, and by M the Mach number after the shock has travelled some small distance x into the non-uniform part, then we may write the change in pressure and particle velocity at the shock as

$$p - p_1 = \left.\frac{dp}{dM}\right|_{M_0} (M - M_0), \quad u - u_1 = \left.\frac{du}{dM}\right|_{M_0} (M - M_0), \tag{7.2.21}$$

with equations (7.2.7) and (7.2.8) giving $u(M)$ and $p(M)$ at the shock front. Substituting (7.2.21) into (7.2.18), writing u_1, p_1, a_1 and ρ_1 in terms of M_0 via the shock jump conditions, and some algebraic manipulation yields

$$\frac{A(x) - A_0}{A_0} = -g(M_0)(M - M_0), \tag{7.2.22}$$

with

$$g(M) = \frac{M}{M^2 - 1}\left(1 + \frac{2}{\gamma + 1}\frac{1 - \mu^2}{\mu}\right)\left(1 + 2\mu + \frac{1}{M^2}\right). \tag{7.2.23}$$

Supposing that propagation over large distances accumulates finite changes in A, we divide the tube into small elements in order that (7.2.22) may be applied to each of these. Although propagation over a finite distance will render the assumed conditions upon entry to an element (uniform state behind the shock) as incorrect, neglect of this and application of (7.2.22) in the limit of infinite subdivision yields the differential equation

$$\frac{1}{A}\frac{dA}{dM} = -g(M). \tag{7.2.24}$$

Integrating we obtain the A-M relation.

It is this relation that is the basis for the theory of geometrical shock dynamics. For details of the mathematical formalism of geometrical shock dynamics the reader is referred to Whitham (1974). This formalism is advantageous from a number of viewpoints. The A-M relation allows the motion of the shock to be computed independently of a determination of the whole of the flow field, a fact which significantly reduces the computational effort over more usual approaches. Furthermore, the dependence of the Mach number upon the area, A, emphasises the

effect of the geometry in which the shock propagates and thus the method is ideal for computing the diffraction of shocks by rigid structures. Analytical solutions for some problems of shock diffraction have been presented by Whitham (1957, 1959) and more general examples have been numerically treated by Henshaw et al. (1986).

The only point in the derivation of the A-M relation that the physical properties of the material in which the shock propagates enter into the development is via the equation of state. The crucial role of the equation of state is in determining the physical quantities immediately behind the shock in terms of the Mach number via the shock jump conditions. In order then to apply the theory, as formulated, to propagation in water it is simply a matter of choosing an appropriate equation of state. The Tait equation of state, discussed in section 7.1, is appropriate for water in the regime of the pressures induced by the passage of an explosively generated shock and using this in the Rankine-Hugoniot jump conditions we find that the expressions of (7.2.7) - (7.2.11) are unchanged, except for the expression for the pressure which becomes

$$p + \pi = \frac{a_0^2 \rho_0}{\gamma(\gamma+1)} \left(2\gamma M^2 - (\gamma - 1)\right), \tag{7.2.25}$$

and the relationship between the sound speed, pressure and density has been noted in (7.1.13). The remainder of the analysis carries through exactly and the A-M relation is given by (7.2.24) with g as given by (7.2.23) and the change of material is embodied in the change in the value of γ.

The motion of shocks in water may then be computed according to the theory of geometrical shock dynamics, but we make the following point. The derivation of the A-M relation proceeds from an assumed initial state behind the shock that is uniform. In the case of the propagation of an underwater blast wave it is clear that this is not so, as evidenced by the exponential character of the pressure decay upon passage of the shock. Due to this non-uniformity in the flow conditions behind the shock we might suppose that the effect of disturbances behind the shock, that

catch up with and modify its motion, is significant. This effect is unaccounted for in the theory of Whitham.

In any case, for propagation in gases the accuracy of the A-M relation has been verified by comparison with a variety of known solutions and, in many cases, the agreement is remarkable. That the accuracy should be so good is not clear. For a full discussion of these comparisons and accuracy related matters the work of Whitham (1958, 1974) should be consulted but the crucial point is as follows. The technique for determining the A-M relation has been neatly described by Whitham as the characteristic rule. This involves substituting for the flow quantities in the equation for the C_+ characteristic in terms of their values at the shock, given as a function of M. The resultant equation gives the variation of M with x (and hence A, as A is a function of x). This is exactly what was done to proceed from equation (7.2.18) to the A-M relation. For the case of propagation down a tube of slowly varying cross section the C_+ characteristic equation is

$$\frac{\partial_t p}{u+a} + \partial_x p + \rho a \left(\frac{\partial_t u}{u+a} + \partial_x u \right) + \frac{\rho a^2 u}{u+a} A'(x)/A(x) = 0, \tag{7.2.26}$$

and the success of the characteristic rule involves this being a good approximation when applied at the shock, that is

$$\frac{\partial_t p}{U} + \partial_x p + \rho a \left(\frac{\partial_t u}{U} + \partial_x u \right) + \frac{\rho a^2 u}{u+a} A'(x)/A(x) = 0 \tag{7.2.27}$$

is well satisfied at the shock. Combining results Whitham deduces that the accuracy of the approximation is based upon the smallness of

$$\left(\frac{1}{U} - \frac{1}{a+u} \right) (\partial_t p + \rho a \partial_t u) \tag{7.2.28}$$

at the shock. Although $(u + a - U)/U$ is zero for $M = 1$, it tends to 0.274 as the Mach number increases to ∞. The characteristic rule thus works well because the second term in (7.2.28) is small at the shock, that is

$$\frac{\partial_t p + \rho a \partial_t u}{\partial_t p} << 1 \tag{7.2.29}$$

at the shock. Whitham notes that in the small perturbation solution used to derive the A-M relation this is indeed the case.

Although the small perturbation solution provides some justification, no really satisfactory explanation has been found for the success of the method. In fact, application of the C_+ characteristic equation at the shock is seen to be somewhat ad-hoc. This consideration and the concern with the influence of non-uniform flow conditions behind the shock provide the motivation for a reconsideration of the propagation of a shock down a tube of slowly varying cross section, the problem that is at the heart of the theory of geometrical shock dynamics.

8

RECONSIDERATION OF GEOMETRICAL SHOCK DYNAMICS

In this chapter we reconsider the propagation of a shock down a tube of slowly varying cross section, the problem that is at the heart of the theory of geometrical shock dynamics. We shall establish that the motion can be described by an infinite sequence of equations and shall furthermore demonstrate that by a process of truncation this sequence can be closed, so that with initial conditions prescribed we can proceed to a solution of the equations. Criteria for the convergence of the closure scheme may be established and in later parts we will truncate at the first, second and third equations in order to perform calculations for physical problems, the results of which validate the approach.

8.1. Shock propagation down a tube of slowly varying cross section

We begin by writing the equations of gas dynamics (equations (7.2.3) - (7.2.5)) in characteristic form. They become

$$C_+ : \quad \partial_t p + (u+a)\partial_x p + \rho a\,(\partial_t u + (u+a)\partial_x u) = -\rho a^2 u A'/A, \tag{8.1.1}$$

$$C_- : \quad \partial_t p + (u-a)\,\partial_x p - \rho a\,(\partial_t u + (u-a)\partial_x u) = -\rho a^2 u A'/A, \tag{8.1.2}$$

$$P : \quad \partial_t p + u\partial_x p - a^2\,(\partial_t \rho + u\partial_x \rho) = 0. \tag{8.1.3}$$

We let S denote the trajectory of the shock, and it is given by

$$S : \quad \dot{x} = a_0 M. \tag{8.1.4}$$

In what follows all total time derivatives, denoted by d_t, will be considered as along the shock so that

$$d_t \equiv \partial_t + a_0 M \partial_x. \tag{8.1.5}$$

In the case of the ratio A'/A, which is only a function of x, we have

$$d_t\,(d_x^n(A'/A)) = a_0 M d_x^{n+1}(A'/A), \tag{8.1.6}$$

with d_x denoting the derivative with respect to x.

We require a number of relations, the crucial ones being that, for ρ, p, u and a having continuous derivatives of all orders, we have on S

$$d_t p + \rho a d_t u = -\left[a_0 M \frac{\rho a^2 u}{a+u} A'/A + \left(\frac{a_0 M}{a+u} - 1\right)(\partial_t p + \rho a \partial_t u)\right], \tag{8.1.7}$$

and

$$\begin{aligned} d_t\left(\partial_t^n(\partial_t p + \rho a \partial_t u)\right) = &-\left[a_0 M \partial_t^{n+1}\left(\frac{\rho a^2 u}{a+u}\right) A'/A\right. \\ &+ a_0 M \sum_{i=1}^{n+1} \binom{n+1}{i} \partial_t^i \left(\frac{1}{a+u}\right) \partial_t^{n+1-i}(\partial_t p + \rho a \partial_t u) \\ &\left. + a_0 M \partial_t^n\left(\partial_t(\rho a)\partial_x u - \partial_x(\rho a)\partial_t u\right) + \left(\frac{a_0 M}{a+u} - 1\right)\partial_t^{n+1}(\partial_t p + \rho a \partial_t u)\right], \quad n \geq 0. \end{aligned} \tag{8.1.8}$$

To establish (8.1.7) we note that

$$d_t p + \rho a d_t u = \partial_t p + \rho a \partial_t u + a_0 M\left(\partial_x p + \rho a \partial_x u\right). \tag{8.1.9}$$

From (8.1.1) we have

$$\partial_x p + \rho a \partial_x u = -\frac{1}{a+u}(\partial_t p + \rho a \partial_t u + \rho a^2 u A'/A), \tag{8.1.10}$$

and substitution into (8.1.9) yields the result. We proceed rapidly to (8.1.8) as follows. Since ρ, p, u and a have continuous derivatives of all orders we have

$$\partial_x \partial_t^n(\partial_t p + \rho a \partial_t u) = \partial_x \partial_t^n \partial_t p + \partial_t^n(\rho a \partial_t \partial_x u) + \partial_t^n\left(\partial_x(\rho a)\partial_t u\right). \tag{8.1.11}$$

Noting that

$$\partial_t^{n+1}\left(\partial_x p + \rho a \partial_x u\right) = \partial_t^{n+1}\partial_x p + \partial_t^n(\rho a \partial_x \partial_t u) + \partial_t^n(\partial_t(\rho a)\partial_x u), \tag{8.1.12}$$

(8.1.11) becomes

$$\partial_x \partial_t^n(\partial_t p + \rho a \partial_t u) = \partial_t^{n+1}(\partial_x p + \rho a \partial_x u) + \partial_t^n(\partial_x(\rho a)\partial_t u - \partial_t(\rho a)\partial_x u). \tag{8.1.13}$$

Now

$$d_t(\partial_t^n(\partial_t p + \rho a \partial_t u)) = \partial_t^{n+1}(\partial_t p + \rho a \partial_t u) + a_0 M \partial_x \partial_t^n(\partial_t p + \rho a \partial_t u), \tag{8.1.14}$$

which, upon use of (8.1.13), becomes

$$\begin{aligned} d_t(\partial_t^n(\partial_t p + \rho a \partial_t u)) = &\partial_t^{n+1}(\partial_t p + \rho a \partial_t u) + a_0 M \partial_t^{n+1}(\partial_x p + \rho a \partial_x u) \\ &+ a_0 M \partial_t^n(\partial_x(\rho a)\partial_t u - \partial_t(\rho a)\partial_x u). \end{aligned} \tag{8.1.15}$$

With the help of (8.1.10) the result follows. We will also need a set of results that relate partial time and space derivatives of the physical quantities p, u, ρ and a at the shock to partial time and space derivatives of lower order and to total time derivatives of partial derivatives of one lower order at the shock. Presentation of the results at this stage will render later results transparent.

We begin by taking $\partial_x^n \partial_t^m$ of each of the equations (8.1.1) - (8.1.3). Noting that

$$\partial_x^n \partial_t^m (AB) = \sum_{i=0}^{n} \sum_{j=0}^{m} \binom{n}{i} \binom{m}{j} \partial_x^i \partial_t^j A \partial_x^{n-i} \partial_t^{m-j} B \tag{8.1.16}$$

for continuously differentiable functions A and B, (8.1.1) - (8.1.3) yield respectively

$$\partial_x^n \partial_t^{m+1} p + (u+a)\partial_x^{n+1} \partial_t^m p + \rho a \partial_x^n \partial_t^{m+1} u + \rho a (u+a) \partial_x^{n+1} \partial_t^m u = -f_1^{n,m}, \tag{8.1.17}$$

$$\partial_x^n \partial_t^{m+1} p + (u-a)\partial_x^{n+1} \partial_t^m p - \rho a \partial_x^n \partial_t^{m+1} u - \rho a (u-a) \partial_x^{n+1} \partial_t^m u = -f_2^{n,m}, \tag{8.1.18}$$

$$\partial_x^n \partial_t^{m+1} p + u \partial_x^{n+1} \partial_t^m p - a^2 \partial_x^n \partial_t^{m+1} \rho - a^2 u \partial_x^{n+1} \partial_t^m \rho = -f_3^{n,m}, \tag{8.1.19}$$

where

$$\begin{aligned} f_1^{n,m} = \sum_{\substack{i=0 \\ i,j \neq 0,0}}^{n} \sum_{j=0}^{m} \binom{n}{i} \binom{m}{j} \Big(& \partial_x^i \partial_t^j (u+a) \partial_x^{n-i+1} \partial_t^{m-j} p \\ & + \partial_x^i \partial_t^j (\rho a) \partial_x^{n-i} \partial_t^{m-j+1} u + \partial_x^i \partial_t^j \left(\rho a (u+a)\right) \partial_x^{n-i+1} \partial_t^{m-j} u \Big) + \partial_x^n \partial_t^m (\rho a^2 u A'/A), \end{aligned} \tag{8.1.20}$$

$$\begin{aligned} f_2^{n,m} = \sum_{\substack{i=0 \\ i,j \neq 0,0}}^{n} \sum_{j=0}^{m} \binom{n}{i} \binom{m}{j} \Big(& \partial_x^i \partial_t^j (u-a) \partial_x^{n-i+1} \partial_t^{m-j} p \\ & - \partial_x^i \partial_t^j (\rho a) \partial_x^{n-i} \partial_t^{m-j+1} u - \partial_x^i \partial_t^j \left(\rho a (u-a)\right) \partial_x^{n-i+1} \partial_t^{m-j} u \Big) + \partial_x^n \partial_t^m (\rho a^2 u A'/A), \end{aligned} \tag{8.1.21}$$

$$\begin{aligned} f_3^{n,m} = \sum_{\substack{i=0 \\ i,j \neq 0,0}}^{n} \sum_{j=0}^{m} \binom{n}{i} \binom{m}{j} \Big(& \partial_x^i \partial_t^j u \partial_x^{n-i+1} \partial_t^{m-j} p \\ & - \partial_x^i \partial_t^j (a^2) \partial_x^{n-i} \partial_t^{m-j+1} \rho - \partial_x^i \partial_t^j \left(a^2 u\right) \partial_x^{n-i+1} \partial_t^{m-j} \rho \Big). \end{aligned} \tag{8.1.22}$$

The crucial point to note is that the functions $f_\ell^{n,m} (\ell = 1,2,3)$ depend upon derivatives of p, u, ρ and a of order $\leq n+m$.

Along the trajectory of the shock we have

$$d_t \left(\partial_x^n \partial_t^m p\right) = \partial_x^n \partial_t^{m+1} p + a_0 M \partial_x^{n+1} \partial_t^m p, \tag{8.1.23}$$

$$d_t \left(\partial_x^n \partial_t^m u\right) = \partial_x^n \partial_t^{m+1} u + a_0 M \partial_x^{n+1} \partial_t^m u, \tag{8.1.24}$$

$$d_t\left(\partial_x^n\partial_t^m\rho\right) = \partial_x^n\partial_t^{m+1}\rho + a_0M\partial_x^{n+1}\partial_t^m\rho. \tag{8.1.25}$$

Using equations (8.1.17) - (8.1.19) and (8.1.23) - (8.1.25) we can obtain expressions for

$$\partial_x^n\partial_t^{m+1}p,\ \partial_x^{n+1}\partial_t^m p,\ \partial_x^n\partial_t^{m+1}u,\ \partial_x^{n+1}\partial_t^m u,\ \partial_x^n\partial_t^{m+1}\rho,\ \partial_x^{n+1}\partial_t^m\rho \tag{8.1.26}$$

at the shock. Routine algebraic manipulation yields

$$\begin{aligned}\partial_x^n\partial_t^{m+1}p = \Big[&\left(a^2+u(a_0M-u)\right)d_t\left(\partial_x^n\partial_t^m p\right) + a_0M\rho a^2 d_t\left(\partial_x^n\partial_t^m u\right)\\ &+\frac{1}{2}a_0M(a+a_0M-u)f_1^{n,m} - \frac{1}{2}a_0M(a-a_0M+u)f_2^{n,m}\Big]/\left(a^2-(a_0M-u)^2\right),\end{aligned} \tag{8.1.27}$$

$$\begin{aligned}\partial_x^{n+1}\partial_t^m p = \Big[&-(a_0M-u)\,d_t\left(\partial_x^n\partial_t^m p\right) - \rho a^2 d_t\left(\partial_x^n\partial_t^m u\right)\\ &-\frac{1}{2}(a+a_0M-u)f_1^{n,m} + \frac{1}{2}(a-a_0M+u)f_2^{n,m}\Big]/\left(a^2-(a_0M-u)^2\right),\end{aligned} \tag{8.1.28}$$

$$\begin{aligned}\partial_x^n\partial_t^{m+1}u = \Big[&\frac{a_0M}{\rho}d_t\left(\partial_x^n\partial_t^m p\right) + (a^2+u(a_0M-u))d_t\left(\partial_x^n\partial_t^m u\right)\\ &+\frac{a_0M}{2\rho a}(a+a_0M-u)f_1^{n,m} + \frac{a_0M}{2\rho a}(a-a_0M+u)f_2^{n,m}\Big]/(a^2-(a_0M-u)^2),\end{aligned} \tag{8.1.29}$$

$$\begin{aligned}\partial_x^{n+1}\partial_t^m u = \Big[&-\frac{1}{\rho}d_t\left(\partial_x^n\partial_t^m p\right) - (a_0M-u)d_t\left(\partial_x^n\partial_t^m u\right)\\ &-\frac{1}{2\rho a}(a+a_0M-u)f_1^{n,m} - \frac{1}{2\rho a}(a-a_0M+u)f_2^{n,m}\Big]/(a^2-(a_0M-u)^2),\end{aligned} \tag{8.1.30}$$

$$\begin{aligned}\partial_x^n\partial_t^{m+1}\rho = \Big[&a_0Ma^2 d_t\left(\partial_x^n\partial_t^m p\right) + a_0M\rho a^2(a_0M-u)d_t\left(\partial_x^n\partial_t^m u\right)\\ &-a^2u(a^2-(a_0M-u)^2)d_t\left(\partial_x^n\partial_t^m\rho\right) + \frac{1}{2}a_0M(a_0M-u)(a+a_0M-u)f_1^{n,m}\\ &-\frac{1}{2}a_0M(a_0M-u)(a-a_0M+u)f_2^{n,m} + a_0M(a^2-(a_0M-u)^2)f_3^{n,m}\Big]\\ &/(a^2(a_0M-u)(a^2-(a_0M-u)^2)),\end{aligned} \tag{8.1.31}$$

$$\begin{aligned}\partial_x^{n+1}\partial_t^m\rho = \Big[&-a^2d_t\left(\partial_x^n\partial_t^m p\right) - \rho a^2(a_0M-u)d_t\left(\partial_x^n\partial_t^m u\right)\\ &+a^2(a^2-(a_0M-u)^2)d_t\left(\partial_x^n\partial_t^m\rho\right) - \frac{1}{2}(a_0M-u)(a+a_0M-u)f_1^{n,m}\\ &+\frac{1}{2}(a_0M-u)(a-a_0M+u)f_2^{n,m} - (a^2-(a_0M-u)^2)f_3^{n,m}\Big]\\ &/(a^2(a_0M-u)(a^2-(a_0M-u)^2)).\end{aligned} \tag{8.1.32}$$

We can deduce expressions for $\partial_x^{n+1}\partial_t^m a$ and $\partial_x^n\partial_t^{m+1}a$ by noting that $a^2 = \gamma p/\rho$. At this point, note that the expressions for the quantities of (8.1.26) involve derivatives of p, u, ρ and a of order $\leq n+m$ as well as the rate of change of $\partial_x^n\partial_t^m p$, $\partial_x^n\partial_t^m u$ and $\partial_x^n\partial_t^m \rho$ following the shock.

To proceed we require some further notation. Let us set

$$\begin{aligned} Q_0 &= M, \\ Q_n &= \partial_t^{n-1}(\partial_t p + \rho a \partial_t u), \quad n = 1, 2, \ldots, \end{aligned} \tag{8.1.33}$$

evaluated at the shock, and write the functions $\partial_x^i\partial_t^j p$, $\partial_x^i\partial_t^j u$ and $\partial_x^i\partial_t^j \rho$ as p_{ij}, u_{ij} and ρ_{ij} when evaluated at the shock front. We will establish by induction that on S, the shock trajectory

$$d_t Q_k = d_t Q_k \left(Q_0, \ldots, Q_{k+1}, A'/A, \ldots, d_x^{k-1}(A'/A)\right), \tag{8.1.34}$$

and

$$\begin{aligned} \partial_x^i\partial_t^j p &= p_{ij}\left(Q_0, \ldots, Q_k, A'/A, \ldots, d_x^{k-1}(A'/A)\right), \\ \partial_x^i\partial_t^j u &= u_{ij}\left(Q_0, \ldots, Q_k, A'/A, \ldots, d_x^{k-1}(A'/A)\right), \\ \partial_x^i\partial_t^j \rho &= \rho_{ij}\left(Q_0, \ldots, Q_k, A'/A, \ldots, d_x^{k-1}(A'/A)\right), \quad i+j = k, \end{aligned} \tag{8.1.35}$$

for $i, j \geq 0$, $k = 1, 2, \ldots$, and that for $k = 0$ we have

$$d_t Q_0 = d_t Q_0(Q_0, Q_1, A'/A), \tag{8.1.36}$$

and

$$\partial_x^i\partial_t^j p = p_{ij}(Q_0),\ \partial_x^i\partial_t^j u = u_{ij}(Q_0),\ \partial_x^i\partial_t^j \rho = \rho_{ij}(Q_0),\ i = j = 0. \tag{8.1.37}$$

For all k the dependence upon Q_ℓ ($\ell = 0, 1, 2, \ldots$) as reflected by (8.1.34) and (8.1.35) is correct. The dependence upon A'/A and its derivatives is secondary since we assume this function to be known. We make the distinction of the case $k = 0$ for completeness.

Let us suppose that $k = 0$. Then the shock jump conditions (equations (7.2.7) - (7.2.9)) give p, u and ρ at the shock as functions of M ($\equiv Q_0$). Hence we write

$$p = p_{00}(Q_0),\ u = u_{00}(Q_0),\ \rho = \rho_{00}(Q_0), \tag{8.1.38}$$

at the shock. Noting that

$$d_t \equiv d_t Q_0 d_{Q_0}, \tag{8.1.39}$$

(d_{Q_0} denotes a derivative with respect to Q_0) equation (8.1.7) gives

$$(d_{Q_0}p + \rho a d_{Q_0}u) d_t Q_0 = -\left[a_0 Q_0 \frac{\rho a^2 u}{a+u} A'/A + \left(\frac{a_0 Q_0}{a+u} - 1\right) Q_1\right]. \tag{8.1.40}$$

Evaluation of $d_{Q_0}p$ and $d_{Q_0}u$ via (8.1.38) and substitution in (8.1.40) for p, u, ρ and a as functions of Q_0 allows us to write

$$d_t Q_0 = d_t Q_0(Q_0, Q_1, A'/A). \tag{8.1.41}$$

Thus (8.1.36) and (8.1.37) are established. Now let us suppose that (8.1.34) and (8.1.35) are true for some $k > 0$. Slight modification is needed if we begin with (8.1.36) and (8.1.37) as being true and this will be indicated as the proof proceeds. Consider some set i, j such that $i + j = k$ and consider $\partial_x^i \partial_t^{j+1} p$, an expression for which is given by (8.1.27). We have already noted that all partial derivatives in this expression are of order $\leq i + j = k$. Hence by our induction hypothesis we can write them as functions of $Q_0, \ldots, Q_k, A'/A, \ldots, d_x^{k-1}(A'/A)$. If $k = 0$ then the expression of (8.1.26) involves only the physical quantities p, u, ρ and a themselves which can be written as functions of Q_0 alone. We must consider the expressions $d_t\left(\partial_x^i \partial_t^j p\right)$ and $d_t\left(\partial_x^i \partial_t^j u\right)$. Consider $d_t\left(\partial_x^i \partial_t^j p\right)$. By the induction hypothesis we have at the shock

$$\partial_x^i \partial_t^j p = p_{ij}\left(Q_0, \ldots, Q_k, A'/A, \ldots, d_x^{k-1}(A'/A)\right). \tag{8.1.42}$$

Now at S

$$\begin{aligned} d_t\left(\partial_x^i \partial_t^j p\right) &= \partial_{Q_0} p_{ij} d_t Q_0 + \ldots + \partial_{Q_k} p_{ij} d_t Q_k + \\ & a_0 M \partial_{(A'/A)} p_{ij} d_x(A'/A) + \ldots + a_0 M \partial_{(d_x^{k-1}(A'/A))} p_{ij} d_x^k(A'/A), \end{aligned} \tag{8.1.43}$$

having made use of (8.1.6). Noting that the induction hypothesis gives $d_t Q_k = d_t Q_k(Q_0, \ldots, Q_{k+1}, A'/A, \ldots, d_x^{k-1}(A'/A))$, we see that $d_t\left(\partial_x^i \partial_t^j p\right)$ is a function of $Q_0, \ldots, Q_{k+1}, A'/A, \ldots, d_x^k(A'/A)$. The consideration of $d_t\left(\partial_x^i \partial_t^j u\right)$ follows exactly as above. Thus we can write

$$\partial_x^i \partial_t^{j+1} p = p_{ij+1}\left(Q_0, \ldots, Q_{k+1}, A'/A, \ldots, d_x^k(A'/A)\right). \tag{8.1.44}$$

Repetition of this argument establishes (8.1.35) for $k+1$. If $k = 0$ then, for example, we have at the shock $d_t p = d_{Q_0} p_{00} d_t Q_0$, which is, using (8.1.36), a function of Q_0, Q_1, and A'/A. Substitution into the expression of (8.1.27) for $\partial_t p$ then allows us to write $\partial_t p = p_{01}(Q_0, Q_1, A'/A)$ which is of the form expressed in (8.1.35) for $k = 1$. To establish the final part of the result we rewrite (8.1.8) using the notation of (8.1.33), whence it becomes

$$\begin{aligned} d_t Q_{k+1} = -\Bigg[& a_0 Q_0 \partial_t^{k+1}\left(\frac{\rho a^2 u}{a+u}\right) A'/A + a_0 Q_0 \sum_{i=1}^{k+1} \binom{k+1}{i} \partial_t^i \left(\frac{1}{a+u}\right) Q_{k-i+2} \\ & + a_0 Q_0 \partial_t^k \left(\partial_t(\rho a)\partial_x u - \partial_x(\rho a)\partial_t u\right) + \left(\frac{a_0 Q_0}{a+u} - 1\right) Q_{k+2} \Bigg], \end{aligned} \tag{8.1.45}$$

an expression in which we note that there is dependence upon derivatives of p, u, ρ and a of order $\leq k+1$. These derivatives in turn depend upon $Q_0, \ldots, Q_{k+1}$, $A'/A, \ldots,$ $d_x^k(A'/A)$, so we write

$$d_t Q_{k+1} = d_t Q_{k+1}\left(Q_0, \ldots, Q_{k+2}, A'/A, \ldots, d_x^k(A'/A)\right), \tag{8.1.46}$$

and the result is established. If $k = 0$ then we have noted above that the first order derivatives of p, u, ρ and a depend upon Q_0, Q_1, and A'/A and so the expression of (8.1.34) is deduced to be true for $k = 1$.

Having established the validity of (8.1.34) and (8.1.36) we make the following observation. The expression for $d_t Q_k$ depends upon Q_{k+1}, so that each differential equation in the sequence described by (8.1.34) and (8.1.36) is coupled to its successor. Noting the definition of Q_k it is clear that the coupling is via a term containing derivatives of one order higher than all other terms in that equation. By truncation of the term involving Q_{N+1}, for some $N \geq 0$, we obtain $N+1$ nonlinear coupled differential equations in the $N+1$ variables $Q_0, \ldots, Q_N$ and provision of initial conditions renders the problem of their solution as well posed. All the coefficient functions in the resultant equations are expected to be differentiable so that the existence of unique solutions is expected. The question of the existence and uniqueness of solutions is, however, beyond the scope of this work, but examination in the next sections of the systems obtained from choosing $N = 0$ and $N = 1$

reveals soluble equations. Once the function $Q_0 (\equiv M)$ is known, the motion of the shock is determined.

8.2. Truncation at the first and second equation

Consider truncation at the first equation, given by (8.1.36). The explicit form of this expression is given by (8.1.40) and rewriting Q_0 as M and Q_1 as $\partial_t p + \rho a \partial_t u$ we have

$$(d_M p + \rho a d_M u)\, d_t M = -\left[a_0 M \frac{\rho a^2 u}{a+u} A'/A + \left(\frac{a_0 M}{a+u} - 1\right)(\partial_t p + \rho a \partial_t u)\right]. \tag{8.2.1}$$

Truncation of the term involving $\partial_t p + \rho a \partial_t u$ and use of (7.2.7) - (7.2.11) in determination of the coefficients of $d_t M$ and A'/A yields

$$d_t M = \frac{-a_0 M}{g(M)} A'/A, \tag{8.2.2}$$

with $g(M)$ given by (7.2.23). Noting that

$$d_t M = d_A M d_x A d_t x = a_0 M A' d_A M, \tag{8.2.3}$$

we see that (8.2.2) becomes equation (7.2.24); the A-M relation.

We are now in a position to make a number of comments about the derivation of the A-M relation in the manner presented in section 7.2. The application of the characteristic rule corresponds simply to truncation of the term $\left(\frac{a_0 M}{a+u} - 1\right)(\partial_t p + \rho a \partial_t u)$. The rule is thus seen to provide an indication of the correct term to truncate in order to close the equations of propagation. We further note that the exact criterion that the A-M relation is a good approximation is that

$$a_0 M \frac{\rho a^2 u}{a+u} |A'/A| >> \left|\frac{a_0 M}{a+u} - 1\right| |\partial_t p + \rho a \partial_t u|. \tag{8.2.4}$$

The left hand side of this inequality gives a representative measure of the effect that the changing area has upon the propagation of the shock. The terms on the right hand side characterise the flow behind the shock. The expression $\left|\frac{a_0 M}{a+u} - 1\right|$ is a measure of the coincidence of the C_+ characteristic and the shock. For $M \to 1$ this term tends to zero, expressing the result that in the sonic limit the leading C_+

characteristic and the shock are coincident. In such a case modifying disturbances propagating along the characteristics do not meet the shock and hence have no influence upon its motion. As $M \to \infty$ this term tends to 0.215 (for $\gamma = 1.4$) indicating the differing trajectories of C_+ and S. In this limit disturbances on the C_+ characteristic overtake the shock and modify its motion. The term $\partial_t p + \rho a \partial_t u$ gives a measure of the non-uniformity of the flow behind the shock. If the state behind the shock is uniform, it has value zero. Hence we can say that the approximation is good when the effect of the geometry upon the shock is much more significant than that of the interaction with and non-uniformity of, the flow behind. We shall consider this quantitatively in later parts. The considerations of Whitham regarding the accuracy of the method have indicated the significance of the term $\left|\frac{a_0 M}{a+u} - 1\right| |\partial_t p + \rho a \partial_t u|$ (see equation (7.2.28)), however, by the process of truncation we have deduced a formal criterion, expressed in (8.2.4), that the theory is good.

Since we now have the facility to truncate at any equation we will truncate at the second equation in order to investigate the degree of improvement attainable. This will also give some indication if any value is to be obtained by truncating at higher equations in the sequence. We will now write $\partial_t p + \rho a \partial_t u$ as Q_1, in which case we have, from (8.1.8), for $n = 0$

$$\begin{aligned} d_t Q_1 = -\Bigg[& a_0 M \partial_t \left(\frac{\rho a^2 u}{a+u} \right) A'/A + a_0 M \partial_t \left(\frac{1}{a+u} \right) Q_1 + a_0 M (\partial_t(\rho a)\partial_x u - \\ & \partial_x(\rho a)\partial_t u) + \left(\frac{a_0 M}{a+u} - 1 \right) \partial_t Q_1 \Bigg]. \end{aligned} \tag{8.2.5}$$

Truncating the term involving $\partial_t Q_1$ ($\equiv Q_2$) gives the closed system of coupled non-linear differential equations

$$\begin{aligned} d_t M &= \frac{-a_0 M}{d_M p + \rho a d_M u} \left[\left(\frac{\rho a^2 u}{a+u} \right) A'/A + \left(\frac{1}{a+u} - \frac{1}{a_0 M} \right) Q_1 \right], \\ &= d_t M(M, Q_1, A'/A), \\ d_t Q_1 &= -a_0 M \left[\partial_t \left(\frac{\rho a^2 u}{a+u} \right) A'/A + \partial_t(\rho a)\partial_x u - \partial_x(\rho a)\partial_t u + \partial_t \left(\frac{1}{a+u} \right) Q_1 \right], \\ &= d_t Q_1(M, Q_1, A'/A). \end{aligned} \tag{8.2.6}$$

Expressions for the first order partial derivatives of p, u, ρ and a, evaluated at the

shock, are obtained from the results of section 8.1. Explicit formulae are shown in appendix 1 and these allow the functions $d_t M$ and $d_t Q_1$ to be evaluated.

Upon provision of the form of the function $A(x)$ and values M_0 and Q_{1_0} of M and Q_1 at $t = 0$, the problem of solution of the system of (8.2.6) is well posed. The differentiability of the functions $d_t M$ and $d_t Q_1$ guarantees the existence and uniqueness of solutions. Note at this point, that although we could formally write down the criterion that the approximation obtained by truncation at the second equation is good, the dependence of this criterion upon second order partial derivatives of flow quantities renders its interpretation as difficult. Due to the complexity of the system (8.2.6), we proceed to investigate shock propagation in a number of simple geometries before implementing the numerical scheme of geometrical shock dynamics. Comparison with observed phenomena and known solutions indicates the validity of the approach as well as allowing a quantitative determination of the inequality (8.2.4) to be made. Before this, however, we consider the convergence of the closure scheme.

8.3. Convergence of the closure scheme

The question of the convergence of the closure scheme presented in section 8.1 is significant and worthy of consideration. In this context we may prove the following result. Let us denote by $\tilde{Q}_0^{(N)}$ the approximation to Q_0 obtained by closing the system of (8.1.34) and (8.1.36) at the N+1'th equation. Supposing that Q_k is continuous for $k = 0, 1, 2, \ldots$ then if

$$\sup_{[0,T]} |Q_{k+1}| \leq (k+1) \sup_{[0,T]} |Q_k|, \; k = 0, 1, 2, \ldots, \tag{8.3.1}$$

we have that

$$\lim_{N \to \infty} \tilde{Q}_0^{(N)} = Q_0, \tag{8.3.2}$$

for times, t, such that

$$t \leq T < \epsilon^{-1}, \quad \epsilon < 1. \tag{8.3.3}$$

We proceed to this result as follows.

We may write the system of (8.1.34) and (8.1.36) as

$$d_t Q_0 = (d_t Q_0 - \alpha h Q_1) + \alpha h Q_1, \qquad (8.3.4-1)$$

$$d_t Q_1 = (d_t Q_1 - \alpha Q_2) + \alpha Q_2, \qquad (8.3.4-2)$$

$$d_t Q_2 = (d_t Q_2 - \alpha Q_3) + \alpha Q_3, \qquad (8.3.4-3)$$

$$\vdots$$

$$d_t Q_{N-1} = (d_t Q_{N-1} - \alpha Q_N) + \alpha Q_N, \qquad (8.3.4-N)$$

$$d_t Q_N = (d_t Q_N - \alpha Q_{N+1}) + \alpha Q_{N+1}, \qquad (8.3.4-N+1)$$

$$\vdots$$

where α and h are functions of M ($\equiv Q_0$) and are given by

$$\alpha = 1 - a_0 M/(a+u), \qquad (8.3.5)$$

$$h = 1/\left(\frac{dp}{dM} + \rho a \frac{du}{dM}\right), \qquad (8.3.6)$$

with a, u, p and ρ in these expressions given by (7.2.7) - (7.2.11). The closure scheme arises from the fact demonstrated in section 8.1 that the expression $d_t Q_N - \alpha Q_{N+1}$ (or $d_t Q_0 - \alpha h Q_1$ in the case $N = 0$) depends only upon $Q_0, \ldots, Q_N$ and the known function A and its derivatives, so that truncation of the term αQ_{N+1} (or $\alpha h Q_1$) yields a closed system of equations. It is significant at this point to note that the functions α and h are bounded over the range of Mach numbers $[1, \infty)$ by

$$0 \leq \alpha \leq \lim_{M \to \infty} (1 - a_0 M/(a+u)) = \epsilon, \qquad (8.3.7)$$

and

$$0 \leq h \leq \frac{\gamma + 1}{6 \rho_0 a_0^2}. \qquad (8.3.8)$$

The bound of (8.3.8) is crude, but it is only the boundedness property that we require. The constant ϵ is a function of γ but for all physically meaningful values of γ is less than 1.

Suppose now that we truncate at equation $N+1$ and solve the resultant system. Then from (8.3.4 - N+1) we obtain an approximation $\tilde{Q}_N^{(N)}$ to Q_N by solution of

$$d_t \tilde{Q}_N^{(N)} = d_t Q_N - \alpha Q_{N+1}. \qquad (8.3.9)$$

Rearranging, this becomes

$$d_t\left(\tilde{Q}_N^{(N)} - Q_N\right) = -\alpha Q_{N+1}, \tag{8.3.10}$$

and integration yields

$$\tilde{Q}_N^{(N)}(t) - Q_N(t) = -\int_0^t \alpha Q_{N+1} dt', \tag{8.3.11}$$

where we have chosen $\tilde{Q}_N^{(N)} = Q_N$ at $t = 0$. We then obtain the bound

$$\begin{aligned}\left|\tilde{Q}_N^{(N)}(t) - Q_N(t)\right| &\leq \epsilon t \sup_{[0,T]} |Q_{N+1}| \\ &\leq \epsilon t(N+1) \sup_{[0,T]} |Q_N|,\end{aligned} \tag{8.3.12}$$

having made use of (8.3.1) and provided $t \leq T$. The function $\tilde{Q}_N^{(N)}$ may now be used to obtain an approximation to the term αQ_N appearing at the extreme right of equation (8.3.4-N) so that an approximation $\tilde{Q}_{N-1}^{(N)}$ to Q_{N-1} may be obtained as a solution of

$$d_t \tilde{Q}_{N-1}^{(N)} = (d_t Q_{N-1} - \alpha Q_N) + \alpha \tilde{Q}_N^{(N)}. \tag{8.3.13}$$

Rearranging and integrating we obtain the bound

$$\left|\tilde{Q}_{N-1}^{(N)}(t) - Q_{N-1}(t)\right| \leq (\epsilon t)^2 (N+1) N \sup_{[0,T]} |Q_{N-1}| / 2!. \tag{8.3.14}$$

Repeating this argument yields

$$\left|\tilde{Q}_0^{(N)}(t) - Q_0(t)\right| \leq \frac{(\gamma+1)}{6\rho_0 a_0^2} (\epsilon t)^{N+1} (N+1)! \sup_{[0,T]} |Q_0| / (N+1)!. \tag{8.3.15}$$

Since Q_0 is continuous on the closed interval $[0, T]$, $\sup_{[0,T]} |Q_0|$ exists and provided

$$\epsilon T < 1, \tag{8.3.16}$$

the result follows and on the interval $[0, T]$ the closure scheme converges to the true solution. Note that the scheme converges despite the growth of the terms Q_k as k increases. If we were to impose the stronger condition that all the Q_k were bounded, by Q say, then we would obtain

$$\left|\tilde{Q}_0^{(N)}(t) - Q_0(t)\right| \leq \frac{(\gamma+1)}{6\rho_0 a_0^2} \frac{(\epsilon t)^{N+1}}{(N+1)!} Q. \tag{8.3.17}$$

In this case as $N \to \infty$, $\tilde{Q}_0^{(N)} \to Q_0$ for all values of t.

We may make a few comments regarding the rate of convergence that we might expect for given physical problems. From (8.3.15) and (8.3.17) if we require a solution of a given accuracy δ such that $\left|\tilde{Q}_0^{(N)}(t) - Q_0(t)\right| < \delta$ for $t \in [0, T]$ then the value of N required to achieve this (not assuming any other knowledge about the Q_k than assumed above) reduces with T. Similarly, the value of ϵ, the bound upon the function α, governs the rate of convergence. In the example of an expanding shock front, such as a spherical wave, the Mach number and hence α will decrease as the shock propagates. The appropriate value of ϵ to be used in the above results would then be α evaluated at the initial Mach number. For weak shocks the value would be significantly less than ϵ so that a solution of desired accuracy can be guaranteed with a smaller value of N. In the limit $M \to 1, \alpha(M) \to 0$ giving rise to rapid convergence over large time intervals.

At this point the area function A has not appeared in the consideration. Its role may be inferred from equations (8.1.7) and (8.1.8). The growth of the terms Q_k depends not only upon the Q_k themselves but upon the ratio A'/A and its derivatives. In the above derived bounds upon $\left|\tilde{Q}_0^{(N)} - Q_0\right|$ a bound upon all of the Q_k, or upon Q_0, appears. This bound will be dependent upon the magnitude of A'/A although the above considerations have not quantified this dependence. We might suppose, however, that larger values of the ratio A'/A would give rise to larger bounds upon the Q_k and thus require truncation at larger N in order that a solution of a required accuracy is guaranteed. This aspect is worthy of further investigation.

We conclude this section with a number of remarks regarding the mathematical structure noted in section 8.1. We have been able to show that the motion of the shock is described by an infinite sequence of differential equations and that by a process of truncation we may close and subsequently solve the system to determine, in an approximate manner, the motion of the shock. The terms we

have chosen to truncate are given as $Q_i = \partial_t^{i-1}(\partial_t p + \rho a \partial_t u)$. We remark that an alternative procedure of approximation may have been followed by noting that the same structure as that discussed here may be established where we choose $Q_i = \partial_t^i p + \rho a \partial_t^i u$. Truncation at the first equation in the sequence so obtained yields the Whitham A-M relation. The second equation in this sequence differs from that presented in section 8.2. In this case it is not so obvious as to which is the appropriate description, but the scheme followed here has been chosen for a number of reasons. Firstly, in the formulation here, the coefficient of the term $\partial_t^{i-1}(\partial_t p + \rho a \partial_t u)$, that we choose to truncate, is $(a_0 M/(a+u) - 1)$, which is very small in the case of weak shocks. In this regime, we may justify truncation on grounds of this smallness. We suppose that the mathematical structure should be independent of the Mach number, so we choose $Q_i = \partial_t^{i-1}(\partial_t p + \rho a \partial_t u)$. If we choose to truncate terms of the form $\partial_t^i p + \rho a \partial_t^i u$, then in the weak shock limit terms remain whose coefficients are $(a_0 M/(a+u) - 1)$.

By choosing $Q_i = \partial_t^{i-1}(\partial_t p + \rho a \partial_t u)$, we obtain a generalisation of the "characteristic rule". The second equation of (8.2.6) is, in fact, the equation for the rate of change of $\partial_t p + \rho a \partial_t u$ along the C_+ characteristic, applied at the shock in a manner analogous to that in which the A-M relation is deduced by applying the C_+ characteristic equation at the shock. Thus to close the sequence of equations at the (N+1)'th equation, we transfer the equation for $d_t Q_N$ along the C_+ characteristic to the shock. Thus we are, in a sense, exploiting the closeness of the C_+ characteristics and the shock, even though the measure of this co-incidence, $(a_0 M/(a+u) - 1)$, is not so small for strong shocks.

That this quantity is not so small in the strong shock limit has led Whitham to propose that it is the smallness of $\partial_t p + \rho a \partial_t u$ that leads to the success of the method, noting the most spectacular success of the approach in the consideration of converging spherical and cylindrical shocks in the strong shock limit. This quantity is equal to zero in the linearised solution for the flow field behind the shock that Whitham uses to deduce the A-M relation. If $\partial_t p + \rho a \partial_t u$ remains small at the shock

then it is not unreasonable to suppose that higher partial time derivatives of this quantity, the Q_i of the closure scheme presented here, will remain small at the shock. In the linearised solution all the Q_i are zero at the shock. The convergence results presented here have exploited the feature that $(a_0 M/(a+u)-1)$ is less than one. Since this term appears as the coefficient of the Q_i that are truncated to achieve closure, if the Q_i themselves are small the term truncated is a product of small terms and we might expect more rapid convergence of the scheme.

We also comment that we may have chosen $Q_i = \partial_x^{i-1}(\partial_x p + \rho a \partial_x u)$, $i = 1, 2, \ldots$, and a similar closure scheme deduced. We reject this approach on a number of grounds. In the first instance the first equation in the resultant sequence, when closed, yields an A-M relation that differs significantly from that of Whitham, which is known to be a good approximation. Secondly, in the linearised solution mentioned above the Q_i so defined are non-zero, unless all derivatives of the area function, $A(x)$, vanish; a case that would be most uninteresting.

Particularly significant in this regard is the recent work of Prasad and Srinivasan (1987, and see also Srinivasan and Prasad, 1985), following that of Maslov (1980). They establish that along the shock trajectory

$$g_1(M)\frac{dM}{dx} + \frac{1}{A}\frac{dA}{dx} + F(M)\frac{\partial M}{\partial x} = 0, \tag{8.3.18}$$

where $g_1(M)$ and $F(M)$ are given functions and M is the Mach number. In shock dynamics M is usually defined only at the shock, but Prasad and Srinivasan define it throughout the fluid so that the expression $\partial M/\partial x$ is meaningful. This is achieved by supposing that the relationship between the Mach number of the shock and the density just behind the shock defines a Mach number in terms of the density throughout the fluid. Thus the term $\partial M/\partial x$ in (8.3.18) may be written as $dM/d\rho\, \partial\rho/\partial x$, where $dM/d\rho$ is a function of M and in (8.3.18) these terms are evaluated at the shock. The definition of M used by Prasad and Srinivasan differs slightly from that used here, but this is not important. In any case, it is a routine matter to show that (8.3.18) and (8.1.7) are equivalent.

Prasad and Srinivasan claim that truncation of the term $F(M)\partial M/\partial x$ yields the appropriate relationship between M and A for a shock propagating down a tube of slowly varying cross section, and make much of the difference between their function $g_1(M)$ and the function $g(M)$ appearing in the A-M relation used by Whitham (equation (7.2.24)). As pointed out by Whitham (1987), the closure carried out by Prasad and Srinivasan is not equivalent to that used to derive (7.2.24). In view of (8.1.7) and its equivalence to (8.3.18), this is obvious.

Consideration of the linearised solution, used to derive the A-M relation, indicates why the closure advocated by Prasad and Srinivasan is inappropriate. Unless A'/A is equal to zero, the term $\partial M/\partial x$ is non-zero, whereas noted above, $\partial_t p + \rho a \partial_t u$ is zero as are all its higher partial time derivatives. This is a further example indicating that many possible closure schemes are available, even though Prasad and Srinivasan have not demonstrated an infinite equation structure as shown here. Consideration of the linearised solution gives strong indication of which is the appropriate closure strategy to adopt.

Further justification of the closure scheme employed here may be obtained by performing computations using the equations of section 8.1 and comparing with known solutions and experimental results. Thus we consider shock propagation first in simple geometries and then general geometries using the numerical scheme to be developed in chapter 9.

8.4. The propagation of strong cylindrical and spherical shock waves

The propagation of cylindrical and spherical shock waves is of interest for two reasons. The function $A(x)$ is known in these cases and furthermore, the equations of one-dimensional flow are exact. In the limit of strong shocks we can obtain analytic solutions to the equations of section 8.2. The mathematical criterion that the Whitham A-M relation is a good approximation may be evaluated, providing some insight into the success of the method.

In appendix 2 equations (8.2.6) are evaluated in the strong shock limit. In the geometries of interest we may write

$$A = 2n\pi x^n, \quad A'/A = n/x, \tag{8.4.1}$$

with $n = 1, 2$ respectively for cylindrical and spherical shocks. Writing $Q = Q_1/(\rho_0 a_0^3)$, the equations describing the propagation are

$$M' = -n\zeta_1 M/x + \zeta_2 Q/M^2, \tag{8.4.2}$$

$$Q' = \tau_1 M(M')^2 + n\tau_2 M^2 M'/x + n^2\tau_3 M^3/x^2 + (\kappa_1 M' + n\kappa_2 M/x)Q/M, \tag{8.4.3}$$

where M' and Q' denote derivatives with respect to x. Expressions for the constants $\zeta_1, \zeta_2, \tau_1, \tau_2, \tau_3, \kappa_1$ and κ_2 may be found in appendix 2, but for common values of γ they are shown in table 8.4.1. It is easiest to proceed by writing (8.4.2) and (8.4.3) as a single second order equation for M. Differentiating (8.4.2) and substituting into (8.4.3) gives

$$M'' + \chi_1(M')^2/M + \chi_2 M'/x + \chi_3 M/x^2 = 0, \tag{8.4.4}$$

with

$$\begin{aligned} \chi_1 &= 2 - \tau_1\zeta_2 - \kappa_1, \\ \chi_2 &= n(3\zeta_1 - \zeta_1\kappa_1 - \zeta_2\tau_2 - \kappa_2), \\ \chi_3 &= -n(\zeta_1 + n(\tau_3\zeta_2 + \zeta_1\kappa_2)), \end{aligned} \tag{8.4.5}$$

and values for these constants may be found in table 8.4.2. If we put $z = \ell n\, x$ then (8.4.4) becomes

$$M'' + \chi_1(M')^2/M + (\chi_2 - 1)M' + \chi_3 M = 0, \tag{8.4.6}$$

with derivatives now with respect to z. Making the further substitution $f = M'/M$ we obtain

$$f' + (\chi_1 + 1)(f - f_1)(f - f_2) = 0, \tag{8.4.7}$$

with f_1 and f_2 satisfying

$$(\chi_1 + 1)f^2 + (\chi_2 - 1)f + \chi_3 = 0, \tag{8.4.8}$$

	γ		
	6/5	7/5	5/3
ζ_1	0.1631	0.1971	0.2254
ζ_2	0.0368	0.0556	0.0743
τ_1	−59.8345	−19.8431	−8.3852
τ_2	−14.9705	−9.6091	−7.2498
τ_3	−1.0924	−1.1541	−1.2011
κ_1	0.9558	1.5097	1.7508
κ_2	0.6811	0.6440	0.6287

Table 8.4.1.

	γ					
	6/5		7/5		5/3	
	$n=1$	$n=2$	$n=1$	$n=2$	$n=1$	$n=2$
χ_1	3.2487	3.2487	1.5936	1.5936	0.8723	0.8723
χ_2	0.2039	0.4079	0.1840	0.3680	0.1916	0.3832
χ_3	−0.2340	−0.6096	−0.2598	−0.6451	−0.2779	−0.6607
f_1	0.3464	0.4548	0.5108	0.6352	0.6575	0.7812
f_2	−0.1590	−0.3155	−0.1961	−0.3916	−0.2257	−0.4518
G_{exp}	−0.1612	−0.3208	−0.1973	−0.3944	−0.2261	−0.4527
ξ	4.4272	8.8544	3.5445	7.0890	3.0338	6.0676
ϵ	0.1120	0.2922	0.0169	0.0466	0.0043	0.0123
x_f	9.4227	3.7029	37.0372	9.4621	–	–

Table 8.4.2.

and we may suppose that $f_1 > f_2$ and their values are shown in table 8.4.2. Integrating twice we obtain

$$M = k_1 x^{f_1} \left(1 + k_2 x^{-(\chi_1+1)(f_1-f_2)}\right)^{1/(\chi_1+1)}, \tag{8.4.9}$$

with k_1 and k_2 as yet undetermined constants. We shall scale our initial distance, x_i, to 1 and here specify initial values M_i and Q_i of M and Q. From (8.4.2) we determine the initial value of M' and so obtain

$$\begin{aligned} M = M_i(f_1 - f_2)^{-1/(\chi_1+1)} \Big[&(f_1 + n\zeta_1 - \zeta_2 Q_i/M_i^3)x^{(\chi_1+1)f_2} \\ &-(f_2 + n\zeta_1 - \zeta_2 Q_i/M_i^3)x^{(\chi_1+1)f_1}\Big]^{1/(\chi_1+1)}. \end{aligned} \tag{8.4.10}$$

It is also useful to obtain from (8.4.2) an expression for Q and it is

$$Q = \frac{M^3}{\zeta_2 x}\left[n\zeta_1 + \left\{\frac{f_2(f_1 + n\zeta_1 - \zeta_2 Q_i/M_i^3)x^{(\chi_1+1)f_2} - f_1(f_2 + n\zeta_1 - \zeta_2 Q_i/M_i^3)x^{(\chi_1+1)f_1}}{(f_1 + n\zeta_1 - \zeta_2 Q_i/M_i^3)x^{(\chi_1+1)f_2} - (f_2 + n\zeta_1 - \zeta_2 Q_i/M_i^3)x^{(\chi_1+1)f_1}}\right\}\right]. \tag{8.4.11}$$

In view of this solution we can make a few comments regarding the propagation of converging and diverging shocks. Consider first converging shocks. In this case $x \in [1, 0)$ with $x \to 0$ as the shock propagates. Near in to the origin we see that

$$M \sim M_i \left(\frac{f_1 + n\zeta_1 - \zeta_2 Q_i/M_i^3}{f_1 - f_2}\right)^{1/(\chi_1+1)} x^{f_2}. \tag{8.4.12}$$

It is interesting to note from this that the variation with x, as characterised by the exponent f_2, is independent of the initial waveform shape described by Q_i, even though this value appears in the coefficient function. If we choose the special initial condition

$$Q_i = (f_2 + n\zeta_1)M_i^3/\zeta_2, \tag{8.4.13}$$

then we obtain the solution

$$M = M_i x^{f_2}. \tag{8.4.14}$$

Whitham notes that the A-M relation admits a solution of this form, with the exponent given by $-n\zeta_1$, and that such a solution appears to correspond to the similarity solution for converging shock waves due to Guderley (1942). In that solution the Mach number varies as in (8.4.14) with the exponents shown as G_{exp}

in table 8.4.2. The close agreement of these values with $-n\zeta_1$ is seen as confirmation that in this converging geometry the A-M relation is a good approximation. In this context the solution of (8.4.14) is that which corresponds to the similarity solution when we truncate at the second equation and the exponent is given by f_2. The agreement with the Guderley exponents is good, the values sometimes slightly better, sometimes slightly worse than those given by the A-M relation.

It is worthwhile to evaluate the terms appearing in the inequality of (8.2.4) as this expression gives the criterion that the A-M relation is a good approximation, and for converging shocks this appears to be the case. This inequality becomes

$$\xi M^3/x >> |Q|, \tag{8.4.15}$$

with

$$\xi = n\eta_1\alpha_2/(1 - 1/(\alpha_1 + \alpha_3)), \tag{8.4.16}$$

and $\eta_1, \alpha_1, \alpha_3$ are as defined in appendix 2. Values of ξ are shown in table 8.4.2. At $x = 1$ the condition that the A-M relation provides a good approximation yields

$$\xi >> |Q_i|/M_i^3, \tag{8.4.17}$$

and we see that for large non-uniformities in the flow conditions behind the shock, as characterised by $|Q_i|$, the A-M relation is not an appropriate solution. For the initial conditions assumed in the derivation of the A-M relation $Q_i = 0$ and so (8.4.17) is satisfied. Using the expression of (8.4.11) and evaluating the limit $x \to 0$ (8.4.15) yields

$$\xi >> |n\zeta_1 + f_2|/\zeta_2 = \epsilon \tag{8.4.18}$$

as the criterion that the A-M relation is a good approximation and values of ϵ are shown in table 8.4.2. This inequality is independent of the initial value of Q. For all γ considered here, inspection of table 8.4.2. indicates that this inequality is well satisfied so that provided (8.4.17) is initially satisfied the A-M relation is a good approximation as the shock converges to the origin. We should perhaps mention at this point that the close agreement with Guderley's solution obtained

from both the A-M relation and truncation at the second equation indicates that the closure scheme converges in this case. Even so, the convergence results of the previous section do not appear to be applicable to the Guderley solution, although given that the form of the solution is known progress in proving convergence in this specific case can possibly be made.

Consider now diverging shocks. In this case $x \in [1, \infty)$ with $x \to \infty$ as the shock propagates. If we consider the particular case $Q_i = 0$ then for $\gamma = 6/5,\ 7/5$ we see from (8.4.10) that at

$$x_f = \left(\frac{f_1 + n\zeta_1}{f_2 + n\zeta_1} \right)^{1/((f_1 - f_2)(\chi_1 + 1))}, \tag{8.4.19}$$

$M = 0$. Values of x_f for $\gamma = 6/5,\ 7/5$ are shown in table 8.4.2 and the values are comparitively small. Since $M \geq 1$ this observation indicates that truncation at the second equation does not provide an adequate description of outgoing shocks in the strong shock limit, which is in confirmation of the comments of Whitham (1974) that the A-M relation is not appropriate for such problems. Although the case $\gamma = 5/3$ does not suffer from the defect of predicting $M = 0$, the value given by (8.4.10) rapidly diverges from that given by the A-M relation again confirming that these descriptions are inappropriate in this case. It is significant, though, that as such a shock propagates the Mach number decreases and the strong shock limit of the equations is itself no longer appropriate.

These features are shown graphically in figure 8.4.1 where the variation of M with x, as predicted by the A-M relation and by truncation at the second equation, has been plotted for the case $\gamma = 7/5$. The initial value of Q was chosen to be zero. We note the close agreement between the two results in the case of the converging geometry and the rapid divergence in the case of an expanding geometry. In the next section, however, consideration of the blast wave produced by an underwater explosion demonstrates an example of propagation into an expanding geometry in which the description afforded by the truncation method developed here provides a very accurate description of the propagation. This case, however, is characterised by a Mach number near to one. Later implementation of a numerical method for

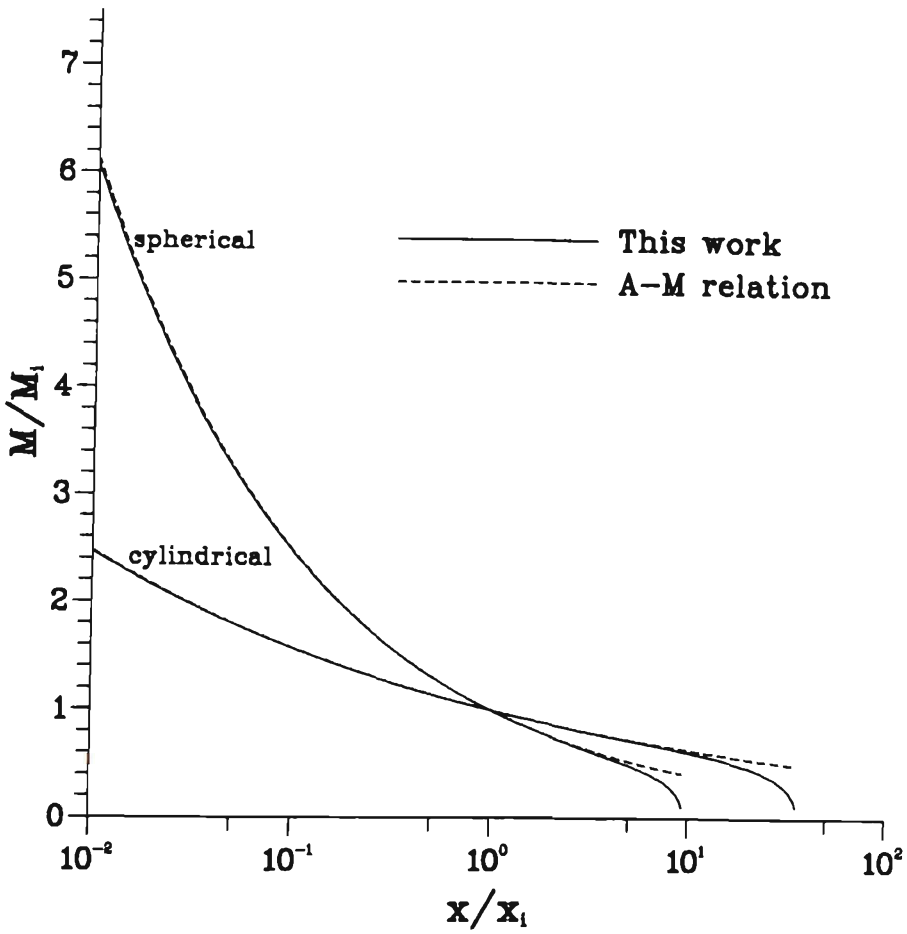

Figure 8.4.1. The Mach number as a function of distance for the propagation of converging and diverging spherical and cylindrical shocks in the strong shock limit.

geometrical shock dynamics will demonstrate that even for stronger shocks in an expanding geometry the method developed here provides an excellent description, despite the failure in the strong shock limit.

8.5. The propagation of a spherical underwater blast wave

The practical problem of the propagation of a spherical underwater blast wave provides an ideal test for the ideas presented in this chapter. The area function is known explicitly , the initial flow conditions behind the shock are non-uniform and there are analytical and experimental results, as discussed in chapter 7, with which we may make comparisons. In order to apply the theory of geometrical shock dynamics using the ideas of this chapter we must make use of the shock jump conditions that result from a description of water using the Tait equation of state. We have already noted that the only expression that differs from those for an ideal gas is that for the pressure (equation (7.2.25)), but despite this the expressions of (8.1.27) - (8.1.32) for partial derivatives of flow quantities evaluated at the shock are unchanged. Consequently, the results of (8.1.34) - (8.1.37) follow and the closure scheme may be applied to propagation in water upon provision of an appropriate value of γ, the quantity analagous to the ratio of specific heats and here chosen as 7.15.

Since the shock is weak we may simplify the analysis by reformulating the results of section 8.1 exploiting this fact. Neglect of entropy changes at the shock allows us to write

$$(p+\pi)\rho^{-\gamma} = \text{constant}, \tag{8.5.1}$$

and as done by Kirkwood and Bethe (1942) we may introduce Riemann functions. Changing notation slightly from that used by those workers we define them as

$$\sigma = \frac{2}{\gamma-1}a + u, \tag{8.5.2}$$

$$\nu = \frac{2}{\gamma-1}a - u, \tag{8.5.3}$$

and note that they differ from those of (7.1.16) and (7.1.17) by a constant factor.

The equations describing propagation down a tube of slowly varying cross section then become

$$\partial_t \sigma + (u+a)\partial_x \sigma = -au\,A'/A, \tag{8.5.4}$$

$$\partial_t \nu + (u-a)\partial_x \nu = -au\,A'/A. \tag{8.5.5}$$

The mathematical structure shown in section 8.1 may then be deduced but the analysis is simpler. In particular we may establish that on the shock trajectory S

$$\begin{aligned} d_t(\partial_t^n \sigma) = -\,a_0 M \Bigg[& \partial_t^n \left(\frac{au}{a+u}\right) A'/A + \sum_{i=1}^{n} \binom{n}{i} \partial_t^i \left(\frac{1}{a+u}\right) \partial_t^{n-i+1}\sigma \\ & + \left(\frac{1}{a+u} - \frac{1}{a_0 M}\right) \partial_t^{n+1}\sigma \Bigg], \quad n = 0,1,2,\ldots, \end{aligned} \tag{8.5.6}$$

and

$$\begin{aligned} \partial_t^{n+1}\nu = -\Big[& (u-a) d_t\,(\partial_t^n \nu) + a_0 M \Big[\partial_t^n (au) A'/A \\ & - \sum_{i=1}^{n} \binom{n}{i} \partial_t^i (u-a) \Big\{ \partial_t^{n-i} \left(\frac{au}{u-a}\right) A'/A + \sum_{j=0}^{n-i} \binom{n-i}{j} \partial_t^j \left(\frac{1}{u-a}\right) \partial_t^{n-i-j+1}\nu \Big\} \Big] \Big] \\ & /[a_0 M - (u-a)], \quad n = 0,1,2,\ldots, \end{aligned} \tag{8.5.7}$$

with all notation as previously defined. If we define

$$Q_i = \partial_t^i \sigma, \quad i = 0,1,2,\ldots \tag{8.5.8}$$

evaluated at the shock then we may establish by induction that

$$d_t Q_k = d_t Q_k(Q_0,\ldots,Q_{k+1},\, A'/A,\, d_x\,(A'/A),\ldots), \tag{8.5.9}$$

and

$$\nu_k = \nu_k(Q_0,\ldots,Q_k,\, A'/A,\, d_x\,(A'/A),\ldots), \tag{8.5.10}$$

where ν_k denotes $\partial_t^k \nu$ evaluated at the shock. The proof follows that of section 8.1. The expression of (8.5.9) is as that of (8.1.34) and (8.1.36) and a similar scheme of closure by truncation results. The simplifying feature induced by neglect of entropy changes is a reduction in the number of dependent flow variables from three (ρ, a and u) to two (a and u).

Since A is known for a spherical geometry we may truncate at any equation and numerically integrate the resultant system of ordinary differential equations.

The first three equations are

$$d_r Q_0 = -\left[\frac{au}{a+u}A'/A + \left(\frac{1}{a+u} - \frac{1}{a_0 M}\right)Q_1\right], \tag{8.5.11}$$

$$d_r Q_1 = -\left[\partial_t\left(\frac{au}{a+u}\right)A'/A + \partial_t\left(\frac{1}{a+u}\right)Q_1 + \left(\frac{1}{a+u} - \frac{1}{a_0 M}\right)Q_2\right], \tag{8.5.12}$$

$$\begin{aligned} d_r Q_2 = -\Bigg[&\partial_t^2\left(\frac{au}{a+u}\right)A'/A + \partial_t^2\left(\frac{1}{a+u}\right)Q_1 + 2\partial_t\left(\frac{1}{a+u}\right)Q_2 \\ &+ \left(\frac{1}{a+u} - \frac{1}{a_0 M}\right)Q_3\Bigg], \end{aligned} \tag{8.5.13}$$

where we have introduced r as the distance variable and converted to derivatives in r noting that $d_t \equiv a_0 M d_r$. Evaluation of the necessary derivatives $\partial_t a$, $\partial_t^2 a$, $\partial_t u$, $\partial_t^2 u$ at the shock is facilitated by (8.5.7), the appropriate equations being

$$\nu_1 = (u-a)\left[d_t \nu_0 + a_0 M \frac{au}{u-a}A'/A\right]/(u-a-a_0 M), \tag{8.5.14}$$

$$\nu_2 = (u-a)\left[d_t \nu_1 + a_0 M\left\{\partial_t\left(\frac{au}{u-a}\right)A'/A + \partial_t\left(\frac{1}{u-a}\right)\nu_1\right\}\right]/(u-a-a_0 M). \tag{8.5.15}$$

In order to make comparisons with the results of the Kirkwood-Bethe theory, the weak shock solution of Rogers and the empirical relationships describing the pressure field we assume that at some initial range R_i the pressure is given by

$$p(R_i) = p_i e^{-t/\tau_i}, \tag{8.5.16}$$

with $t = 0$ denoting the time of arrival of the shock, p_i the peak pressure and τ_i the time constant of the assumed exponential decay. We may evaluate initial values of $\partial_t p$ and $\partial_t^2 p$ at the shock as

$$(\partial_t p)_i = -p_i/\tau_i, \quad (\partial_t^2 p)_i = p_i/\tau_i^2, \tag{8.5.17}$$

and knowledge of these quantities facilitates evaluation of initial values of Q_1 and Q_2. Denoting the ambient flow quantities by a subscript 0, and assuming that the ambient pressure p_0 is much less than the constant π appearing in the Tait equation of state we obtain from (7.1.13) that

$$a_0^2 \approx \gamma\pi/\rho_0, \tag{8.5.18}$$

and substitution into (7.2.25) gives the pressure at the shock as

$$p = \frac{2a_0^2\rho_0}{(\gamma+1)}(M^2-1). \tag{8.5.19}$$

Given the initial pressure p_i we may calculate from this expression the initial Mach number M_i.

To obtain the initial value Q_{1_i} of Q_1 we first note from (7.1.13) and (8.5.1) that

$$\partial_t a = \frac{\gamma-1}{2\rho a}\partial_t p, \tag{8.5.20}$$

so that evaluated at the shock the initial value is

$$(\partial_t a)_i = \frac{-(\gamma-1)p_i}{2\rho_i a_i \tau_i}, \tag{8.5.21}$$

having made use of (8.5.17). Now (8.5.2) and (8.5.3) give

$$\partial_t a = \frac{\gamma-1}{4}(\partial_t\sigma + \partial_t\nu), \tag{8.5.22}$$

and at the shock

$$\nu_1 = \frac{4}{\gamma-1}\partial_t a - Q_1. \tag{8.5.23}$$

Substituting into (8.5.14) we have

$$\frac{4}{\gamma-1}\partial_t a - Q_1 = (u-a)\left[d_t\nu_0 + a_0 M\frac{au}{u-a}A'/A\right]/(u-a-a_0M). \tag{8.5.24}$$

Now

$$\nu_0(M) = \frac{2}{\gamma-1}a(M) - u(M), \tag{8.5.25}$$

so that

$$d_t\nu_0 = a_0 M d_M\nu_0 d_\tau M. \tag{8.5.26}$$

Furthermore

$$Q_0 = \frac{2}{\gamma-1}a(M) + u(M), \tag{8.5.27}$$

so that

$$d_\tau M = d_\tau Q_0/d_M Q_0 \tag{8.5.28}$$

and $d_\tau Q_0$ is given by (8.5.11). Substituting these into (8.5.24) we obtain

$$Q_1 = \frac{(u-a-a_0M)\left(\frac{4\partial_t a}{\gamma-1}\right) + \frac{a_0M(u-a)au\,d_M\nu_0}{(u+a)d_MQ_0}\frac{A'}{A} - a_0Mau\frac{A'}{A}}{(u-a-a_0M) + a_0M(u-a)\left(\frac{1}{a+u} - \frac{1}{a_0M}\right)d_M\nu_0}, \tag{8.5.29}$$

and substitution of initial values yields the initial value of Q_1. In a similar manner we may obtain the initial value of Q_2. This evaluation requires knowledge of the initial value of $\partial_t^2 a$ and this is obtained using (8.5.17) in the expression

$$\partial_t^2 a = \frac{\gamma - 1}{2\rho a}\left[\partial_t^2 p - \left(\frac{\gamma + 1}{2}\right)\frac{(\partial_t p)^2}{\rho a^2}\right]. \tag{8.5.30}$$

In his paper Rogers (1977) compares his weak shock solution with the results of the Kirkwood-Bethe theory and the experimental relationships that characterise an underwater blast wave. We now include the results computed using the theory developed here in the comparison. In the Kirkwood-Bethe theory the expression for the pressure depends only upon the scaled range r/r_c, where r_c is the radius of the charge, and the time constant also scales with r_c. In the example of TNT presented by Rogers the initial range is $R_i = 10r_c$, the initial peak pressure is $p_i = 1.396 \times 10^8\, pa$ and the initial time constant is $13.9 \times 10^{-2} r_c\, \mu sec$, for r_c measured in metres. The ambient sound speed and density are taken as $1476\, ms^{-1}$ and $10^3 kg\, m^{-3}$ respectively, and (8.5.19) then yields an initial Mach number of $M_i = 1.11$. To proceed with the computation all distances are scaled with respect to R_i, all velocities with respect to a_0 and density with respect to ρ_0. In this way the time scale becomes R_i/a_0 so that the scaled initial time constant is 0.21267. The parameter ℓ_i that appears in Rogers' expressions for peak pressure and time constant (equation (7.1.33)) may be written as

$$\ell_i = \tau_i a_i/(M_i^2 - 1), \tag{8.5.31}$$

if the peak pressure is eliminated in favour of the Mach number, and it is noted that using the Tait equation of state the value β appearing in (7.1.26) and (7.1.27) is equal to $(\gamma + 1)/2$.

To perform the comparison we close the system of (8.5.9) and numerically integrate the resultant equations making use of the above initial data. In this way we may determine the variation of M and τ with the distance of propagation. The expressions for the peak pressure given by Rogers and experiment may be used in (8.5.19) to evaluate the variation of the Mach number with distance. We have

chosen to truncate at the first, second and third equations ((8.5.11) - (8.5.13)). Truncation of (8.5.11) yields the A-M relation of Whitham and we shall refer to this as the zeroth order solution. Truncation of (8.5.12) will be said to yield the first order solution with the second order solution given by truncation of (8.5.13). The variation of the Mach number is shown in figure 8.5.1 and the time constant in figure 8.5.2. The numerical integration was performed using a fourth order Runge-Kutta method. In order to evaluate the time constant via the definition of (7.1.34) we evaluate $\partial_t a$ at the shock via (8.5.24) and then obtain $\partial_t p$ from (8.5.20). Note that a value of Q_1 is required in this determination, so in order to obtain an estimate of this quantity we must compute at least the first order solution. If, however, we set $Q_1 = 0$ in this expression and use the value of M obtained from the Whitham theory then we would obtain a value for $\partial_t a$, and hence τ, but the value would be meaningless. The value so obtained would be dependent only upon the Mach number and thus give in no way an indication of the flow conditions in the near neighbourhood of the shock front which such a quantity by definition must. Indeed, if such a computation were performed in this case at $t = 0$ the value so obtained for the time constant would not even agree with that value input as the initial condition. Expanding on this point, the derivation of the A-M relation assumes an initial flow field behind the shock that is uniform, and explicitly neglects the changing flow field behind the shock as it propagates down a slowly varying tube. Thus application of the A-M relation can give no consistent information regarding the nature of this flow field.

Consider now the variation of Mach number shown in figure 8.5.1. We note the excellent agreement between the first order solution and that of Rogers. The experimental result lies between the zeroth and first order solutions. This is perhaps an indication that the assumption of an initially exponentially decaying pressure field is not an exact representation of the true behaviour, however, the closeness of the results suggests that this assumption is not bad. The excellent agreement over two orders of magnitude of distance with the analytic expression of Rogers

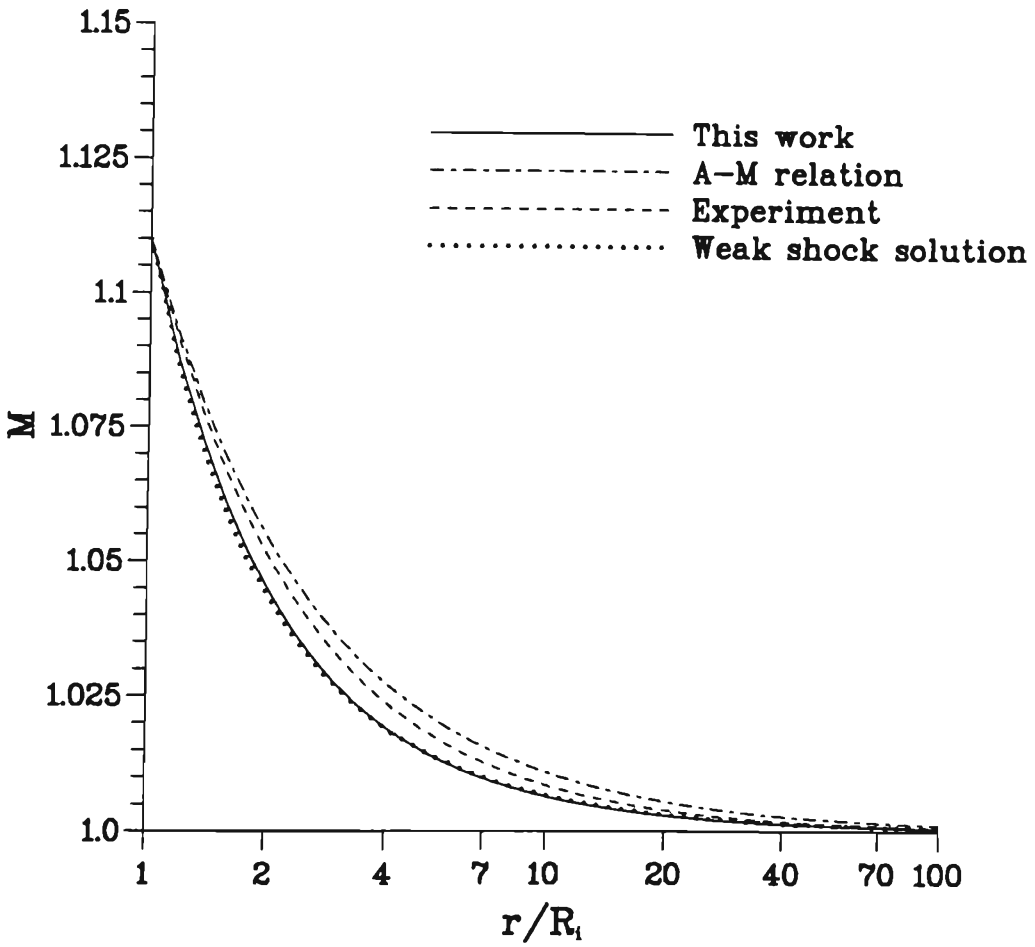

Figure 8.5.1. The Mach number as a function of range for the spherical blast wave produced by an underwater explosion.

provides validation of the approach of this chapter as the initial conditions used for the computation of the first order solution are obtained from the assumption of an initially exponentially decaying wave form. We further note that at large distances the zeroth and first order solutions tend towards each other after first diverging. This is due to the decay of the shock to an acoustic wave, which is the limiting case of both solutions. The results of the Kirkwood-Bethe theory for this example are not explicitly shown as they are almost indistinguishable from those of Rogers' solution.

The time constant data is shown in figure 8.5.2. Shown are the results of computation to first and second order, the experimental relationship, the weak shock result of Rogers and data from the Kirkwood-Bethe theory presented in Rogers' paper. We note that we must compute to second order to obtain an accurate expression for the time constant. This is no surprise. In order to obtain a very good approximation to the Mach number we must compute to first order, one order higher than the quantity (M) we wish to determine. The time constant is a first order quantity and in order to compute it accurately we expect that it is necessary to calculate a solution to one higher order. We also note the excellent agreement with the Kirkwood-Bethe theory. It is significant that for all results the rate of increase of τ decreases as the shock propagates. This is expected on the grounds that the pulse decays to an acoustic wave and in this limit the rate of increase of τ is equal to zero. As noted in chapter 7, Rogers has pointed out some of the deficiencies of the experimental expression for the time constant. The rate of growth of τ that it predicts differs significantly from that predicted by theoretical methods having a sound basis and this further demonstrates the limited applicability of this empirical relationship.

The theory of geometrical shock dynamics is based upon the consideration of a shock propagating down a tube of slowly varying cross section. We may consider the shock as having been generated by the motion of a piston in this tube. This example indicates how we may determine the motion of the shock given the motion

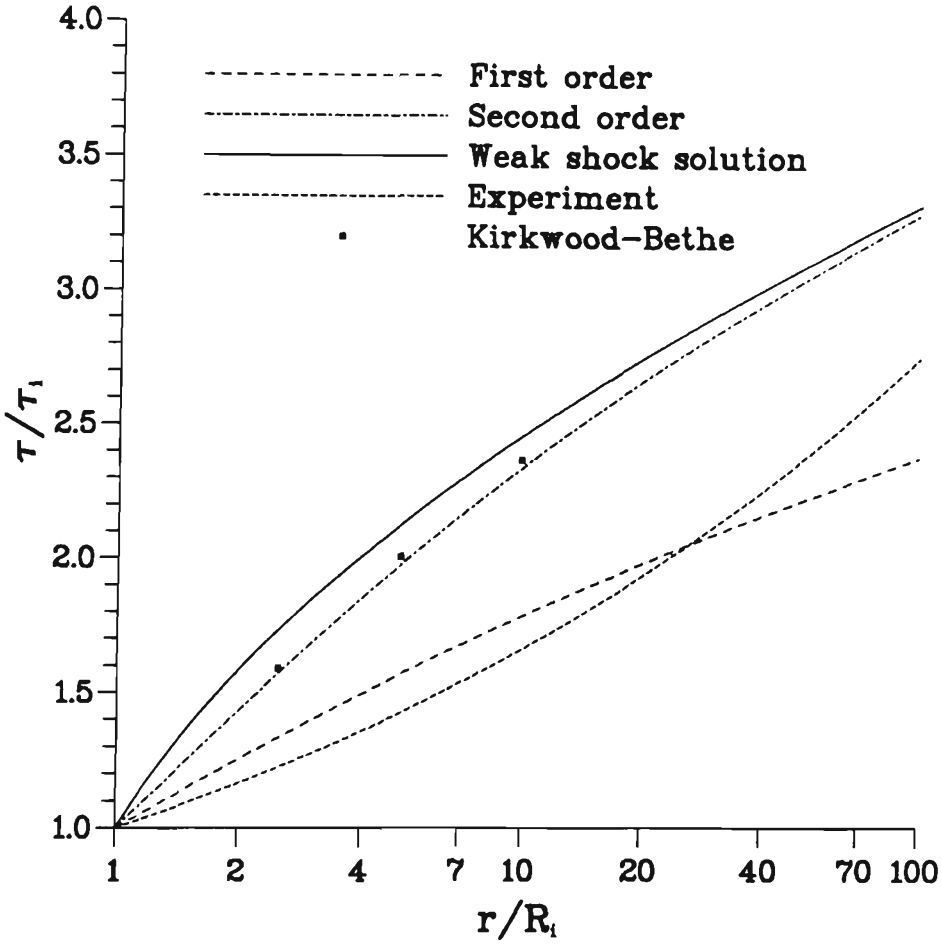

Figure 8.5.2. The time constant of the decay of the pressure produced by the passage of an underwater blast wave, as a function of range.

of the piston. Suppose we denote by $X(t)$ the position of the piston as a function of time, then since the piston moves with the fluid we have

$$d_t X(t) = u, \tag{8.5.32 - 1}$$

$$d_t^2 X(t) = \partial_t u + u\partial_x u, \tag{8.5.32 - 2}$$

$$d_t^3 X(t) = \partial_t(\partial_t u + u\partial_x u) + u\partial_x(\partial_t u + u\partial_x u), \tag{8.5.32 - 3}$$

$$\vdots$$

For shock dynamics to be applicable we must suppose that a shock is immediately formed and in this case $d_t X(0)$ will give the speed of the fluid just behind the shock at $t = 0$. From the shock jump conditions we obtain the initial value of the Mach number ($\equiv Q_0$). We have established that at the shock $\partial_t u$ and $\partial_x u$ are functions of M, Q_1 and A'/A which is assumed known. Evaluation of (8.5.32-2) at $t = 0$ using these functions gives the initial value of Q_1. This is analagous to the way in which we have proceeded here to the initial value of Q_1 given the initial value of $\partial_t p$ at the shock. Successive evaluation of higher initial time derivatives of $X(t)$ yields successive initial values of the Q_i. With initial conditions specified the system of ordinary differential equations describing the propagation of the shock may be solved. The motion of the shock is thus determined given the motion of the piston generating it.

In concluding this section we emphasise the excellent agreement obtained with the analytical solution of Rogers for an explosively generated shock propagating underwater. This consideration has been limited to the simplifying geometry of a spherical wave. In the next chapter a numerical method of geometrical shock dynamics will be developed incorporating the ideas formulated in this chapter. Once this scheme is developed we may compute the diffraction of underwater blast waves in general geometries, a feature not possible using the theories of Rogers or Kirkwood and Bethe.

9

NUMERICAL IMPLEMENTATION OF GEOMETRICAL SHOCK DYNAMICS

9.1. The numerical scheme

The A-M relation of Whitham may be used to propagate a shock front by introducing rays, normal to the front, which define a local shock tube down which we consider that the element of the shock front propagates. The geometry of the rays yields the local tube area and the A-M relation the local speed of propagation. If we denote by $\mathbf{x}$ the position vector of some point on the shock front, then the motion of the shock is given by

$$\frac{d\mathbf{x}}{dt} = a_0 M \mathbf{n}, \tag{9.1.1}$$

with $\mathbf{n}$ the unit vector normal to the shock that defines the direction of propagation.

This is the spirit of the computational method of geometrical shock dynamics, as implemented by Henshaw et al. (1986) and it is this scheme which we shall use with some modification. As in that scheme, (9.1.1) will be solved at a set of N node points $\mathbf{x}_i(t)$ $(i = 1, 2, \ldots, N)$ that we choose to represent the shock front. We will restrict our attention to two dimensional problems so the shock is represented as a one dimensional curve, and we write

$$\mathbf{x}_i(t) = (x_i(t), y_i(t)) . \tag{9.1.2}$$

In the scheme of Henshaw et al., equation (9.1.1) is integrated in time at each node point using a second order accurate leap frog scheme. In this application we employ a fourth order Runge-Kutta method.

In the original numerical scheme a simple finite difference approximation to the local tube area is used. This is a successful approach because the A-M relation gives the Mach number explicitly as a function of the area. In attempting to solve

equations (8.2.6) we require an expression for A' as well as A, and the complexity of these equations and lack of knowledge of an expression for $A(x)$ prevents integration that would yield an explicit relationship between A and M. Thus we seek to determine A'/A from the local geometry and then will integrate equations (8.2.6) in time in order to determine Q_1 and M at the shock front.

Consider two adjacent points on the shock front as shown in figure 9.1.1. Suppose that the points on the shock are not only parameterised with respect to time, t, but also with respect to the instantaneous arclength along the shock. We denote the arclength at t by $\xi(t)$. The adjacent points are separated by the length $\delta\xi(t)$, so that the points under consideration are $\mathbf{x}(\xi(t), t)$ and $\mathbf{x}(\xi(t)+\delta\xi(t), t)$. At this point on the shock the local tube area is $\delta\xi(t)$ and we consider how this varies in time. Using (9.1.1) we can determine the position of the two points at the short time, δt, later. We have to first order in δt

$$\mathbf{x}(\xi(t), t) \to \mathbf{x}(\xi(t), t) + a_0 M(\xi(t), t)\,\mathbf{n}(\xi(t), t)\,\delta t, \tag{9.1.3}$$

and

$$\mathbf{x}(\xi(t)+\delta\xi(t), t) \to \mathbf{x}(\xi(t)+\delta\xi(t), t) + a_0 M(\xi(t)+\delta\xi(t), t)\,\mathbf{n}(\xi(t)+\delta\xi(t), t)\,\delta t. \tag{9.1.4}$$

Expanding terms in (9.1.4) to first order in small $\delta\xi(t)$ we have

$$\begin{aligned}\mathbf{x}(\xi(t)+\delta\xi(t), t) \to\ & \mathbf{x}(\xi(t), t) + \frac{\partial \mathbf{x}(\xi(t), t)}{\partial \xi(t)}\delta\xi(t) \\ & + a_0\left(M(\xi(t), t) + \frac{\partial M(\xi(t), t)}{\partial \xi(t)}\delta\xi(t)\right)\left(\mathbf{n}(\xi(t), t) + \frac{\partial \mathbf{n}(\xi(t), t)}{\partial \xi(t)}\delta\xi(t)\right)\delta t,\end{aligned} \tag{9.1.5}$$

whence we obtain

$$\begin{aligned}\delta\xi(t+\delta t) &= |\mathbf{x}(\xi(t)+\delta\xi(t), t+\delta t) - \mathbf{x}(\xi(t), t+\delta t)| \\ &\approx \left|\frac{\partial \mathbf{x}(\xi(t), t)}{\partial \xi(t)} + a_0\left(M(\xi(t), t)\frac{\partial \mathbf{n}(\xi(t), t)}{\partial \xi(t)} + \frac{\partial M(\xi(t), t)}{\partial \xi(t)}\mathbf{n}(\xi(t), t)\right)\delta t\right|\delta\xi(t).\end{aligned} \tag{9.1.6}$$

Retaining terms to first order in small δt we have

$$\begin{aligned}\delta\xi(t+\delta t) &\approx \left(\left|\frac{\partial \mathbf{x}(\xi(t), t)}{\partial \xi(t)}\right|^2 + 2a_0\frac{\partial \mathbf{x}(\xi(t), t)}{\partial \xi(t)}\cdot\right. \\ &\qquad \left.\left(M(\xi(t), t)\frac{\partial \mathbf{n}(\xi(t), t)}{\partial \xi(t)} + \frac{\partial M(\xi(t), t)}{\partial \xi(t)}\mathbf{n}(\xi(t), t)\right)\delta t\right)^{\frac{1}{2}}\delta\xi(t) \\ &\approx \left(1 + a_0 M(\xi(t), t)\frac{\partial \mathbf{x}(\xi(t), t)}{\partial \xi(t)}\cdot\frac{\partial \mathbf{n}(\xi(t), t)}{\partial \xi(t)}\delta t\right)\delta\xi(t),\end{aligned} \tag{9.1.7}$$

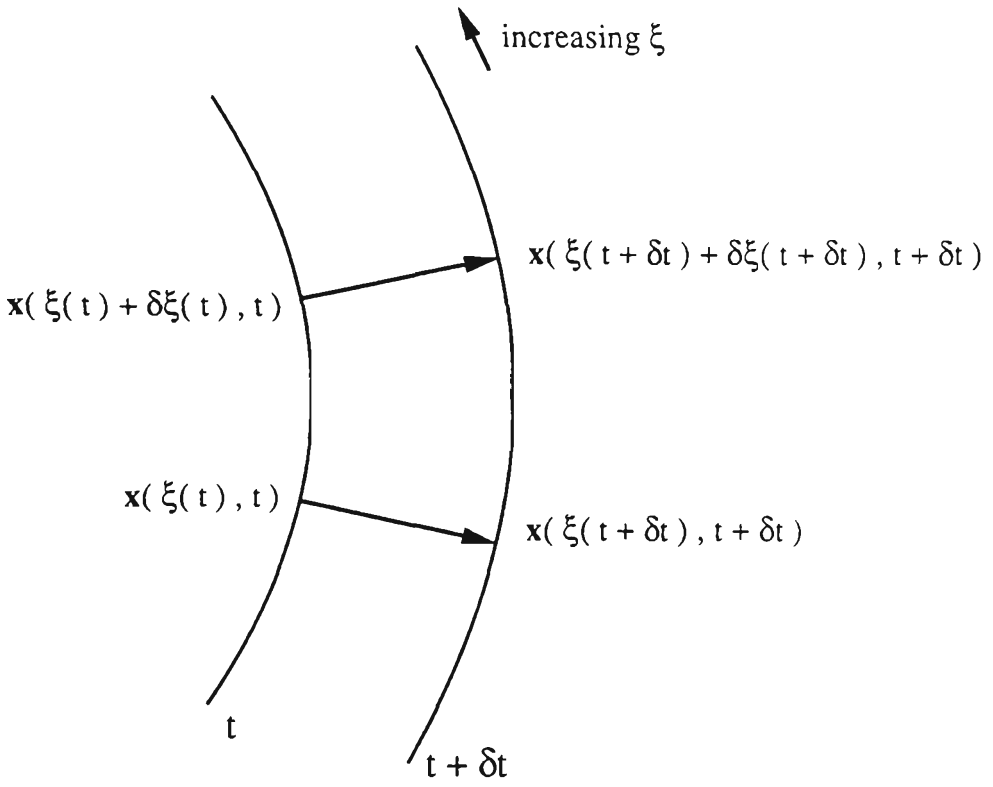

Figure 9.1.1. The geometry of a propagating shock front.

since

$$\mathbf{n}(\xi(t),t)\cdot\frac{\partial\mathbf{x}(\xi(t),t)}{\partial\xi(t)}=0. \tag{9.1.8}$$

Hence

$$\frac{\delta\xi(t+\delta t)-\delta\xi(t)}{\delta\xi(t)\delta t}\approx a_0M(\xi(t),t)\frac{\partial\mathbf{x}(\xi(t),t)}{\partial\xi(t)}\cdot\frac{\partial\mathbf{n}(\xi(t),t)}{\partial\xi(t)}. \tag{9.1.9}$$

Noting that $\delta\xi(t)$ is the local area, A, we have in the limit $\delta t\to 0$ that

$$\frac{1}{A}\frac{dA}{dt}=a_0M(\xi(t),t)\frac{\partial\mathbf{x}(\xi(t),t)}{\partial\xi(t)}\cdot\frac{\partial\mathbf{n}(\xi(t))}{\partial\xi(t)}. \tag{9.1.10}$$

In the case of interest, the normal to the front is given by

$$\mathbf{n}(\xi(t),t)=\left(\frac{\partial y(\xi(t),t)}{\partial\xi(t)},\quad -\frac{\partial x(\xi(t),t)}{\partial\xi(t)}\right). \tag{9.1.11}$$

Since at the shock front $d_tA\equiv a_0Md_xA$, we note that (9.1.10) allows determination of A'/A from the geometry of the shock front and the Mach number distribution on it. All quantities in (8.2.6) are thus known and we can integrate these equations in time, simultaneously with the integration of (9.1.1), using the Runge-Kutta scheme.

In order to evaluate the quantities required in equations (9.1.10) and (9.1.11) we fit a cubic spline to the shock front with the parametrisation being with respect to the arclength along the shock. This is achieved numerically as discussed in chapter 4, with the notation for the spline as described in that chapter. In order that the shock front is adequately resolved we are guided by the resolution condition of Henshaw et al. in selecting the appropriate number of node points. If we denote by $\delta\xi_{av}$ the average arclength between nodes then this criterion is

$$\delta\xi_{av}=\xi_N/N=k_1<<1, \tag{9.1.12}$$

where ξ_N is the length of the shock front and k_1 is usually taken to be 0.01. This condition provides a lower bound on the number of node points, N, used to represent the shock front. In order to maintain this resolution as the solution is iterated in time, the point insertion/deletion scheme of Henshaw et al. is implemented. In expansive regions of the flow extra points are added in order that the shock front

is adequately resolved. In compressive regions points are deleted which effectively fits a shock-shock, or discontinuity in the Mach number distribution on the shock. The shock-shock corresponds to the triple point in Mach reflection. The point spacing is tested after every time step and we demand that

$$\sigma_{min} < \delta\xi_i/\delta\xi_{av} < \sigma_{max}. \tag{9.1.13}$$

If $\delta\xi_i < \sigma_{min}\delta\xi_{av}$, the node $\mathbf{x}_i$ is deleted. If $\delta\xi_i > \sigma_{max}\delta\xi_{av}$ a new point is inserted by evaluating the spline functions at $\xi_{i-1} + \delta\xi_i/2$. Typically we choose σ_{min} and σ_{max} as 0.5 and 1.5 respectively. We should note at this point, that when considering propagation about convex corners it was found that to obtain an adequate solution of equations (8.2.6) the insertion of points should not occur while the shock is propagating around the corner. After the shock has propagated around the corner points may be inserted to maintain the resolution of the shock. Any addition of points prior to this corrupted the solution. When using this scheme to reproduce the Whitham theory (setting $Q_1 \equiv 0$), though, it was found that it was essential to add points during the propagation around the corner in order to obtain a solution of the highest accuracy. If points were only added after propagation around the corner then the solution, although acceptable, exhibited a small error. No adequate reason has been found for this behaviour.

For compressive flows, such as propagation into concave corners, it was found necessary to employ the two step smoothing procedure of Henshaw et al. every 10 to 50 iterations in order to dampen high frequency errors. If we denote by $\tilde{\mathbf{x}}_i(t)$ the smoothed position of the i'th node, and by $\tilde{M}_i(t)$ and $\tilde{Q}_{1_i}(t)$ the smoothed values of M and Q_1 at the i'th node, then this procedure is given by

$$\tilde{\mathbf{x}}_i(t) = \frac{1}{2}\left(\mathbf{x}_{i-1}(t) + \mathbf{x}_{i+1}(t)\right), \tag{9.1.14}$$

$$\tilde{M}_i(t) = \frac{1}{2}\left(M_{i-1}(t) + M_{i+1}(t)\right), \tag{9.1.15}$$

$$\tilde{Q}_{1_i}(t) = \frac{1}{2}\left(Q_{1_{i-1}}(t) + Q_{1_{i+1}}(t)\right). \tag{9.1.16}$$

Such smoothing is unnecessary in the case of expansive flows.

To account for boundaries Henshaw et al. propagate all node points interior to the boundaries and then determine the points on the boundaries so that the shock meets them at right angles. This reflects the fact that the rigid boundary is indeed a ray and that propagation is along a ray, perpendicular to the shock front. In this work, however, we wish to investigate shock diffraction about convex corners of obtuse angle in which such a method would fail. Thus we propagate points on the boundaries such that their trajectory is always along the wall. This is achieved by clamping the spline representing the shock front at the boundary. To deal with sharp corners we must compute a smoothed boundary, and the smoothing is performed by circular segments. In order to select an appropriate time step we are guided by the considerations of Henshaw et al. In that scheme the time step, δt, is chosen such that

$$\frac{\delta t}{\delta \xi_{min}} = \frac{\delta t}{\min_{i,t} \delta \xi_i(t)} \leq \frac{\delta t}{\sigma_{min} \delta \xi_{av}} < k_2 = O(1), \tag{9.1.17}$$

where the inequality follows from (9.1.12) and k_2 is usually chosen to be equal to 0.2. This relation is the Courant-Friedrichs-Lewy condition and in the work of Henshaw et al. gave stability in all cases run. In this application (9.1.17) provides an upper bound on the selection of a time step, δt. In order that the solution remains accurate in cases where sharp corners are smoothed by arcs of small radius we further reduce the length of the time step.

To validate the scheme developed the value of Q_1 was set identically equal to zero. Equations (8.2.6) then reduce to those of Whitham. Problems of shock diffraction by convex and concave corners where analytic solutions exist in the strong shock limit were then computed. These examples are as those used by Henshaw et al. to validate their scheme. The results were found to be in excellent agreement with the analytical solutions.

9.2. Computational results

Application of the numerical scheme allows us to investigate shock diffraction by concave and convex corners. In all computations the ambient sound speed,

a_0, was set equal to one. Figure 9.2.1 shows the successive shock profiles as an initially plane shock of initial Mach number 10 is diffracted by a concave corner of 30° deviation. We note the appearance of the Mach stem and the constant angle that the trajectory of the triple point makes with the wall. Both the theory of Whitham and three shock theory give expressions for the dependence of this angle upon the deviation of the corner and Whitham (1957) has shown good agreement between the two results in the limit of strong shocks. The dependence determined numerically here differs little from that of Whitham. This is not unexpected as consideration of the propagation of cylindrical and spherical waves in the strong shock limit has indicated an extraordinary range over which the Whitham theory should be valid in the case of a compressive geometry.

Recalling the results of that consideration we expect that the behaviour in an expanding geometry should differ. Thus we consider the diffraction of an initially plane shock by convex corners and figure 9.2.2 shows successive shock profiles for the propagation around a corner of deviation 90° of a shock wave of initial Mach number 4. The significant feature that we observe is the appearance of an inflection point in the shock shape near the wall. The theory of Whitham does not predict such a feature of the shock shape, the curvature of the shock being of the one sign in that theory (Whitham 1957, 1974).

We recall the results of Lighthill (1949) in his analysis of the diffraction of a shock of any strength by sharp corners of small deviation. In that work, it is predicted that for shocks with an initial Mach number greater than 2.531 such an inflection point is indeed a feature of the diffracted shock's shape, in the case of a convex corner. We further note the experimental work of Skews (1967a,b) in which the shapes of shock waves diffracted by sharp convex corners of large angular deviation were photographically captured. We illustrate such a result in figure 9.2.3, for a corner of 90° deviation and initial Mach number of 4. The corner is at (0,0). The solid line represents the experimental shock shape. Since there are no time and length scales in such a geometry the solution for the shock

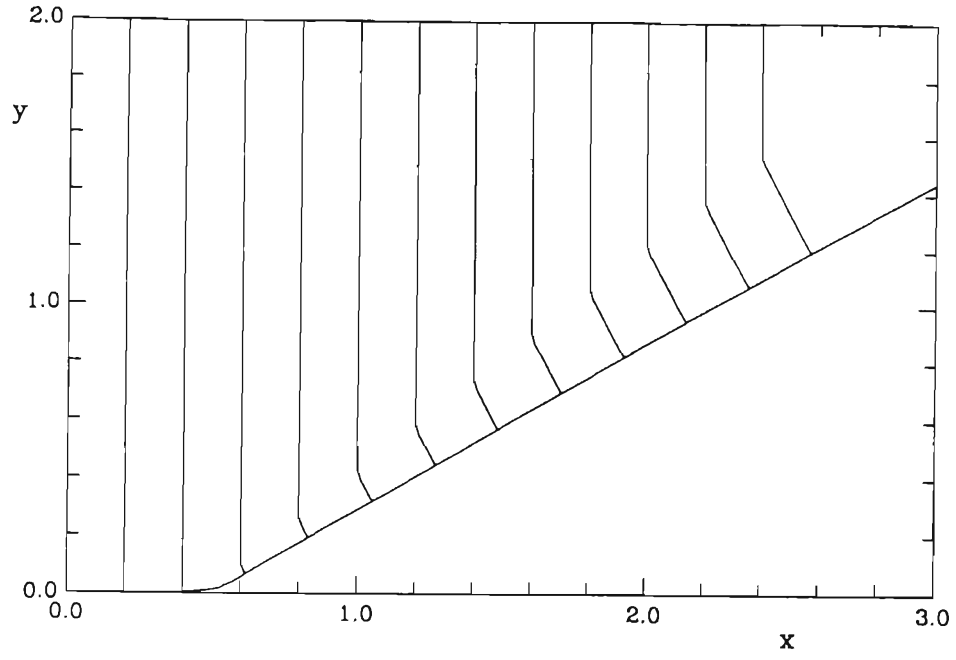

Figure 9.2.1. Diffraction of a plane shock wave by a concave corner of 30 ° deviation.

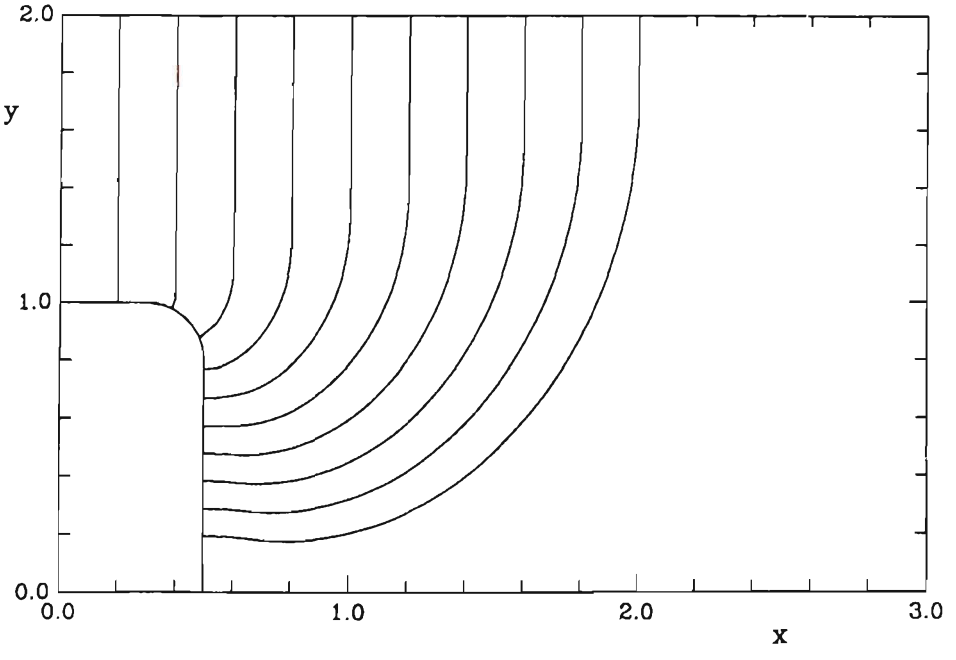

Figure 9.2.2. Diffraction of a plane shock wave by a convex corner of 90 ° deviation.

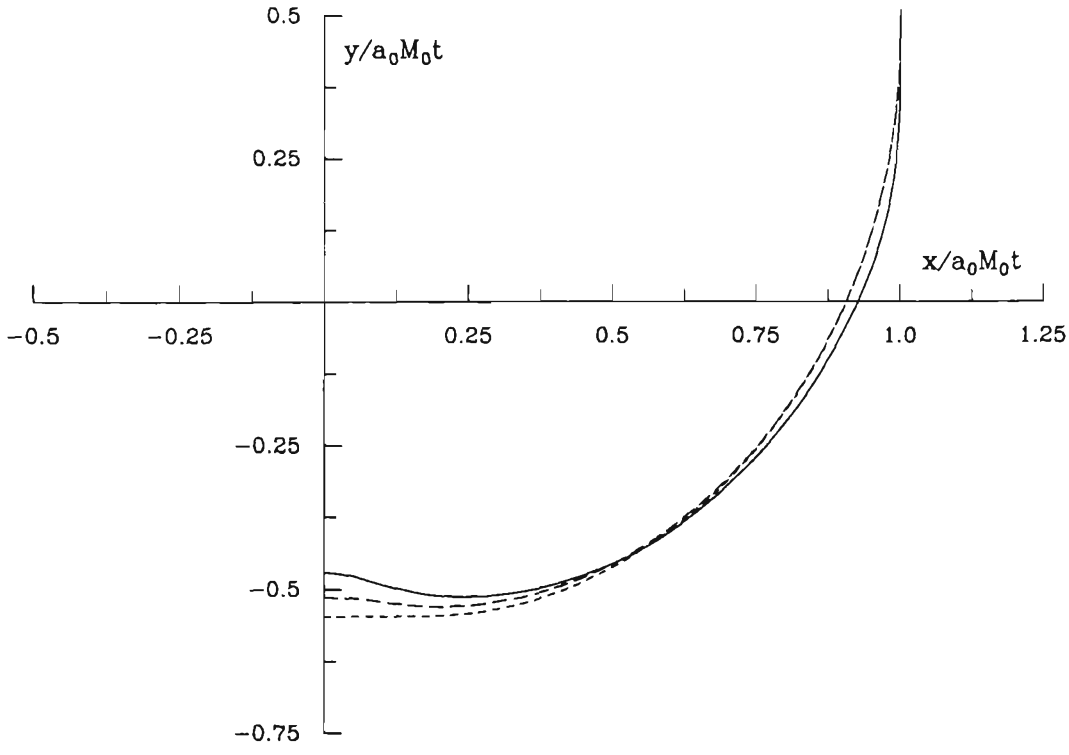

Figure 9.2.3. Comparison of shock shapes for diffraction by a convex corner of 90° deviation.
——— Experiment (Skews 1967a). – – – This work. - - - - - Whitham.

shape is self similar in time. The dashed shock shapes were computed using the numerical scheme described in the preceeding section. The shape computed using the results of this work provides a description of the inflection point. The solution as determined by the theory of Whitham is less accurate. At this point, we note that the computed shock shapes were determined by smoothing the corner using circular arcs.

We can gain an indication of the success of the method of this work, independent of the manner in which we smooth the corner, by computing the Mach number at the wall as a function of the wall deviation. Since the solution is a similarity solution, this value remains constant after the shock has propagated around the corner. This is a feature of the solution of the equations of geometrical shock dynamics even when the corner is smoothed (see Whitham, 1974). The result for an initial Mach number of 4 is shown in figure 9.2.4. The solid line denotes the variation predicted by the theory of Whitham. The squares denote the experimental values obtained by Skews (1967a), with the dashed line fitted to this experimental data. The circles denote the values obtained from the numerical scheme implemented here. We note the excellent agreement obtained between the results computed here and the experimental data. The numerical results are only shown up to an angle of 110°. Beyond this angle the numerical scheme did not yield a solution that exhibited a constant value of the Mach number at the wall. This is believed to be purely a feature of the numerical scheme. For smaller angles the Mach number at the wall oscillated slowly about a mean value ($\pm.02$), but for angles greater than 110° decayed away at a fairly constant rate. In any case, the agreement is excellent with the prediction of the inflection point in the shock shape being a particularly spectacular feature. Despite the failure of the equations of propagation truncated at the second equation when applied to propagation in the strong shock limit in an expanding geometry, for more moderate values of the Mach number, such as in this example, the truncated equations provide an excellent description of propagation into an expanding geometry.

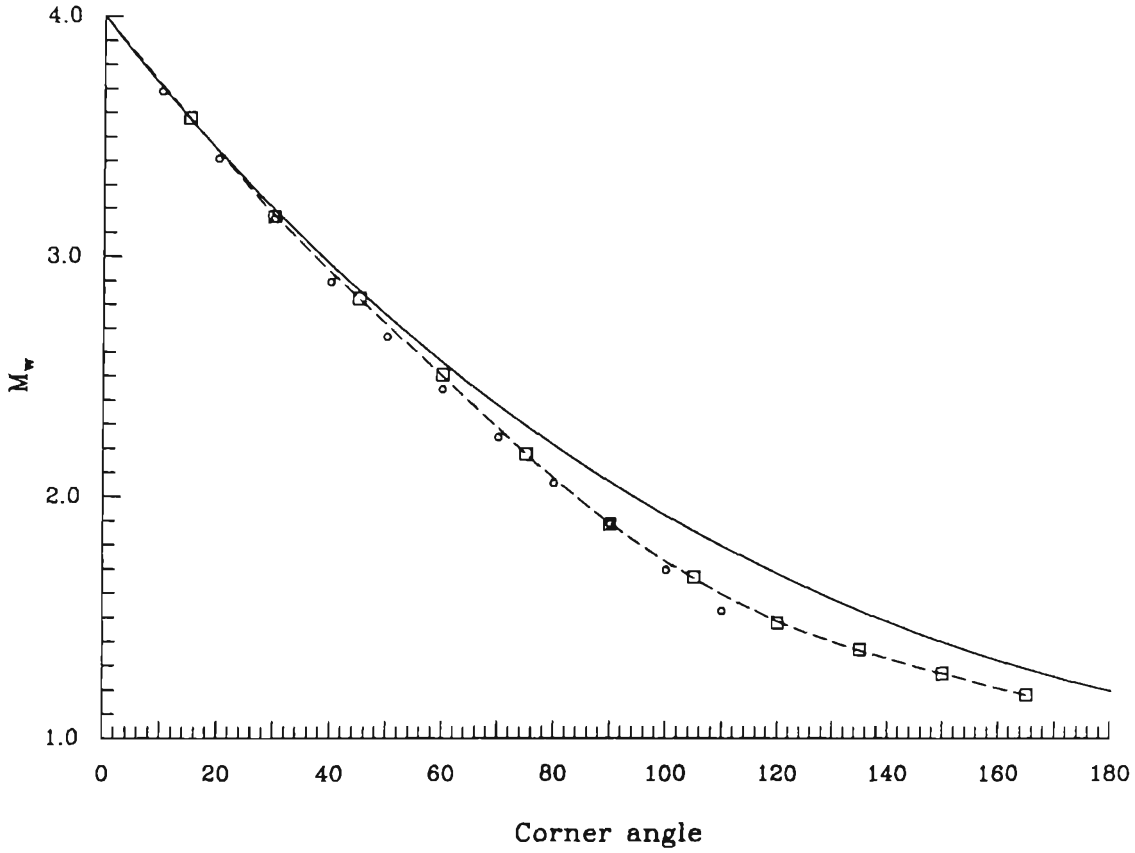

Figure 9.2.4. Comparison of experimental and theoretical results for the Mach number at the wall after diffraction by a convex corner, as a function of the corner angle. ——— Whitham. □ Experiment (Skews 1967a). ○ This work. The dashed line is a curve fitted to the experimental data.

From the structure of the equations of propagation we can deduce that an inflection point must indeed be a feature of the shock shape. We may write the first equation in our infinite sequence as

$$\frac{dM}{dt} = \frac{-a_0 M \rho a^2 u A'/A}{(a+u)(d_M p + \rho a d_M u)} + \frac{\left(1 - \frac{a_0 M}{a+u}\right)}{(d_M p + \rho a d_M u)} Q_1. \tag{9.2.1}$$

At the wall $dM/dt = 0$, so that here we have

$$-\chi_1 \dot{A}/A + \chi_2 Q_1 = 0, \tag{9.2.2}$$

where χ_1 and χ_2 are positive constants, since they are functions of M. Since the wall is a ray propagation is parallel to it and we have here that

$$\frac{\partial \mathbf{x}}{\partial \xi} = (\sin\theta, \cos\theta), \tag{9.2.3}$$

where θ is the deviation of the convex corner measured below the horizontal, ξ is the arclength along the shock as described in the previous section and $\mathbf{x}$ is the position vector of a point on the shock front. From (9.1.10) we obtain

$$\dot{A}/A = a_0 M \left(\sin\theta \frac{\partial^2 y}{\partial \xi^2} - \cos\theta \frac{\partial^2 x}{\partial \xi^2}\right). \tag{9.2.4}$$

It is a simple matter to show that

$$\frac{d^2 y}{dx^2} = \left(\sin\theta \frac{\partial^2 y}{\partial \xi^2} - \cos\theta \frac{\partial^2 x}{\partial \xi^2}\right) / \sin^3\theta, \tag{9.2.5}$$

so that (9.2.2) yields

$$\frac{d^2 y}{dx^2} = \frac{\chi_2 Q_1 \sin^{-3}\theta}{\chi_1 a_0 M}, \tag{9.2.6}$$

at the wall. Now for $\theta \in [0, \pi]$ $\sin\theta \geq 0$. Since the flow behind the shock is decaying we have $Q_1 < 0$ so that at the wall $\frac{d^2y}{dx^2} \leq 0$. On that part of the shock near to the undisturbed part we have $\frac{d^2y}{dx^2} > 0$ and since the shock shape is a continuous curve there must exist some point at which $\frac{d^2y}{dx^2} = 0$, namely the inflection point. Provided our assumption that $Q_1 < 0$ is valid, then the existence of an inflection point is independent of the Mach number in this theory.

It is pertinent to make a few comments regarding the full range of experimental results presented by Skews (1967a). He notes that it is the inflection point that

gives rise to the smaller Mach number at the wall than the value predicted by the theory of Whitham. In the theory presented here the existence of an inflection point for all Mach numbers indicates a predicted Mach number less than that of the Whitham theory, although for small Mach numbers the difference is negligible. The results of Skews indicate that for weaker shocks (initial Mach number < 3) the Mach number at the wall is greater than the value predicted by Whitham's theory. In this context we recall the result of Lighthill that in the case of small corner angles an inflection point is only evident for $M > 2.531$. We further recall that the theory of geometrical shock dynamics, when applied to diffraction by convex corners in the case of weak shocks, predicts that the speed of propagation of the first disturbance along the shock is half its correct value (Whitham 1957). These results suggest some deficiency in the approach of geometrical shock dynamics in considering the propagation of weak shocks, although in this last example it is found that the Mach number at the wall is predicted with good accuracy by the theory of geometrical shock dynamics. This result further suggests that perhaps it is the neglect of transverse flow behind the shock that causes disagreement. It might be supposed that in the case of weak shocks the influence of the transverse flow is of the same order as that of the varying area, or the longitudinal flow that has been accounted for in this work. Further investigation is required to clarify this point.

We conclude with some example computations of the diffraction of an initially plane weak shock in water, in which the initial flow field behind the shock is not uniform as characterised by a non-zero initial value of Q_1. The computations were performed using the equations of propagation truncated at the second equation. We have chosen the initial Mach number to be 1.11 and the initial value of Q_1 is -0.381. This value of the Mach number is a typical value for a shock wave produced by an underwater explosion and a non-zero value of Q_1 may be due to an exponential decay of the pressure. Successive shock profiles for propagation about convex and concave corners of 30° deviation are shown in figure 9.2.5. For

propagation about a convex corner the shock advances into an expanding geometry and the Mach number at the wall decreases. The variation of the Mach number with horizontal distance, x, for this example is shown in the first frame of figure 9.2.6. Also shown is the variation computed using the A-M relation. In the initial stages of the propagation, when the wave is plane, the theory developed here predicts the slow decay of the Mach number due to the interaction of the shock with the non-uniform flow behind. This feature is not described by application of the A-M relation. Geometrical shock dynamics utilising the A-M relation predicts that the Mach number at the wall after propagation about the corner should be constant and the numerical results confirm this. The departure from this for large x is due to the accumulation of numerical errors. The result computed using the theory of the previous chapter also yields an approximately constant value of the Mach number at the wall, this value being only slightly less than that obtained from the A-M relation. Due to the non-zero value of Q_1 the Mach number continues to decay, but at a very slow rate.

The results for diffraction by a concave corner are most interesting. Once the shock strikes the corner Mach reflection occurs and the Mach number at the wall rises to a value of about 1.315, this value being approximately common to the results computed by both methods. As the shock propagates the triple point moves away from the wall, its trajectory denoted by the dashed line in figure 9.2.5. Whitham's theory of geometrical shock dynamics predicts that the Mach number at the wall should be constant and the graph of figure 9.2.6 reflects this, the oscillation about the true value being numerical in its origin. The equations of propagation, truncated at the second equation, predict that after propagation about the corner the Mach number decays away, at an approximately constant rate. This is due to the influence of the non-uniform flow conditions behind the shock. This rate of decay appears to be greater than that for the initially plane wave. The compressive geometry not only causes the Mach number to initially increase, but also Q_1 and this manifests itself in the increased rate of decay of M.

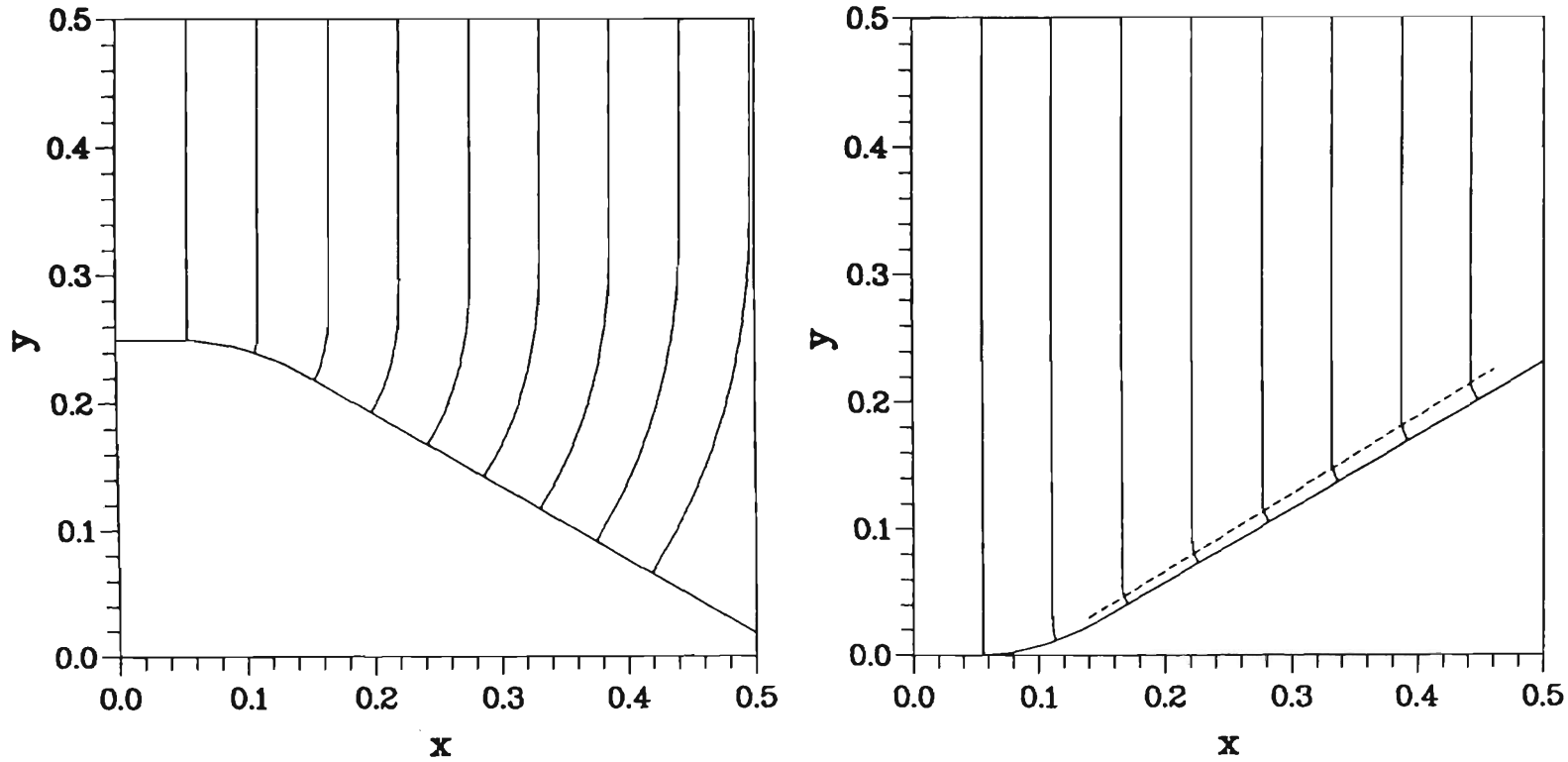

Figure 9.2.5. The diffraction of an underwater blast wave by convex and concave corners of 30° deviation. The dashed line denotes the trajectory of the triple point in the case of the concave corner.

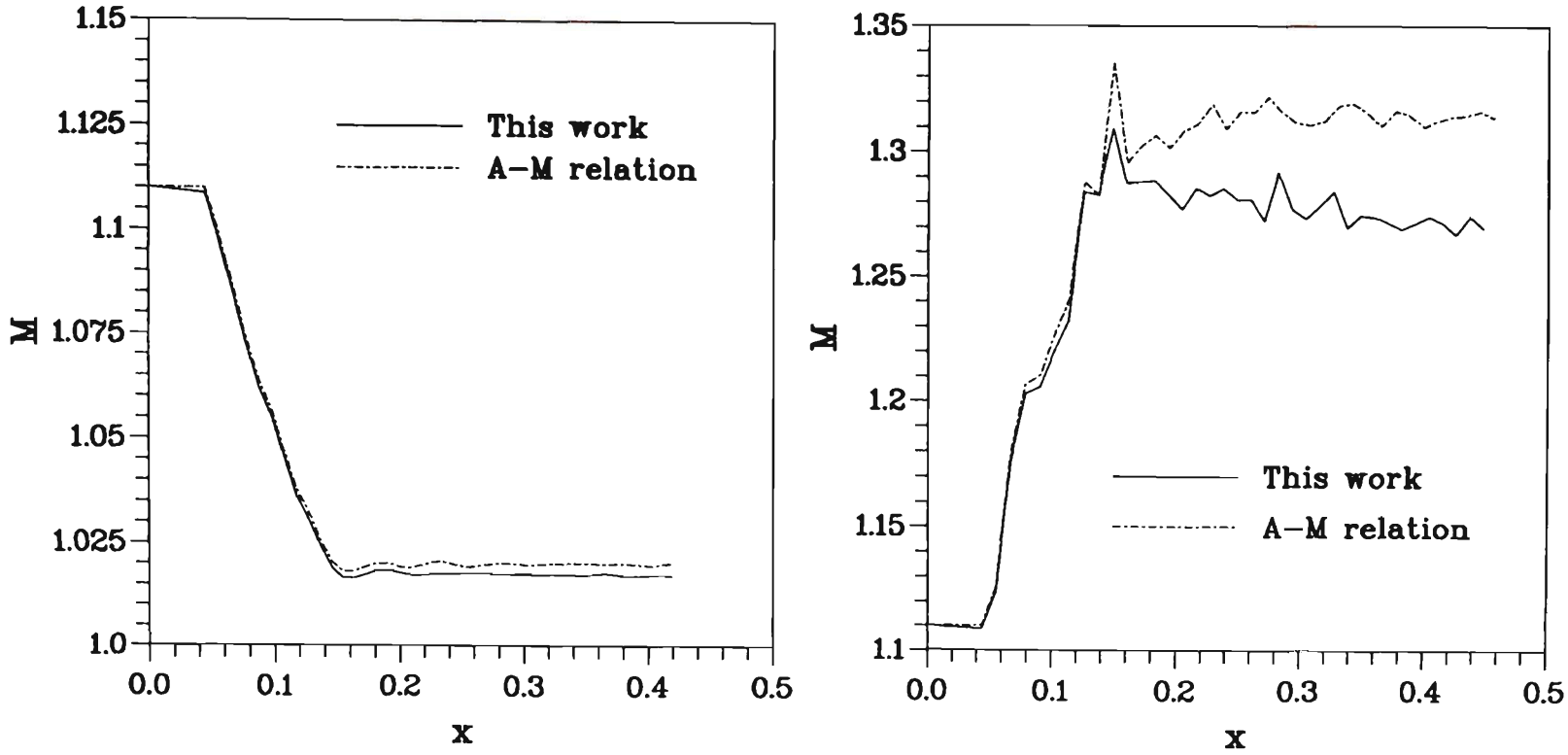

Figure 9.2.6. The Mach number at the wall as a function of x for propagation as illustrated in figure 9.2.5. The frames are respectively for diffraction by a convex and concave corner.

10

CONCLUDING REMARKS AND FUTURE DIRECTIONS

In this volume we have presented the results of mathematical modelling undertaken of underwater explosion bubble motion and underwater blast wave propagation. It is these phenomena that are expected to be the principal damage causing agents of an underwater explosion. It is worthwhile to briefly consider the significant results of this investigation, an exercise that gives clear indication of future research directions.

In the first instance we have considered global conservation of momentum via the Kelvin impulse, and exploited this concept in undertaking elementary modelling of explosion bubble motion in which the bubble is constrained to remain spherical throughout its lifetime. In this approach the velocity potential of the flow induced by bubble motion is represented by singularities and ordinary differential equations describing the bubble radius and centroid position as functions of time are deduced. These may be solved numerically with little expense, a feature that is particularly advantageous in the consideration of motion in geometries in which there is no simplifying symmetry and full numerical computation of the motion is expensive. The geometries that we can successfully treat are those whose boundary conditions can be satisfied by appropriate image sets.

From the early motion of spherical bubbles we have attempted to infer aspects of the motion of real bubbles which, in the later stages of their life, deform from spherical shape and develop high speed liquid jets. The direction of migration at the end of the bubble life or first pulsation, as predicted by the spherical model, has been identified as the direction in which the jet is formed in the case of non-spherical collapse. Determination of the null impulse state in the case of buoyant cavitation bubble motion above a rigid boundary in an axisymmetric geometry has confirmed the validity of this proposition, the results of numerical simulations

using the boundary integral method providing the necessary confirmatory data. It is at the null impulse state that the oppositely acting buoyancy and Bjerknes forces balance and the bubble centroid does not migrate upon collapse.

The study of explosion bubble motion using the spherical model has further provided indications of the criteria under which the bubble will rebound, despite significant deformation from spherical shape occurring during collapse. These criteria are motion in the neighbourhood of the null impulse state and motion characterised by a small strength parameter.

In order to confirm the correctness of these criteria the boundary integral method utilised to compute cavitation bubble motion has been modified in order to compute the motion of deforming explosion bubbles. This investigation has necessitated the implementation of a second order time integration scheme and smoothing of the bubble surface and potential function on this surface in order to numerically capture rebound. The results of these computations have confirmed the criteria proposed as necessary for the rebound of a non-spherical bubble, but the growth of jets upon rebound has been demonstrated and it appears that the high pressures that exist within the bubble upon collapse will not suppress jetting motion, only delay it.

The computation of the pressure field in the fluid during collapse has given insight into the mechanism of jet formation and the reasons for the apparent success of employing a spherical model to predict aspects of the motion of deforming bubbles. During collapse the bubble undergoes a period of rapid acceleration. The significant feature of the pressure field of an accelerating bubble is a peak of pressure in the fluid, located behind the bubble, in a direction that closely correlates with the direction of the acceleration. It is this region of maximum pressure that drives the jet into the bubble. Since such a maximum of pressure is a feature of the flow field induced by an accelerating spherical bubble it becomes apparent that identifying the direction of migration (which is almost co-incident with the direction of the acceleration, due to the motion upon collapse almost beginning

from rest) of a spherical bubble upon collapse with the direction of the jet has a firm physical basis. The computation of the Kelvin impulse for collapsing non-spherical bubbles and comparison with the value computed using the spherical model provides further confirmation of the validity of employing this model to provide information regarding the later motion of deforming bubbles, as well as indicating limitations of the approach.

To date all computations of bubble dynamics using the boundary integral method have only been able to proceed up until the time that the jet impacts upon the far side of the bubble. In this work we have considered the impact and determined the appropriate initial conditions that prevail in the doubly connected flow domain immediately following the instant of impact. A boundary integral algorithm has been developed to compute the subsequent motion of the toroidal bubble, this algorithm exploiting a cut in the doubly connected geometry in order that the flow domain may be considered as simply connected. The computed motion of the toroidal bubble has indicated the oscillatory motion of such a bubble, which is in qualitative agreement with the results of recent experimental observations. Of further significance is the demonstration that upon transition to the toroidal geometry the peak of pressure in the flow field, which prior to the transition is located behind the jet and driving it inwards, is located ahead of the bubble. For collapse in the neighbourhood of a rigid boundary the peak of pressure after the transition to the toroidal geometry will be located between the bubble and the boundary. This phenomenon will occur in all cases where the jet is directed towards the boundary, except perhaps where only a thin film of fluid separates the bubble from the boundary, and this region of high pressure may produce a significant loading of the nearby boundary and may be the cause of damage to it.

Much further work presents itself in view of the results presented here. The theory of spherical bubble dynamics exploits the Kelvin impulse in the derivation of equations of motion and by its definition we expect that the Kelvin impulse and jet direction will be similarly directed. The work of Blake and his co-workers

has explicitly exploited this feature to determine the direction of the jet, the magnitude of the impulse not appearing in the consideration. Thus it remains as a task to attempt to determine further characteristics of the jet from a knowledge of the distance of inception (γ), the strength of the buoyancy force (δ) and the strength of the explosion (ϵ); the physical parameters that govern the motion. We expect that the magnitude of the Kelvin impulse should enter the consideration. Particular features of the jet that we wish to determine include its breadth and speed, although to proceed in such an endeavour requires a precise mathematical definition of these quantities. It seems reasonable that some averaged quantity would be appropriate.

In any case, the recent work of Paull and Blake (1990) has considered various quantities that are conserved throughout the motion of a bubble, following the work of Benjamin (1987) and Longuet-Higgins (1989). The underlying theme of this investigation is the hope that these conservation principles may be exploited in the same way that the Kelvin impulse has been exploited to determine features of the bubble upon collapse. We recall in this context that the Kelvin impulse arises naturally in consideration of momentum conservation. To proceed in such an investigation would be considerably aided by attention to the physical interpretation of these conservation expressions. Some of the quantities, such as momentum and energy, are familiar, but others, such as the circulation based radial moment of momentum, are less so.

An alternate approach may be empirical in nature. With the speed of modern computers it is possible to calculate the motion of bubbles over large regions of the physical parameter space and we could then compile data concerning the variation of quantities such as the jet speed and width with the physical parameters, and attempt to fit empirical relations describing the variation. For such relations to have any applicability beyond those regions of the parameter space over which data has been compiled they must have some basis in theory. The investigation of conservation quantities may provide such a basis so an investigation incorporating

both the compilation of empirical data and consideration of conservation quantities appears to be an appropriate course of action in this endeavour.

The phenomenon of rebound demonstrated in the computations presented here must be interpreted in view of the experimental evidence compiled during, and since, WWII that the rebound is accompanied by the emission of an acoustic wave of finite amplitude. Indeed, in the context of underwater explosion research, these secondary pressure waves have received much attention as possible secondary damage causing agents. Although the computations presented here give an indication of the physical circumstances under which such emissions should be enhanced by the suppression of jetting, the incompressible model utilised here can provide no description of this phenomenon. It would be of interest to investigate this matter further. Equations describing spherical oscillations in a fluid of low compressibility have been given (see Prosperetti, 1987, for a derivation as well as reference to previous works of significance in this field), but the general problem of the generation of waves of finite amplitude upon the rebound of a non-spherical bubble requires numerical treatment. Indeed, the motion in an incompressible fluid is a much simpler problem yet it requires application of the boundary integral method. A first approach may be to employ a boundary integral method to compute solutions of the wave equation but this would provide a solution consistent only to $O(c^{-1})$ where c is the speed of sound. It is thus apparent that a more elaborate numerical approach to the problem is necessary. Some interesting phenomena could be expected. For instance, we would suppose that upon the rebound of an element of the bubble surface the wave so emitted has a front with a shape similar to that of the surface from which it was emitted. Around the edges of the jet we might expect that the normal to the wavefront there is directed towards the axis of symmetry and so some focussing effect may be observed. Such speculation must be confirmed by theoretical and experimental investigation. We would further suppose that far enough away from the bubble the emitted wave would exhibit much similarity to a spherical wave.

Having developed an algorithm for the computation of the motion of toroidal bubbles many further phenomena are conceivably now accessible to numerical investigation. A spectacular feature of the computation of cavitation bubble motion near a free surface is the generation of a sharp spike upon the free surface as demonstrated in the work of Blake et al. (1987). Accompanying the formation of this spike is a jet piercing the bubble, directed away from the free surface. The computation to date has only been completed up until the time that the jet pierces the bubble. Subsequent to this time the collapse of the free surface spike will generate an outgoing travelling wave. In the case where the bubble is caused by an underwater explosion, its oscillatory motion will force this wave motion. In order to make an attempt at computing this free surface motion it is necessary to compute the motion of the bubble once it has evolved into toroidal form. This can now be achieved. Although not specifically related to bubble phenomena, the method developed here may also be applied to the transition to a doubly connected flow domain that occurs upon the overturning of steep surface waves on water.

The feature of this model that is perhaps most contentious is the lack of a detailed description of the mechanism by which the two contacting surfaces break down and become one as the jet impacts upon the far side of the bubble. This phenomenon is worthy of much further attention. Studies have addressed this matter with Oguz and Prosperetti (1989) considering the effect of surface tension in the contact of liquid surfaces. A related study is that of Chesters and Hofman (1982) in which the thin layer of fluid between two approaching bubbles is considered. Neither of these studies, however, consider in detail the process by which the initial breakup of the surface occurs.

Such a study is essential in view of the experimental results of Vogel et al. (1989) in which several examples of motion in a doubly connected geometry exhibit behaviour different from that indicated by the computations presented here. Due to the small scale of the bubbles considered in that work surface tension is expected to be a dominant influence as the surfaces come together. Clarification of the role

of surface tension, viscosity and compressibility in the process of liquid contact is a source of much further research and essential to a complete understanding of the evolution into, and subsequent motion of toroidal bubbles.

The investigation of the motion of a shock wave down a tube of slowly varying cross section has yielded a technique whereby non-uniform flow conditions behind the shock may be accounted for in the theory of geometrical shock dynamics. It has been demonstrated that the equations of motion yield a mathematical structure in which the motion of the shock is described by an infinite sequence of ordinary differential equations. If we denote by Q_i $(i = 0, 1, 2, \ldots)$ the dependent variables in this sequence then it has been found that the rate of change of Q_i depends only upon $Q_0, \ldots, Q_{i+1}$ and so by truncation of the term involving Q_{i+1} these equations are closed, and we may prove certain results pertaining to the convergence of the closure scheme.

Of greater practical significance is the comparison of shock motion computed using these equations with known solutions and experimental results. Calculation of the propagation of a spherical underwater blast wave yields the Mach number and time constant as functions of distance and the agreement with analytic solutions is excellent. Furthermore, computation of the diffraction of initially plane shock waves by convex corners predicts the observed inflection point in the shock shape near the wall, a feature not evident in the theory of geometrical shock dynamics as developed by Whitham.

The higher terms in the infinite sequence are, in fact, functions of higher derivatives of the flow quantities, evaluated at the shock. Closure of the infinite sequence at higher equations includes higher derivatives in the description of the motion of the shock and thus allows some account to be taken of non-uniform flow conditions behind the shock. When these equations of propagation are implemented in the numerical scheme of geometrical shock dynamics we have a powerful technique for the rapid and accurate computation of the motion of shock waves. Since only quantities evaluated at the shock are necessary for the description of the motion,

any numerical algorithm need only include a discrete representation of the shock front rather than the whole flow domain, a simplification that reduces considerably the computational effort. With account now able to be taken of non-uniform flow conditions behind the shock a much wider class of problems in shock propagation is amenable to solution by the method of geometrical shock dynamics.

In order to apply geometrical shock dynamics to propagation in water it is necessary to employ an appropriate equation of state and utilise the Rankine-Hugoniot shock jump conditions to write the flow quantities immediately behind the shock in terms of the Mach number. By following this procedure we may formulate the theory of geometrical shock dynamics for other materials upon provision of an appropriate equation of state. In this way shock propagation in a variety of materials could be investigated exploiting the economy of computational effort required in the implementation of the method.

The example of weak shock diffraction by convex corners of small angular deviation suggests some deficiency in the approach of geometrical shock dynamics in this regime. Although the theory well predicts the value of the Mach number at the wall after the shock has diffracted around the corner, the theory predicts that the speed of propagation of the first disturbance that originates from the corner is half its correct value. Although the work undertaken here allows account to be made of longitudinal non-uniformities in the flow field behind the shock it is not unreasonable that in the case of weak shock waves the influence of tangential variations of flow quantities behind the shock may contribute to the same order as the longitudinal variation and changing area of the tube. By averaging the equations of motion across the area of the shock tube these variations are excluded from the mathematical description. It is perhaps worthwhile, then, that future research address this question to determine if a mathematical structure as presented here may be demonstrated if tangential flow is allowed for in the description. Such an investigation must also address the question of the exact conditions under which the slowly varying equations in one space dimension provide an adequate description

of shock propagation down a tube of varying cross section.

In conclusion, the modelling undertaken here has provided considerable information regarding the principal physical phenomena associated with an underwater explosion. We have developed approximate techniques for predicting the direction of jet formation upon the collapse of an underwater explosion bubble and have utilised the boundary integral method to provide a more complete description of the explosion bubble phenomenon, including the evolution into toroidal form. The generalisation of geometrical shock dynamics is particularly suited to computing the diffraction of an underwater blast wave by targets. With these techniques available, we have a sound theoretical base upon which to assess the potential for damage to structures by underwater explosions.

APPENDIX 1

First order partial derivatives at the shock

Application of the results of section 8.1 (equations (8.1.27) - (8.1.32)) for the partial derivatives of the flow quantities at the shock in the case $n = m = 0$ yields

$$\partial_t p = \Big[\left((a^2 + u(a_0 M - u))d_M p + a_0 M \rho a^2 d_M u\right) d_t M + a_0 M \rho a^2 u(a_0 M - u) A'/A \Big] / (a^2 - (a_0 M - u)^2), \tag{A1-1}$$

$$\partial_x p = -\Big[\left((a_0 M - u)d_M p + \rho a^2 d_M u\right) d_t M + \rho a^2 u(a_0 M - u) A'/A \Big] / (a^2 - (a_0 M - u)^2), \tag{A1-2}$$

$$\partial_t u = \Big[\left(\frac{a_0 M}{\rho} d_M p + (a^2 + u(a_0 M - u))d_M u\right) d_t M + a_0 M a^2 u A'/A \Big] / (a^2 - (a_0 M - u)^2), \tag{A1-3}$$

$$\partial_x u = -\Big[\left(\frac{1}{\rho} d_M p + (a_0 M - u) d_M u\right) d_t M + a^2 u A'/A \Big] / (a^2 - (a_0 M - u)^2), \tag{A1-4}$$

$$\partial_t \rho = \Big[\left(a_0 M d_M p + a_0 M \rho (a_0 M - u) d_M u - u(a^2 - (a_0 M - u)^2) d_M \rho\right) d_t M + a_0 M \rho u (a_0 M - u)^2 A'/A \Big] / \left((a_0 M - u)(a^2 - (a_0 M - u)^2)\right), \tag{A1-5}$$

$$\partial_x \rho = -\Big[\left(d_M p + \rho (a_0 M - u) d_M u - (a^2 - (a_0 M - u)^2) d_M \rho\right) d_t M + \rho u (a_0 M - u)^2 A'/A \Big] / \left((a_0 M - u)(a^2 - (a_0 M - u)^2)\right), \tag{A1-6}$$

and using $a^2 = \gamma p/\rho$ we obtain

$$\partial_t a = -\frac{1}{2}\Big[\left(\frac{1}{\rho a}(a^2(\gamma u + (1-\gamma)a_0 M) - \gamma u (a_0 M - u)^2) d_M p + (1-\gamma) a_0 M a (a_0 M - u) d_M u + \frac{au}{\rho}((a_0 M - u)^2 - a^2) d_M \rho\right) d_t M + (1-\gamma) a_0 M a u (a_0 M - u)^2 A'/A \Big] / \left((a_0 M - u)(a^2 - (a_0 M - u)^2)\right), \tag{A1-7}$$

$$\partial_x a = \frac{1}{2}\Big[\Big(\frac{1}{\rho a}\left(a^2 - \gamma(a_0 M - u)^2\right) d_M p + (1-\gamma) a (a_0 M - u) d_M u$$

$$- \frac{a}{\rho}(a^2 - (a_0 M - u)^2) d_M \rho \Big) d_t M + (1-\gamma) a u (a_0 M - u)^2 A'/A \Big] \qquad (A1-8)$$

$$/\left((a_0 M - u)(a^2 - (a_0 M - u)^2)\right).$$

APPENDIX 2

Equations of shock propagation in the strong shock limit

From the shock jump conditions (equations (7.2.7) - (7.2.11)), we have as $M \to \infty$

$$u \sim a_0 \alpha_1 M, \; p \sim \rho_0 a_0^2 \alpha_1 M^2, \; \rho \sim \rho_0 \alpha_2, \; a \sim a_0 \alpha_3 M, \tag{A2-1}$$

where

$$\alpha_1 = \frac{2}{\gamma+1}, \quad \alpha_2 = \frac{\gamma+1}{\gamma-1}, \quad \alpha_3 = \frac{2\mu'\gamma}{\gamma+1}, \tag{A2-2}$$

with μ' the limiting value of μ, given as

$$\mu' = \sqrt{\frac{\gamma-1}{2\gamma}}. \tag{A2-3}$$

Substituting into the expressions of appendix 1 and using $d_t \equiv a_0 M d_x$ we find

$$\partial_t u \sim a_0^2 M(\nu_1 M' + \nu_2 M A'/A), \tag{A2-4}$$

$$\partial_x u \sim -a_0(\nu_3 M' + \nu_2 M A'/A), \tag{A2-5}$$

$$\partial_t \rho \sim a_0 \rho_0(\nu_4 M' + \nu_5 M A'/A), \tag{A2-6}$$

$$\partial_x \rho \sim -\rho_0(\nu_4 M' + \nu_5 M A'/A)/M, \tag{A2-7}$$

$$\partial_t a \sim a_0^2 M(\nu_6 M' + \nu_7 M A'/A), \tag{A2-8}$$

$$\partial_x a \sim -a_0(\nu_8 M' + \nu_7 M A'/A), \tag{A2-9}$$

where $M' = d_x M$, and

$$\begin{aligned} &\nu_1 = \frac{8}{\gamma+1}, \quad \nu_2 = \frac{4\gamma}{(\gamma+1)^2}, \quad \nu_3 = \frac{6}{\gamma+1}, \quad \nu_4 = \frac{6(\gamma+1)}{(\gamma-1)^2}, \\ &\nu_5 = \frac{2}{\gamma-1}, \quad \nu_6 = \frac{2\mu'\gamma(3\gamma-5)}{(\gamma^2-1)}, \quad \nu_7 = \frac{2\mu'\gamma(\gamma-1)}{(\gamma+1)^2}, \quad \nu_8 = \frac{4\mu'\gamma(\gamma-2)}{\gamma^2-1}. \end{aligned} \tag{A2-10}$$

If we further note that

$$\frac{a^2u}{a+u} \sim a_0^2\eta_1 M^2, \quad \frac{\rho a^3}{(a+u)^2} \sim a_0\rho_0\eta_2 M, \quad \frac{\rho a u(a+2u)}{(a+u)^2} \sim a_0\rho_0\eta_3 M, \tag{A2-11}$$

with

$$\eta_1 = \frac{2\gamma(\gamma-1)}{(1+\gamma\mu')(\gamma+1)^2}, \quad \eta_2 = \frac{\gamma^2\mu'}{(1+\gamma\mu')^2}, \quad \eta_3 = \frac{2\gamma\mu'(\gamma\mu'+2)}{(\gamma-1)(\gamma\mu'+1)^2}, \tag{A2-12}$$

then we may write

$$\partial_t\left(\frac{\rho a^2 u}{a+u}\right) \sim a_0^3\rho_0 M^2\left(\beta_1 M' + \beta_2 M A'/A\right), \tag{A2-13}$$

where

$$\beta_1 = \eta_1\nu_4 + \eta_2\nu_1 + \eta_3\nu_6, \quad \beta_2 = \eta_1\nu_5 + \eta_2\nu_2 + \eta_3\nu_7. \tag{A2-14}$$

Furthermore, we have

$$\partial_x(\rho a)\partial_t u - \partial_t(\rho a)\partial_x u \sim \rho_0 a_0^3 M(\beta_3(M')^2 + \beta_4 M M' A'/A), \tag{A2-15}$$

with

$$\begin{aligned}\beta_3 &= \nu_3(\alpha_2\nu_6 + \alpha_3\nu_4) - \nu_1(\alpha_2\nu_8 + \alpha_3\nu_4),\\ \beta_4 &= \nu_2\alpha_2(\nu_6 - \nu_8) + (\nu_3 - \nu_1)(\alpha_2\nu_7 + \alpha_3\nu_5),\end{aligned} \tag{A2-16}$$

and

$$\partial_t\left(\frac{1}{a+u}\right) \sim -(\kappa_1 M' + \kappa_2 M A'/A)/M, \tag{A2-17}$$

with

$$\kappa_1 = (\nu_1+\nu_6)/(\alpha_1+\alpha_3)^2, \quad \kappa_2 = (\nu_2+\nu_7)/(\alpha_1+\alpha_3)^2. \tag{A2-18}$$

Substitution into (8.2.6) yields

$$Q_1' = a_0^3\rho_0\left(\tau_1 M(M')^2 + \tau_2 M^2 M' A'/A + \tau_3 M^3(A'/A)^2\right) + (\kappa_1 M' + \kappa_2 M A'/A)Q_1/M, \tag{A2-19}$$

where

$$\tau_1 = \beta_3, \quad \tau_2 = \beta_4 - \beta_1, \quad \tau_3 = -\beta_2. \tag{A2-20}$$

We also have from (8.2.6) that

$$M' = -\zeta_1 M A'/A + \zeta_2 Q_1/(\rho_0 a_0^3 M^2), \tag{A2-21}$$

with

$$\begin{aligned}\zeta_1 &= \alpha_2\alpha_3^2/\left((\alpha_1+\alpha_3)(2+\alpha_2\alpha_3)\right),\\ \zeta_2 &= \left(1 - 1/(\alpha_1+\alpha_3)\right)/(2\alpha_1 + \alpha_1\alpha_2\alpha_3).\end{aligned} \tag{A2-22}$$

REFERENCES

ABRAMOWITZ, M. & STEGUN, I.A. 1965, *Handbook of Mathematical Functions*, Dover.

ARONS, A.B. 1954, Underwater explosion shock wave parameters at large distances from the charge, *J. Acoust. Soc. Am.* **26**, 343-45.

BAKER, G.R. & MOORE, D.W. 1989, The rise and distortion of a two-dimensional gas bubble in an inviscid liquid, *Phys. Fluids A* **1**, 1451-59.

BATCHELOR, G.K. 1967, *An Introduction to Fluid Dynamics*, Cambridge University Press.

BENJAMIN, T.B. 1987, Hamiltonian theory for motions of bubbles in an infinite liquid, *J. Fluid Mech.* **181**, 349-79.

BENJAMIN, T.B. & ELLIS, A.T. 1966, The collapse of cavitation bubbles and the pressures thereby produced against solid boundaries, *Phil. Trans. R. Soc. Lond. A* **260**, 221-40.

BLAKE, J.R. 1988, The Kelvin impulse: Application to cavitation bubble dynamics, *J. Aust. Math. Soc. Ser. B* **30**, 127-46.

BLAKE, J.R. & CERONE, P. 1982, A note on the impulse due to a vapour bubble near a boundary, *J. Aust. Math. Soc. Ser. B* **23**, 383-93.

BLAKE, J.R. & GIBSON, D.C. 1981, Growth and collapse of a vapour cavity near a free surface, *J. Fluid Mech.* **111**, 123-40.

BLAKE, J.R. & GIBSON, D.C. 1987, Cavitation bubbles near boundaries, *Ann. Rev. Fluid Mech.* **19**, 99-123.

BLAKE, J.R. & PROSPERETTI, A. 1989, Dynamics of underwater explosion bubbles, Final report to the Office of Naval Research, Grant No. N00014-89-J-1791.

BLAKE, J.R., TAIB, B.B. & DOHERTY, G. 1986, Transient cavities near boundaries. Part 1. Rigid boundary, *J. Fluid Mech.* **170**, 479-97.

BLAKE, J.R., TAIB, B.B. & DOHERTY, G. 1987, Transient cavities near boundaries. Part 2. Free surface, *J. Fluid Mech.* **181**, 197-212.

BRYANT, A.R. 1944, Photographic measurements of the size, shape and movement of the bubble produced by 1-oz charges of polar ammon gelignite detonated underwater at a depth of 3 feet, in Hartmann and Hill, 1950.

CHAHINE, G.L. 1977, Interaction between an oscillating bubble and a free surface, *Trans. ASME J. Fluids Eng.* **99**, 709-15.

CHAHINE, G.L. 1982, Experimental and asymptotic study of non-spherical bubble collapse, *Appl. Sci. Res.* **38**, 187-97.

CHAHINE, G.L. 1990, Numerical modelling of the dynamic behaviour of bubbles in non-uniform flow fields, in *Proc. 1990 Symposium on Numerical Methods for Multiphase Flows,* Toronto.

CHAHINE, G.L. & PERDUE, T.O. 1988, Simulation of the three-dimensional behaviour of an unsteady large bubble near a structure, in *Proc. 3rd Int. Colloq. on Bubbles and Drops,* Monterey.

CHESTERS, A.K. & HOFMAN, G. 1982, Bubble coalescence in pure liquids, *Appl. Sci. Res.* **38**, 353-61.

COLE, R.H. 1948, *Underwater Explosions*, Princeton University Press.

DeBOOR, C. 1978, *A Practical Guide to Splines,* Springer-Verlag, New York.

GIBSON, D.C. 1968, Cavitation adjacent to plane boundaries, in *Proc. 3rd Aust. Conf. on Hydraulic and Fluid Mechanics,* Institution of Engineers, Sydney, Australia, 210-14.

GIBSON, D.C. & BLAKE, J.R. 1982, The growth and collapse of bubbles near

deformable surfaces, *Appl. Sci. Res.* **38**, 215-24.

GUDERLEY, G. 1942, Starke kugelige und zylindrische Verdichtungsstösse in der Nähe des Kugelmittelpunktes bzw der Zylinderachse, *Luftfahrtforschung* **19**, 302-12.

GUERRI, L., LUCCA, G. & PROSPERETTI, A. 1981, A numerical method for the dynamics of non-spherical cavitation bubbles, in *Proc. 2nd Int. Colloq. on drops and bubbles,* California, 175-81.

HAMMITT, F.G., 1980, *Cavitation and Multiphase Flow Phenomena,* McGraw-Hill.

HARTMANN, G.K. & HILL, E.G. (Eds.), 1950, *Underwater Explosion Research,* Vol. II, Office of Naval Research, Washington, D.C.

HENSHAW, W.D., SMYTH, N.F. & SCHWENDEMAN, D.W. 1986, Numerical shock propagation using geometrical shock dynamics, *J. Fluid Mech.* **171**, 519-45.

HERRING, C. 1941, Theory of the pulsations of the gas bubble produced by an underwater explosion, *NDRC Division 6 Report C4-sr20*, and in revised form, dated 1949, in Hartmann and Hill, 1950.

HILLIAR, H.W. 1919, (British) Department of Scientific Research and Experiment Report RE 142 19.

HOLT, M. 1977, Underwater explosions, *Ann. Rev. Fluid Mech.* **9**, 187-214.

KEYS, D.A. 1921, A piezoelectric method of measuring explosion pressures, *Phil. Mag.* **42**, 473-88.

KIRKWOOD, J.G. & BETHE, H.A. 1942, Progress report on the pressure wave produced by an underwater explosion I, OSRD report no. 588.

KIRKWOOD, J.G. & BRINKLEY, S.R. 1945, Theory of the propagation of shock waves from explosive sources in air and water, OSRD report No. 4814.

KUCERA, A. 1991, A boundary integral method applied to the growth and collapse of bubbles near a rigid boundary, *J. Comp. Phys.* To appear.

KUCERA, A. & BLAKE, J.R. 1988, Computational modelling of cavitation bubbles near boundaries, in *Computational Techniques and Applications CTAC-87*, (Eds. J. Noye and C. Fletcher), North-Holland, 391-400.

LAMB, H. 1923, The early stages of a submarine explosion, *Phil. Mag.* **45**, 257-65.

LAMB, H. 1932, *Hydrodynamics*, Cambridge University Press.

LANDAU, L.D. 1945, On shock waves at large distances from the place of their origin, *Soviet Journal of Physics* **9**, 496-500.

LAUTERBORN, W. 1980, Cavitation and coherent optics, in *Cavitation and Inhomogeneities in Underwater Acoustics,* (ed. W. Lauterborn) Springer-Verlag, New York, 3-12.

LAUTERBORN, W. 1982, Cavitation bubble dynamics - new tools for an intricate problem, *Appl. Sci. Res.* **38**, 165-78.

LAUTERBORN, W. & BOLLE, H. 1975, Experimental investigations of cavitation bubble collapse in the neighbourhood of a solid boundary, *J. Fluid Mech.* **72**, 391-99.

LAUTERBORN, W. & HENTSCHEL, W. 1985, Cavitation bubble dynamics studied by high speed photography and holography: Part I, *Ultrasonics* **23**, 260-68.

LAUTERBORN, W. & VOGEL, A. 1984, Modern optical techniques in fluid mechanics, *Ann. Rev. Fluid Mech.* **16**, 223-44.

LIGHTHILL, M.J. 1949, The diffraction of blast I, *Proc. Roy. Soc. A* **198**, 454-70.

LONGUET-HIGGINS, M.S. 1989, Some integral theorems relating to the oscillation of bubbles, *J. Fluid Mech.* **204**, 159-66.

LONGUET-HIGGINS, M.S. & COKELET, E.D. 1976, The deformation of steep surface waves on water. I. A numerical method of computation, *Proc. Roy. Soc. A* **350**, 1-26.

LORD RAYLEIGH, 1917, On the pressure developed in a liquid during the collapse of a spherical void, *Phil. Mag.* **34**, 94-8.

LUNDGREN, T.S. & MANSOUR, N.N. 1991, Vortex ring bubbles, *J. Fluid Mech.* In press.

MASLOV, V.P. 1980, Propagation of shock waves in the isentropic nonviscous gas, *J. Sov. Math.* **13**, 119-63.

MILNE-THOMSON, L.M. 1960, *Theoretical Hydrodynamics*, MacMillan & Co. Ltd. London.

MOORE, D.W. 1963, The boundary layer on a spherical gas bubble, *J. Fluid Mech.* **16**, 161-76.

NAUDE, C.F. & ELLIS, A.T. 1961, On the mechanism of cavitation damage by non-hemispherical cavities in contact with a solid boundary, *Trans. ASME J. Basic Eng.* **83**, 648-56.

OGUZ, H.N. & PROSPERETTI, A. 1989, Surface-tension effects in the contact of liquid surfaces, *J. Fluid Mech.* **203**, 149-71.

OGUZ, H.N. & PROSPERETTI, A. 1990, A generalization of the impulse and virial theorems with an application to bubble oscillations, *J. Fluid Mech.* **218**, 143-62.

OSBORNE, M.F.M. & TAYLOR, A.H. 1946, Non-linear propagation of underwater shock waves, *Phys. Rev.* **70**, 322-28.

PAULL, R. & BLAKE, J.R. 1990, Conserved quantities for axisymmetric cavities near boundaries, *Bull. Aust. Math. Soc.* **41**, No. 2, 215-22.

PENNEY, W.G. 1941, British Report RC-142.

PENNEY, W.G. & DASGUPTA, H.K. 1942, British Report RC-333.

PENNEY, W.G. & PRICE, A.T. 1942, On the changing form of a nearly spherical submarine bubble, in Hartmann & Hill, 1950.

PLESSET, M.S. & CHAPMAN, R.B. 1971, Collapse of an initially spherical vapour cavity in the neighbourhood of a solid boundary, *J. Fluid Mech.* **47**, 283-90.

PLESSET, M.S. & MITCHELL, T.P. 1956, On the stability of the spherical shape of a vapour cavity in a liquid, *Quart. Appl. Math.* **13**, 419-30.

POCHÉ, L.B. 1972, Underwater shock-wave pressures from small detonators, *J. Acoust. Soc. Am.* **51**, 1733-37.

PORITSKY, H. 1952, The collapse or growth of a spherical bubble or cavity in a viscous fluid, *Proc. First U.S. Nat'l Congr. Appl. Mech., ASME,* 813-21.

PRASAD, P. & SRINIVASAN, R. 1988, On methods of calculating successive positions of a shock front, *Acta Mechanica*, **74**, 81-93.

PROSPERETTI, A. 1987, The equation of bubble dynamics in a compressible liquid, *Phys. Fluids* **30**, 3626-28.

RAMSAUER, C. 1923, Die massenbewegung des wassers bei unterwasserexplosionen, *Ann. d. Physik,* **72**, 265.

ROGERS, P.H. 1977, Weak-shock solution for underwater explosive shock waves, *J. Acoust. Soc. Am.* **62**, 1412-19.

ROSS CHAPMAN, N. 1985, Measurement of the wave form parameters of shallow explosive charges, *J. Acoust. Soc. Am.* **78**, 672-81.

SEDOV, L.I. 1945a, On certain unsteady compressible fluid motions, *Prik. Mat.*

Mekh. **9**, 293-311.

SEDOV, L.I. 1945b, On unsteady motions of a compressible fluid, *C.R. (Dokl.) Acad. Sci. URSS* **47**, 91-3.

SEYBERT, A.F., SOENARKO, B., RIZZO, F.J. & SHIPPY, D.J. 1985, An advanced computational method for radiation and scattering of acoustic waves in three dimensions, *J. Acoust. Soc. Am.* **77**, 362-68.

SHIFFMAN, M. & FRIEDMAN, B. 1944, On the best location of a mine near the sea bed, in Hartmann and Hill, 1950.

SHIMA, A., TAKAYAMA, Y., TOMITA, Y. & MIURA, N. 1981, An experimental study on effects of a solid wall on the motion of bubbles and shock waves in bubble collapse. *Acustica* **48**, 293-301.

SKEWS, B.W. 1967a, The shape of a diffracting shock wave, *J. Fluid Mech.* **29**, 297-304.

SKEWS, B.W. 1967b, The perturbed region behind a diffracting shock wave, *J. Fluid Mech.* **29**, 705-19.

SNAY, H.G. 1960, The hydrodynamic background of radiological effects of underwater nuclear explosions, *US Naval Radiol. Def: Lab. Rev. Lect.* No. 103, Vol. 2, 1-52.

SRINIVASAN, R. & PRASAD, P. 1985, On the propagation of a multi-dimensional shock of arbitrary strength, *Proc. Indian Acad. Sci. (Math. Sci.)* **94**, 27-42.

SWIFT, E. & DECIUS, J.C. 1947, Measurement of bubble pulse phenomena, III, Radius and period studies, in Hartmann and Hill, 1950.

TAIB, B.B. 1985, *Boundary Integral Methods Applied to Cavitation Bubble Dynamics*, Ph.D. Thesis, University of Wollongong, Australia.

TAYLOR, G.I. 1942, Vertical motion of a spherical bubble and the pressure sur-

rounding it, in Hartmann and Hill, 1950.

TAYLOR, G.I. 1950, The formation of a blast wave by a very intense explosion. I. Theoretical discussion, *Proc. Roy. Soc. A* **201**, 159-74.

TAYLOR, G.I. & DAVIES, R.M. 1943, The motion and shape of the hollow produced by an explosion in a liquid, in Hartmann and Hill, 1950.

TOMITA, Y. & SHIMA, A. 1986, Mechanisms of impulsive pressure generation and damage pit formation by bubble collapse, *J. Fluid Mech.* **169**, 535-64.

VOGEL, A., LAUTERBORN, W. & TIMM, R. 1989, Optical and acoustic investigations of the dynamics of laser-produced cavitation bubbles near a solid boundary, *J. Fluid Mech.* **206**, 299-338.

WALTERS, J.K. & DAVIDSON, J.F. 1962, The initial motion of a gas bubble formed in an inviscid liquid. Part 1. The two-dimensional bubble, *J. Fluid Mech.* **12**, 408-17.

WHITHAM, G.B. 1957, A new approach to problems of shock dynamics. Part I. Two dimensional problems, *J. Fluid Mech.* **2**, 146-71.

WHITHAM, G.B. 1958, On the propagation of shock waves through regions of non-uniform area or flow, *J. Fluid Mech.* **4**, 337-60.

WHITHAM, G.B. 1959, A new approach to problems of shock dynamics. Part II. Three-dimensional problems, *J. Fluid Mech.* **5**, 369-86.

WHITHAM, G.B. 1974, *Linear and Nonlinear Waves*, Wiley.

WHITHAM, G.B. 1987, On shock dynamics, *Proc. Indian Acad. Sci. (Math. Sci.)* **96**, No. 2, 71-3.